UNIVERSITY OF CALIFORNIA SAN DIEGO

Upwelling and circulation dynamics in the Southern California Current System

A Dissertation submitted in partial satisfaction of the requirements
for the degree Doctor of Philosophy

in

Oceanography

by

Caroline Ford Lowcher

Committee in charge:

Uwe Send, Chair
Theresa Chereskin
Sarah Gille
Art Miller
Mark Ohman
Geno Pawlak

2023

The Dissertation of Caroline Ford Lowcher is approved, and it is acceptable in quality and form for publication on microfilm and electronically.

University of California San Diego

2023

DEDICATION

To Dad, thanks for the inspiration, encouragement, and support over the years and for always being there for me.

TABLE OF CONTENTS

LIST OF FIGURES

LIST OF TABLES

ACKNOWLEDGEMENTS

I would like to acknowledge my advisor, Uwe Send, for training me to become a more critical thinker and a better scientist. I would like to acknowledge my PhD committee, Teri Chereskin, Sarah Gille, Art Miller, Mark Ohman, and Geno Pawlak, for their helpful feedback and comments over the years. Thanks to all of those in the Send lab for their dedication and hard work in maintaining the plethora of ocean observations, especially to Matthias Lankhorst for all of your help over the years.

Thank you to Mike Muglia and John Bane. Mike, for getting me started in the field while I was in high school, keeping me going while I was in college, and advocating for me all along the way, thank you. John, since college your excellent teaching, advising, and words of wisdom both in and outside of academia have been very helpful, thank you. I am so grateful to both of you for showing me the ropes, figuratively and literally, and for continuing to teach me things to this day.

A very special thank you to my parents who have showed me unconditional love and support throughout the PhD process and my whole life. My dad's passion for being in or on the water got me interested in the ocean at a young age and inspired me to pursue higher education in oceanography. I would like to thank my sisters for their endless positivity and cheering me on through the challenges. Thanks to my grandpa who instilled an importance of education starting at a young age and fostering my desire to learn, and to my family for rooting me on in my pursuits and endeavors. I would like to recognize the many mentors I have had for their guidance and their encouragement to pursue my goals and to my friends for bringing the fun in along the way.

Chapter 1, in part is currently being prepared for submission for publication of the material. Lowcher, Caroline; Send, Uwe; Lankhorst, Matthias. The dissertation author was the primary researcher and author of this material.

Chapter 2, in part is currently being prepared for submission for publication of the material. Lowcher, Caroline; Send, Uwe; Lankhorst, Matthias. The dissertation author was the primary researcher and author of this material.

Chapter 3, in part is currently being prepared for submission for publication of the material. Lowcher, Caroline; Send, Uwe; Lankhorst, Matthias. The dissertation author was the primary researcher and author of this material.

Chapter 4, in part is currently being prepared for submission for publication of the material. Lowcher, Caroline; Send, Uwe; Lankhorst, Matthias. The dissertation author was the primary researcher and author of this material.

VITA

2015 Bachelor of Science in Applied Mathematics, University of North Carolina at Chapel Hill

2015 Bachelor of Arts in Interdisciplinary Studies Oceanography, University of North Carolina at Chapel Hill

2023 Doctor of Philosophy in Oceanography, Scripps Institution of Oceanography, University of California San Diego

ABSTRACT OF THE DISSERTATION

Upwelling and circulation dynamics in the Southern California Current System

by

Caroline Ford Lowcher

Doctor of Philosophy in Oceanography

University of California San Diego, 2023

Uwe Send, Chair

Southern California is part of an eastern boundary upwelling system (EBUS). This region is ecologically productive and socioeconomically significant, and how EBUS will respond to future changes in climate is of scientific and societal interest. Long-term monitoring is a key component for assessing how EBUS will be impacted by climate change and long timeseries of mooring observations are the focus of this dissertation.

Anomalous poleward flow was observed in southern California prior to and during the 2014 marine heatwave and 2015 – 2016 El Niño. Prior to the El Niño, local forcing drove a strengthened wind stress curl and a more persistent Southern California Eddy (SCE). The poleward recirculation of the SCE into the Southern California Bight (SCB) brought more waters from the California Current and North Pacific Subtropical Gyre closer to the coast. During the 2015 – 2016 El Niño, remote forcing drove persistent elevated coastal sea levels which forced poleward geostrophic flows and advected tropical waters into the SCB.

A volume budget was performed for southern California and this motivated developing an upwelling index. The upwelling index includes cross-shore geostrophic transport by using sea level changes right at the coast, accounting for coastal processes such as coastally trapped waves. Low-frequency upwelling anomalies indicate decreased vertical transport during the 2014 – 2016 upwelling seasons concurrent with the large-scale climate phenomenon in these years. This upwelling index is a practical tool for analyzing upwelling requiring minimal in-situ observations.

The upwelling forcing is valuable for assessing the physical impact on the coastal ocean, but it may not represent the oceanic response to upwelling. Multiple physical and biogeochemical properties are used to examine the coastal oceanic response to upwelling alongside the upwelling forcing. Event statistics are calculated using the long record of in-situ measurements, in addition to investigating the low-frequency in-situ anomalies. EBUS are susceptible to harmful algal blooms and a particularly pronounced red tide is examined alongside the physical processes that supported the red tide.

INTRODUCTION

The southern California Current System (SCCS) is of intense oceanographic interest and socioeconomic relevance due to its sensitivity to climate phenomena and the pronounced impacts on biogeochemistry (e.g., shoaling of corrosive waters, Nam et al., 2011) and ecosystem (fish stocks, algal blooms, etc.). As part of an eastern boundary upwelling system (EBUS), the biologically productive waters in the SCCS shape and support the ecosystem structure and dynamics, contributing significantly to California's fisheries and shellfish industries. Concerns of climate change and the influence of climate phenomena, like El Niño, call to further our understanding of the multiple temporal scales of variability in these systems.

The SCCS is the southern sector of the California Current System (CCS) and includes the regional flows from southern California to Baja California. The circulation is characterized by alternating alongshore flows with seasonal features that establish the upwelling system. Offshore is the California Current (CC) which is an eastern boundary current whose relatively shallow and broad equatorward flow makes up the eastern limb of the North Pacific anticyclonic gyre. Inshore of the CC and over the continental slope is the poleward California Undercurrent (CU), with a subsurface maximum at 250 m (Lynn and Simpson, 1987) that may shoal onto the shelf (Lynn and Simpson, 1990; Gay and Chereskin, 2009; Todd et al., 2011). During fall and winter, a poleward coastal surface current can be found from Baja California to Point Conception, California, and this is the Southern California Countercurrent (SCC; Reid et al., 1958; Hickey, 1979). This flow may continue northward beyond Point Conception as the Davidson Current (Hickey, 1979; Lynn and Simpson, 1987) or it can meander offshore and get entrained in to the southward flowing CC. While the SCC can be continuous from Baja California, it may also

emerge as the eastern segment of the Southern California Eddy (SCE). The SCE is a seasonal cyclonic feature generated when a branch of the CC turns eastward roughly near the US-Mexico border (Reid et al., 1958; Hickey, 1979; Lynn and Simpson, 1987; Lynn and Simpson, 1990, Di Lorenzo 2003).

Part of the southern California circulation includes the overturning upwelling cell. In southern California the upwelling season typically occurs in spring when equatorward winds intensify and drive coastal upwelling in two ways. First, upwelling favorable winds cause upwelling by moving water offshore in a shallow surface Ekman layer known as coastal Ekman divergence. Another way water is upwelled is due to a decrease in the equatorward winds near the coast that creates a positive wind stress curl and generates net divergence in the surface water forcing water upward (Smith, 1968; Hickey, 1979). This is known as curl-driven upwelling. The cross-shore velocity structure consists of offshore Ekman flow near the surface that is fed by onshore flow at depth and the alongshore transport may be important at times for maintaining the volume budget (Smith, 1981; Werner and Hickey, 1983; Winant et al. 1987, Lentz and Chapman, 2004; Davis, 2010; McCabe et al., 2015). The overturning upwelling cell raises isopycnals near the coast resulting in cooler, nutrient-rich waters that fuel biological productivity. When equatorward winds weaken or reverse, the alongshore and cross-shore currents may reverse followed by a relaxation of isopycnals (Send et al., 1987; Winant et al. 1997, Cudaback et al., 2005; Melton et al., 2009). Within the upwelling season and in other times of the year, synoptic atmospheric processes cause intensification and relaxation in the wind field resulting in high-frequency upwelling events (Dorman and Winant 1995, Dorman et al. 2000, Fewings et al. 2016). These can drive large fluctuations in the physical and biogeochemical properties (Aguirre et al. 2021), shoal hypoxic and corrosive waters on the shelf (Grantham et al.

2004, Fabry et al. 2008, Feely et al. 2008), and set up cross-shore transport that impacts larval distribution and retention (Roughgarden et al., 1988; Farrell et al., 1991; Roughan et al., 2006).

Climate events, like El Niño, have suppressed upwelling or forced downwelling reducing the productivity normally found in coastal waters (Chelton et al., 1982; Simpson, 1984; Bograd and Lynn, 2001). El Niños are known to have physical and biological impacts along the US west coast. Sea surface temperatures (SST) increase, sea levels near the coast rise, and upwelling systems may be modified through changes in stratification and upwelling-favorable winds (Chelton, 1981; Norton et al., 1985; Jacox et al. 2015, Zaba and Rudnick, 2016). In turn this has several biogeochemical consequences such as a reduction in nutrient availability that reduces primary production and this consequence propagates through the food web and to higher marine trophic levels (McLain and Thomas, 1983; Bograd and Lynn, 2001; Chavez et al., 2002). What marks the 2015 - 2016 El Niño as rare is the preceding 2014 marine heatwave which initiated the basin-wide ocean warming that was augmented by the 2015 - 2016 El Niño. These climate phenomena raise broad questions about the anomalous behavior in the oceans and atmosphere that they generated and how they may have impacted ocean physical processes and the biogeochemistry.

The chapters in this dissertation examine these overlying questions in addition to characterizing the circulation and upwelling dynamics in southern California. Chapter 1 assesses anomalous poleward flow from in-situ observations along the coast and relates these circulation anomalies to local and remote forcings. A water mass analysis further contextualizes the extent of anomalous horizontal circulation in the years prior to, during, and after the 2014 marine heatwave and the 2015 – 2016 El Niño. Chapter 2 uses moorings and glider data to study the volume budget for southern California as well as to approximate the heat budget. The results

from the volume budget help derive an upwelling index using coastal tide gauges and a wind reanalysis which is then compared to other upwelling indices to assess its performance over high and low frequencies. Chapter 3 describes the physical and biogeochemical response to synoptic upwelling events and computes upwelling event statistics to present the interannual variability of synoptic upwelling in addition to investigating the low-frequency variability in upwelling. The horizontal velocities are typified over the upwelling and relaxation phases and the evolution of the flow field is examined. Chapter 4 reviews a red tide event that occurred in southern California in 2020, and the physical processes that conditioned the coastal ocean for the dominance of *Lingulodinium polyedra.*

CHAPTER 1

Anomalous Poleward Flow and Water Masses off Southern California related to the 2014 Marine Heatwave and the 2015 - 2016 El Niño

Abstract

The 2014 North Pacific marine heatwave and 2015 - 2016 El Niño set record high sea surface temperature anomalies off southern California. These climate events were responsible for the persistent anomalous warming that occurred throughout the region. During this time, and in the previous 1 - 2 years, coastal moorings off southern California show pronounced anomalous poleward flow along with changes in source water masses. Even after these large-scale events, recurring heatwaves in the North Pacific have prevailed, with some coinciding with poleward flow anomalies and alterations in source waters. Observations in the coastal ocean characterize the spatial extent of poleward flow and capture the frequency of poleward flow anomalies. The poleward flows in the years prior to and during the large-scale climate phenomena are driven by poleward wind stress anomalies and/or equatorial forcing. A water mass analysis of source water variability along isopycnal surfaces reveals changes in the horizontal advection consistent with the alongshore flow dynamics, i.e., more Pacific Subarctic Water and Eastern North Pacific Central Water during periods of regional poleward wind forcing and more tropical waters during periods of equatorial forcing. These alongshore currents and resulting changes in water mass composition may be important for regional changes in heat, stratification, and upwelling of source waters.

1.1 Introduction

During 2014 – 2015, the North Pacific marine heatwave and the El Niño brought anomalously warm ocean temperatures all along the US west coast (Bond et al. 2015; Zaba and Rudnick 2016; Jacox et al. 2016; Frischknecht et al. 2017; Chao et al. 2017). The 2014 marine heatwave was an unusual phenomenon where atmospheric forcing, i.e., wind stress and heat flux changes, due to teleconnections between the North Pacific and equatorial regions caused the water to warm (Wang et al. 2014; Bond et al. 2015; Di Lorenzo and Mantua 2016). This was followed by the 2015 - 2016 El Niño which continued these warm conditions. Furthermore, a series of marine heatwaves have occurred in the North Pacific causing additional warming of the upper ocean over 2018 – 2021 (Amaya et al. 2020; Fumo et al. 2020; Weber et al. 2021; Wei et al. 2021; Barkhordarian et al. 2022). Coastal currents measured by moorings in southern California captured unusual poleward flow prior to, during, and after the 2014 marine heatwave and the 2015 - 2016 El Niño. The moorings have continued to measure episodes of anomalous poleward flow over the more recent years, i.e., 2019 - 2021, during which several marine heatwaves occurred. The poleward flow anomalies observed by the moorings may be responsible for preconditioning and/or modifying the climate events and contributing to the anomalous oceanic conditions during this time.

The southern California Current System (SCCS) is the southern part of the California Current System (CCS) and includes the regional flows from southern California to Baja California that make up the eastern portion of the North Pacific subtropical gyre (Figure 1.1). The circulation is characterized by alongshore flows with seasonal features that establish the upwelling system. Offshore is the California Current (CC) which is an eastern boundary current with relatively shallow and broad equatorward flow. The CC makes up the eastern limb of the

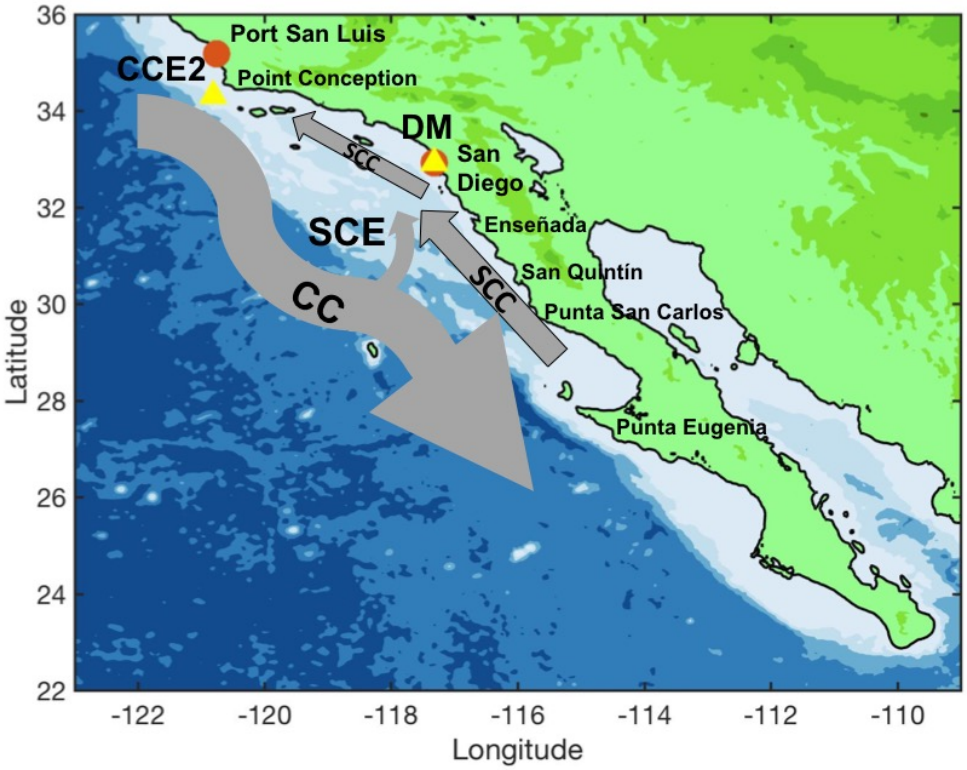

Figure 1.1: California and Baja California with the CCE2 and DM moorings (circles) and nearby tide gauges (triangles) at Port San Luis and San Diego. Arrows show the regional circulation and are not drawn to scale but schematically represent the general flow features.

North Pacific anticyclonic gyre. Inshore of the CC and over the continental slope is the poleward California Undercurrent (CU) whose subsurface maximum lies at 250 m (Lynn and Simpson, 1987). During fall and winter, a poleward coastal surface current can be found from Baja California to Point Conception, California and this is the Southern California Countercurrent (SCC; Reid et al. 1958; Lynn and Simpson 1987; Todd et al. 2011; Rudnick et al. 2017). If the flow is continuous northward beyond Point Conception, then this is referred to as the Davidson Current (Hickey 1979; Collins et al. 2003; Marchesiello et al. 2003). The SCC is found either as a continuous flow from Baja California or emerging as the eastern segment of the Southern California Eddy (SCE). The SCE is a seasonal cyclonic feature generated when a branch of the CC turns eastward roughly near the US-Mexico border (Reid et al. 1958; Hickey 1979; Lynn and Simpson 1987; Lynn and Simpson 1990; Di Lorenzo 2003). This branch bifurcates with one

limb going towards the south while the other bends northward into the Southern California Bight (SCB) supporting the SCC (Chereskin and Niiler 1994). In the SCB and off Baja California, near surface flows are typically southward during spring when upwelling winds are strongest. In summer and fall the winds relax and poleward flow develops (Reid et al. 1958; Lynn and Simpson 1987; Valle-Rodríguez and Trasviña-Castro 2017).

Another wind-driven current system in the eastern Pacific is south of the North Pacific subtropical gyre and includes the zonal equatorial currents. These currents are a response to the troughs and ridges in the thermocline set up by wind forcing associated with the Intertropical Convergence Zone (ITCZ). This is shown as a schematic in the larger inset in Figure 1.2. The

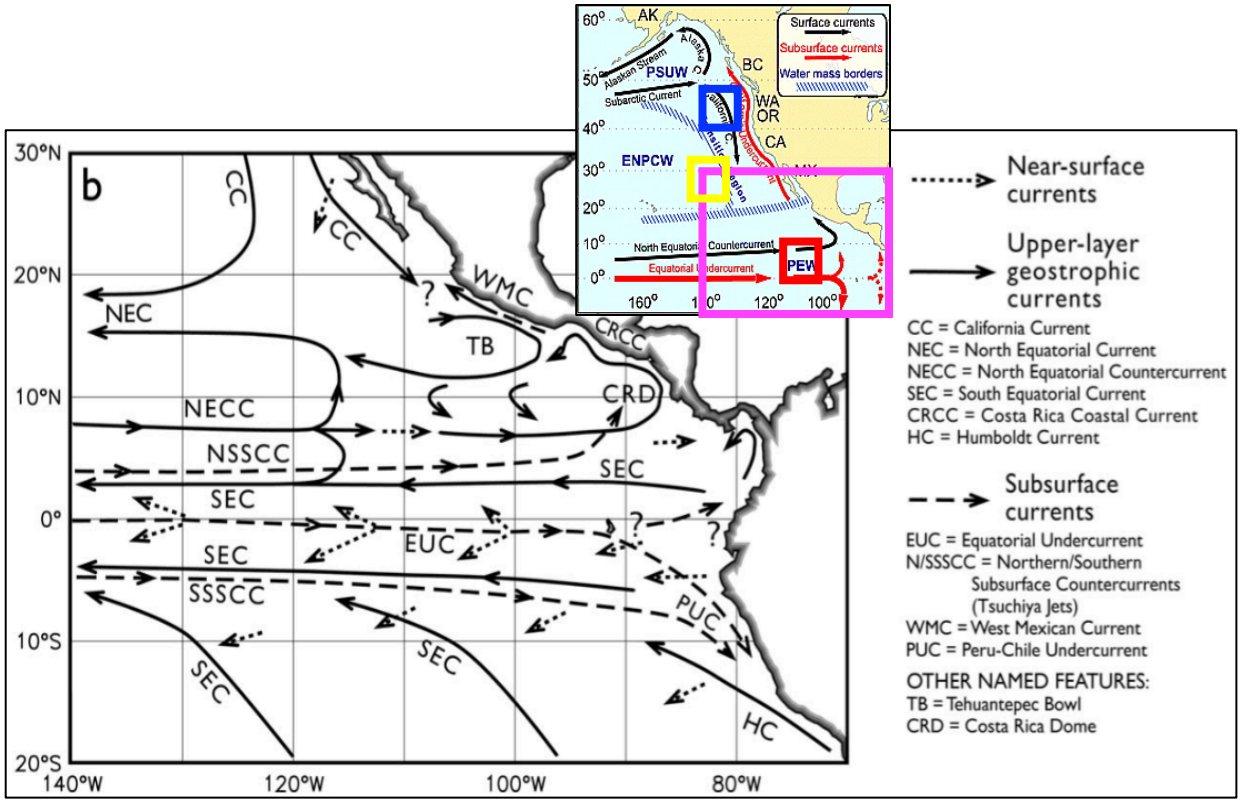

Figure 1.2: Larger panel is adopted from adopted from Kessler (2006) and schematically represents circulation in the eastern tropical Pacific. The subset in the upper right corner is modified from Thomson and Krassovski (2010) and illustrates the larger-scale circulation features in the eastern Pacific. The magenta box shows the geographical region of the larger panel. The blue box is the source region for Pacific Subartic Water (PSUW), the yellow box is the source region for Eastern North Pacific Central Water (ENPCW), and the red box is the source region for Pacific Equatorial Water (PEW) used in Section 1.4.

North Equatorial Countercurrent (NECC) carries warm tropical water from the warm pool in the western Pacific to the eastern Pacific. The NECC flows between 5°N and 10°N, and its meridional extent varies seasonally, reaching the coast in the fall and winter (Kessler 2006; Strub and James 2002b). Upon reaching the coastline, the NECC merges into the Costa Rica Coastal Current (CRCC), a northward flowing current on the east side of the Costa Rican dome that turns offshore near 13°N. At subthermocline depths, part of the CRCC is able to continue northward along the coast and becomes the West Mexican Current (WMC; Kessler 2006; Gómez-Valdivia et al. 2015). Around 17°N the WMC reaches the surface in association with strengthening of the local winds and flows up to the Gulf of California with poleward flow strongest in the second half of the year (Kessler 2006; Zamudio et al. 2007; Godínez et al. 2010; Gómez-Valdivia et al. 2015). The surface portion of this flow may become southward in spring during the upwelling season when the CC has a broader southward extent (Strub and James 2002b; Kessler 2006). Observations and model results indicate that this flow can cross the mouth of the Gulf of California and continue northward along Baja California under periods of persistent remote forcing, such as during El Niño (Godínez et al. 2010; Gómez-Valdivia et al. 2015). Even though the CRCC and the WMC are latitudinally contiguous, Kessler (2006) noted a distinct difference in the structure of these two poleward flows, suggesting that the two are separate and unrelated.

Poleward flow anomalies in southern California are possible via increased recirculation from the SCE or from more persistent poleward flow off Baja California. Regarding the former, a more coherent SCE can be attributed to sustained recirculation of offshore waters into the SCB that then continue northwards. Previous studies have demonstrated that the wind stress curl is an important formation mechanism for the SCE, and variability in the strength or distribution of the curl field can modify inshore poleward flow (Oey 1999; Di Lorenzo 2003). Regarding

continuous alongshore flow off the west coast of North America, there have been few observations made in the Northeast Pacific, and there is ambiguity in the interplay of regional currents across latitudes between Central America and Baja California that could contribute to the connectivity of poleward flows. Of particular interest are the two transition regions between the CRCC and the WMC and further north between the WMC, Gulf of California, and Baja California. In the first, it is possible for connectivity of poleward flows due to a leakage of CRCC waters east of the Tehuantepec Bowl (TB in Figure 1.2; Reyes-Hernández et al. 2016). South of the entrance of the Gulf of California, a cyclonic circulation can recirculate CC waters onshore and northward along Baja California when forced by the wind stress curl and offshore propagating Rossby waves (Godínez et al. 2010). Another mechanism for flow to cross the mouth of the Gulf of California is from eddy genesis at the coast on mainland Mexico near the entrance. Continuous anticyclonic eddy shedding elevates sea surface height (SSH) in the eddy footprint which forms a ridge-like feature that imparts poleward geostrophic flow on the offshore side of the ridge (Figure 1a in Zamudio et al. 2007).

Increased poleward flow in the SCB should coincide with changes in the composition of source water masses. Greater recirculation of the SCE is expected to bring fresher and cooler waters from the CC, whereas continuous alongshore flow from the south advects water with warmer and saltier properties. Changes in source water composition can aid in identifying the horizontal circulation features that are responsible for enhanced poleward flow. The forcing behind these changes can be remote, which can drive a continuous SCC along Baja California, or more locally driven sources, which can cause greater recirculation in the SCE. This distinction will be discussed next in the context of El Niño.

Teleconnections through the ocean and atmosphere linked to El Niño cause changes over large scales. El Niño oceanic teleconnections are remote disturbances in the tropical Pacific that move away from these regions. These teleconnections reach the extratropics and impact midlatitude systems via coastally trapped waves (CTWs). Equatorially-generated CTWs begin when westerly wind bursts in the western equatorial Pacific excite eastward propagating Kelvin waves (McPhaden et al. 1988). When the Kelvin waves reach South America, they generate CTWs that propagate northward along the North American west coast (Enfield and Allen 1980; Spillane et al. 1987; Ramp et al. 1997; Meyers et al. 1998). Reported propagation speeds of SSH range widely from 40 – 300 km/day (Enfield and Allen 1980; Huyer and Smith 1985; Meyers et al. 1998; Strub and James 2002b-c). The downwelling CTWs raise sea levels and subduct isopycnals. Within an El Niño event, multiple CTWs can be present in records of SSH and upper ocean heating (Meyers et al. 1998; Kosro 2002; Chen et al. 2016; Chao et al. 2017). The sequence of CTWs propagating poleward encourages continuous conditions of elevated coastal sea level, which may impart alongshore geostrophic flows. Anomalous poleward flow related to El Niño has been reported over various coastlines in the North Pacific, most notably during the 1982 - 1983 and 1997 - 1998 El Niño events (Huyer and Smith 1985; Kosro 2002; Durazo and Baumgartner 2002; Lynn and Bograd 2002; Strub and James 2002b-c). Both Kessler (2006) and Strub and James (2002b) present evidence of elevated coastal sea levels from the equator north to Mexico related to El Niño Southern Oscillation (ENSO) activity. This may encourage the CRCC to maintain its poleward trajectory along the coast rather than bending offshore (Kessler 2006). Further north near the Gulf of California, El Niño-driven elevated coastal SSH can cause a branch of the WMC to continue poleward along Baja California (Godínez et al. 2010). Such continuous low-latitude forcing that elevates coastal SSH and encourages poleward geostrophic

flow along the North American continent may support connectivity of poleward flows between the NECC, CRCC, and WMC (Strub and James 2002b; Kessler 2006; Godínez et al. 2010).

Atmospheric teleconnections related to El Niño occur over faster timescales, e.g., days to weeks, than El Niño oceanic teleconnections, e.g., months. Atmospheric teleconnections are associated with the strength and distribution of the North Pacific High and Low pressure systems, and they have been shown to alter local wind fields (Rasmusson and Wallace 1983; Alexander et al. 2002). This results in changes in the wind field and heat flux. Wind reversals may directly drive poleward flow during El Niño years and cause onshore transport (Simpson 1984; Huyer and Smith 1985; Ramp et al. 1997). Alternatively, weakened upwelling favorable winds may allow poleward flows to occur due to pre-existing alongshore pressure gradients (APGs; Hickey and Pola 1983; Melton et al. 2009; Fewings et al. 2015). Atmospheric teleconnections that cause changes in the SCCS will be referred to as local forcing, while oceanic teleconnections that cause changes in the SCCS will be referred to as remote forcing. The influence of local and remote forcing from El Niño varies along the US west coast with southern California exhibiting both types (McLain and Thomas 1983; Bograd and Lynn 2001; Strub and James 2002b-c; Hermann et al. 2009; Frischnecht et al. 2015).

Glider velocities in the SCCS found no evidence of significant poleward flow during the 2014 marine heatwave and the 2015 - 2016 El Niño (Zaba and Rudnick 2016, Rudnick et al. 2017). However, this result may be due to the low inshore temporal resolution of the glider as it makes cross-slope transects. Previous investigations of the 2015 - 2016 El Niño indicate remotely, e.g., CTWs, and locally, e.g., weakened winds, forced anomalies off California (Zaba and Rudnick 2016; Chao et al. 2017; Frischknecht et al. 2017). Both the remote and local forcing will be examined in this chapter regarding their influence on the observed anomalous poleward

flow. The mooring observations analyzed later in this chapter were collected over the last 1 - 2 decades and are among the few long-term in-situ timeseries that directly measure coastal currents along the west coast. The unusual poleward flow reported by the instruments in the 1 - 2 years prior to these climate phenomena and in subsequent years in which marine heatwaves occurred prompts us to ask whether the poleward flow anomalies are a local or large-scale phenomenon, what caused the flow anomalies, and whether they facilitated and impacted the climate events.

The organization of this chapter is as follows. Data acquisition and data processing are described in Section 1.2. This section also reviews the alongshore momentum balance and describes the methods used in this chapter to assess the poleward flow anomalies and the impact they had on the SCCS. Section 1.3 presents analysis of the interannual variability of flow anomalies over the last two decades and the roles of remote and local forcing. The anomalous forcing of alongshore currents is discussed in context of basin-scale climate variability, and this is followed by a water mass analysis in Section 1.4 to examine the impact of poleward flows in the SCB prior to the 2014 - 2016 climate phenomena. The alongshore spatial connectivity of poleward flow anomalies is considered in Sections 1.3 and 1.4, and the key results are summarized in Section 1.5.

1.2 Data and Methods

1.2.1 Data Sets

Two multidisciplinary surface moorings have been deployed off Point Conception, California (CCE2) and Del Mar, California (DM) since 2010 and 2006, respectively (Figure 1.1). CCE2 is 25 km offshore and the bottom depth is about 840 m deep, and DM is 5 km offshore and in 90 m water depth. Downward looking 75 kHz and 300 kHz RD Instruments Workhorse Broadband acoustic Doppler current profilers (ADCP) are mounted on the CCE2 and DM

moorings, respectively, and measure velocity over ~15-500 m water depths at CCE2 and over ~5-100 m water depths at DM. ADCP observations are daily averaged and vertically averaged over 4 m bins at CCE2 and over 2 m bins at DM. At CCE2 a current meter was deployed in 2010 instead of an ADCP, so for this year velocity measurements were made only at 20 m depth, which biases vertically averaged horizontal velocities for this year. The DM and CCE2 velocity measurements are presented in Section 1.3 as part of the anomalous poleward flow discussion. Both moorings are equipped with temperature, salinity, and dissolved oxygen sensors. At DM the sensors are deployed at 35 and 90 m depths and at CCE2 these measurements are made at 76 m depth. These measurements are used in the water mass analysis in Section 1.4.

SSH is downloaded from the Copernicus Marine and Environment Monitoring Service (CMEMS) GLORYS product for examining coastal SSH anomalies (SSHa) over the North Pacific. The GLORYS product is an ocean reanalysis with 1/12˚ horizontal resolution and daily average outputs. Additional information on the generation and forcing of this product is given in Lellouche et al. (2021). GLORYS SSHa are useful in the coastal ocean where altimetry data are questionable and in-situ measurements of sea level are lacking. This data set is used in Section 1.3 as part of the analysis on anomalous poleward flow. Comparisons of SSHa from GLORYS with US west coast tide gauges show good agreement and high correlations providing confidence for utilizing this reanalysis product in understanding sea level variability (Amaya et al. 2022). The GLORYS SSH data is available from 1993 - mid-2020 but it is not run after mid-2020, so to extend sea level coverage from mid-2020 to early 2022 another sea level product from CMEMS is used that comes from their forecasting product, the Global Ocean Physics Analysis and Forecast.

The CMEMS Forecast product has the same spatial resolution as the GLORYS product. The two products overlap in the first five months of 2020, which allows for a comparison in sea level. Sea level from the forecasting product is lower than sea level from GLORYS, so a site-dependent correction is made for this bias. The correlations and root mean square (rms) errors between the GLORYS and the adjusted Forecast daily sea level data were estimated at San Diego and Port San Luis over January 2020 – May 2020 and are listed in Table 1.1. The adjusted Forecast data are also compared against daily tide gauge data over January 2020 – December 2021, where both products have the temporal mean removed (Table 1.1). A description of how the tide gauge data are handled is given below. Like Amaya et al. (2022), we find that GLORYS data are well correlated with tide gauge measurements when compared over January 1993 – May 2020, where both products have the temporal mean removed (Table 1.1).

Table 1.1: Correlations (*R*) and rms errors (RMSE) between different sea level products. Correlations between the CMEMS GLORYS and the adjusted Forecast products use daily data from Jan. 2020 – May 2020, correlations between the adjusted CMEMS Forecast product and daily tide gauge data are from Jan. 2020 – Dec. 2021, and correlations between the CMEMS GLORYS product and tide gauges are from Jan. 1993 – May 2020. Time periods for correlation calculations are based on how long the daily data products overlap one another. Correlations between the adjusted CMEMS Forecast product and the tide gauges as well as correlations between the CMEMS GLORYS product and the tide gauges have the temporal mean removed over the comparison period since the different products have different offsets.

	San Diego					**Port San Luis**			
	Forecast Adjusted		GLORYS			Forecast Adjusted		GLORYS	
	R	RMSE (m)	*R*	RMSE (m)		*R*	RMSE (m)	*R*	RMSE (m)
GLORYS	0.98	0.008				0.98	0.010		
Tide Gauge	0.74	0.032	0.92	0.029		0.74	0.036	0.93	0.026

Additionally, CMEMS distributes a gridded altimetry product that provides absolute dynamic topography (ADT), which is the sum of the mean dynamic topography and sea level anomaly. This product is made on a 0.25° grid with daily output and covers 1993 to 2022. These

sea level data are used in the more offshore regions in the SCCS and are incorporated in the analysis in Section 1.3 regarding alongshore poleward flows. Altimetry SSH is also part of the water mass analysis performed in Section 1.4 and is used to approximate the SCE. Additionally, CMEMS provides surface geostrophic currents derived from the altimetry sea level data. Geostrophic currents are utilized in Section 1.4 where they are incorporated as a component in approximating the total flow field, and the particular use of these currents is discussed in detail under that section.

Daily tide gauge data at Port San Luis (PSL) and San Diego (SD) are provided by the University of Hawaii Sea Level Center (1993 – 2019; Caldwell et al. 2015) and NOAA's Center for Operational Oceanographic Products (2020 – 2021; Figure 1.1). Tide gauge data have the trend removed over 1993 - 2021 and adjusted sea level is obtained by applying an inverse barometer correction. Surface pressure for this correction is gathered from National Centers for Environmental Prediction (NCEP) North American Regional Reanalysis (NARR; Mesinger et al. 2006). Coastal sea level measurements from the tide gauges support the discussion of anomalous poleward flow in Section 1.3.3.

To represent the wind field in the eastern North Pacific, the Cross-Calibrated Multi-Platform (CCMPv2) product from Remote Sensing Systems provides a gridded reanalysis wind product that covers the global ocean and uses satellite, buoy, and ERA Interim model wind data at a spatial resolution of 0.25° (Mears et al. 2022). Data are produced 6-hourly, calibrated to be 10 m winds, and are extracted over 2000 - 2022. Wind stress is computed as,

$$\boldsymbol{\tau} = \rho_a c_d \boldsymbol{U}^2, \tag{1}$$

where ρ_a is the density of air, c_d is the drag coefficient, and $\boldsymbol{U}$ contains the u and v components of the wind velocity. The drag coefficient is parameterized using the approach demonstrated in

Edson et al. (2013) that is originally derived in Hersbach (2011). Wind stress is daily averaged and has an 80-day low-pass filter applied. These data are utilized in the assessment of the dynamics of poleward flow in Section 1.3. Additionally, in Section 1.4 a second application of the wind data is required to approximate the contribution of Ekman currents to the total flow. More information on this approach is provided in Section 1.4.

Hydrographic data from the World Ocean Database (WOD) 2013 (Boyer et al. 2013) were extracted for the water mass analysis in Section 1.4. Water mass properties downloaded were temperature, salinity, and dissolved oxygen. Data selection was made using the *WODselect* tool (https://www.nodc.noaa.gov/OC5/SELECT/dbsearch/dbsearch.html). As in Bograd et al. (2019), these data were obtained from three 10° x 10° boxes centered on 45°N, 135°W; 27°N, 139°W, and 5°N, 108°W (Figure 1.2), and are representative of Pacific Subarctic Upper Water (PSUW), Eastern North Pacific Central Water (ENPCW), and Pacific Equatorial Water (PEW), respectively.

1.2.2 Alongshore Momentum Balance

An objective of this chapter is to assess the anomalous poleward flow. The alongshore momentum balance is presented, and previous results are reviewed for the balance of terms in this equation on the shelf and upper slope. Then, the different ways poleward flow can arise from the alongshore momentum equation are examined.

The linearized depth-averaged alongshore momentum equation can be written as,

$$v_t + fU = -\rho^{-1} p_y + (\rho H)^{-1}(\tau_y^w - \tau_y^b), \quad (2)$$

where the acceleration and the Coriolis terms are on the left-hand side of the equation, balanced by the alongshore pressure gradient (APG), the wind stress, and the bottom friction terms on the right-hand side. In equation (2), ρ is the seawater density and H is the water depth. Previous

work has suggested that the Coriolis term is small or uncorrelated with other terms in the alongshore momentum equation, leaving the momentum balance between the local acceleration, the APG, the wind stress, and the bottom friction (Lentz and Winant 1986; Hickey et al. 2003).

Nearshore and on the inner shelf in southern California, the surface and bottom layers overlap, and much of the forcing is explained by the frictional terms in equation (2; Lentz and Winant 1986). However, further north off northern California, Lentz (1994) reported that both the wind stress and the APG drive inner shelf flows. The local acceleration helps to balance the forcing terms in equation (2), but the Coriolis term has been found to be uncorrelated with these other terms on the shelf and is often assumed to be not as important in the momentum balance (Lentz and Winant 1986; Hickey et al. 2003). Moving further away from the coastline, on the mid and outer shelves the influence of the bottom friction term decreases while the APG becomes more important (Lentz and Winant 1986; Harms and Winant 1998; Hickey et al. 2003). Offshore of the shelf and on the upper slope, the Coriolis term may be more important in the alongshore momentum balance, and away from frictional boundary layers in southern California the Coriolis term may be balanced by the barotropic APG on longer periods, e.g., approximately monthly and longer (Connolly et al. 2014). Hickey et al. (2003) found that on the upper slope and shelf in the SCB up to half of the velocity variance is explained by the APG and the wind. Thus, previous work has demonstrated the significance of both the wind stress and the APG as important forcing terms in the alongshore momentum balance on the shelf and upper slope.

Using equation (2), different scenarios are examined that drive poleward flow based on the relative strength of the forcing terms in this equation. When the APG term exceeds the surface frictional forcing, then the APG dominates and accelerates the alongshore flow. The large-scale APG may be related to the seasonality of the gyre-scale circulation, and changes in

steric height along the coast can alter the direction of the coastal sea surface slope (Sturges 1974; Reid and Mantyla 1976; Hickey and Pola 1983). Reid and Mantyla (1976) found a mean annual poleward decrease in sea elevation over Baja California and southern California. These results suggest a poleward APG force present throughout most of the year for this area; however, this is not equivalently reflected in the flow regime. Southward flow over the shelf and offshore persists much of the year in the SCCS despite a poleward APG force. This region is heavily influenced by the wind stress. During the upwelling season, equatorward winds dominate driving southward surface flows over the shelf, but when these winds weaken during the relaxation season the APG becomes more influential on coastal currents (Harms and Winant 1998; Fewings et al. 2015). At higher frequencies, intermittency in the wind forcing gives rise to relaxation events in between upwelling episodes. During the relaxations when the wind stress is weaker, poleward flow develops (Send et al. 1987; Winant et al. 2003; Cudaback et al. 2005; Melton et al. 2009; Vazquez and Gomez-Valdes 2018).

While the APG is considered a forcing term, it is also an oceanic response to the wind field. In particular, when alongshore variations exist in the alongshore winds, the coastal response can be a gradient in sea level. It has been shown that in-situ measurements, e.g., currents and temperature, in southern California are correlated best with winds to the south of the SCCS suggesting that remote propagation from regions south of the SCCS are significant (Lentz and Winant 1986; Hickey et al. 2003; Pringle and Riser 2003). Wind-driven effects at latitudes below those of the SCCS can generate CTWs that propagate poleward. The poleward propagation of CTWs can be evident in the sea level and observed sites of wind-generated CTWs include regions off central America, mainland Mexico, and Baja California (Enfield and Allen 1983; Zamudio et al. 2002; Zamudio et al. 2008; Flores-Vidal et al. 2014). One way to generate

CTWs and influence the APG is to have an alongshore variation in the alongshore wind field. For example, a wind relaxation to the south may cause a sea level convergence in this southerly region that imposes a poleward pressure gradient force. Another way the wind field can alter the APG is through alongshore variations in the wind stress curl. Oey (1999) found that alongshore gradients in the wind stress curl induce a sea level difference responsible for forcing poleward flows. In southern California, the equatorward weakening in the wind stress curl (Winant and Dorman 1997; Oey 1999; Di Lorenzo 2003) would drive a poleward decrease in the sea level. These few examples reveal how the pressure gradients in the coastal ocean respond to wind forcing.

Lastly, equation (2) shows that when upwelling-favorable winds reverse they can directly push water poleward (Huyer and Smith 1985; Lentz and Winant 1986). This happens in wintertime when storms off California drive poleward winds that push water poleward on the shelf off Point Conception and in the Santa Barbara Channel (Cudaback et al. 2005; Melton et al. 2009). Off of Central America and mainland Mexico tropical storms and hurricanes form in the summer and fall. On rare occasions these storms may track up to Baja California and southern California and are characterized by poleward wind anomalies that can force coastal currents (Lentz and Winant 1986; Wei et al. 2021).

1.2.3 Alongshore Velocity Anomaly Regression and Regression Setup

The alongshore momentum balance is used to perform a regression analysis. The objective of the regression analysis is to assess whether interannual variability in the low-frequency poleward flow anomalies at DM and CCE2 can be replicated by the forcing terms in equation (2), namely the APG and the wind stress respectively. With the APG term, the interest is in how this term is influenced by remote forcing generated in regions south of southern

California. At low frequencies, the local acceleration term in equation (2) becomes negligible, and equation (2) simplifies to,

$$0 = -\rho^{-1}p_y + (\rho H)^{-1}(\tau_y^w - \tau_y^b), \quad (3)$$

where the Coriolis term is also dropped. Near a coastal boundary this term must become negligible and previous studies have found this term to be uncorrelated with the other terms in equation (3) on the shelf (Lentz and Winant 1986; Hickey et al. 2003). While equation (3) uses the local APG, the local APG does not distinguish between remote forcing originating from equatorial dynamics, e.g., oceanic teleconnections (Enfield and Allen 1980; Meyers et al. 1998), versus the wind-driven remote forcing off central America, mainland Mexico, or Baja California (Enfield and Allen 1983; Zamudio et al. 2002; Zamudio et al. 2008; Flores-Vidal et al. 2014). All of these signals can propagate into southern California and modify the local APG. Therefore, since the local APG does not separate remote forcing from the multiple regions south of southern California, the local APG is approximated as a function of remote forcing from multiple regions south of southern California. Over these lower frequencies, the remote pressure signals propagate into southern California at a lag that is negligible, and the local APG is modeled as,

$$p_y \approx p_y^{QP} + p_y^1 + p_y^2 + p_y^3 + p_y^{res}. \quad (4)$$

In equation (4), p_y^{QP} is the gyre-scale APG capturing equatorial and low latitude processes between the equator and Costa Rica (Figure 1.3). This term reflects oceanic teleconnections like El Niño Kelvin waves that reach South America and propagate to higher latitudes. The next three terms in equation (4) are p_y^1, p_y^2, and p_y^3 and they denote the APGs off of Central America, mainland Mexico, and Baja California, respectively. Lastly, p_y^{res} is a residual APG term that accounts for all other processes influencing the local APG. Remote forcing is a factor that can modify the local APG, in addition to other processes that can influence the APG. Since the

objective is to understand if/how remote forcing caused the observed poleward flow anomalies, the APG is modeled in equation (4) to investigate this idea.

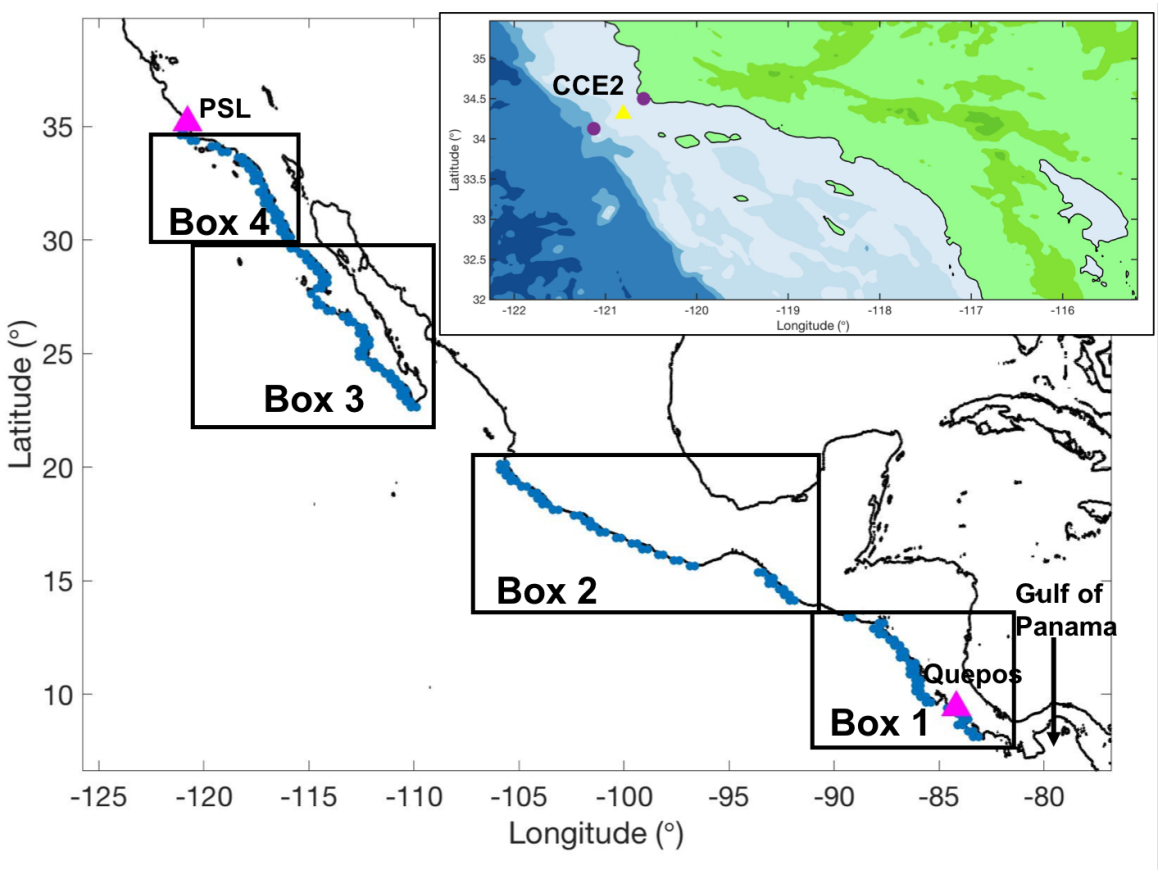

Figure 1.3: CCMPv2 grid cells used for averaging coastal wind stress. Black boxes outcrop the four regions where coastal alongshore wind stress is averaged. Box 1 is Central America, Box 2 is over mainland Mexico, Box 3 represents Baja California, and Box 4 is the SCCS. Magenta triangles are the coastal sea level locations used in the gyre-scale APG. The subset shows the locations, Point Conception and ~60 km offshore, where SSH is taken to estimate geostrophic velocity at CCE2. The CCE2 mooring is marked by the yellow triangle.

For the regression analysis, p_y^{QP} is approximated using coastal sea level at Quepos, Costa Rica and Port San Luis (PSL), USA (Figure 1.6). Given the good agreement of the GLORYS and the CMEMS Forecast products with the tide gauge data (Table 1.1), SSH from the GLORYS (1993 - 2020) and the CMEMS Forecast (2020 - 2022) products are obtained at Quepos and PSL. Both locations have the sea level detrended over the record. The southerly station is selected to be at this latitude because it is approximately where the NECC reaches the coast. Secondly, the

latitudinal meanderings of the ITCZ and corresponding trade winds set up localized currents that decorrelate the local sea level in the Gulf of Panama from gyre-scale changes in SSH (Enfield and Allen 1980). This suggests selecting a location outside of the Gulf of Panama. Additionally, equatorial Kelvin waves that propagate poleward as CTWs have a phase speed of ~180 km/day (Enfield and Allen 1980), which implies a lag of ~15 days between Quepos and PSL and this is negligible at the low frequencies that will be investigated. Therefore, the sea level difference between Quepos and PSL is used instead of the local sea level difference around Quepos. By taking the large-scale APG between Quepos and Port San Luis, equatorial processes, e.g., equatorial Kelvin waves, that reach subtropical latitudes and higher are included. Over low frequencies, an individual CTW event may not be significant but if multiple CTWs are generated this signal should produce a cumulative change in the low-pass filtered APG. Previous studies have reported that during El Niños there are several propagating sea level disturbances that originate at low latitudes and propagate poleward (Enfield and Allen 1980; Meyers et al. 1998; Kosro 2002), and when filtered these events should reveal a cumulative positive SSHa.

The pressure gradient terms p_y^1, p_y^2, and p_y^3 in equation (4) are, in part, forced by the wind field in these regions. The wind field and variability in the wind forcing can cause a sea level change at the coast. In the Northern Hemisphere and on the west coast this disturbance propagates poleward as a CTW. To approximate this influence of the wind field on the APGs off Central America, mainland Mexico, and Baja California, the pressure gradient is simply modeled as the alongshore wind stress. For each of these regions, coastal alongshore wind stress is averaged within ~60 km of the coast and over the latitudes of each region to create a single timeseries of the wind field. The latitudinal extent of these regions is illustrated by the boxes in Figure 1.3 and listed in Table 1.2.

With the pressure gradient term in equation (3) discussed, the next term to estimate is the local wind forcing in the SCCS. This component is accounted for by averaging the coastal winds in southern California, similarly to how the alongshore wind stress was treated in the three remote regions. The geographical extent of the winds used for the SCCS is illustrated in Figure 1.3 and listed in Table 1.2.

Table 1.2: Input variables used for the velocity regression analysis. Also listed are the data sources for each input variable, the latitudinal range of variable, and the wind box in Figure 1.3 that the wind region corresponds to.

Input Variable	Data Source	Latitudinal Range	Wind Stress Box
Gyre-scale APG	GLORYS, CMEMS Forecast	9.5° - 35°N	
Central American wind stress	CCMPv2	9.5° - 13.5°N	Box 1
Mainland Mexico wind stress	CCMPv2	14° - 20°N	Box 2
Baja California wind stress	CCMPv2	22.5° - 29.5°N	Box 3
SCCS wind stress	CCMPv2	30° - 34.6°N	Box 4

The final term in equation (3) is the bottom stress. This term is approximated as,

$$\tau_y^b = \rho r v, \tag{5}$$

where r is a linear bottom drag coefficient with units of velocity and is taken to be 5×10^{-4} m/s consistent with other studies in southern California (Lentz and Winant 1986; Hickey et al. 2003; Pringle and Riser 2003). In equation (5), v is the depth-averaged alongshore velocity. At CCE2, the velocity is averaged over the upper 100 m, presuming that other forces remove momentum such as frontal instabilities, eddies, and westward propagating Rossby waves. For instance, alongshore winds are typically upwelling favorable year-round and can drive upwelling fronts that form off headlands and detach from the coastline (Atkinson et al. 1986; Castelao et al. 2006; Kahru et al. 2012). Off Point Conception, eddies have been documented to occur in the western

part of the Santa Barbara Channel (Oey 1996; Harms and Winant 1998; Nishimoto and Washburn 2002; Brzezinski and Washburn 2013). Furthermore, model data of the alongshore flow field in the vicinity off Point Conception illustrate offshore propagating signals with phase speeds in agreement with Rossby wave dynamics (Todd et al. 2011). The proximity of the CCE2 mooring located off the headland at Point Conception subjects it to these different processes which may remove momentum from the system in the upper ocean. These processes are separate from the influence of bottom stress, but they will be parameterized similarly.

Using the approximations of the bottom friction, the wind stress, and the APG, equation (3) is rewritten as,

$$\mathrm{r}H^{-1}v = \rho^{-1}\left(a_1 p_y^{QP} + H^{-1}(a_2\tau^{w_1} + a_3\tau^{w_2} + a_4\tau^{w_3})\right) + a_5(\rho H)^{-1}\tau^{w_4}, \qquad (6)$$

where a_i are the regression coefficients and the terms on the right-hand side will be regressed against the alongshore velocity. This equation shows how the proxies for the APG and the alongshore wind stress will be regressed against the alongshore velocity. It is emphasized that the residual term, p_y^{res}, is not included in equation (6) because the objective is to understand how much of the remote forcing can explain the poleward flow anomalies. All input variables used in the regression analysis are listed in Table 1.2 and these variables are the same for the regression analysis at DM and CCE2.

Given the number of gaps and the shorter length of the CCE2 ADCP timeseries, a proxy of the upper 100 m averaged alongshore flow is created to include variability from the decade prior to the ADCP record. This extends coverage from 2010 - 2021 to 2000 - 2021, thus adding an additional decade to the analysis. Alongshore geostrophic flow is computed from coastal SSH and altimetry measurements ~60 km offshore to represent the alongshore flow off Point Conception (Figure 1.3). Coastal SSH at Point Conception comes from monthly low-passed

GLORYS data for 2000 – mid-2020 and the CMEMS Forecast data from mid-2020 - 2022. The choice for using altimetry data offshore at ~60 km is to capture the average flow between the coast and ~60 km offshore. This is approximately twice the distance offshore as the CCE2 mooring. A correlation analysis (not presented) indicated that geostrophic flow utilizing the offshore location at ~60 km is better correlated with the upper 100 m averaged flow from the CCE2 ADCP than with geostrophic velocities that used SSH at 30 km offshore.

The linear best fit of the geostrophic velocity to the upper 100 m averaged flow at CCE2 agrees well with the ADCP observations (Figure 1.4). Even though the geostrophic proxy of the flow does not include baroclinic changes with depth, the adjusted geostrophic velocity in Figure 1.6 has a correlation of 0.83 and a rms error of 0.056 m/s suggesting that it is a suitable approximation of the upper 100 m averaged flow.

All timeseries used in the regression analysis have the annual cycle removed and are low-pass filtered over 80 days to focus on the low-frequency interannual variability. At DM the annual cycle is computed from 2006 - 2021 and at CCE2 the annual cycle is computed over 2000 - 2021. The velocity anomalies are annually averaged for the regression analysis. The DM

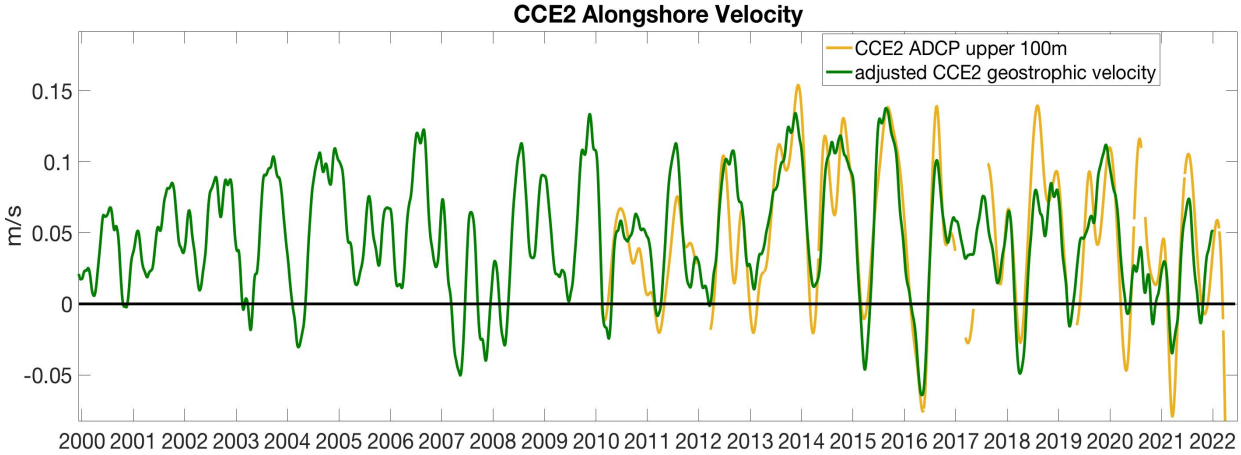

Figure 1.4: CCE2 ADCP velocities averaged over the upper 100 m verse geostrophic velocities scaled and offset to best fit the ADCP velocity timeseries. The correlation between the two timeseries is 0.83 and the rms error is 0.056 m/s. The geostrophic timeseries is scaled by a factor of 0.795 and has an offset of 0.047 m/s to best match the ADCP observations.

alongshore velocity annual cycle is a minimum in March, so the averaging period starts in March and goes until February of the next year (Figure 1.5). At CCE2 the minimum occurs ~3 weeks later, so the averaging period starts in April.

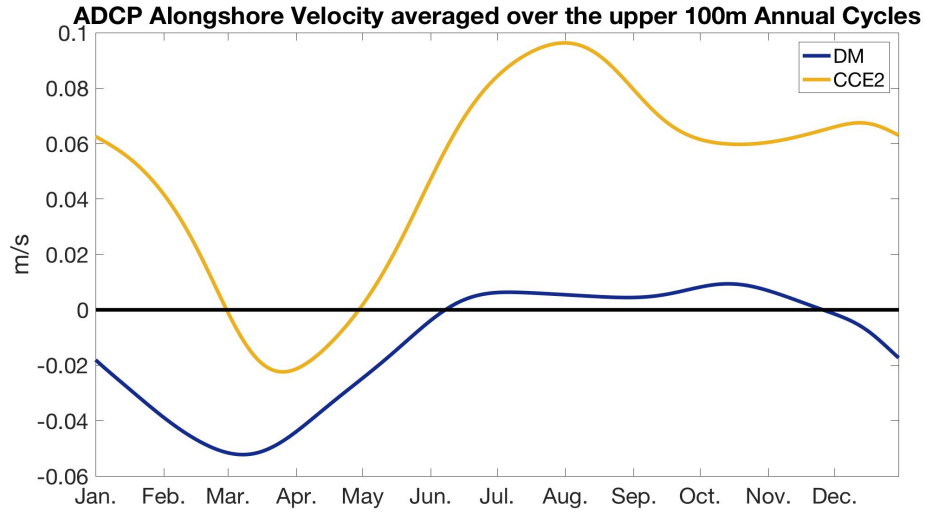

Figure 1.5: Annual cycle of alongshore velocity from ADCP data at DM and CCE2. For DM this is depth-averaged velocity and for CCE2 this is velocity averaged in the upper 100 m.

The regression will be repeated using only the gyre-scale APG and one set of winds. This was not known a priori, but it will be shown in Section 1.3 that the reduced regression reproduces much of the variability as the full regression. At DM the reduced regression uses the Baja California winds because these winds have a higher correlation with the depth-averaged alongshore flow than the SCCS wind stress (not shown), in agreement with other findings (Lentz and Winant 1986, Hickey et al. 2003). At CCE2, the adjusted geostrophic flow is best correlated with the SCCS wind stress (not shown), so this is used in the reduced regression.

1.2.4 Water Mass Inverse Problem and Solution Method

To understand the impacts of the poleward flow anomalies, the water mass composition is evaluated in Section 1.4. This section reviews the regional water masses, presents the water mass inverse problem, and explains the linear inverse method developed to determine the water

mass composition from the in-situ measurements at the coastal moorings. Then, the water mass property fluctuations, which are solved for as part of the method developed for determining the composition, are presented to demonstrate the reasonable solutions from the newly developed inverse method. A more thorough examination of the solutions that justifies using these results is reported in Appendix A.

1.2.4.1 Regional Water Masses

In the eastern North Pacific, there are three main source water masses (Tibby 1941, Reid et al. 1958, Roden 1971, Thomson and Krassovski 2010, Bograd et al. 2019). These are the Pacific Subarctic Upper Water (PSUW) from the North Pacific near the Gulf of Alaska, the Eastern North Pacific Central Water (ENPCW) from the North Pacific subtropical gyre, and the Pacific Equatorial Water (PEW) which originates from lower latitudes (Figure 1.2). PSUW is fresher, cooler, and oxygen-rich due to surface cooling and freshwater input from precipitation, riverine output, and ice melt and it is carried equatorward by the CC (Roden 1971). PEW is warmer, saltier, and oxygen-poor and it is brought poleward via the CU and the SCC (Wyrtki 1967). ENPCW consists of eastern subtropical mode water which is formed from deep mixed layers of low potential vorticity in the wintertime that restratify in summer and lie in a density space between 1024 - 1025.4 kg/m^3 (Hautala and Roemmich 1998, Auad et al. 2011).

The three source waters advect into southern California, and the relative composition of water masses sheds insight on the circulation (Tibby 1941, Roden 1971, Bograd et al. 2019). Mooring observations at DM measure temperature, salinity, and oxygen at 35 and 90 m depth and the same measurements are made at CCE2 at 75 m depth. Measurements of these three water mass properties can be used to determine the relative contribution of source water masses below the mixed layer where properties are conservative.

Bograd et al. (2019) examined these three source water masses in southern California using California Cooperative Oceanic Fisheries Investigations (CalCOFI) ship-based measurements to classify source waters based on their physical and biogeochemical content. The CalCOFI data provide a long timeseries dating back to 1950 of in-situ measurements that are currently collected four times a year. These quarterly measurements cover the SCB and region offshore with a spatial resolution between ~40 – 80 km, but the temporal resolution misses the high-frequency variability along with events that occur between CalCOFI cruises. The temporal changes in the coastal ocean that occur between CalCOFI cruises can be important as they may contain transitions in source water mass composition, e.g., just prior to the 2014 marine heatwave and the 2015 - 2016 El Niño. In the process of defining source water mass properties, Bograd et al. (2019) only used the mean source water property temperature-salinity profiles over a particular depth range, which does not include the upper ocean (Figure 1b in Bograd et al. 2019). While this decision may have been a conservative cut off to stay below the mixed layer, this misses the source water mean properties on shallower isopycnals. This lower density space, i.e., 1024 - 1025.4 kg/m^3, is where subtropical mode water resides and it is an important contributor to ENPCW. By using coastal fixed-point measurements maintained over the last ~15 years, the source water analysis includes the high frequency variability of source water composition in the upper ocean and provides insight into the transitions in the water mass composition prior to large-scale climate phenomena like El Niño.

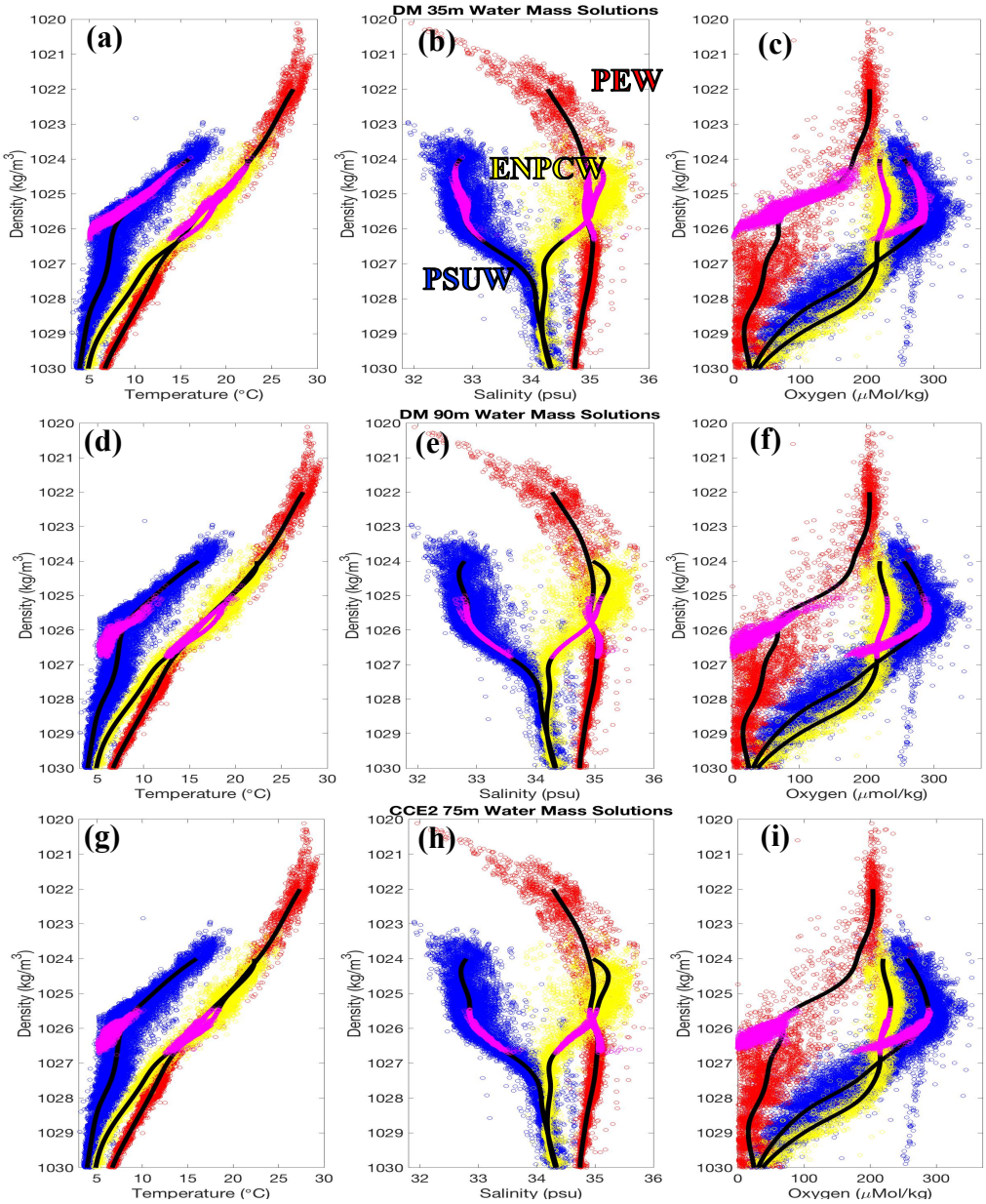

Figure 1.6: WOD water mass property characteristics for (a), (d), and (g) temperature, (b), (e), and (h) salinity, and (c), (f), and (i) oxygen. WOD Ocean Station Data were extracted from the colored boxes in Figure 1.2. The blue, yellow, and red circles represent properties of PSUW, ENPCW, and PEW, respectively. Black curves are the median fit of a water mass property in density space for each source water mass. Also shown are the water mass solver derived properties (magenta circles) when the solver was executed at DM 35 m, DM 90 m, and CCE2 75 m depths.

The water masses are classified based on their temperature, salinity, and oxygen characteristics. Ocean Station Data from the World Ocean Database (WOD) are extrapolated from the boxes shown in the inset in Figure 1.2. This step is similar to Bograd et al. (2019).

Ocean Station Data are hydrographic data from ship-based measurements and the profiles of temperature, salinity, and oxygen are shown in Figure 1.6. The black lines in Figure 1.6 show the fitted mean properties while the scatter on an isopycnal can also be quantified.

1.2.4.2 Solving the Water Mass Composition

The water mass inverse problem uses a set of equations including the three water mass properties and the mass conservation equation,

$$T_{PSUW}X_{PSUW} + T_{PEW}X_{PEW} + T_{ENPCW}X_{ENPCW} = T_{OBS}, \quad (7)$$

$$S_{PSUW}X_{PSUW} + S_{PEW}X_{PEW} + S_{ENPCW}X_{ENPCW} = S_{OBS}, \quad (8)$$

$$O_{PSUW}X_{PSUW} + O_{PEW}X_{PEW} + O_{ENPCW}X_{ENPCW} = O_{OBS}, \quad (9)$$

$$X_{PSUW} + X_{PEW} + X_{ENPCW} = 1. \quad (10)$$

Here X is the fraction of each source water mass and T, S, and O are the mean temperature, salinity, and oxygen, respectively, of the water mass on an isopycnal. The right-hand side of equations (7) - (10) are the observed daily averaged water mass properties for any given day provided by the moorings. X can be solved as an over-determined system if the source water mass properties were exactly known/fixed. Given the spread in sampled station data in Figure 1.6, some deviations, T', S', and O', can be allowed in the source water properties. By allowing for such departures from the property mean, this may allow for solutions closer to the observations and account for uncertainty in the source water property mean. In doing so, there are now many unknowns and possible solutions, and the system now becomes a mixed-determined problem. The system of equations can be rewritten as follows,

$$(T+T')_{PSUW}X_{PSUW} + (T+T')_{PEW}X_{PEW} + (T+T')_{ENPCW}X_{ENPCW} = T_{OBS}, \quad (11)$$

$$(S+S')_{PSUW}X_{PSUW} + (S+S')_{PEW}X_{PEW} + (S+S')_{ENPCW}X_{ENPCW} = S_{OBS}, \quad (12)$$

$$(O+O')_{PSUW}X_{PSUW} + (O+O')_{PEW}X_{PEW} + (O+O')_{ENPCW}X_{ENPCW} = O_{OBS}, \quad (13)$$

$$X_{PSUW} + X_{PEW} + X_{ENPCW} = 1. \quad (14)$$

In the system of equations above there are twelve unknowns, three of which are the source water fractions, i.e., X, and the nine others are the deviations from the mean source water properties. Before solving the overdetermined system, one more stipulation is added. This includes restricting the percentage of each water mass to be non-negative as there can be no less than 0% of any source water mass.

We will first solve this without salinity, so equations (11), (13), and (14) are re-written in to matrix notation,

$$GX = d, \quad (15)$$

where G is a matrix that contains the coefficients of the terms on the left-hand side of equations (11), (13), and (14), X is a column vector of the water mass fractions, and d is a column vector using the values on the right-hand side of equations (11), (13), and (14). Thus, G and d are,

$$G = \begin{bmatrix} T_{PSUW} + T'_{PSUW} & T_{PEW} + T'_{PEW} & T_{ENPCW} + T'_{ENPCW} \\ O_{PSUW} + O'_{PSUW} & O_{PEW} + O'_{PEW} & O_{ENPCW} + O'_{ENPCW} \\ 1 & 1 & 1 \end{bmatrix},$$

$$d = \begin{bmatrix} T_{OBS} \\ O_{OBS} \\ 1 \end{bmatrix}.$$

The approach for solving the mixed-determined problem is an iterative procedure that begins with taking equation (15) and making an initial guess for the temperature and oxygen fluctuations. For this guess, T' and O' are prescribed to be 0°C and 0 μmol/kg, respectively. Menke (2012) provides a solution for this inverse problem where $T' = O' = 0$ which is,

$$X = [G^T W_e G]^{-1} G^T W_e d. \quad (16)$$

In equation (16), superscript T denotes the matrix transpose. W_e is a diagonal matrix that weights the data since the magnitudes and the units of the water properties differ. Two of the weights are

the inverse of the temperature and oxygen sensor errors squared while the last diagonal element of the weight matrix is assigned to be 0.001^{-1}. Using the sensor errors in the weighted matrix accounts for instrument noise and allows for a small discrepancy between the solutions and the observations. The choice of 0.001^{-1} is arbitrary but effectively constrains the water mass fractions to closely sum up to 1. W_e is not needed to solve for an exact solution to equation (15), but by permitting a small misfit, the temperature, salinity, and oxygen required from each of the water masses deviates less from the water masses' mean property value when compared to the temperature, salinity, and oxygen required when there is no weighted matrix (not shown). Once the source water fractions, X, are solved for, this information is used to solve for the water mass salinity deviations, S', in equation (12).

Equation (12) is re-arranged and re-written in to matrix notation as,

$$S'X = S_{OBS} - SX, \tag{17}$$

where on the right-hand side of equation (17) the mean salinities for each of the regional water masses are removed from the in-situ salinity. The solution for the underdetermined system in equation (17) from Menke (2012) is,

$$S'^{T} = X(X^{T}X)^{-1}(S_{OBS} - SX). \tag{18}$$

After solving for S' using equation (18), all twelve unknowns have been solved for or prescribed an initial value, and the objective is to find a set of unknowns that will minimize the following function,

$$\sum_i [\frac{{T_i'}^2}{{\sigma_{T_i}}^2} + \frac{{O_i'}^2}{{\sigma_{O_i}}^2}]. \tag{19}$$

Here i represents each water mass and σ is the standard deviation over the specified property and water mass. In equation (19), the summation is done over all six terms, thus taking in to consideration all three water masses and the temperature and oxygen fluctuations are normalized

by the respective variance, where the latter is based on observations. It is noted that by solving for the salinity fluctuations in equation (18), this method inherently minimizes the size of S'. Because this step occurs before evaluation of equation (19), the salinity fluctuations are minimized before the temperature and oxygen fluctuations and therefore may be preferentially treated by this approach.

Using the value determined by equation (19) and the initial guesses for T' and O', MATLAB's *fminsearch* tool makes use of the Nelder-Mead simplex algorithm, a nonlinear optimization method, to make a new guess for the temperature and oxygen fluctuations. The iteration procedure in the Nelder-Mead simplex algorithm is described in Lagarias et al. (1998), and the steps outlined above are repeated until a solution is reached. Once the algorithm converges upon a solution that minimizes the function in equation (19), these become the final solutions for the property deviations and the water mass fraction for a given day. This is executed for each time step, where each step is treated independently such that no information from a prior time step influences the solution for the subsequent time step.

1.2.4.3 Water Property Fluctuations

The source water mass property fluctuations, T', S', and O', solved for by the water mass analysis are compared against the variability in the Ocean Station Data for each of the source water regions. The fluctuations from the water mass analysis are similar to or smaller than the deviations in Ocean Station Data for each water mass (Figure 1.6). At larger densities the routine selects water mass properties that are slightly biased in temperature and oxygen towards the lower range of values at both sensor depths. This occurs around 1026 kg/m^3 which is in the density range of CU waters. The CU carries low oxygen, low pH waters poleward typically between 100 - 300 m along the shelf and upper slope off of North America. In the SCB, the CU

can shoal, and characteristic densities of the CU are occasionally measured at the moorings. Recent data indicate a declining trend in dissolved oxygen influencing PEW (Meinvielle and Johnson 2013; Bograd et al. 2015). Changes in the low latitude region of this source water may be responsible for recent modifications of CU waters and may explain the bias in temperature and oxygen at these larger densities.

The size of the source water mass property fluctuations, i.e., the fluctuations are smaller than the variability in the WOD data in Figure 1.6, suggests that the results from this method of determining the composition are reasonable. A more thorough examination of the results is presented in Appendix A, and this test of the solutions provides the confidence to analyze the water mass composition results in Section 1.4.

1.2.5 SCE Index

To represent the presence or intensity of the SCE, an index is constructed based on the alongshore SSH differences. The index is used in Section 1.4 to support the hypothesis that the SCE is responsible for much of the seasonal variability in the water mass anomalies.

The alongshore difference in sea level indicates geostrophic cross-shore flow, which is one aspect of the SCE. Coastal poleward geostrophic flow is another aspect of the SCE. This component of the SCE is not included as part of the SCE index because coastal poleward flow may also be associated with continuous alongshore flow from Baja California. Thus, including the cross-shore sea level difference, i.e., geostrophic alongshore flow, as a part of the SCE index may be misleading when poleward flows originate from lower latitudes. Therefore, only the alongshore difference in sea level is included for the SCE index. The alongshore sea level difference is useful for representing onshore flows while the DM ADCP measures the alongshore flow so the two timeseries will be assessed together to detect when the SCE may be present. The

SCE index is computed by differencing SSH from CMEMS altimetry data at two alongshore locations (Figure 1.7). The locations of these sites bracket the southern section of the SCB, which effectively isolates the onshore movement of waters.

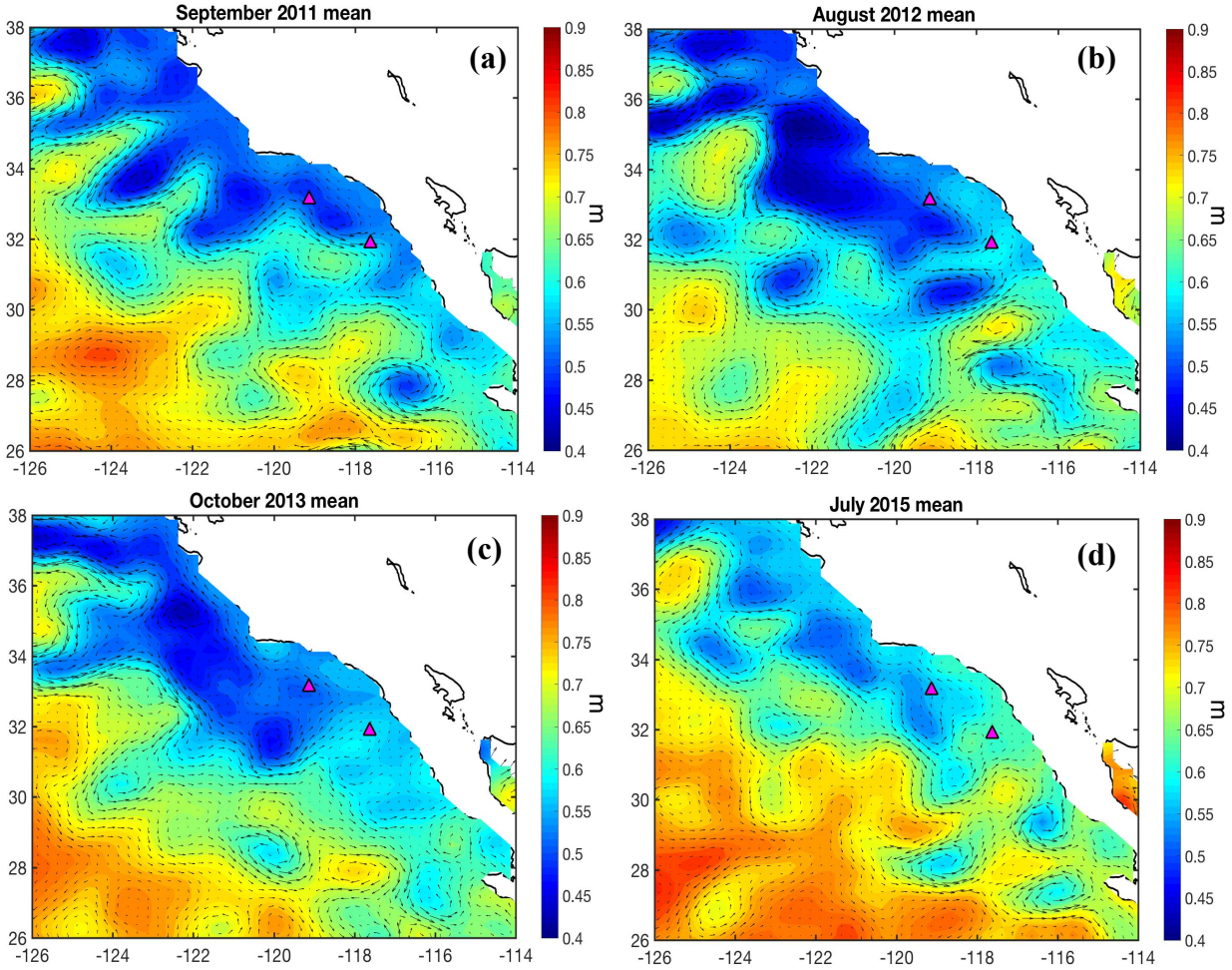

Figure 1.7: Monthly averaged CMEMS SSH for (a) September 2011, (b) August 2012, (c) October 2013, and (d) July 2015. Magenta triangles show the northerly and southerly locations used in the SCE index.

To validate the SCE index (Figure 1.8), monthly averaged altimetry SSH maps from CMEMS are assessed against the index. Figure 1.7 shows maps of monthly averaged SSH for four months. These months were selected based on the higher values in the SCE index in Figure 1.8, so it is expected that SSH maps should indicate a stronger presence of the SCE, e.g., larger alongshore SSH gradients in the SCB. In these maps, lower SSH in the SCB is surrounded by higher SSH offshore and to the south. Offshore, higher SSH shows the southward trajectory of

the CC and off of the SCB part of the CC wraps around on the south side of the region of lower SSH and works its way inshore separating the lower SSH from the coastline. The maps show the cyclonic nature of the SCE and the geostrophic flow induced by the spatial distribution of SSH. Qualitatively, higher values in the SCE index are representative of more onshore flow off the US-Mexico border as part of the SCE, and this index along with the DM ADCP measured alongshore flow is a practical way to characterize the strength of recirculation in the SCB.

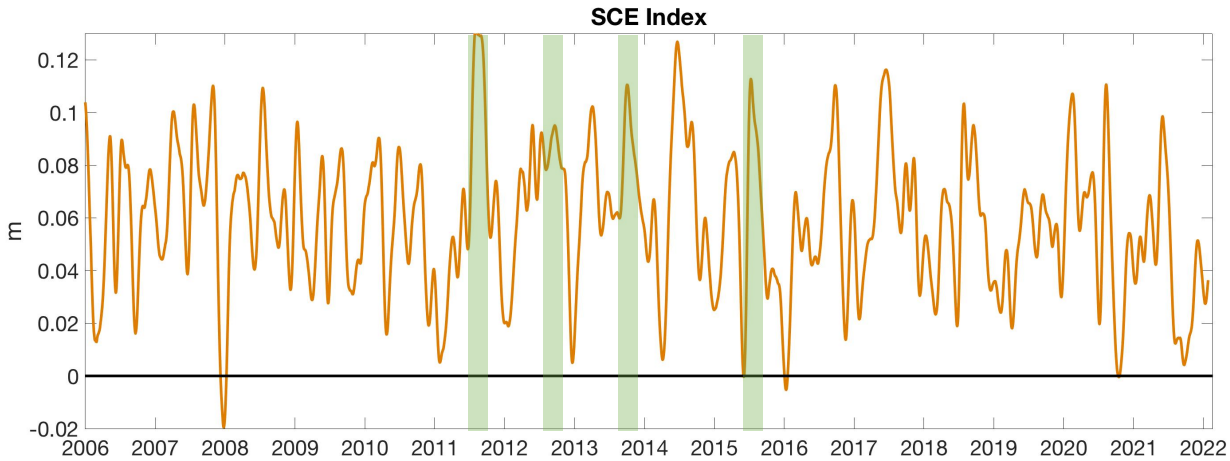

Figure 1.8: Southern California Eddy (SCE) index which is the alongshore difference in SSH from altimetry data. The locations used in constructing the SCE index are shown in Figure 1.7. Shaded periods denote when the SCE index is high, and these periods are compared to monthly averaged altimetry SSH in Figure 1.7.

1.2.6 Wind Stress Curl

Previous studies offer evidence that the wind stress curl is tied to coastal poleward flow in the SCB with poleward flow lagging behind the wind stress curl by 2 - 4 months (Chelton 1982; McCreary et al. 1987; Oey 1999; Di Lorenzo 2003). The curl-driven forcing of coastal poleward flow may be a result of a Sverdrup balance or due to an alongshore gradient in the wind stress curl adjusting sea level to drive an APG (Bray et al. 1999; Oey 1999). In the latter, alongshore differences in the curl strength can result in alongshore differences in the offshore Ekman divergence and lowering of sea level. Wind stress curl is larger off Point Conception and

weaker in the SCB (Winant and Dorman 1997; Di Lorenzo 2003). This alongshore curl gradient establishes an APG whose direction is opposite to that of the curl gradient.

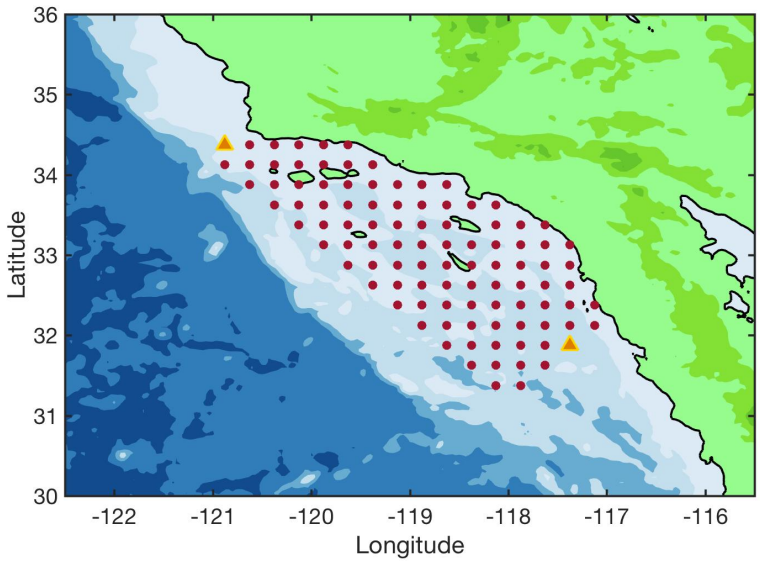

Figure 1.9: CCMPv2 grid points where the wind stress curl is averaged over to create a regional representation of the curl. Orange triangles mark the northerly and southerly locations used in computing the alongshore difference in the wind stress curl.

To represent the wind stress curl forcing, two timeseries are generated. In the first, the wind stress curl is averaged over the SCB, and in the second the alongshore difference in the wind stress curl is computed using a location off Point Conception and a location off the US-Mexico border (Figure 1.9). The southern location used in the second curl timeseries is the same southern site used in computing the SCE index.

1.2.7 Particle Trajectories

Particle trajectories are examined in Section 1.4 to qualitatively assess horizontal flows off southern California and Baja California at times when there were anomalous amounts of more tropical waters. Trajectories are computed based on combining 1/4° CMEMS geostrophic velocities with Ekman estimated velocities as,

$$u = u_g + u_e, \quad v = v_g + v_e. \tag{20}$$

In equation (20), subscripts g and e denote the geostrophic and Ekman horizontal velocities, respectively. Ekman velocities are derived from wind stress as,

$$u_e = \frac{1}{\rho f d}\tau^y, \quad v_e = -\frac{1}{\rho f d}\tau^x, \tag{21}$$

where ρ is the density of seawater, f is the Coriolis parameter, and d is the thickness of the Ekman layer. Wind stress is calculated from the 1/4° CCMPv2 wind data and the Ekman layer is assumed to be 50 m in equation (21; Chereskin 1995). Using the combined geostrophic and Ekman currents, particle trajectories are computed by solving,

$$\boldsymbol{u} = \frac{d\boldsymbol{X}}{dt}. \tag{22}$$

In this equation, $\boldsymbol{u}$ contains the total Eulerian horizontal velocities and $\boldsymbol{X}$ is the Lagrangian position along the trajectory. Particle trajectories are integrated backwards for 45 days. Trajectories run successively with one day separating each of the trajectories. Close to the coast, it is possible for particle trajectories to run in to the coastline. Thus, there is a trade off with selecting locations that are close to the coast yet do not result in trajectories that immediately run in to the coastline. Particle trajectories were also run using 1/3° Ocean Surface Current Analysis Real-time (OSCAR) data and the interpretation from these results is similar to those presented below using the CMEMS geostrophic velocities with Ekman derived currents from the CCMPv2 data; therefore these are not shown.

1.3 ADCP Observations and Velocity Regression Results and Discussion

A chapter objective is to assess the anomalous poleward flow. First, the alongshore flow from the ADCP observations at the coastal moorings are examined. Then, the results from the regression analysis on the alongshore velocity anomalies are discussed. The regression analysis

shows that the regressed velocity anomalies reproduce the periods of poleward flow, so this motivates investigating the interannual variability in the input variables, i.e., the gyre-scale APG and the wind stress. This section ends with relating the poleward flow anomalies to the 2014 marine heatwave, the 2015 – 2016 El Niño, and the recurring marine heatwaves in 2019 – 2021.

1.3.1 ADCP Observations

Observations from DM and CCE2 capture distinctly more poleward flow in 2012 - 2015, 2018, and periodically between late 2019 - early 2022. Cumulative displacements plots show the time integral of the Eulerian alongshore velocity at 40 m and 20 m depths for DM and CCE2, respectively (Figure 1.10). At DM this includes 2006 – early 2022 and at CCE2 2010 - early 2022. Characteristic flow at both sites include southward flows in the first half of the year and poleward flows in the second half of the year. Southward flows in the first half of the year are due to equatorward winds during the upwelling season that drive alongshore flows. In Figure 1.10, equatorward currents decrease the cumulative displacement while poleward flows result in a more positive displacement. In California, upwelling-favorable winds tend to relax in the second half of the year. This is the relaxation season in which it is common for displacement trajectories to exhibit minimal or slightly positive displacement.

Colored years in Figure 1.10 stand out from the other years by demonstrating less negative or more positive displacement in some part of the year. These anomalous behaviors in the cumulative displacement are signs of poleward flow anomalies. Poleward flow anomalies can be from weaker equatorward currents, i.e., typically during the upwelling season, as well as from greater poleward flow, i.e., generally during the relaxation season. Years containing unusual amounts of anomalous poleward flow are objectively determined as follows. First, the annual cycle is computed over 2006 – 2021 for DM and 2010 – 2021 for CCE2 and removed to

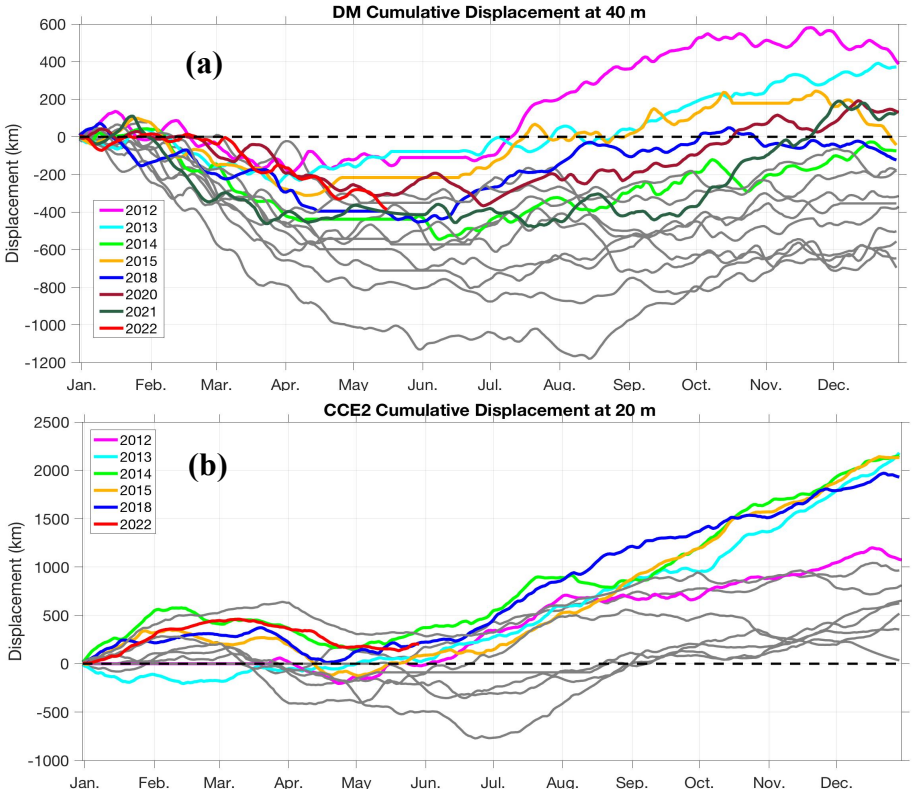

Figure 1.10: ADCP cumulative displacement curves for each year at (a) DM 40 m depth between 2006-early 2022 and (b) CCE2 20 m depth between 2010 - early 2022. 2012 - 2015, 2018, 2020 - 2021 (DM only), and 2022 curves are highlighted in color. Zero displacement accounts for broken sensor or no mooring in water. Positive values denote northward displacement and negative values denote southward displacement.

construct alongshore velocity anomalies. These anomalies are normalized by the standard deviation, where the standard deviation is computed for each calendar day. The normalized values are depicted in Figure 1.11a. Within any given year, the timeseries in Figure 1.11a shows fluctuations in the sign of the values, even in years where there are large positive values such as in 2012 – 2015. Because some years may contain a few days that exceed one standard deviation above the daily mean but that are otherwise near normal or below the mean in the rest of the calendar year, e.g., 2006 at DM, the criteria for determining whether a year exhibits anomalous poleward flow is based on the number of days in a year that are above the annual cycle. Therefore, the number of days in a calendar year that exceed the annual cycle are summed and normalized by the number of days of ADCP observations in that year (Figure 1.11b). The

normalization accounts for bias that may be introduced in years where there is less ADCP coverage such as in 2017 at CCE2. Years where the observations exceed the annual cycle for at least 45% of the time are considered to be anomalous. Figure 1.11b shows that these anomalous years are 2012 - 2015, 2018, and 2020 – 2022 and are visually apparent in Figure 1.10.

Many of the curves for the anomalous years in Figure 1.9 have poleward or less weakened equatorward displacement in the first few months of the calendar year. In the summer and fall, larger poleward velocities occur in the anomalous years that cause increased displacement from the middle to the end of the calendar year. By the end of the year, these colored years obtain significant net displacement. This strong positive displacement reaches up to 500 km of integrated displacement at DM and 2000 km at CCE2. Hence, in-situ measurements show enhanced poleward flow for southern California during 2012 - 2015, 2018, and late 2019 - early 2022 bringing attention to the large-scale 2014 marine heatwave, the 2015 - 2016 El Niño, the two years before these climate phenomena, and the various marine heatwaves in 2018 - 2021.

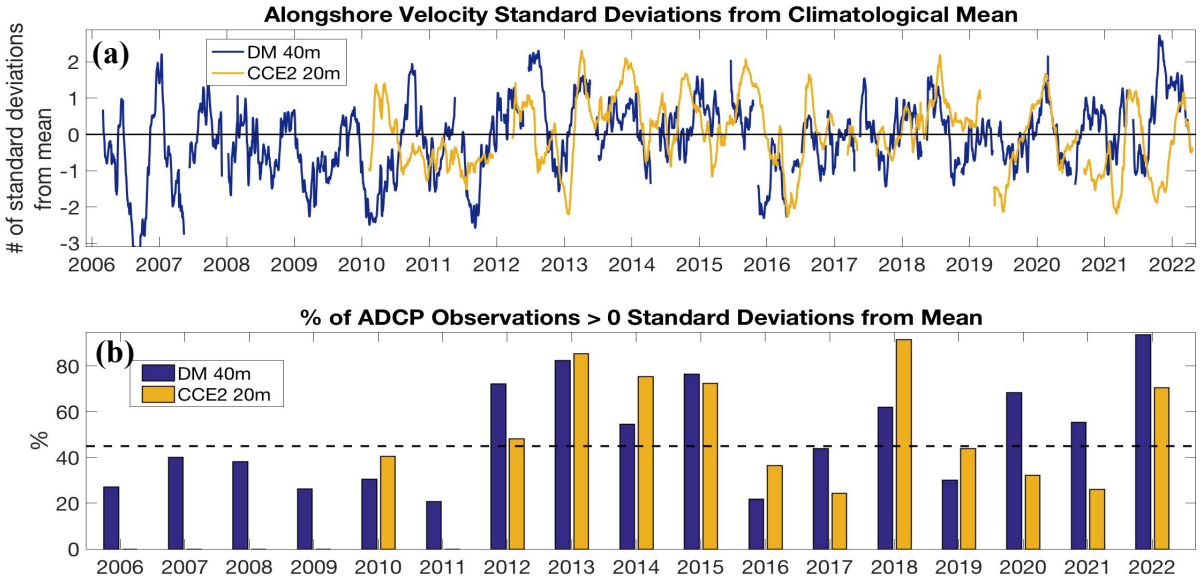

Figure 1.11: (a) Number of standard deviations from the climatological mean for the alongshore velocity at DM 40 m depth and at CCE2 20 m depth. The climatological mean for each calendar day is derived based on the averages over 2006 - 2021 at DM and 2010 - 2021 at CCE2. Positive values denote more poleward flow. (b) The percentage of ADCP observations from (a) in each year that have a positive number of standard deviations from the mean. Black dashed line shows the 45% threshold.

Anomalous poleward flow has been documented in previous El Niños (Huyer and Smith 1985; Lynn and Bograd 2002; Kosro 2002), so it is not surprising that there is anomalous poleward flow in 2015. Less has been reported on the circulation features in southern California during regional and large-scale marine heatwaves. The poleward flow anomalies in these years will be examined to understand how they may be related to the heatwaves.

1.3.2 Regression Results

The regression analysis is performed at DM and CCE2, where the low-pass filtered anomalies from the right-hand side of equation (6) are regressed against the low-pass filtered velocity anomalies, i.e., the left-hand side of equation (6). The annual averages in Figure 1.12 for the velocity regression (red curve) use the reduced regression. The fully regressed velocities using all variables are not shown since they are similar to the red curves in Figure 1.12. In addition to the reduced regression annual averages and the ADCP/geostrophic velocity anomaly annual averages in Figure 1.12, there are also the annual averages from the estimated velocity anomalies based on the fixed coefficients from the momentum equation in equation (6; yellow curve).

At DM, the annual averages are typically below 0 m/s prior to 2012, but an abrupt change occurs in 2012 with 2012 - 2015 seeing notably higher averages (Figure 1.12a). This transition emphasizes a change in the flow regime starting two years prior to the prolonged warming from the 2014 marine heatwave and the 2015 - 2016 El Niño. The annual averages between the DM ADCP velocity anomalies, the reduced regression velocity anomalies, and the momentum equation velocity anomalies are well correlated with one another (Table 1.3). At DM the

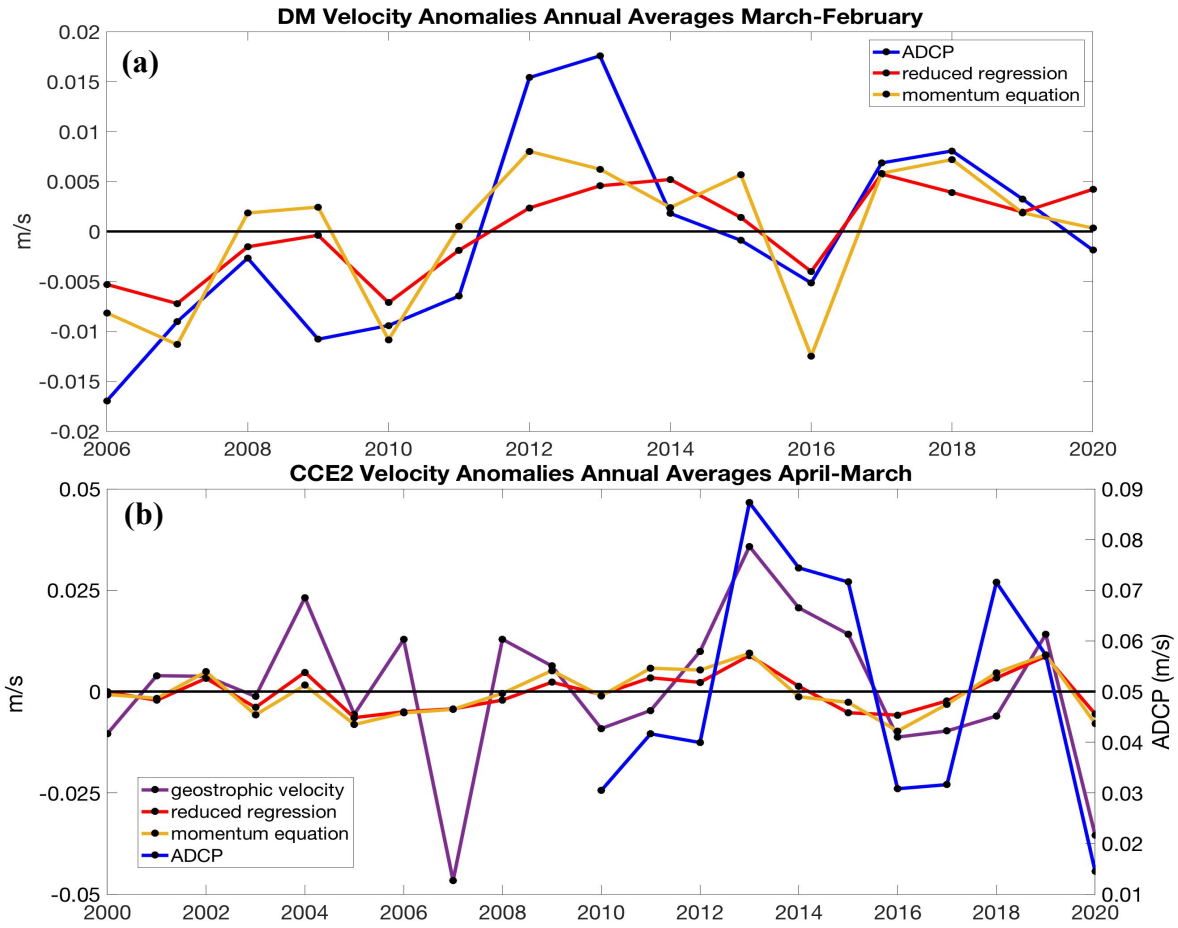

Figure 1.12: Annual averages of velocity anomalies from the in-situ measurements, the reduced regression, and the momentum equation for (a) DM and (b) CCE2. Annual averages are computed over March – February for DM and April – March for CCE2. Note for (b) the ADCP averages are based on the total alongshore velocity, not the anomalies so the y axis scales are different. Note the different x axis scales in (a) and (b).

momentum equation estimate of velocity anomalies tends to produce larger magnitude fluctuations than the regression (Figure 1.12a), but both have nearly the same correlation and rms error with the ADCP observations in Table 1.3. If the regression coefficients perfectly matched the momentum equation coefficients, then the regression coefficients would be 1. At DM, all of the regression coefficients are less than 1.

At CCE2 there are larger disagreements in the trend over the annual averages (Figure 1.12b) which is reflected in the lower correlations compared to DM (Table 1.3). The transition to more positive velocity anomalies beginning in 2012 is less abrupt at CCE2, with this shift more

pronounced starting in 2013. The interannual variability from 2010 onward in the annual averages of the regressed and momentum balance velocity anomalies show some semblance to the interannual variability of the ADCP velocity annual averages. Most of the regression coefficients for CCE2 in Table 1.3 are less than 1.

Table 1.3: Rms error, correlation coefficients, and regression coefficients for the annual averages of alongshore velocity anomalies based on the ADCP observations, geostrophic velocity, regression analysis, and momentum equation. Rms errors and correlations in parenthesis are the results from using the input variables in the reduced regression. Correlations marked with an * are significant at the 95% level. The 95% confidence interval for the regression coefficients are provided. Correlations listed are at a lag of 0 years. The regression equation is,
$\tau H^{-1} v = \rho^{-1}(a_1 p_y^{QP} + H^{-1}(a_2 \tau^{w_1} + a_3 \tau^{w_2} + a_4 \tau^{w_3})) + a_5 (\rho H)^{-1} \tau^{w_4}$.

Site	RMS error m/s	Correlation Coefficient	Regression Coefficients 95% CI
DM Annual Averages: ADCP & Regressed Anomalies	0.007 (0.007)	0.79* (0.76*)	$a_1 = 0.339 \pm 0.038$ $a_1 = 0.320 \pm 0.036$ $a_2 = -0.064 \pm 0.081$ $a_3 = 0.436 \pm 0.094$ $a_4 = 0.453 \pm 0.062$ $a_4 = 0.754 \pm 0.041$ $a_5 = 0.383 \pm 0.062$
DM Annual Averages: ADCP & Momentum Equation Approximated Anomalies	0.008 (0.007)	0.78* (0.73*)	
CCE2 Annual Averages: Geostrophic & Regressed Anomalies	0.008 (0.004)	0.63* (0.55*)	$a_1 = 0.484 \pm 0.057$ $a_1 = 0.626 \pm 0.057$ $a_2 = -0.082 \pm 0.124$ $a_3 = 2.033 \pm 0.146$ $a_4 = -0.489 \pm 0.096$ $a_5 = 1.216 \pm 0.090$ $a_5 = 0.978 \pm 0.068$
CCE2 Annual Averages: Geostrophic & Momentum Equation Approximated Anomalies	0.011 (0.005)	0.47* (0.52*)	

While there are some discrepancies between the strength of the anomalies approximated by the regressed and momentum balance estimated timeseries, these analyses performed at both sites in southern California share the low-frequency interannual variability in the annual averages (Figure 1.12). The higher correlation at DM gives confidence in finding the origin of poleward flow anomalies for the years 2012 - 2015, 2018, and 2019 – 2021. The results from the simplified regression analyses will be examined more closely in the next section to ascertain the

gyre-scale APG and the wind stress contributions in forcing the positive anomalies and how these may be related to the multiple climate phenomena that occurred throughout 2014 - 2021.

1.3.3 Gyre-Scale APG vs. Wind Stress Forcing

The results from the regression analysis showed that a number of years between 2012 and 2021 had positive velocity anomaly annual averages; this motivates analyzing the contributions from the gyre-scale APG and the corresponding wind stress used in the reduced regression. The gyre-scale pressure gradient and the wind stress off Baja California/SCCS for DM/CCE2 are weighted by the reduced regression coefficients. These two components are illustrated in Figure 1.13. For the momentum equation coefficients, the variability of the APG and the wind stress would be the same as the variability from the reduced regression but with different scaling factors; therefore, these are not shown. Separating the contribution of the gyre-scale APG and the

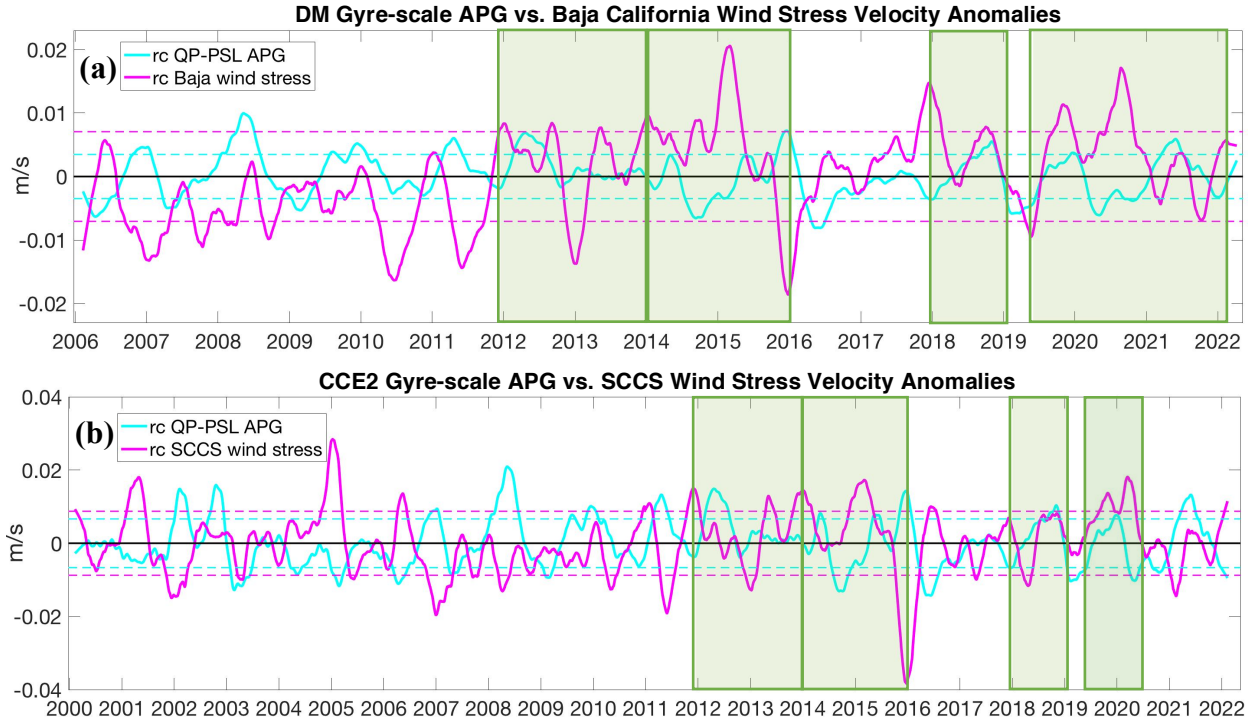

Figure 1.13: Gyre-scale APG velocity anomaly and wind stress velocity anomaly from the reduced regression analysis at (a) DM where wind stresses are off of Baja California and (b) at CCE2 using wind stresses in the SCCS. Dashed lines are one standard deviation. Shaded periods highlight events of poleward flow anomalies. Note the different x axis scales in (a) and (b).

wind stress to the regressed flow anomalies assists in identifying causes of poleward flow anomalies on annual time scales. In Figure 1.13, four periods are highlighted exhibiting positive anomalies from Figure 1.12 that overlap with poleward flow anomalies measured by the ADCP and in the geostrophic velocity timeseries.

1.3.3.1 2012 - 2013

In the first period from 2012 - 2013 the gyre-scale APG and the wind stress velocity anomaly components contain positive anomalies. Initially the wind stress drives the positive velocity anomalies but by late spring/early summer the wind stress velocity anomalies weaken and the gyre-scale APG velocity anomalies are dominant. In summer 2012, model forecasts predicted an El Niño (NOAA Climate Prediction Center as cited in Ludescher et al. 2014 and Su et al. 2014) which did not happen, but there are propagating sea level anomalies along the North American coastline beginning in spring - summer (Figure 1.14). SSHa are computed by

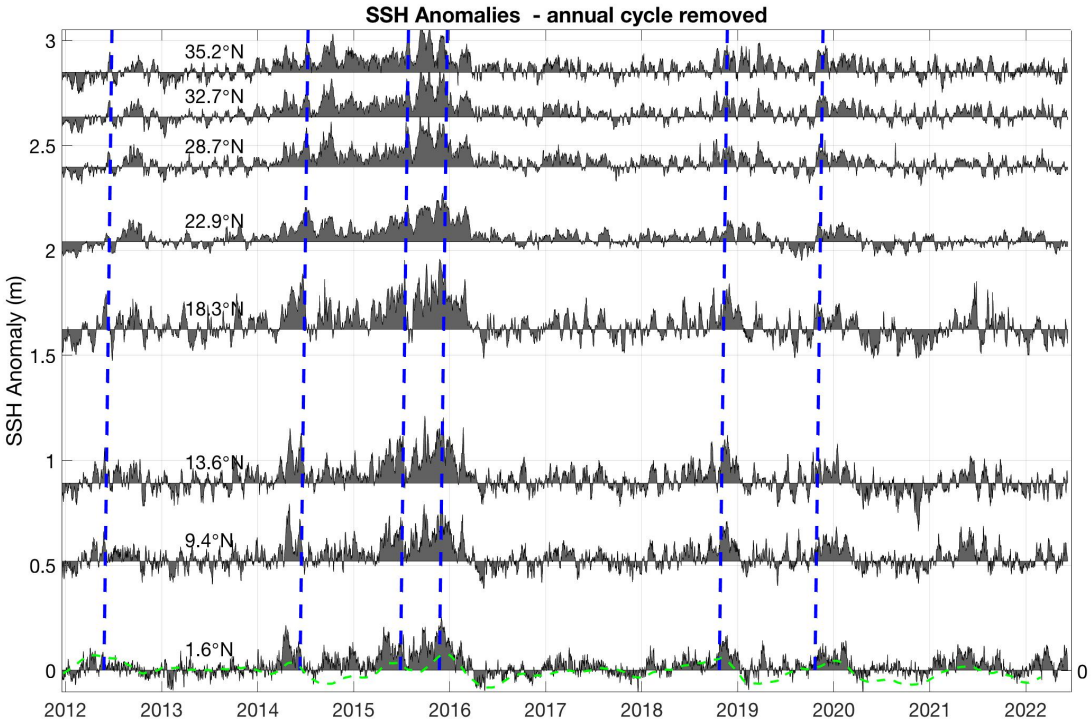

Figure 1.14: GLORYS SSHa over various latitudes in the North Pacific at coastal locations. Blue dashed lines represent a CTW phase speed of 180 km/day. Green dashed curve is the gyre-scale APG anomaly low-pass filtered over 100 days.

removing the annual cycle from the SSH where the annual cycle is calculated over 1993 – 2018. The propagating features in April 2012 have speeds similar to observed CTWs in the North Pacific (Enfield and Allen 1980; Huyer and Smith 1985; Meyers et al. 1998; Strub and James 2002b). By September 2012, positive monthly averaged sea level anomalies stretch from the equator up to central California in a thin coastal band (Figure 1.15a). Oceanic teleconnections appear to have spread from the tropical Pacific up to midlatitudes and the positive SSHa along the coastline imply poleward geostrophic flow anomalies.

The gyre-scale APG anomaly timeseries weakens in fall and the positive velocity anomalies are supplemented by an increase in the wind stress velocity anomalies (Figure 1.13). In 2013, positive wind velocity anomalies persist peaking in spring and again in winter. The winter 2013 - 2014 peak was observed in other regions of the North Pacific and attributed to the atmospheric ridge that drove the 2014 marine heatwave (Bond et al. 2015; Whitney 2015).

1.3.3.2 2014 - 2015

The second period includes 2014 and 2015 and begins with continued positive wind stress velocity anomalies from winter 2013 (Figure 1.13). Intermittent positive gyre-scale APG anomalies supplement the positive wind stress anomalies to support poleward flow anomalies and there are three events when the gyre-scale APG exceeds one standard deviation. The first event in spring 2014 follows increased equatorial activity when strong westerly wind bursts (WWB) in the tropical equatorial Pacific generated equatorial Kelvin waves (Menkes et al. 2014; McPhaden 2015; Hu and Fedorov 2016). These waves propagated eastward toward South America and upon reaching the coast continued to propagate poleward (Figure 1.14). The increase in the gyre-scale APG forcing is likely due to the WWB creating downwelling Kelvin waves that raised sea level anomalies in a thick band near the equator and coastally at low

latitudes suggesting continuous poleward flow anomalies over these latitudes was possible (Figure 1.15b). An El Niño was anticipated, but unusually strong easterly winds across the

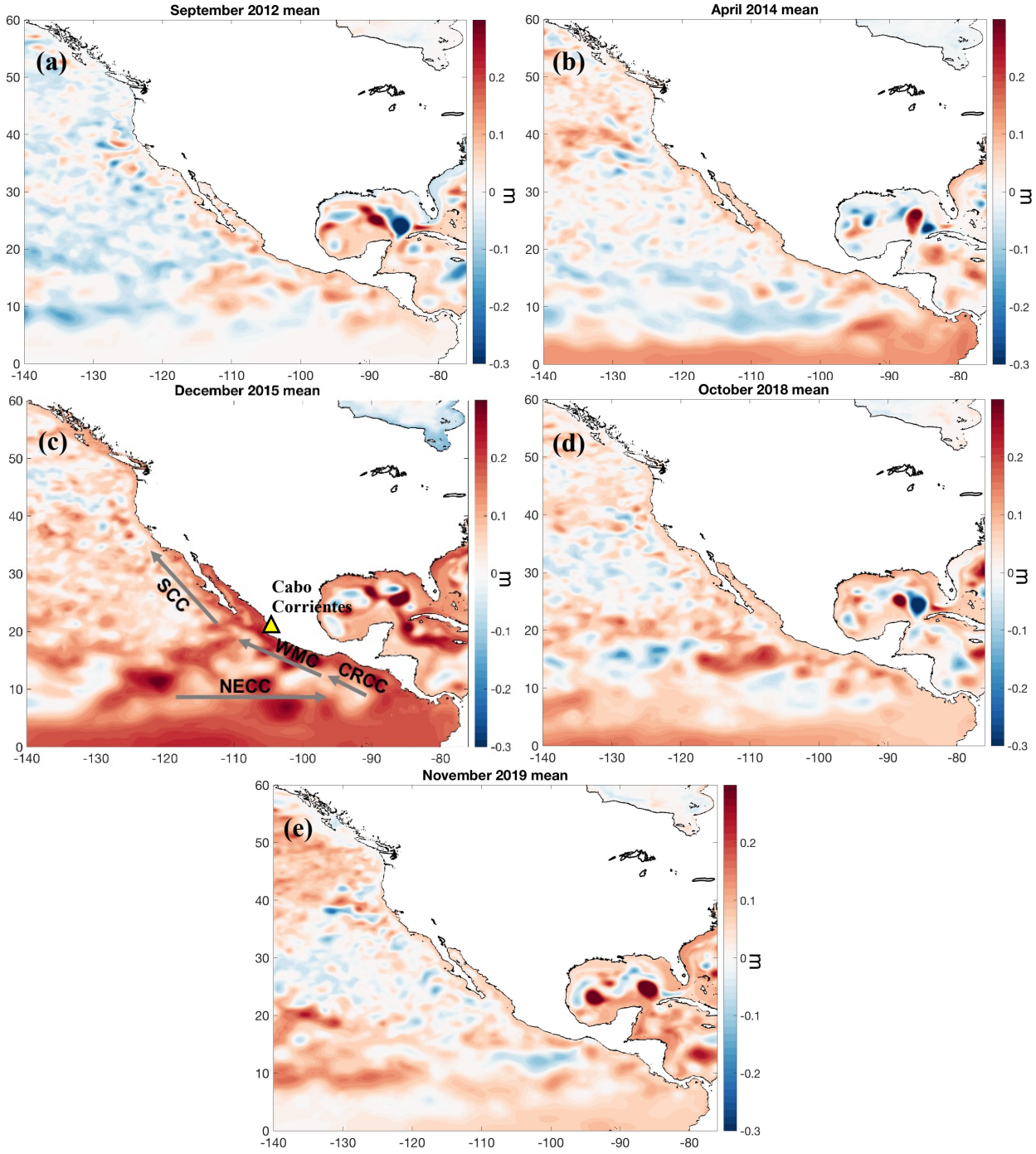

Figure 1.15: GLORYS SSHa averaged over (a) September 2012, (b) April 2014, (c) December 2015, (d) October 2018, and (e) November 2019. Yellow triangle in (c) shows the location of Cabo Corrientes while arrows are schematic representations of regional currents.

equatorial Pacific shut down the El Niño spin up (Ludescher et al. 2014; Menkes et al. 2014; Tollefson 2014; Hu and Fedorov 2016; Levine and McPhaden 2016).

In the following spring - summer and fall - winter of 2015, the second and third gyre-scale APG escalations happen (Figure 1.13). Equatorial WWB generated a series of eastward propagating Kelvin waves (Chen et al. 2016) that reached southern California in late spring-early summer followed by continued successions of sea level anomalies propagating up the coast in fall and winter (Figure 1.14). The cumulative effect of these CTWs raised the gyre-scale APG velocity anomaly (Figure 1.13).

By December 2015, most of the North Pacific exhibits anomalously higher SSH values with large positive anomalies dominating near the equator and the coast (Figure 1.15c). The sustained positive sea level anomalies suggest continuous poleward geostrophic flow anomalies offshore of the coastal SSHa band. Figure 1.15c shows a branch of higher SSHa crossing the Gulf of California that has previously been observed in altimetry data as a result of eddy genesis near Cabo Corrientes and becomes more frequent during El Niño when Kelvin waves propagate poleward from the equator (Zamudio et al. 2001; Zamudio et al. 2007). This mechanism, preconditioned by high CTW activity, can explain how the positive SSHa crossed over the Gulf of California in fall 2015. The implied continuity of poleward geostrophic flow suggests connectivity between southern California and low latitude regions.

The remotely forced CTWs are more closely examined in tide gauge measurements of sea level in southern California (Figures 1.16a and 1.16b). Coherent fluctuations in the in-situ sea level measurements occur alongside changes in the ADCP measured alongshore flow during the passage of multiple CTWs. As the waves propagate through, they ride along the thermocline raising SSHa, increasing the alongshore flow, and subducting isopycnals (not shown). CCE2 is

located on the outer edge of the coastal waveguide, so there will be some modulation and dampening of the CTWs. The local alongshore wind stresses at the mooring sites are largely equatorward (Figure 1.16c), thus not favorable for driving the downwelling anomalies.

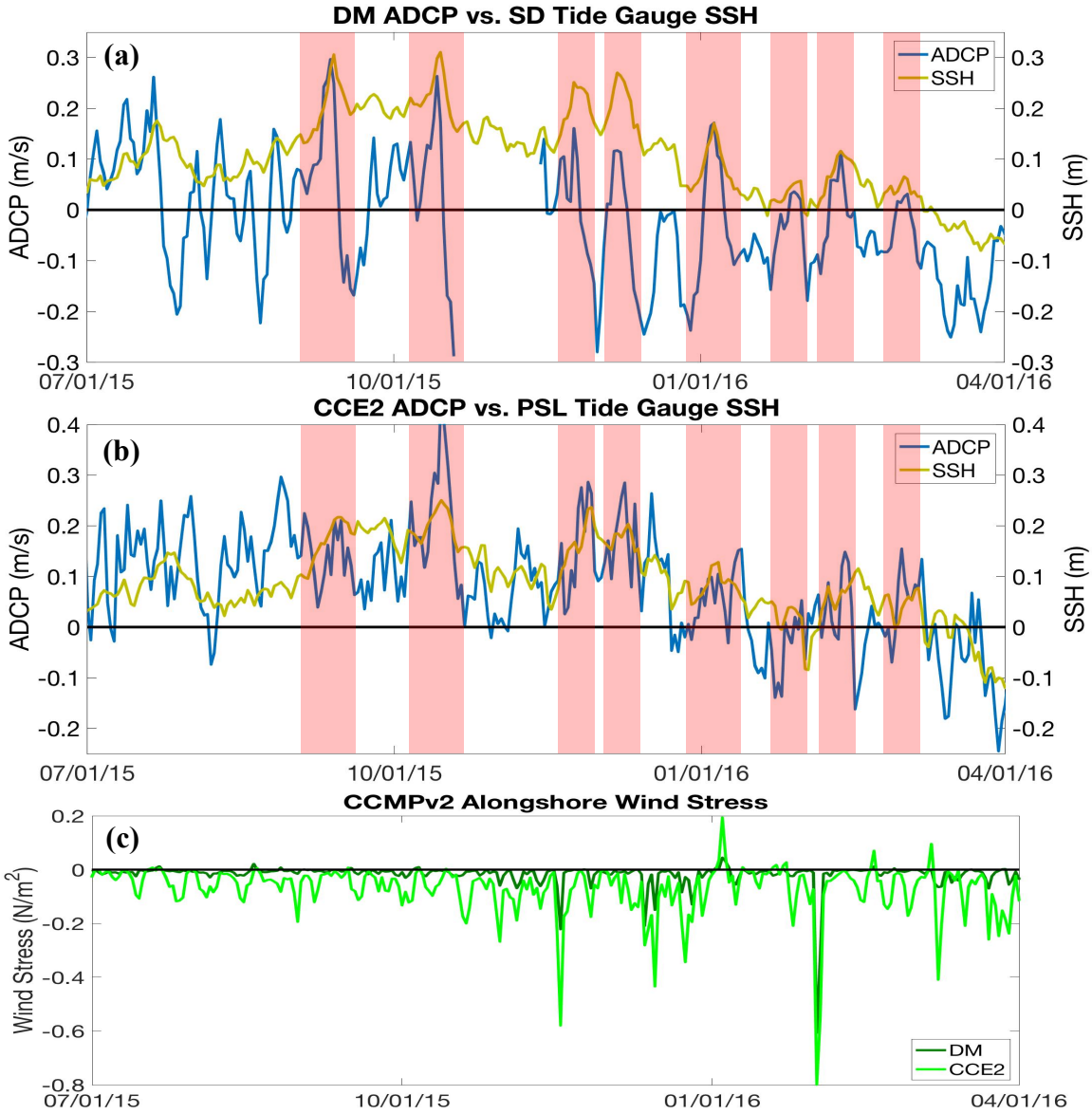

Figure 1.16: ADCP alongshore velocity and coastal tide gauge SSH for (a) DM and (b) CCE2. At DM the alongshore velocity is at 40 m depth and at CCE2 the alongshore velocity is at 20 m depth. Highlighted periods are CTW events based on Figure 1.14. (c) CCMPv2 alongshore wind stress near DM and CCE2.

In this second period of poleward flow anomalies, the wind velocity anomalies were persistently positive up until late 2015 off Baja California, while in southern California the wind

velocity anomaly peaked in winter 2014/2015. Toward the end of 2015, the wind stress velocity anomalies in both regions hit a record low (Figure 1.13). In this transition, the strong upwelling favorable winds shut down the influence of El Niño in the CCS (Frischknecht et al. 2017). Robinson (2016) noted unusually weak winds off Baja California persisting from spring 2014 through summer 2015 that were unrelated to the 2015 - 2016 El Niño but were responsible for the regional warming from spring 2014 – spring 2015. Similarly, in southern California Zaba and Rudnick (2016) reported weaker winds in 2014 - summer 2015 that contributed to anomalous heating of the upper ocean. The positive wind anomalies reported here appear to have affected much of the CCS during the 2014 marine heatwave and the 2015 - 2016 El Niño.

1.3.3.3 2018

The next period of positive flow anomalies occurs in 2018 and contains both weakened upwelling favorable winds and positive gyre-scale APG velocity anomalies. These anomalies occur during the August 2018 Baja California – southern California marine heatwave (Fumo et al. 2020; Wei et al. 2021) and the increase in the gyre-scale APG velocity anomalies can be attributed to remote forcing from poleward propagating CTWs (Figure 1.14). In October, positive SSHa developed at the equator and along the coast (Figure 1.15d) and the Oceanic Niño Index (ONI) reflects a weak El Niño state (not shown). This equatorial forcing, as well as weakened upwelling favorable winds, caused the regional marine heatwave (Fumo et al. 2020; Wei et al. 2021; Figure 1.13). The weakened equatorward winds and CTWs also caused positive flow anomalies in summer - fall 2018 (Figure 1.13; Fumo et al. 2020; Wei et al. 2021).

The positive Baja California wind velocity anomalies began in 2017, however ADCP data in 2017 did not meet the criteria to classify this year as anomalous. This classification is dependent on the twelve-month averaging period, and had the average period been shifted, then

2017 would have been marked as anomalous at DM. Similarly, the CCE2 2019 annual averages are positive in Figure 1.12b due to positive anomalies in the wind field supplemented by positive anomalies in the gyre-scale APG (Figure 1.13b), but the CCE2 ADCP data did not report a significant number of days of poleward flow anomalies that categorized this year as anomalous (Figure 1.10). However, if the annual average window computations were shifted later, then this would have led to 2019 being classified as anomalous. Thus, there are some sensitivities to the classification of an anomalous year based on the averaging window.

1.3.3.4 Fall 2019 - 2021

ADCP flow anomalies at DM indicate that from fall 2019 - 2021 there were more poleward flow anomalies (Figure 1.11). The low-frequency positive flow anomalies in these years at DM and CCE2 do not persist through the entire period but are more episodic in nature (Figure 1.11a). Much of the anomalous flow is considered to be due to positive wind stress velocity anomalies off Baja California and southern California (Figure 1.13). The gyre-scale APG does increase in fall 2019 and in 2021, possibly due to the propagation of CTWs from the equator (Figure 1.14). In the latter of these two years, the propagating SSHa do not appear to continue across the Gulf of California and northwards. Monthly averaged SSHa for November 2019 illustrate that a thin band of positive coastal sea level set up along the coast from the equator northward to California (Figure 1.15e). In addition to the wind stress forcing, there are some periods in these years when equatorial forcing also may have contributed to positive flow anomalies. These years coincided with marine heatwaves in the North Pacific (Amaya et al. 2020; Weber et al. 2021; Barkhordarian et al. 2022) and there may be a connection between these events and the changes in the wind field off Baja California and southern California.

1.3.4 Large-scale Climate Phenomena and their Impact on Poleward Flow

During the years of anomalous poleward flow between 2012 and 2021, there were many large-scale climate phenomena that took place. Some of these phenomena originated as equatorially forced, e.g., El Niño, while others persisted in the North Pacific, e.g., North Pacific marine heatwaves, and were caused by atmospheric events. It is of interest to examine how the poleward flow anomalies may be related to these larger climate phenomena. In many of the four time periods classified as having positive anomalous flow conditions in Figure 1.13, there is an exchange in dominancy between the gyre-scale pressure gradient and the wind stress forcing poleward flow anomalies. On several accounts increases in the gyre-scale APG velocity anomalies reach and exceed one standard deviation above the mean and these coincided with an El Niño or with advanced conditions suggesting a possible El Niño, e.g., summer 2012, spring 2014, spring and fall/winter 2015, and winter 2018/2019 (Figure 1.13). The influence of remote forcing during these times on poleward flow anomalies in southern California demonstrate the large spatial scale equatorial processes can have in the eastern North Pacific.

Other periods of poleward flow anomalies coincided with atmospheric events, e.g., winter 2013/2014, winter 2014/2015, summer 2017, summer 2019, etc. Positive wind velocity anomalies seen throughout the periods of anomalous poleward flow in Figure 1.13 may be related to larger-scale atmospheric phenomena occurring over the years of positive flow anomalies. Two potential mechanisms are considered to explain how these larger-scale atmospheric changes influence the winds off southern California and Baja California.

First, the atmospheric ridge that led to the 2014 marine heatwave is reviewed. The persistent ridge of atmospheric pressure formed in the Northeast Pacific near the Gulf of Alaska and yielded positive sea level pressure anomalies in that region (Figure 1.17a, Figure 2 in Bond

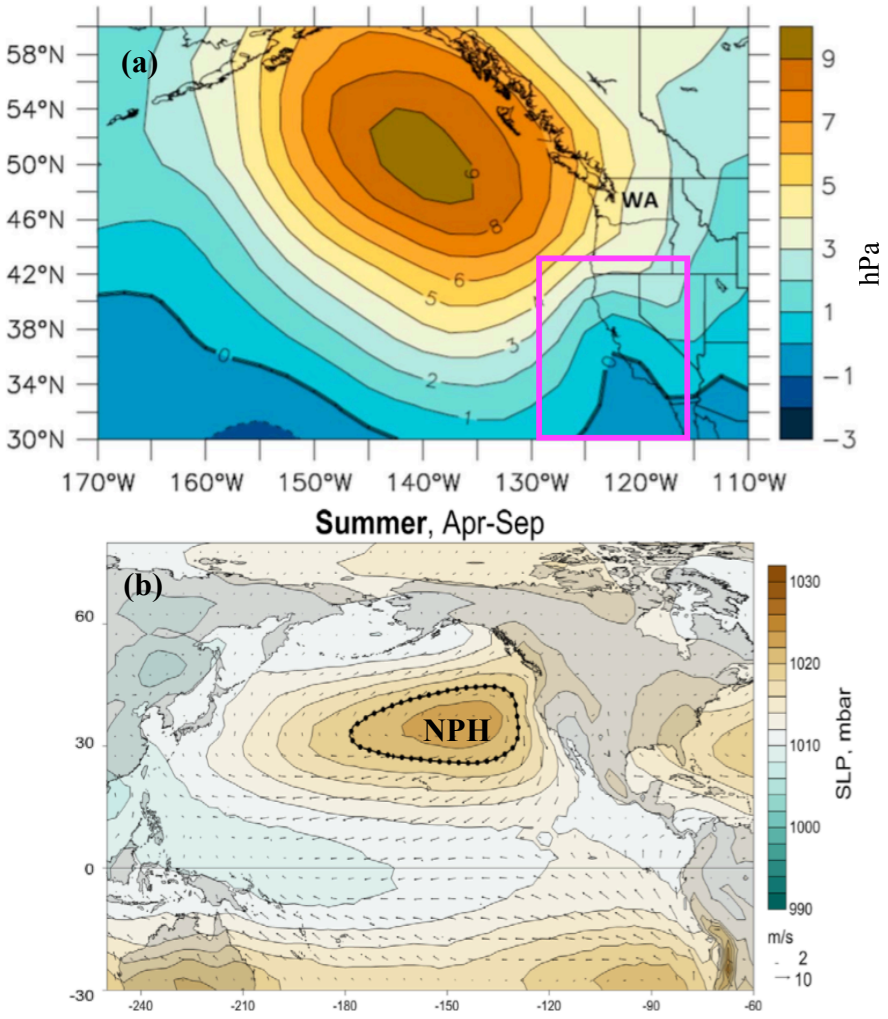

Figure 1.17: (a) Mean sea level pressure anomalies over October 2013 through January 2014 adapted from Bond et al. (2015). (b) Sea Level Pressure summer seasonal climatology adapted from Fiedler and Mantua (2017). Dotted contour is the 1020 mbar isobar. NPH stands for the North Pacific High.

et al. 2015; Wang et al. 2014; Bond et al. 2015; Swain et al. 2017). The negative vorticity anomaly associated with the ridge of positive sea level pressure anomalies drives an anticyclonic circulation. In California, the isobar anomalies deflect northward (magenta box in Figure 1.17a), which alongside the negative vorticity anomaly would lead to poleward geostrophic wind anomalies. This would counteract the typical southward winds that prevail off California. Examples of when the atmospheric ridge is present with poleward wind velocity anomalies in Figure 1.13 are in winters 2013/2014 and 2014/2015. An atmospheric ridge returned during the

more recent marine heatwaves of 2019 – 2021 and the intensity and frequency of these events are attributed to anthropogenic changes and greenhouse gases (Weber et al. 2021, Barkhordarian et al. 2022).

A second mechanism to explain the local wind may be influenced by the large-scale pressure systems is due to a weakened North Pacific High. In the summertime, the climatological mean contains a North Pacific High that is broadened and strengthened, and this drives southward winds off of California (Figure 1.17b). When this high pressure is reduced, it weakens the zonal gradient in the atmospheric pressure, thereby weakening the magnitude of the meridional geostrophic winds. Amaya et al. (2020)'s North Pacific High Intensity index shows a weakened summertime North Pacific High in 2013 - 2015, 2017, and 2019. Summertime positive wind velocity anomalies in these years may have resulted from the weakened North Pacific High, with the weakening in 2019 driving the 2019 North Pacific marine heatwave (Amaya et al. 2020).

Based on the analysis presented above, poleward flow anomalies in southern California appear to be related to anomalous atmospheric forcing over the North Pacific along with heightened equatorial activity. The flow anomalies over 2012 – 2021 appear to be related to large-scale mechanisms, e.g., El Niños and marine heatwaves, and may serve as an indicator for these phenomena. To further characterize the equatorial and wind forcing of poleward flow anomalies, water mass properties are examined to address the impact of flow anomalies on source waters in southern California.

1.4 Water Mass Analysis Results and Discussion

The anomalous poleward flow investigated in the previous section is suspected to have caused changes in the water mass composition. This section analyzes the long-term and seasonal

means in the water mass composition, the water mass anomalies along isopycnals, and the relationship between the SCE and the water mass anomalies. This section also examines the wind stress curl against the SCE index and particle trajectories to qualitatively assess the horizontal flow field for select periods of interest.

1.4.1 Long-term and Seasonal Means

Results from the water mass analysis show that at the shallower DM sensor, the long-term mean is made up of about 60% PSUW with the other 40% coming from PEW (Figure 1.18). At 90 m depth, the mean composition is about 40% PSUW and nearly 60% PEW, which differs from the mean at 35 m depth. The long-term means and Figure 1.18 demonstrate how the water mass fractions change with depth. The dependence of the mean composition on depth

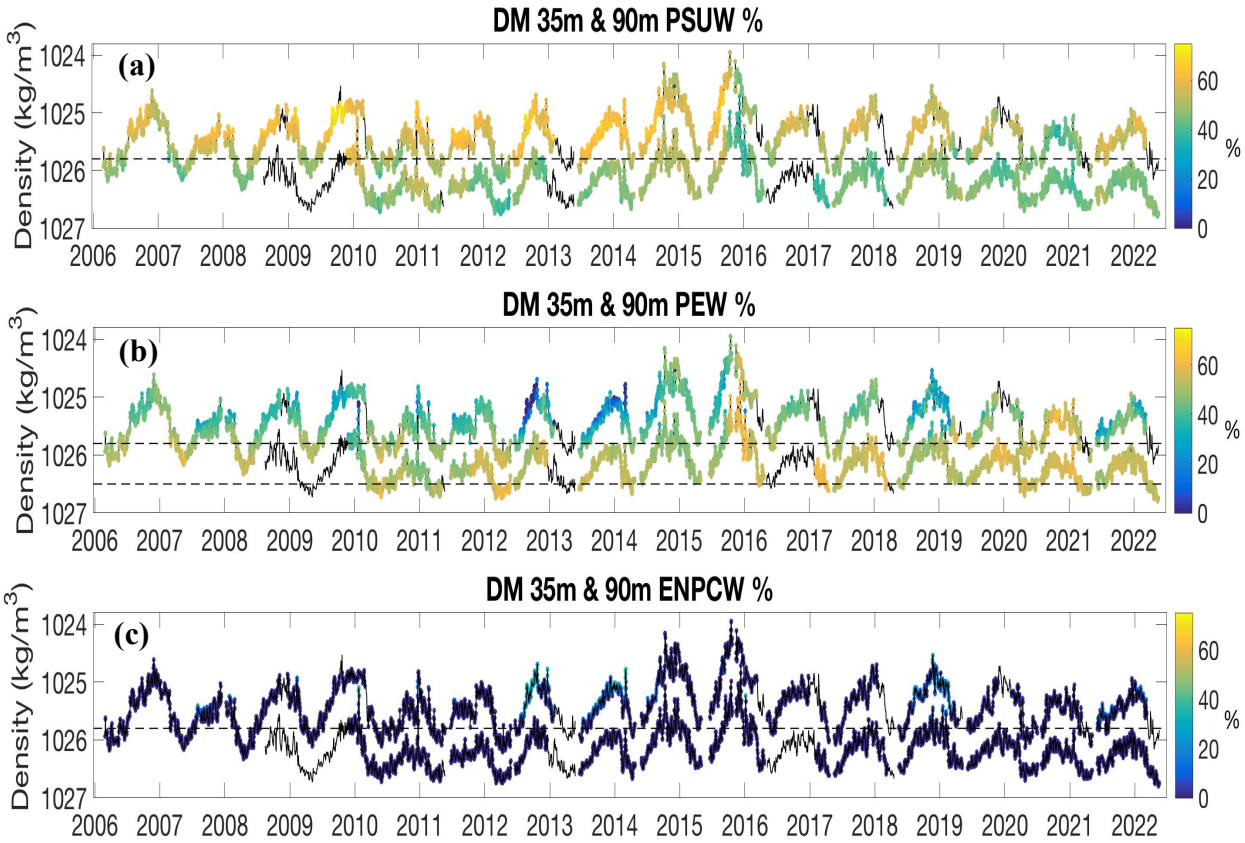

Figure 1.18: Density timeseries (black) at DM 35 m (upper lines) and 90 m depth (lower lines) with colored circles reporting the percentage of (a) PSUW, (b) PEW, and (c) ENPCW from the water mass analysis. Horizontal dashed lines mark the 1025.8 and the 1026.5 kg/m^3 densities.

demonstrates that PSUW makes up a greater proportion at lower densities while at larger densities the fraction of PEW becomes higher. In this long-term mean, only source waters from the north and south contribute to the temporal average. Similarly, at CCE2, only the north and south water masses contribute to the record-long mean with the former making up about 55% of the composition and the latter about 45% (Figure 1.19).

Changes in water mass percentages at a fixed depth may be caused by a change in density or by a change on an isopycnal. For the former, vertical heaving of isopycnals may alter relative ratios of source waters. This is due to the isopycnal dependence of the water mass composition. On seasonal timescales, the variability in water composition is partly related to this vertical heaving. When denser waters are brought up through upwelling processes in spring, the percentage of PEW measured by the sensor increases (Figure 1.18b). During the relaxation season in summer/fall, densities decrease and more PSUW is present (Figure 1.18a).

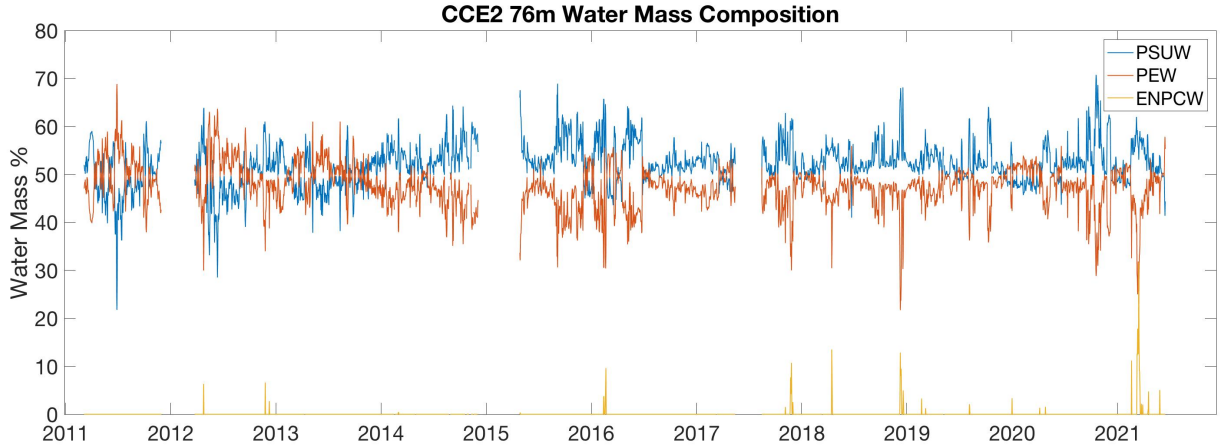

Figure 1.19: Water mass composition from the source water mass analysis at CCE2 75 m depth.

Bograd et al. (2019) analyzed the seasonal mean water mass composition on select isopycnals and the long-term variability from the CalCOFI data in southern California. The long-term variability in Bograd et al. (2019) is only presented at a few locations and does not consider the long-term variability in the upper ~100 m, so the results presented here are only compared against the seasonal means from Bograd et al. (2019) on select isopycnals. Additionally, the

isopycnals used to show the seasonal means from Bograd et al. (2019) are not within the range of isopycnals measured by the 75 m sensor at CCE2 so a comparison is made only at DM. Near the DM mooring, ~40 km offshore of DM, and on the 25.8 kg/m^3 isopycnal, Bograd et al. (2019) indicate that PSUW concentrations have a year-round mean of ~52% (Bograd et al. 2019; their Figure 2) which is close to what is seen in Figure 1.18a. For PEW on this isopycnal, their results demonstrate a year-round mean of 28% (Bograd et al. 2019; their Figures 2 and 3c) while Figure 1.18b shows a higher year-round mean closer to that of PSUW. Better agreement in PEW fractional composition is found on the 1026.5 kg/m^3 isopycnal. Bograd et al. (2019) report a year-round PEW mean of ~52% (their Figures 2 and 3c) while those in Figure 1.18b indicate a mean of ~58%. The discrepancy on the 1025.8 kg/m^3 isopycnal is related to the influence of ENPCW. In Bograd et al. (2019) the lower PSUW mean is compensated for by ENPCW, which has a mean of ~20%, whereas the results reported in Figure 1.18c do not have ENPCW contributing significantly to the long-term mean.

1.4.2 Isopycnal Anomalies

To determine changes in source water composition due to horizontal advection, i.e., source water changes on an isopycnal, the isopycnal median of the water mass composition is estimated and removed as follows. Density is binned in step sizes of 0.1 kg/m^3 and the median percentage of each water mass is computed for each bin. The median percentages corresponding to the density observed at a given moment are removed at each time step to create the water mass anomalies. Thus, for each sensor there are three timeseries of anomalies, one for each water mass. This effectively removes changes in water masses due to vertical heaving of isopycnals. Figure 1.20 shows the source water anomalies from the 35 and 90 m sensors at DM and from the

75 m sensors at CCE2. These water mass anomalies are on varying isopycnals as they sweep past the sensors.

At 35 m depth for DM, the PSUW and PEW anomalies display a seasonal variability whereby a positive anomaly in one water mass is compensated for by an almost equal anomaly of negative sign in the other water mass. Generally, positive PSUW anomalies cycle through summer/fall and positive PEW anomalies occur in winter/spring (Figure 1.20a). This seasonal behavior suggests changes in horizontal pathways of flow in the SCB that are also seasonal, and this is examined in Section 1.4.3. At the deeper DM site and at CCE2, the magnitudes of the

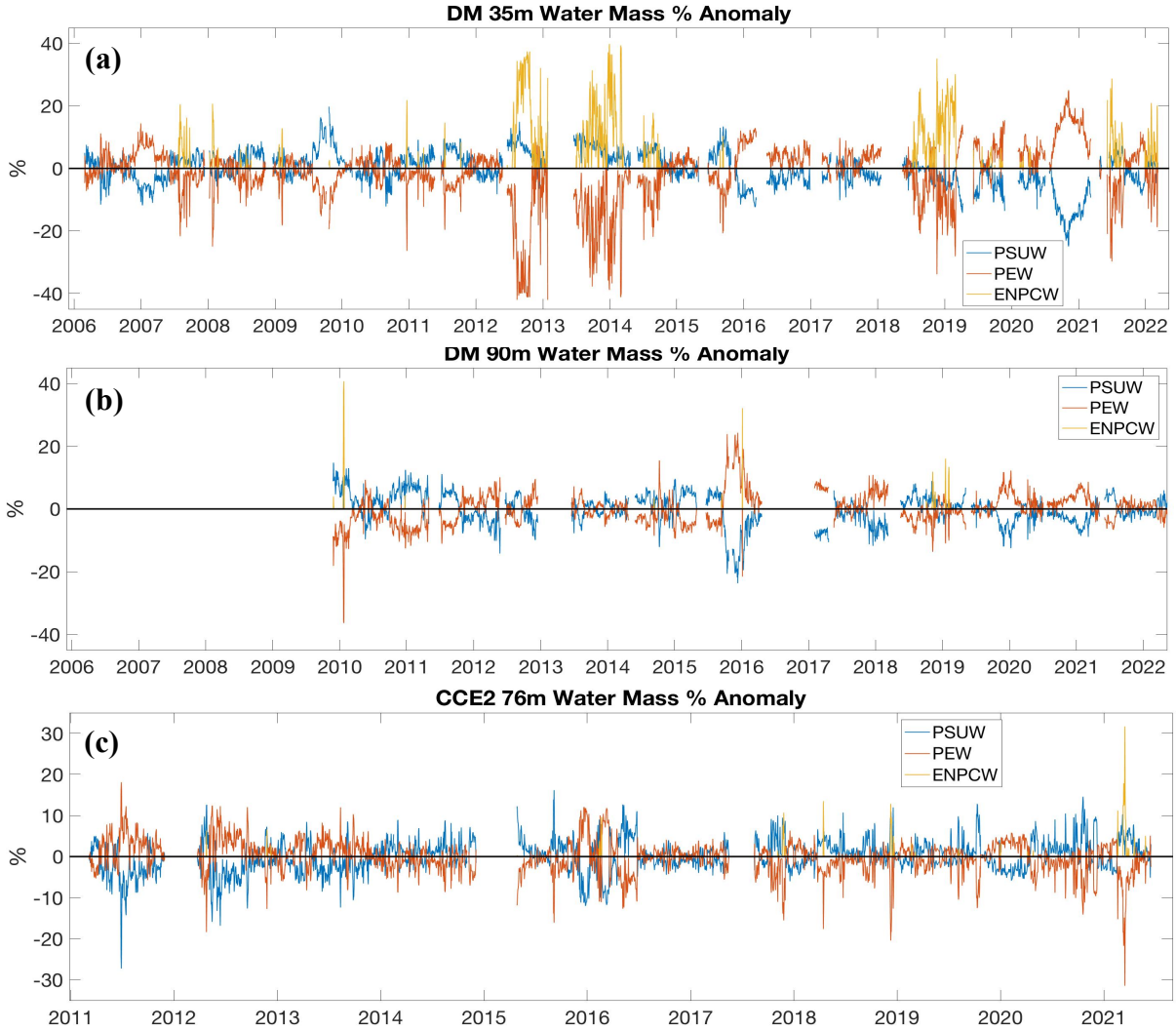

Figure 1.20: Water mass anomalies on isopycnals at (a) DM 35 m, (b) DM 90 m, and (c) CCE2 75 m depths. Note the different x axes for DM and CCE2.

PSUW and PEW anomalies are similar but of different signs (Figures 1.20b and 1.20c). The behavior of these anomalies do not appear to be seasonally variable.

The largest water mass anomalies measured by the 35 m sensor at DM reached and exceeded 30%. This occurred in 2012, 2013, 2018, and 2021 with increased ENPCW and PSUW anomalies that were compensated for by decreased PEW anomalies, except for in 2018 when PSUW anomalies remain weakly negative. Of the years exhibiting anomalous poleward flow at DM, 2012 and 2013 show the largest poleward alongshore displacement and this coincides with the large ENPCW anomalies (Figures 1.10 and 1.20a). The positive ENPCW anomalies at DM 35 m depth are not present at the deeper DM sensor nor at CCE2 suggesting that water mass anomalies can have spatial differences both horizontally and vertically within the SCB. The other years of anomalous poleward flow, 2014 and 2015, do not have as large anomalies but contain positive PSUW and ENPCW anomalies with negative PEW anomalies in summer and then switch to positive PEW and negative PSUW anomalies in fall/winter. We caution that the strength of the anomalies at the shallower sensor in these two years is not well known since the density does not reach these low values in other years in the timeseries. Both 2019 and 2020 also exhibit notable positive PEW anomalies. The presence of these anomalies also persists under periods of positive poleward flow anomalies (Figure 1.11a). At the deeper 90 m sensor, the most significant anomalies take place at the end of 2015 and early 2016 when positive PEW anomalies reach nearly 25% and are compensated for by negative PSUW anomalies of similar magnitude (Figures 1.20b). Water mass anomalies at the CCE2 75 m depth do not show pronounced anomalies during years of anomalous poleward flow, but like at DM, positive PEW anomalies are present at the end of 2015 - early 2016 and at the end of 2019 (Figure 1.20c).

1.4.3 Southern California Eddy

1.4.3.1 Seasonal Behavior and SCE Index

The timeseries of the water mass anomalies at DM 35 m depth suggested that there might be some seasonality in the variability of the anomalies on isopycnals (Figure 1.20a). One potential mechanism to explain the seasonal variability in the water mass anomalies is the Southern California Eddy (SCE). In spring, alongshore winds are upwelling favorable and strong, and in summer the nearshore winds relax causing the wind stress curl to increase. Model results suggest that the wind stress curl is responsible for setting up the SCE, with variability in the yearly location of the SCE linked to the wind stress curl field (McCreary et al. 1987; Di

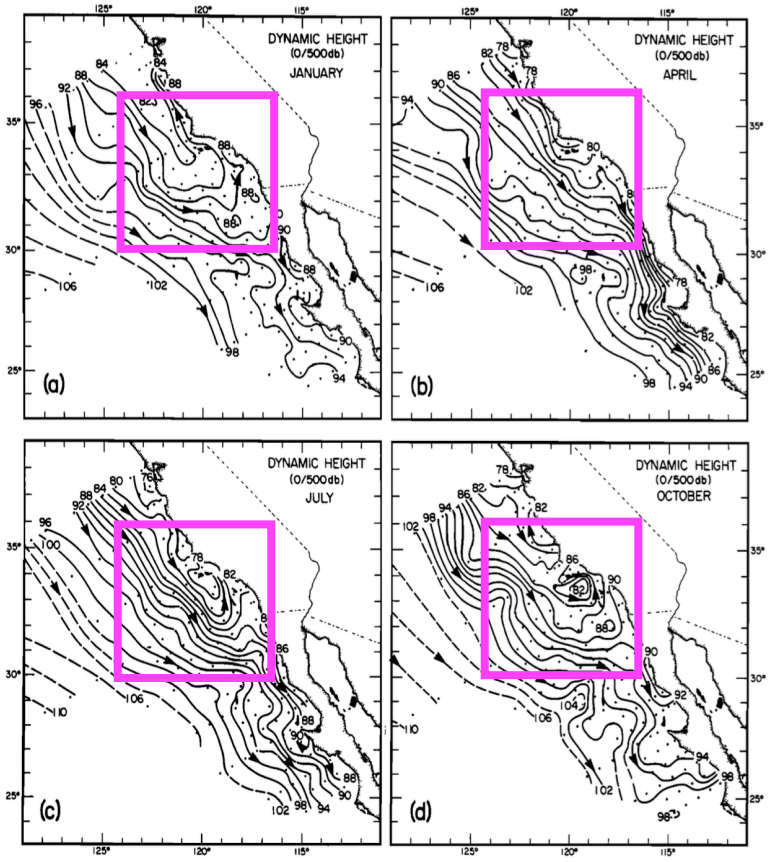

Figure 1.21: Mean dynamic height (dyn cm) of the surface relative to 500 dbar for four periods over about 60 days for (a) January, (b) April, (c) July, and (d) October, adopted from Lynn et al. (1982). Magenta boxes encompass the region of recirculation.

Lorenzo 2003). Dynamic height at the surface demonstrates the cyclonic recirculation in the SCB (Figure 1.21). On the south side of this seasonal cyclonic feature water is advected onshore into the Bight. This is a branch of the CC carrying PSUW and could be responsible for the cyclical nature of the PSUW anomalies at the DM 35 m in Figure 1.20a.

We hypothesize that this is the mechanism responsible for the seasonal variability in the water mass anomalies at DM 35 m depth (Figure 1.20a) and for circulating PSUW and ENPCW in the upper ocean to the coastal region of southern California. ENPCW may be mixed with PSUW as these waters advect eastward across the Pacific Northwest and turn southward as the CC (Reid et al. 1958). Another potential mechanism for bringing ENPCW into southern California is entrainment in the CC offshore of the SCE under a stronger SCE presence. Roden (1971) describes a transition zone between subarctic waters from the north and subtropical

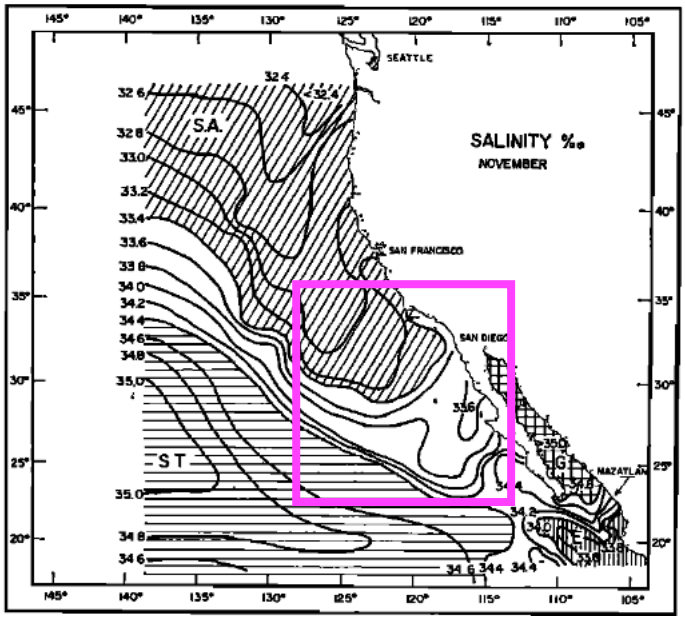

Figure 1.22: November sea surface salinity from ship-based measurements off of the US west coast. Unshaded region is the transition zone between subarctic (SA) and subtropical (ST) waters. Magenta box shows the region offshore of southern California where the transition zone moves eastward with one branch turning northward into the SCB. Figure modified from Roden (1971).

waters from the west, and the isohalines characteristic of this zone recirculate into the SCB (Figure 1.22).

When the cross-shore flow is onshore and the alongshore flow is poleward, then this may be indicative of the spin up of the SCE. It is proposed that the seasonal spin up of the SCE yields more positive anomalies of PSUW near the coast. Periods of both onshore and poleward flow are shaded in Figure 1.23a and this is qualitatively compared to the monthly low-pass filtered water mass anomalies at DM 35 m depth (Figure 1.23b). The water mass anomalies in Figure 1.23b are the same as those in Figure 1.20a but with a monthly filter applied. In most years, the shaded periods of onshore and poleward flows coincide with positive and/or increasing PSUW and/or ENPCW anomalies (Figure 1.23). These positive and/or increasing anomalies are compensated

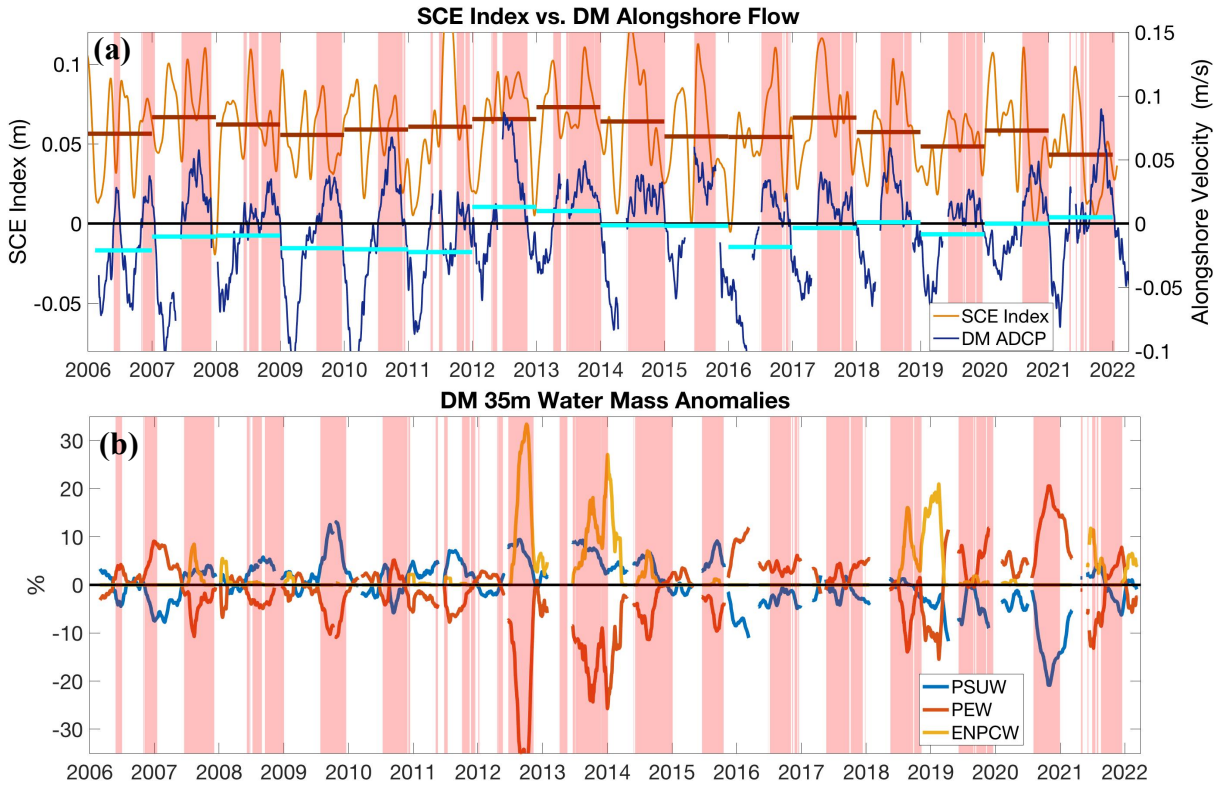

Figure 1.23: (a) SCE index and DM seasonally filtered alongshore flow at 40 m depth. Horizontal bars are the annual averages estimated over the calendar year. Shaded periods are when both the SCE index and alongshore flow are positive, i.e., onshore and poleward flows. (b) Monthly filtered water mass anomalies at DM 35 m depth. The shaded periods are the same from (a).

with negative and/or decreasing PEW anomalies. This behavior may be a due to the appearance of the SCE which turns CC waters towards the coast and northward into the SCB and brings onshore more PSUW and at times ENPCW (Figure 1.23b).

Most of the time the SCE index is positive (Figure 1.23a), but onshore flow does not have to be recirculated northward as it may turn southward after moving onshore (Chereskin and Niiler 1994). If the local currents at DM are southward, then the water masses advected onshore via the SCE may not reach DM. This demonstrates how poleward flow can be important for advecting PSUW and ENPCW anomalies past the DM mooring. There are some events in Figure 1.23b when there are positive and increasing PEW anomalies during shaded periods such as in 2006 and 2020. Despite these contradictions to the hypothesis that the SCE brings more PSUW and ENPCW anomalies inshore, these periods show that while the SCE index is positive it is decreasing and therefore cross-shore flow is weakly onshore. Additionally, there are two ambiguous periods, i.e., 2016 and 2017, when there is onshore and poleward flow but mild changes in the water mass anomalies. These are special cases that will be addressed later. Next, a more detailed review is given of the SCE index, coastal poleward flow, and water mass anomalies during 2012 – 2013, 2014 - 2015, 2016 – 2017, 2018, and 2019 - 2021.

1.4.3.2 2012 - 2013

Beginning with 2012 and 2013, these two years demonstrate similar behaviors. The more coherent SCE in 2012 and 2013, e.g., higher SCE annual averages in Figure 1.23a, combined with larger poleward flows at DM (Figure 1.23a) agrees with the timing of increased PSUW and ENPCW anomalies (Figure 1.23b). PSUW anomalies increase first followed by increased ENPCW a couple of months later. These are compensated for by large negative PEW anomalies. If ENPCW were advected into the CC upstream, then it is expected that the increase in PSUW

and ENPCW anomalies would be simultaneous. Instead, the lag between the two water masses supports some other mechanism for bringing ENPCW into the SCB. One possibility is entrainment into the CC due to a strong SCE. These waters may get entrained and make their way onshore such as in Figure 1.22. In Figure 1.10a, the cumulative alongshore displacement in 2012 and 2013 show the largest net poleward displacement by the end of the year. This is in part due to the less southward flow during the upwelling season (Figure 1.23a), i.e., positive velocity anomalies (Figure 1.10a), and stronger poleward flow in summer - fall in these years (Figures 1.11a and 1.23a). The higher annual averages in the DM alongshore flow and the SCE index indicate a more pronounced SCE in 2012 and 2013 and that this caused the large positive PSUW and ENPCW anomalies that were compensated for by large negative PEW anomalies. In the two years before the 2014 marine heatwave and the 2015 – 2016 El Niño, water mass anomalies show increased water from the north, i.e., PSUW, and from the west, i.e., ENPCW.

1.4.3.3 2014 - 2015

Both 2014 and 2015 are consistent with the hypothesis that the SCE brings more PSUW and/or ENPCW to the coast. This is shown by the positive PSUW and ENPCW anomalies during the shaded periods in these years (Figure 1.23b) alongside a positive SCE index and poleward flow (Figure 1.23a). The positive PSUW and ENPCW anomalies coincide with negative PEW anomalies. These positive anomalies and the annual averages in the SCE index and alongshore flow (Figure 1.23a) are not as large as their respective values in 2012 and 2013. During the marine heatwave in 2014, water mass anomalies favor waters that originate from the north and west. The same is true for the summer of 2015 during the 2015 – 2016 El Niño.

In fall 2015, the SCE index decreases to become briefly negative in winter (Figure 1.23a), and the positive PSUW anomalies are replaced by positive PEW anomalies at both depths

at DM and at CCE2 (Figures 1.20 and 1.23). The PEW/PSUW anomalies reach some of their highest/lowest values over the ~15-year period. The large change in water mass composition suggests significant advection from the south. The anomalous poleward flow during this time was discussed in Section 1.3 and is associated with an increase in the gyre-scale APG during the 2015 – 2016 El Niño. The gyre-scale APG increased due to the multiple CTWs that raised and sustained coastal sea levels in the latter months of 2015 (Figures 1.13, 1.14, and 1.15c). The SCE index decreased and became temporarily negative (Figure 1.23a); thus, the poleward advection occurring at the end of 2015 is not related to the SCE but is rather attributed to continuous coastal poleward flow from the south. The persistent remote forcing in the second half of 2015, along with a weakening in the SCE, likely drove coherent poleward flow along Baja California and into southern California, and consequentially changed the water mass composition in favor of PEW. To further argue this, particle trajectories assist in determining the alongshore displacement of flow that reaches southern California at this time and are presented in Section 1.4.5.

1.4.3.4 2016 - 2017

As noted earlier, water mass anomalies in 2016 and 2017 appear not to support the hypothesis that the seasonal appearance of the SCE advects more PSUW inshore (Figure 1.23a). This unusual behavior will be examined, and an explanation is given to rationalize the atypical response in water mass anomalies. In both 2016 and 2017 high values in the SCE index coincide with stronger poleward flow at DM and positive PEW anomalies (Figure 1.23). It is suggested that re-entrainment of PEW waters via the SCE causes the continued positive PEW anomalies. As part of the regional circulation, the SCC flows poleward where it reaches the northern region of the SCB. It may either continue northward around Point Conception, i.e., the Davidson

Current, or flow offshore and re-enter the CC. When the latter happens, the waters in this branch are subject to being mixed in with CC waters and re-introduced into the bight via the SCE upon its seasonal spin up. This will be tested using particle trajectories in Section 1.4.5 and may elucidate why there are positive PEW anomalies in 2016 and 2017.

1.4.3.5 2018

The positive PEW anomalies endured through 2016 and 2017 but were replaced in 2018 by positive ENPCW anomalies (Figure 1.23b). At this time, the SCE index increased contemporaneously with enhanced poleward flow at DM (Figure 1.23a). This is a unique occurrence because the signs of the ENPCW and PSUW anomalies opposed one another, particularly in the second pulse of positive ENPCW anomalies during winter. The first pulse of ENPCW anomalies is concurrent with the increase in the SCE index and alongshore flow at DM, and ENPCW anomalies are primarily compensated for by negative PEW anomalies. The positive ENPCW anomalies represent the higher salinity and the higher oxygen at this time. Glider observations also measure higher salinity in 2018, and Argo data indicate that a region of high salinity formed in 2015 in the North Pacific subtropical gyre and was advected eastward into the CCS over the next 2 - 3 years (Ren and Rudnick 2021). The eastward advection of this high salinity water overlaps in space with the region of ENPCW in the subtropical gyre (Roden 1971). The advection of ENPCW into the CC alters the ratio of PSUW to ENPCW explaining the 2018 increase in ENPCW anomalies and decrease in PSUW anomalies.

Between pulses of positive ENPCW anomalies, the ENPCW and PEW anomalies approach 0%, with PEW values becoming weakly positive. These anomaly reversals may be related to the regional marine heatwave off of northern Baja California which set record high temperatures in southern California, exceeding all measurements made over the previous century

(Fumo et al. 2020; Wei et al. 2021). Unlike the 2014 marine heatwave which was over the North Pacific, the 2018 marine heatwave was a regional event in Baja California and southern California. Off Baja California, both local, e.g., winds, and remote, e.g., CTWs, forcing contributed to the regional heatwave which lasted for about one month before dissipating (Fumo et al. 2020; Wei et al. 2021). Both the gyre-scale APG and the wind stress velocity anomalies in Figure 1.13a are positive at this time. Thus, some of the poleward flow in this year may have had origins from further south and this may be reflected in the increasing of the negative PEW anomalies in Figure 1.23b. Following the termination of the heatwave was the second pulse of positive ENPCW waters. It is not clear whether this second pulse is a different batch of ENPCW anomalies or the same waters from the first pulse but advected southward past the mooring. However, the presence of ENPCW a couple of kilometers from the coast in 2018 highlights the importance of understanding the horizontal circulation that carries subtropical gyre waters from the open ocean all the way to the shelf.

1.4.3.6 2019 - 2021

Multiple North Pacific marine heatwaves occurred throughout 2019 - 2021 (Amaya et al. 2020; Weber et al. 2021; Barkhorarian et al. 2022) and these events may have influenced the source waters. In late fall – early winter of 2019, the magnitudes of the PEW and PSUW anomalies increase (Figure 1.23b) and this is contemporaneous with poleward flow anomalies (Figure 1.11a). These results suggest alongshore advection of PEW from lower latitudes. There are poleward propagating SSH in the last few months of 2019 (Figure 1.14) and these remote forcings, along with a weaker SCE (lower annual average in Figure 1.23a), may have led to conditions favoring more PEW.

During the weak 2018 - 2019 El Niño, there were similar magnitudes of remote forcing in fall 2018 and fall 2019 (Figure 1.13). The stronger SCE index in 2018 (annual average in Figure 1.23a) may have encouraged more onshore recirculation explaining the increased ENPCW anomalies. While in 2019, the overall weaker SCE index may have reduced onshore flows permitting more alongshore flow from further south.

The marine heatwave re-emerged in 2020 along with another episode of PEW anomalies (Figures 1.20 and 1.23b). The dynamical forcing (Figure 1.13) differs from other occurrences of positive PEW anomalies, e.g., falls of 2015 and 2019. The positive Baja California wind stress velocity anomalies (Figure 1.13a) encourage positive flow anomalies (Figure 1.11a) that are contemporaneous with positive PEW anomalies (Figures 1.20 and 1.23b). Two possible scenarios may explain these observations. First, wind stress can directly drive poleward flow, and second, alongshore variations in the alongshore wind field can result in an APG.

There are a few days in August that do have positive wind stresses (not shown), but the monthly low-pass filtered Baja California wind stresses are more positive than the southern California wind stresses in mid-2020 (Figure 1.24). This convergence in the wind field can pile up water and cause a poleward APG force. There is a mild increase in the anomalies in the

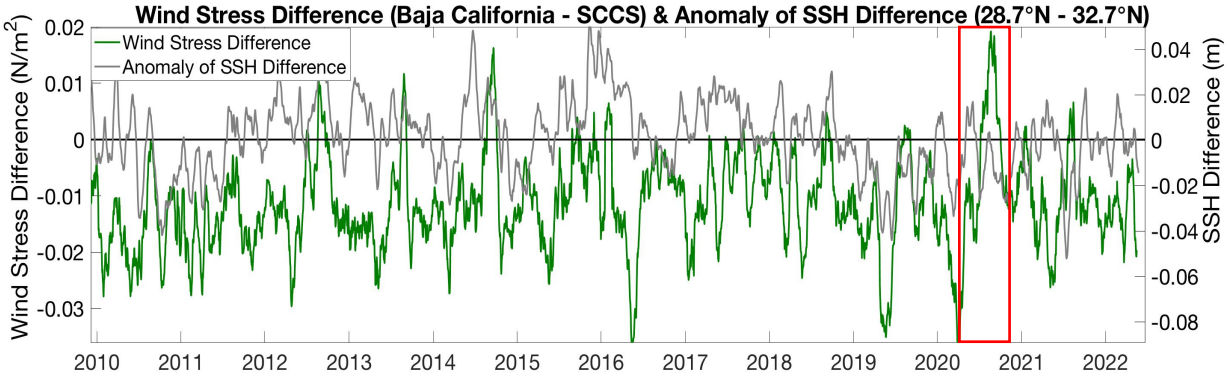

Figure 1.24: Differences in monthly-filtered alongshore wind stress between Baja California and the SCCS. Also shown is the anomaly of the SSH difference between Baja California and southern California from GLORYS data. Red box shows the period in which the wind stresses off of Baja California are more positive than the wind stresses in the SCCS.

alongshore sea level difference between Baja California and southern California (Figure 1.24), however it is not clear that this is significant enough to cause the anomalous observations in the alongshore flow and in the source waters.

This wind effect may also generate CTWs as energy is transferred from potential energy, e.g., piling up of water, to kinetic energy, e.g., CTWs. CTWs can leak energy offshore as Rossby waves, and model results have found that both APGs and Rossby waves can accelerate and shoal the undercurrent (McCreary and Chao 1985; Marchesiello et al. 2003; Pringle and Dever 2009; Connolly et al. 2014; Thomson and Krassovski 2010; Gomez-Valdivia et al. 2017). There are mild positive SSHa between Baja California and southern California (Figure 1.14). The phase speed of the propagating SSHa is ~278 km/day in agreement with other reports of wind-driven CTW phase speeds for this area (Christensen et al. 1983; Enfield and Allen 1983; Merrifield and Winant 1989).

CTWs and APGs can shoal the CU and potentially mix CU waters, i.e., PEW, across isopycnals. Cross-isopycnal mixing is speculative but could occur from multiple processes, e.g., upwelling, vertical tidal mixing, breaking internal waves, etc. Despite the modest amplitude in the alongshore difference in sea level and coastal SSHa (Figures 1.14 and 1.24), the remote forcings in 2018 and 2019 (Figure 1.13) along with higher amounts of PEW in 2019 (Figures 1.20 and 1.23b) may have preconditioned the coastal ocean such that a small perturbation, like the wind convergence event, could excite the positive PEW anomalies.

The heatwave returns in 2021 and a heightened SCE index occurs alongside positive PSUW and ENPCW anomalies (Figure 1.23). For the first time in ~2.5 years, the PSUW anomalies are positive indicating a change in the source water ratios in the CC.

Increased PEW anomalies in falls of 2019, 2020, and 2021 occur around the time the North Pacific marine heatwaves peaked. Poleward flow anomalies (Figure 1.11a) in the presence of a lower SCE index (Figure 1.23a) permitted positive PEW anomalies (Figures 1.20 and 1.23b). It is not clear whether there is an association between the heatwaves, the poleward flow, and the PEW anomalies. The poleward flow and the PEW anomalies are suggested to be a result of the remote forcing in 2019 – 2021. However, equatorial forcing and the North Pacific marine heatwaves may be linked via atmospheric teleconnections between the equator and the North Pacific. Amaya et al. (2020) found the North Pacific High weakening during the 2019 heatwave was assisted by remote SST forcing from the equator and a difference between the 2014 and 2019 marine heatwaves is the season when the heatwaves occurred. The 2014 heatwave began in winter and the 2019 heatwave took place more over summer. The seasonal timing of these events may impact the SCCS differently, e.g., poleward flow anomalies associated with the SCE bringing positive PSUW and ENPCW anomalies as in 2013 - 2015 versus poleward flow anomalies from alongshore advection of more tropical waters like in 2019.

1.4.3.7 Water Mass Anomalies Conclusion

Results from the water mass analysis describe the seasonal cycle of source water composition as well as interannual variability in the SCB related to changes in horizontal advection. Mean water mass composition documents a tradeoff between PSUW and PEW with depth, with the proportion of PEW increasing on denser isopycnals. This study has proposed that the seasonal cycle in the water mass anomalies at DM 35 m depth is related to the seasonal spin up of the SCE. Larger annual averages of the SCE index in 2012 and 2013 alongside enhanced nearshore poleward flow and anomalous PSUW and ENPCW indicate a strengthened and more coherent SCE. During the 2014 marine heatwave and the 2015 – 2016 El Niño, water mass

anomalies are supportive of the hypothesis that the SCE brings more PSUW and ENPCW onshore and in to the SCB. At the end of 2015, El Niño driven changes in the water mass composition caused increased PEW anomalies in the bight which persisted over the next couple of years. This behavior is broken up in 2018 when CC waters are modified, and during the North Pacific marine heatwaves in 2019 – 2021 when greater PEW anomalies emerge. The interannual variability in the water mass anomalies may be linked to the numerous large-scale climate phenomena that took place between 2012 and 2021.

1.4.4 Wind Stress Curl Forcing of SCE

The purpose of this section is to evaluate whether there is a relation in the low-frequency interannual variability of the wind stress curl (and/or its alongshore gradient) with the regional APG. The wind stress curl has previously been reported to be an important driver of coastal poleward flow and the SCE (Oey 1999; Di Lorenzo 2003). In Section 1.3, the regional APG was modeled by equation (4) for the regression analysis because the objective was to determine southerly regions of anomalous remote forcing. Remote forcing is one factor that can influence the regional APG, but other processes such as the wind stress curl can also modify the APG. Here, the emphasis is on the association between the wind stress curl and the regional APG. The regional APG is approximated as the difference in sea level in the SCB and is taken as the SCE index.

The annual cycles of the regionally-averaged wind stress curl, the alongshore curl difference, and the SCE index are computed over 2000 – 2021 and are displayed in Figure 1.25. All the annual cycles remain positive throughout the year and have a minimum in the winter. The annual cycles for the wind field and the SCE index peak in spring and summer, respectively. There is a 3 – 4 month lag between the peak in the annual cycles in the wind field and the SCE

index with the wind field peaking first, similar to what other studies found regarding the wind stress curl and poleward flow. The annual cycles of the wind field peak ~2 months earlier than the model results of Di Lorenzo (2003). This difference in timing of the peak may be related to the minimally, if at all, overlapping time periods over which the annual cycle is computed in Di Lorenzo (2003) versus here, and decadal variability over these different time periods may contribute to these differences.

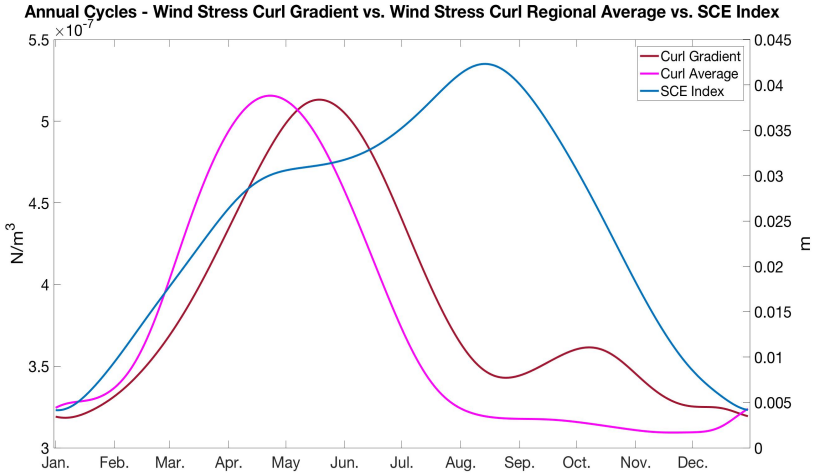

Figure 1.25: Annual cycles of the alongshore curl difference, the regional curl average, and the SCE index calculated over 2000 - 2021.

To understand whether there is a relation in the interannual variability of the wind stress curl and pseudo APG, the annual cycles calculated over 2000 - 2021 are removed and the anomalies are annually averaged over the calendar year (Figure 1.26). Over 2006 – 2021, the annual averages of the wind stress curl gradient anomalies and the SCE index anomalies generally follow the same trends. The annual averages of the curl average anomalies and the annual averages of the SCE index anomalies are less agreeable. The 2012 and 2013 positive annual averages in both of the curl timeseries and the SCE index align with the presence of anomalous ENPCW (Figure 1.23b). The higher annual averages in the SCE index in 2012 and 2013 are not unique. Some years in the first decade of the timeseries in Figure 1.26 also contain

higher annual averages, e.g., 2001 and 2005. The behavior in the annual averages for these years differs from the behavior in the curl annual averages. Generally, the variability in the annual averages from 2006 onward suggests that there may be some relation between the wind stress curl and the SCE index, i.e., the APG, and such long-term variability in the wind stress curl may be linked to the PDO as Davis and Di Lorenzo (2015) demonstrated that they were not independent of each other.

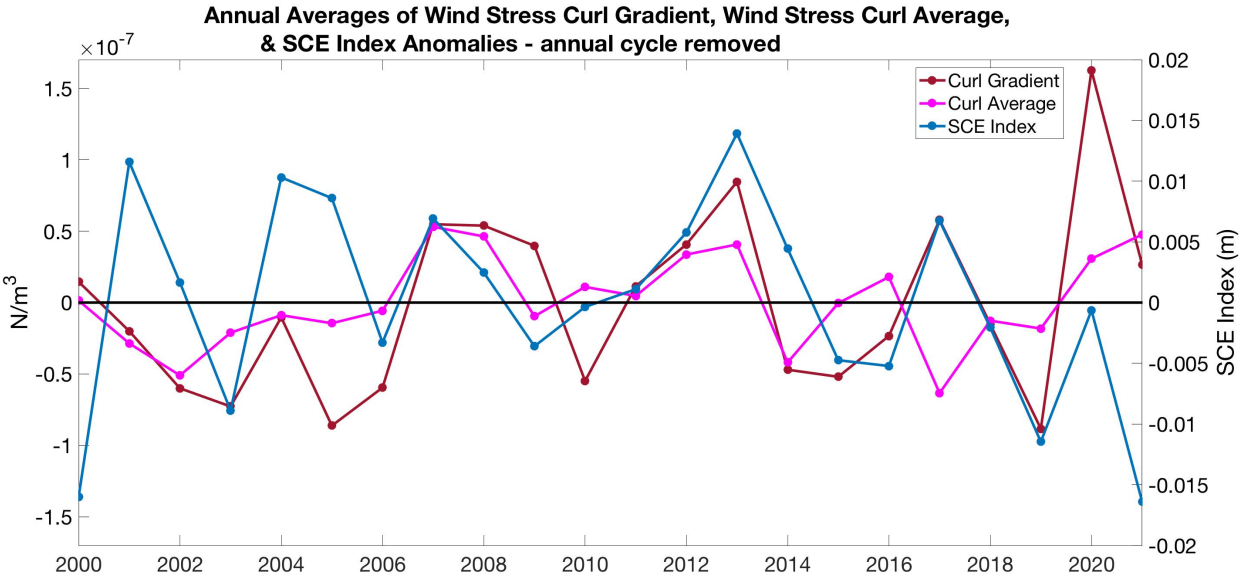

Figure 1.26: Annual averages over the anomalies of the wind stress curl gradient, the regionally averaged wind stress curl, and the SCE index. Anomalies are based on removing the annual cycle. Annual averages are computed over the calendar year.

As exemplified by equation (4) in Section 1.3, other processes such as remote forcing can influence the APG aside from the wind stress curl and these can modify the low frequency variability in the APG. Examples include El Niño, marine heatwaves, and the alongshore inhomogeneity in the alongshore wind stress. These processes can alter the APG, overpower the curl-driven forcing, and cause discrepancies between the wind stress curl and the APG. However, Figure 1.26 suggests that like the other aforementioned processes, the wind stress curl can modify the APG. Given this relationship between the wind stress curl and the SCE index and placing it in context of the agreeability between the SCE index and the water mass anomalies,

these results suggest that the wind stress curl over southern California is one factor influencing source waters over the region.

1.4.5 Particle Trajectories

Particle trajectories allow for a qualitative analysis of the coastal regional flow regime to further explore periods of unusual water mass anomalies in Section 1.4.3. This includes during the 2015 - 2016 El Niño when positive PEW anomalies arrived and during 2016 - 2017 when positive PEW anomalies persisted despite evidence of the seasonal resurgence of the SCE. Trajectories are useful to help explain anomalous poleward flow and the impact of the flow anomalies on regional water mass anomalies, e.g., as in the 2015 - 2016 El Niño, and to provide an explanation for the maintained positive PEW anomalies in 2016 and 2017. During the El Niño, particle trajectories are computed at three locations: off San Diego, Punta San Carlos, and south of the tip of Punta Eugenia (Figure 1.27). Particle trajectories start at the locations in Figure 1.27 designated by a white circle with a cross and the horizontal velocities are integrated backwards. We will show that there are time periods in the second half of 2015 when trajectories can be connected across the three sites implying continuous poleward flow along the Baja peninsula that coincides with the transition in water mass composition in Figure 1.23b.

1.4.5.1 2015

Trajectories off San Diego show multiple branches of onshore movement between 28°N and 32°N as part of the SCE recirculation (Figure 1.27). However, one group of particle trajectories follow a path that is more strictly in the alongshore direction (Figure 1.27a). These

trajectories began in September and originated off Punta Eugenia, i.e., ~470 km south of San

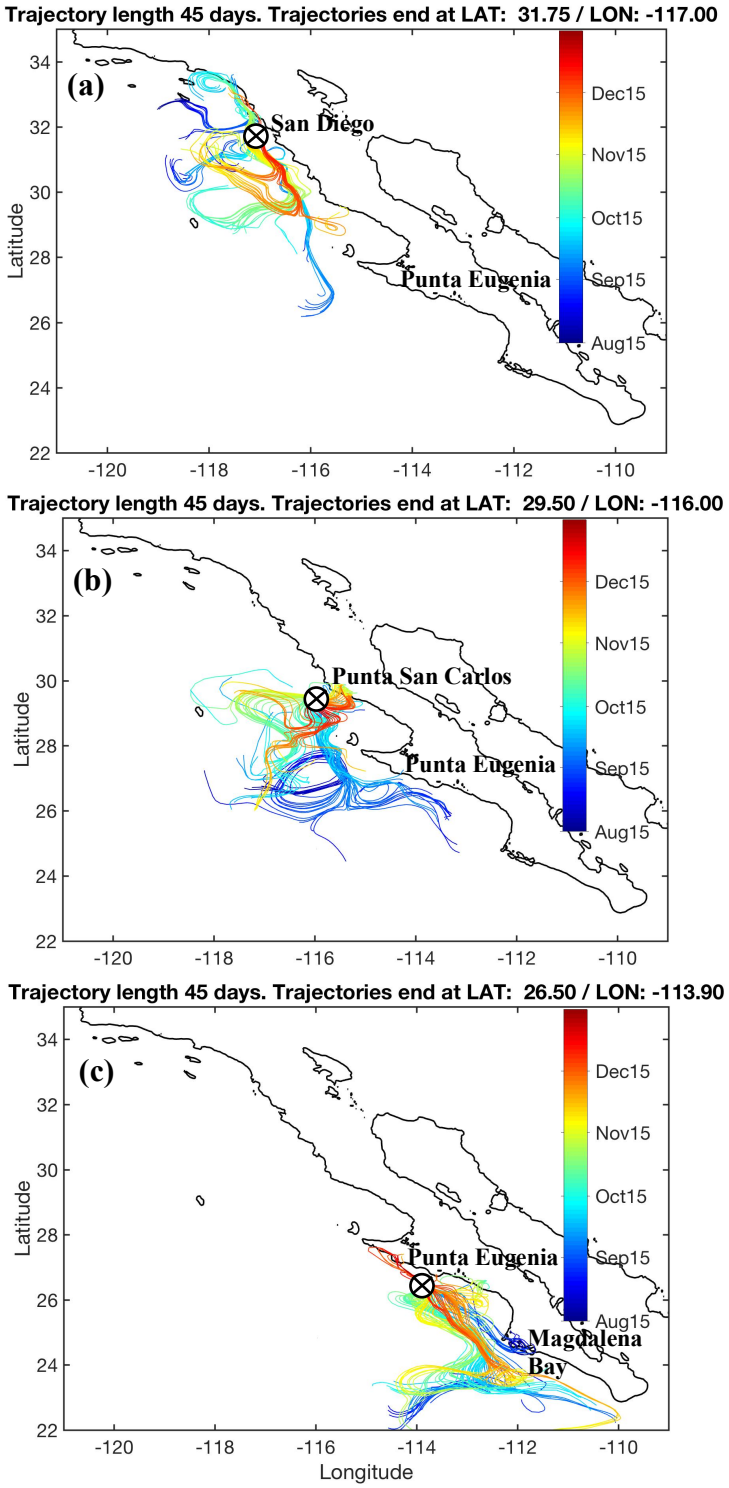

Figure 1.27: 2015 backwards integrated particle trajectories that end off of (a) San Diego, (b) Punta San Carlos, and (c) Punta Eugenia. Particle trajectories run for 45 days between August and December, and the ending location is marked as a circle with a cross.

Diego. A few other trajectories come from ~28.5°N, i.e., just north of Punta Eugenia. Since many of the trajectories flow by Punta San Carlos, this justifies running particle trajectories that end at this site (Figure 1.27b).

Along central Baja California, there are numerous meanders and eddy-like behavior in many of the trajectories. Despite the mesoscale noise, there are several trajectories, e.g., those beginning in August - September, that curve around Punta Eugenia and extend down to ~26°N. Nearly all of the trajectories beginning in August and September extend at least as far south as Punta Eugenia which rationalizes running a final simulation of particle trajectories ending at this location.

In Figure 1.27c, particle trajectories initiate between Magdalena Bay and the tip of Baja California, indicating poleward alongshore flow from August through December. There is less meandering in trajectory paths with fairly direct flow. Based on the trajectories at the three sites over August and September, the results suggest continuous alongshore flow through Baja and southern California. Net alongshore displacement over these latitudes is more than 1100 km and the implied poleward advection can explain the positive PEW anomalies at this time (Figure 1.23b).

Particle trajectories that run northward reflect the increased strength of the poleward APG force (Figure 1.13). Additionally, these trajectories have a limited cross-shore influence implying that upwelling favorable winds are not significant. Typically upwelling-favorable wind stresses push net offshore Ekman transport, which would cause backward integrated particle trajectories to emanate from the coastline. However, positive Baja California wind stress velocity anomalies persist through most of the calendar year reducing the offshore Ekman transport (Figure 1.13a).

The positive wind anomalies assist in keeping particle trajectories near the coast and facilitate poleward displacement.

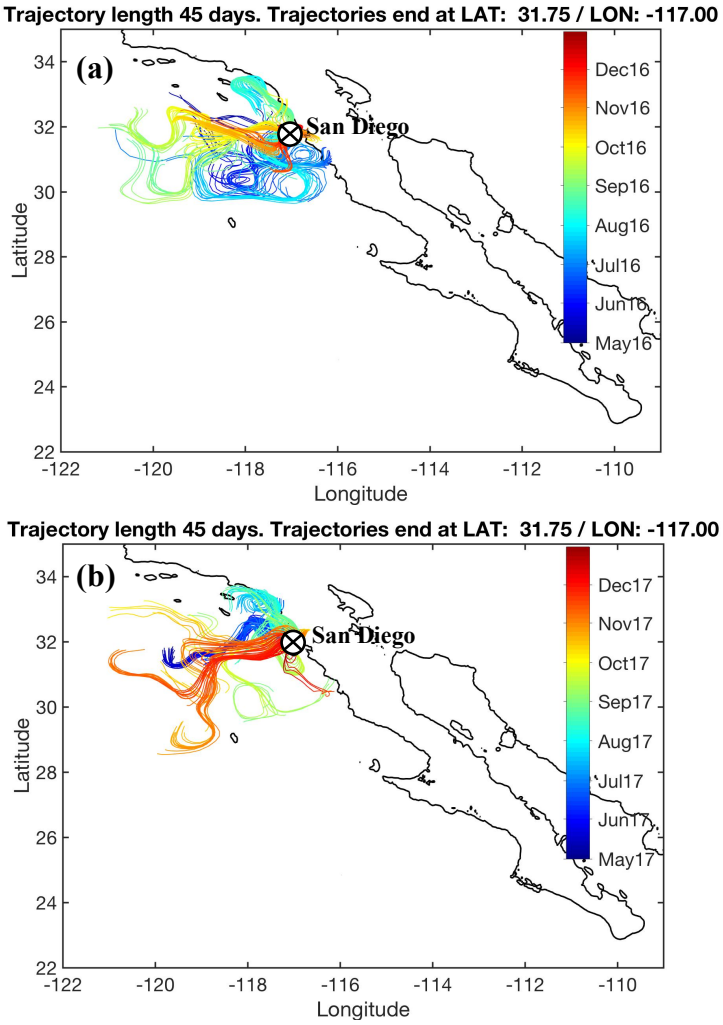

Figure 1.28: Particle trajectories that end off of San Diego and run between May and December in (a) 2016 and (b) 2017.

1.4.5.2 2016 - 2017

Particle trajectories are also useful for determining the cause of the positive PEW anomalies in 2016 and 2017 (Figure 1.23b). They can help distinguish between (1) continuous alongshore advection from Baja California or (2) re-entry via the SCE. The trajectories for 2016 and 2017 are displayed in Figure 1.28. In 2016 many of the trajectories illustrate meanderings in the flow field but in general there appears to be advection onshore, from the north, or

recirculating within the bight for most of the year. The lack of alongshore advection off Baja California in 2016 does not support continued alongshore flow that maintains the positive PEW anomalies in Figures 1.20b and 1.23b.

In 2017, trajectories are mostly moving onshore or from the north. Presumably the trajectories that come onshore stem from the CC. Like in 2016, in 2017 the trajectories indicate the SCE to be the mechanism for continued positive PEW anomalies as there is a lack of evidence of advection from the south. In summary, the positive PEW anomalies persisting in the SCB after the 2015 - 2016 El Niño are predominately due to the recirculation of PEW waters in the SCE that were originally advected in to the region from the south in 2015 during the El Niño.

1.4.5.3 2019 - 2020

Particle trajectories were also analyzed for the second half of 2019 and 2020 but limited evidence exists to show alongshore advection from the trajectory paths (not shown). Particle trajectories were run over this time period, but the results were inconclusive. Off the US-Mexico border, most of these trajectories ran in to the coastline, and further south near Punta San Carlos only trajectories beginning in November and December came from the south covering a distance of ~220 km (not shown). In 2020, at both of these sites most of the trajectories originate from the north or show recirculation patterns (not shown). Thus, this method does not provide evidence of poleward flows in fall of 2019 and 2020 covering large alongshore distances.

1.5 Conclusion

The 2014 North Pacific marine heatwave was the largest heatwave off the US west coast ever recorded and was followed by the 2015 - 2016 El Niño which maintained the anomalously warm conditions (Di Lorenzo and Mantua 2016). Record-high SSTa were set off southern and Baja California exceeding 6°C, and anomalously warm conditions continued during the marine

heatwaves of 2018 - 2021 (Di Lorenzo and Mantua 2016; Gentemann et al. 2017; Amaya et al. 2020; Barkhordarian et al. 2022). Many of the published studies on the 2014 marine heatwave and 2015 - 2016 El Niño focused on the anomalous heating, with less attention given to changes in the velocity field. The measurements of the coastal currents presented here are among the few in-situ observations made of the flow field during the time. They captured anomalous poleward flow that existed in multiple years between 2010 - 2020, and the years of anomalies behavior were consistent at two southern California sites. The moorings provide long timeseries of continuous information about the alongshore flow and the water mass properties, further characterizing the impact, timing, and evolution of these basin-wide climate events in southern California.

Beginning in 2012, the regression analysis revealed poleward flow anomalies were initiated by weakened upwelling-favorable winds that were reinforced by low latitude remote forcing. Throughout the rest of the year, and in 2013, positive flow anomalies were supported by positive anomalies in the wind stress off Baja California and moderate low latitude forcing (Figure 1.13). Fall and winter positive wind stress velocity anomalies over these years, in 2014/2015, and again in 2017 (Figure 1.13) may be associated with the atmospheric ridge in the North Pacific responsible for triggering the 2014 marine heatwave (Wang et al. 2014; Bond et al. 2015; Di Lorenzo and Mantua 2016; Swain et al. 2017). Summertime positive wind stress velocity anomalies from 2013 - 2015 and 2017 (Figure 1.13) initiated many of the fall/winter wind stress velocity anomaly peaks and may be related to a weakened North Pacific High (Amaya et al. 2020). The poleward flow anomalies in 2012 and 2013 were contemporaneous with larger amounts of PSUW and ENPCW (Figure 1.23b). These water mass anomalies coincided with larger annual averages in the SCE index (Figure 1.23a). This suggested a

stronger, more coherent SCE responsible for moving waters onshore and advecting them northward. We proposed that the seasonal spin up of the SCE brought more PSUW and/or ENPCW into the SCB, and the interannual variability of the SCE is partly attributed to low-frequency variability in the wind stress curl (Figure 1.26). Wind stress curl forcing in and of itself or in relation to spatial gradients in the curl may cause spatial pressure gradients that drive horizontal advection in support of cyclonic recirculation, and these modulations in the wind field may be connected to the weakened upwelling favorable winds at the coast (Figure 1.13) and weakening of the summertime North Pacific high-pressure system or PDO (Oey 1999; Davis and Di Lorenzo 2015; Amaya et al. 2020).

In 2014 and 2015 poleward flow anomalies were driven by both the wind stress and the gyre-scale APG (Figure 1.13). Equatorial forcing from a falsely projected El Niño in 2014 briefly succeeded as the primary variable in facilitating poleward flow anomalies. This remote forcing returned even stronger in 2015 when multiple equatorial Kelvin waves propagated poleward as CTWs (Figures 1.14 and 1.15c). Moorings and tide gauges captured the influence of equatorial forcing in the acceleration of the alongshore flow and raised sea levels (Figure 1.16). The change in the source water regime to a greater proportion of PEW waters began in fall 2015 and was observed at 35 and 90 m depth (Figures 1.20b and 1.23b). Particle trajectories illustrate the long distances over which poleward advection occurred extending along Baja and southern California (Figure 1.27). Poleward flow likely continued up through Canada as implied by coastal raised sea levels (Figure 1.15c). Wind stress velocity anomalies led and assisted in causing positive flow anomalies until the end of 2015 when they flipped to become unusually strong out of the north (Figure 1.13). Both the gyre-scale APG and the wind stress velocity anomalies aided in creating poleward flow anomalies, with the former driving alongshore

advection and the latter minimizing offshore movement of waters in the Ekman layer (Figures 1.13 and 1.27). At the coast fu is considered to be less significant in the alongshore momentum balance, but offshore the strengthened APG force may also contribute to retaining waters close to the coast by enforcing onshore geostrophic flow. The rapid reversal of wind stress velocity anomalies at the end of 2015 switched from facilitating poleward flow anomalies to acting against it and the El Niño (Figure 1.13). Ultimately, this contributed to the shutdown of El Niño in California (Frischknecht et al. 2017).

The sustained presence of PEW waters at DM from the El Niño at the end of 2015 through 2017 seem to be due to the SCE recirculating this water mass. The inshore poleward flow set up in these years in southern California was part of the eastern limb of the SCE. This was deduced by the negative remote forcing velocity anomalies (Figure 1.13), positive SCE index contemporaneous with ADCP measured poleward flow (Figure 1.23a), and particle trajectories (Figure 1.27). In the two years after the El Niño, dominant forcing reverted back to the wind field while anomalous southerly waters persisted in the region (Figures 1.13 and 1.23b).

In 2018 water mass anomalies transitioned to a new regime where positive ENPCW anomalies were compensated for by negative PEW and PSUW anomalies (Figure 1.23b). This unique behavior indicated a change in CC source water ratios. A large patch of anomalously salty water in the central Pacific moved eastward towards the CCS (Ren and Rudnick 2021). This mass advected into the CC and circulated onshore near the DM mooring, exemplifying the large distance traversed by these waters, i.e., mid-gyre to within 3 km of the coastline, and emphasizing the importance of cross-shore exchange between open ocean and coastal processes. These more oligotrophic waters can influence the coastal ecosystem by supplementing the source waters available for upwelling.

Throughout 2019 - 2021, marine heatwaves transpired in the North Pacific and poleward flow anomalies were episodic in nature. Poleward flow anomalies in these years were influenced by the positive wind stress velocity anomalies in addition to the gyre-scale APG forcing in the winters of 2018/2019 and 2019/2020 (Figure 1.13). The positive PEW anomalies in 2019 and 2020 exceeded those in 2015 at DM 35 m depth (Figure 1.23b). The positive PEW anomalies in fall 2019 appear to be related to equatorial forcing (Figures 1.13 and 1.14), while the fall 2020 PEW anomalies may be associated with the alongshore inhomogeneity in the alongshore wind field (Figure 1.24). The resultant change in source waters in these years due to large-scale climate phenomena can influence upwelling by changing the biogeochemical properties and can modify the nutrient contents available for uptake during upwelling processes.

Aside from source water variability of upwelled waters, another potential impact on the upwelling process is poleward flow. Briefly touched upon above, the APG force that can push water poleward also drives cross-shore geostrophic transport. In southern California the APG force is primarily poleward throughout the year which gives rise to onshore geostrophic flow (Hickey and Pola 1983). In the upper ocean during the upwelling season, onshore geostrophic flow reduces the amount of vertical transport at the bottom of the Ekman layer required by a mass balance (Colas et al. 2008; Marchesiello and Estrade 2010; Jacox et al. 2014). The pressure gradients that influence the flow field and upwelling circulation are largely barotropic in the SCCS and are set up by sea level differences such as by alongshore inhomogeneity in the wind field, CTWs, and remote forcing from low latitude dynamics. This highlights the importance of the APG in both the alongshore flow and in the upwelling system. The latter of these is an objective of Chapter 2 in which an upwelling index is derived for southern California and the role of the APG on upwelling is discussed further in the next chapter.

As part of an eastern boundary upwelling system, the biologically productive waters in the SCCS shape and support the ecosystem structure and the dynamics contributing significantly to California's fisheries and shellfish industries. Thus, there are socioeconomic motives for needing to understand the variability and changes in this environment. During the prolonged heating in 2014 - 2016, warm anomalies were associated with wide-spread ecosystem impacts. Zooplankton invertebrates like the pelagic red crab and krill, native to Baja California, were found as far north as Monterey Bay and near the California-Oregon border, respectively (McDermott 2015; Ohman et al. 2017). Another invertebrate, the market squid, is mostly caught in southern California, but during this time there was a latitudinal change with increased landings in Monterey Bay (Urton, 2014; Leising et al. 2015). Enhanced poleward flow and source water anomalies were contemporaneous with the presence of tropical and subtropical species at higher latitudes along the US west coast.

The approach presented here for calculating the composition of source waters is advantageous because it requires a small set of in-situ measurements, relying only on density and oxygen. Its practicality can lend itself useful for being applied in other regions where such measurements exist. One consequence of climate change is increased frequency of intense El Niños, and recent reports show that long-term trends in source water mass properties include decreased dissolved oxygen in the CCS (Meinvielle and Johnson 2013; Bograd et al. 2015; Wang et al. 2019). This raises a concern that equatorial waters may intensify and increase in the CCS or that prolonged periods of hypoxia and ocean acidification in the coastal environment will be more common. Long-term monitoring of such changes in the coastal ocean is critical for understanding the variability in pH and dissolved oxygen, and the consequences this conditioning has on the ecosystem health as well as the financial impact on the fisheries industry.

1.6 Acknowledgements

We thank Jeff Sevadjian for providing quality control on the ADCP data. Support for the CCE2 mooring comes from the NOAA Ocean Observing and Monitoring Division and Ocean Acidification Program (NA15OAR4320071). The CCE2 mooring is a part of the international OceanSITES program where quality controlled data are available online at ftp://data.ndbc.noaa.gov/data/oceansites/DATA/CCE2/. CCMP Version-2.0 vector wind analyses are produced by Remote Sensing Systems and data are available at www.remss.com. CMEMS products used in this chapter including the GLORYS SSH data can be found at https://data.marine.copernicus.eu/products. Tide gauge data from the UHSLC can be obtained at https://uhslc.soest.hawaii.edu/. NCEP NARR surface pressure is downloaded from https://psl.noaa.gov/thredds/catalog/Datasets/NARR/monolevel/catalog.html. World Ocean Database data are available at https://www.nodc.noaa.gov/OC5/SELECT/dbsearch/dbsearch.html.

Chapter 1, in part is currently being prepared for submission for publication of the material. Lowcher, Caroline; Send, Uwe; Lankhorst, Matthias. The dissertation author was the primary researcher and author of this material.

1.7 Appendix A: Verification of Water Mass Analysis Solutions

The results from the method used to determine the water mass composition are examined in multiple ways to check that the results are consistent with the observations and that the solver derived solutions are the solutions that minimize the water mass property deviations from the mean. These tests use the observations and estimated water mass composition at DM 35 m depth. First, the water mass property anomalies, i.e., where the isopycnal mean is removed, are examined from the observations and the reproduced water mass properties. Then, the solutions from the inverse method are compared to manually derived solutions. Last, the sensitivity of the

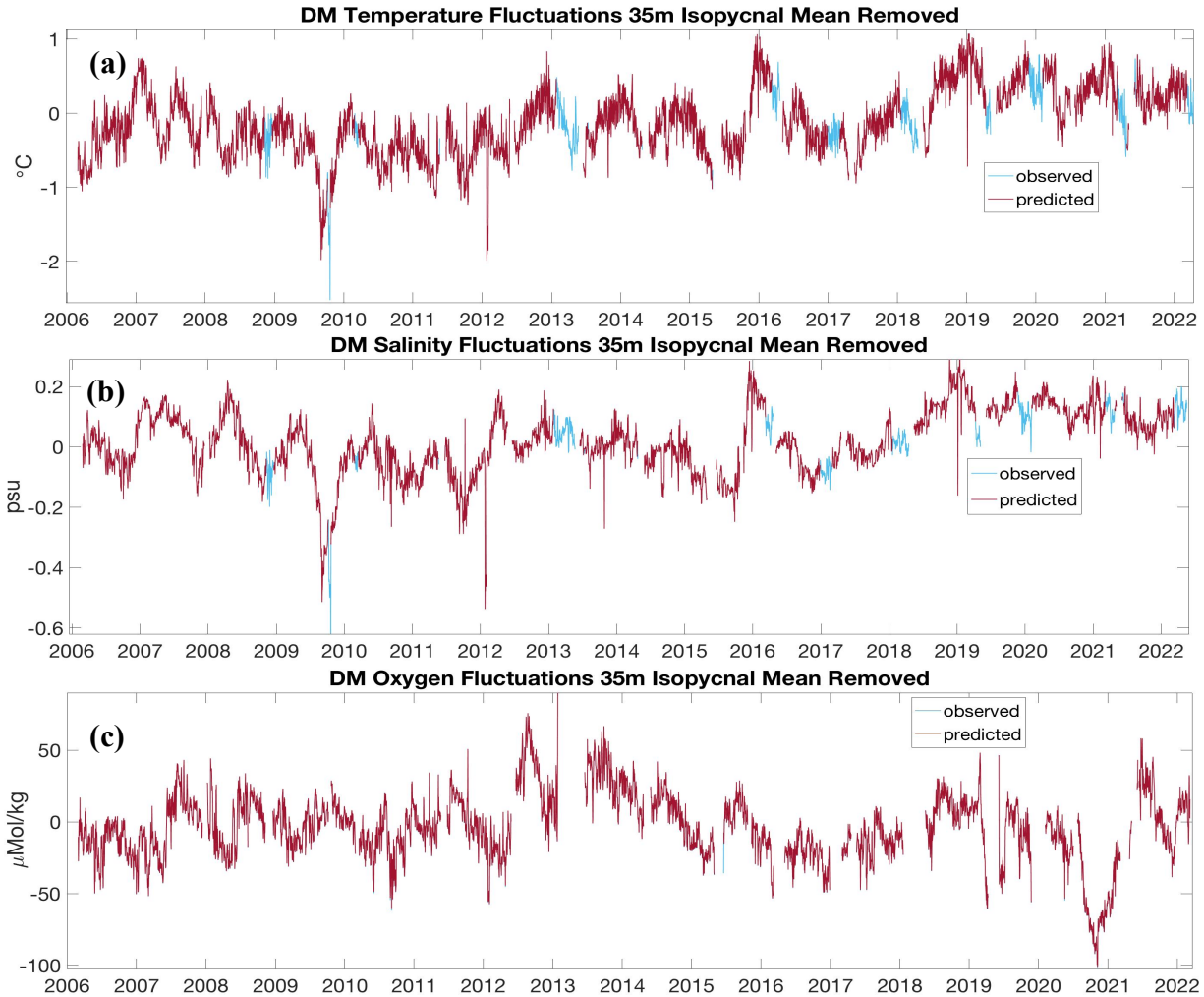

Figure 1.29: DM 35 m observed and predicted residuals for (a) temperature, (b) salinity, and (c) oxygen. The residuals are based on removing the mean isopycnal water property.

method is assessed by perturbing the temperature and comparing the perturbed temperature results to the non-perturbed results.

1.7.1 Water Property Residuals

The water mass composition is tested to see if it can reproduce the observed fluctuations in temperature, salinity, and oxygen. In this assessment, the mean temperature, salinity, and oxygen on an isopycnal are removed and the time series of the observed and predicted water mass property residuals are shown in Figure 1.29. These time series of the observed and predicted residuals are nearly indistinguishable from each other. This demonstrates the ability of this method to replicate the variability in the in-situ water mass property measurements.

Table 1.4: Comparison of predicted and observed water mass properties on September 21, 2012 at DM 35 m depth given various water mass compositions and the required fluctuations needed to match the in-situ measurements. Density on this day is 1025 kg/m^3. Abbreviations T, S, and O denote temperature, salinity, and oxygen, respectively, and primes signify fluctuations of the specified water mass property.

	(1) Water Mass Results	**(2) Water Mass Results w/ Fluct.**	**(3) Isopycnal Mean Comp.**	**(4) Isopycnal Mean Comp. w/ Fluct.**	**(5) Small ENPCW %**	**(6) Small ENPCW % w/ Fluct.**
PSUW/ PEW/ ENPCW %	65/0/35	65/0/35	59/41/0	59/41/0	59/26/15	59/26/15
PSUW/ PEW/ ENPCW T'	0/0/0	0.55/0/0.31	0/0/0	0.05/0.05/0	0/0/0	0.03/0.03/ 0.02
PSUW/ PEW/ ENPCW S'	0/0/0	-0.06/0/ -0.03	0/0/0	-0.12/-0.12/0	0/0/0	-0.15/ -0.15/ -0.15
PSUW/ PEW/ ENPCW O'	0/0/0	2.75/0/0.35	0/0/0	45/45/0	0/0/0	35/35/2
Predicted/ Observed T	14.19/14.65	14.65/14.65	14.60/14.65	14.65/14.65	14.62/14.65	14.65/ 14.65
Predicted/ Observed S	33.63/33.57	33.57/33.57	33.69/33.57	33.57/33.57	33.72/33.57	33.57/ 33.57
Predicted/ Observed O	263.60/ 265.49	265.49/ 265.49	220.69/ 265.49	265.69/ 265.49	235.30/ 265.49	268.05/ 265.49

1.7.2 Manual Checks

Since the composition is largely made up of PSUW and PEW, it is unusual for ENPCW to be present. ENPCW appears more often at the shallower DM sensor than at the deeper DM sensor (Figure 1.18c) and is present on isopycnals that agree with the density space of this water mass that was found by Hautala and Roemmich (1998). The appearance of ENPCW in the water mass analysis occurs in summer – fall 2012, summer – fall 2013, 2018, and 2021 (Figure 1.18c). To assess the robustness of the water mass results in these unusual periods, observed temperature, salinity, and oxygen values are selected at DM 35 m depth for one day during the summer – fall 2012 period and compared against predicted temperature, salinity, and oxygen from multiple possible water mass fractional compositions.

Table 1.4 demonstrates that the fractional composition of the regional water masses resulting from the water mass analysis best explains the observed water mass properties. Even without permitting fluctuations in the mean temperature, salinity, and oxygen for each regional water mass, the predicted water mass properties are quite similar to the observed values (Table 1.4). For comparison, a more typical water mass composition is tested that uses the mean isopycnal composition. The predicted water mass properties using this composition are shown in Table 1.4 as well as the property fluctuations needed to make the predicted water mass properties match the observations. This more typical composition cannot reproduce the observations without requiring significantly large oxygen fluctuations that are on the outer range of the WOD measured properties in Figure 1.5. In order to predict oxygen that agrees with the in-situ measured oxygen, a substantial amount of ENPCW is required. For example, another test is shown in Table 1.4 where ENPCW contributes mildly to the composition and sizable oxygen fluctuations are still required for the PSUW and PEW water masses. Thus, during periods of

higher salinity and oxygen values, the in-situ water mass properties are best reproduced when ENPCW contributes to the fractional composition of water masses.

In contrast, the water mass composition is also tested on days when ENPCW is excluded to verify that this composition is the one that minimizes the water property fluctuations. Table 1.5 takes a day when there is estimated to be no contribution from ENPCW and the water property fluctuations required to match the observations are minimal. In comparison, if there was even some small amount of ENPCW, the water property fluctuations needed to match the observations are larger such that the value from equation (19) is bigger. While these fluctuations are within those shown by the WOD data in Figure 1.5, compositions similar to this one, i.e., where there is a small amount of ENPCW, do not minimize the value in equation (19), and as such the method excludes ENPCW as part of the composition.

Table 1.5: Comparison of predicted and observed water mass properties on January 7, 2010 at DM 35 m depth given various water mass compositions and the required fluctuations needed to match the in-situ measurements. Density on this day is 1025 kg/m^3. Abbreviations T, S, and O denote temperature, salinity, and oxygen, respectively, and primes signify fluctuations of the specified water mass property.

	(1) Water Mass Results	**(2) Water Mass Results with Fluctuations**	**(3) Small ENPCW %**	**(4) Small ENPCW % with Fluctuations**
PSUW/ PEW/ ENPCW %	60/40/0	60/40/0	62/33/5	62/33/5
PSUW/ PEW/ ENPCW T'	0/0/0	-0.07/-0.06/0	0/0/0	-0.01/0/0
PSUW/ PEW/ ENPCW S'	0/0/0	0/0/0	0/0/0	-0.14/-0.14/-0.14
PSUW/ PEW/ ENPCW O'	0/0/0	-0.98/-7.91/0	0/0/0	-12/-13/-12
Predicted/ Observed T	14.54/14.47	14.47/14.47	14.48/14.47	14.47/14.47
Predicted/Observed S	33.49/33.49	33.49/33.49	33.63/33.49	33.49/33.49
Predicted/Observed O	222.11/218.20	218.40/218.20	230.65/218.20	218.32/218.20

1.7.3 Temperature Perturbation

The water mass analysis assumes that the water mass properties are conservative which requires measurements to be below the surface mixed layer. In the mixed layer, temperature may no longer be conservative due to diurnal solar heating, so performing a water mass analysis is inappropriate. To assess how frequently the mixed layer depth (MLD) reaches 35 m depth, i.e., the shallower sensor at DM, first the MLD is estimated based on a density difference of 0.125 kg/m^3 from density at 10 m depth at DM. This is approximately the depth of the shallowest sensor on the mooring, and the value for density difference was selected according to Levitus (1982). For the purpose of estimating the larger values of MLD, this method is suitable for understanding how conservative temperature is at 35 m depth. Most of the time the MLD is shallower than 30 m and rarely does the MLD exceed 35 m (Figure 1.30). The periods when MLD is 35 m or deeper occur in 2009 and 2010; thus when analyzing the water mass composition in years of anomalous poleward flow, i.e., 2012 - 2015, 2018, and 2019 – 2021, the results are not influenced by a non-conservative temperature.

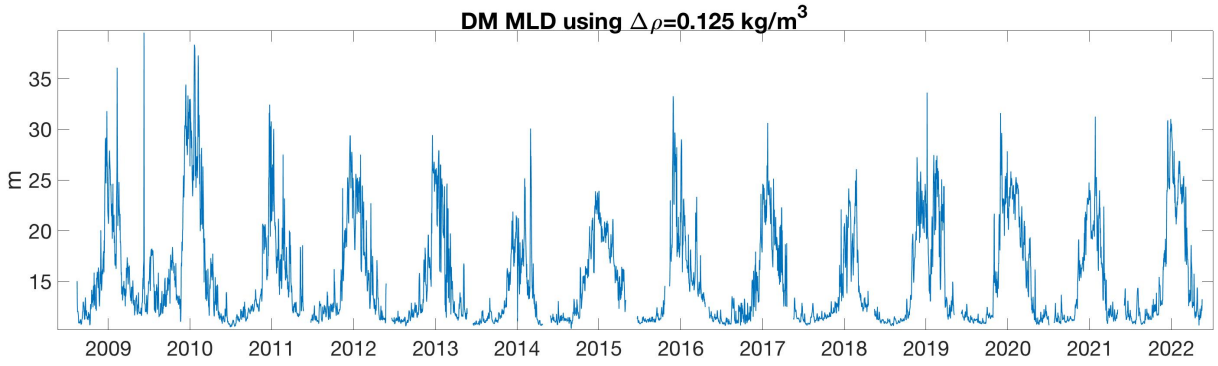

Figure 1.30: MLD at DM estimated by a density difference of 0.125 kg/m^3 from density at 10 m using mooring data.

Furthermore, the impact of surface heating on influencing temperatures at 35 m depth can be assessed. To demonstrate this sensitivity, the temperature is perturbed by 1.5°C and the water mass composition is re-solved. Figures 1.31a and 1.31b depict the contribution from each source water mass from the unperturbed temperature and when 1.5°C is added to the in-situ temperature, respectively. Comparing these results shows that there are small differences in the overall magnitudes of PSUW and PEW. In the perturbed solution there is less separation between the record-long means of PSUW and PEW, indicating a closer balance of mean PSUW and PEW percentage on an isopycnal. Yet, the variability and changes in years of poleward flow anomalies remains persistent. This is encouraging and indicates the robustness of the interpretations of the solutions from the water mass analysis.

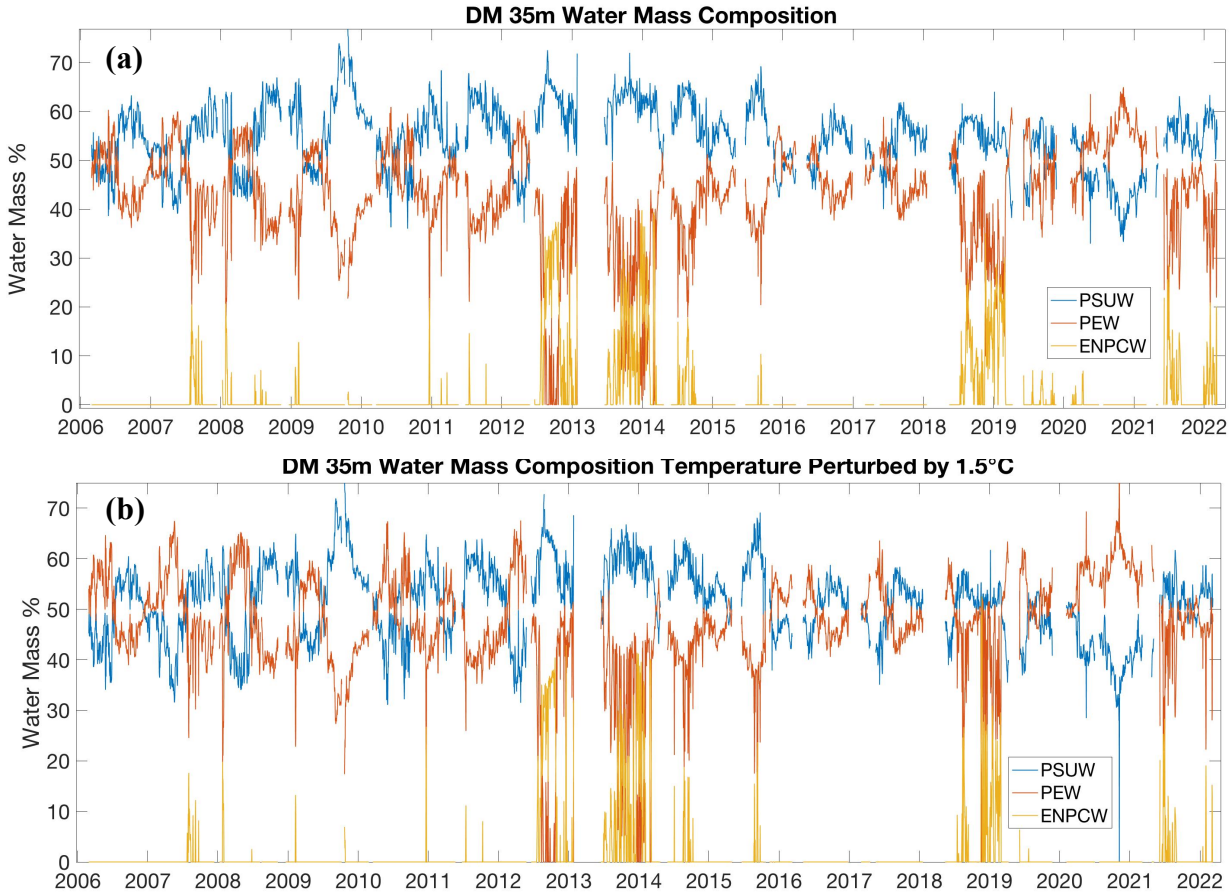

Figure 1.31: Water mass composition from the source water mass analysis at (a) DM 35 m and (b) DM 35 m depth when the in-situ temperature measurement is increased by 1.5°C.

CHAPTER 2

Southern California Control Volume Transport Estimates

Abstract

Eastern boundary upwelling systems (EBUS) are ecologically and economically productive regions found along the world's major ocean basins. This chapter quantifies upwelling in southern California using a volume budget. Simplifications in the geostrophic component of the volume budget lead to developing an upwelling index for southern California. The newly developed upwelling index relies on geostrophic calculations using coastal sea level variability. The upwelling index presented here requires minimal observational platforms and is relatively simple to apply in other EBUS regions, provided coastal sea level measurements and reasonably accurate wind data are available. In the annual cycle, there is year-round upwelling that is strongest in spring, generally geostrophic convergence into the box, and Ekman divergence out of the box. Interannual variability of the new upwelling index reveals there is persistently less upward vertical transport during the 2014 marine heatwave and the 2015 - 2016 El Niño due to weaker upwelling favorable winds. In fall – winter 2015, greater onshore geostrophic transport driven by remote forcing weakens the upward volume flux. However, a transition in the wind field to upwelling favorable conditions exceeds the geostrophic anomalies and causes anomalous upwelling. On synoptic timescales, upwelling amplitudes are about 0.26 Sv on average and upwelling typically lasts for about 8 days. At all timescales of interest, the Ekman divergence and geostrophic convergence are important processes driving and altering the vertical transport. The volume transport calculations are also applied to a heat budget. The heat budget reveals regional warming during the 2014 marine heatwave and the 2015 – 2016 El Niño. Onshore heat

fluxes and atmospheric heat fluxes contribute to the anomalous warming in 2014, while heat advected from the south support the increased temperatures in southern California during the 2015 – 2016 El Niño.

2.1 Introduction

Eastern boundary upwelling systems (EBUS) are highly productive ecosystems with large economic value and significant societal interest. These biologically and financially productive regions are adjacent to coastlines, which increases their societal value due to the myriad of influences they have on coastal communities, e.g., weather, recreational usage in the coastal ocean, ocean acidification, harmful algal blooms, cross-shore exchange of nutrients, etc. In California, the ocean-based economy is valued at $45 billion annually (ERG 2016). As one of the world's major EBUS, California's fish and shellfish industries are dependent on the coastal ocean which is where upwelling occurs.

Quantifying upwelling proves challenging considering that the vertical velocities are too weak to record in direct current measurements. Given the difficulty of measuring upwelling directly, several studies have analyzed upwelling using wind estimates and Ekman theory (Bakun 1973; Pickett and Paduan 2003; Bograd et al. 2009). Wind stress from atmospheric models have been used to evaluate upwelling and generate upwelling indices (Bakun 1973; Schwing et al. 1996). This approach has been successful along some coastlines, however, coastal mountains, the strong bend in coastline at Point Conception, and a complex island system have hindered approximations of upwelling off southern California (Bakun 1973). For upwelling estimates, a wind product must account for these features in southern California.

EBUS share similar features like equatorward winds driving equatorward surface flows, poleward undercurrents, offshore Ekman and vertical transport, positive wind stress curl in a

coastal band, and steep continental shelves. In the California EBUS, the California Current (CC) is the broad, meandering equatorward flow near the surface and at depth is the poleward subsurface California Undercurrent (CU). In the California Current System (CCS), equatorward winds cause offshore Ekman transport in a surface layer that is approximately 50 m thick (Chereskin 1995). In the most simplified view, the overturning upwelling cell comprises offshore Ekman transport balanced by onshore geostrophic transport and vertical upwelling. In southern California the upwelling season is in spring-summer when the equatorward winds intensify and drive coastal upwelling in two ways.

Equatorward winds along the coast drive upwelling by moving water in the Ekman layer offshore, which is replaced by upwelled waters from below, referred to as coastal divergence. Additionally, decreases in equatorward winds near the coast create a positive wind stress curl. This curl causes a horizontal divergence in offshore Ekman flow with greater offshore transport under stronger alongshore winds and weaker offshore transport inshore where the winds are sheared. To maintain a mass balance, the divergence due to the wind shear forces water upwards, known as Ekman suction or curl-driven upwelling. Both upwelling mechanisms raise isopycnals, shoal the nutricline, and increase chlorophyll concentrations (Chelton 1982; Di Lorenzo 2003; Rykaczewski and Checkley 2008). The first upwelling mechanism takes place within O(10) km of the coastline while curl-driven upwelling occurs over O(10-100) km. The vertical velocities from these upwelling processes are O(1-10) m/day with faster rates inshore due to both mechanisms and slower velocities offshore from curl-driven upwelling (Münchow 2000; Pickett and Paduan 2003; Dever et al. 2006).

One widely-used estimate of upwelling is the coastal upwelling index, otherwise known as the Bakun index, produced by National Oceanic Atmospheric Association (NOAA)

Environmental Research Division (ERD). The Bakun index has been a valuable resource tool for coastal oceanographic research and fisheries studies in EBUS for the last approximately 60 years. It uses sea level pressure (SLP) from modeled atmospheric pressure fields to compute the geostrophic wind velocities and makes an adjustment to the wind for frictional effects prior to calculating wind stress. The alongshore component of the wind stress then goes into calculating the offshore Ekman transport (Bakun 1973; Schwing et al. 1996). For interannual variability dating back to the late 1960s and broad spatial coverage, the index is effective in describing changes in upwelling and oceanic conditions (Schwing et al. 2006; Bograd et al. 2009).

However, there are three major shortcomings to the Bakun index. First, data are produced every 3° latitude, and the coarse resolution of the index does not include local atmospheric, topographic, and oceanic effects on upwelling (Halliwell and Allen 1987; Dorman and Winant 2000). For instance, coastal mountains in southern California cause a discontinuity in the atmospheric pressure field used in the Bakun index and therefore overestimate the atmospheric pressure gradient and thus the geostrophic winds (Bakun 1973). Beginning in the late 20th century, the spatial resolution in the atmospheric model increased to 1°, but there is still a concern about the coarseness of such spatial scales. Second, since the index includes only the alongshore and not the cross-shore wind stress, it does not fully account for upwelling from the wind stress curl since it does not incorporate alongshore gradients in the cross-shore wind stress, $\partial\tau^x/\partial y$. Third, previous studies suggest that the geostrophic cross-shore flow may enhance or reduce the strength of upwelling based on the direction of the alongshore pressure gradient (APG; Colas et al. 2008; Davis 2010; Marchesiello and Estrade 2010; Jacox et al. 2018). Reid and Mantyla (1976) and Hickey and Pola (1983) found a positive poleward pressure gradient force for southern and central California during most months of the year. The onshore

geostrophic flow driven by a consistent poleward APG force may reduce the upwelling strength in southern California, which would not be reflected in the Bakun index. These shortcomings contribute significantly to the uncertainty in the accuracy of the Bakun index for southern California, supporting the need for deriving an upwelling index that is more representative of the region.

More recent attention on the third shortcoming of the Bakun index, the cross-shore geostrophic flow, has emphasized its importance in modifying the strength and variability of vertical transport. The importance of this mechanism has been addressed in more recent upwelling indices like the Coastal Upwelling Transport Index (CUTI) as well as in other upwelling studies (Davis 2010; Marchesiello and Estrade 2010; Jacox et al. 2018). The cross-shore geostrophic flow responds to the APG, with the sign of the cross-shore geostrophic flow dictated by the direction of the APG. A poleward APG force acts in opposition to offshore Ekman flow thereby reducing vertical transport or leading to downwelling, while an equatorward APG force supports vertical transport by increasing offshore transport.

The predominantly poleward APG force in southern California has a mean and seasonal cycle characterized by net onshore geostrophic flow in the upper 500 m that is surface intensified (Roemmich 1989; Bograd et al. 2001). Assuming there is no vertical flow at 500 m, previous studies have found that for a defined region in southern California that is bounded by the coast on one side, the Ekman transport that diverges out of the region is balanced by geostrophic transport that converges into the region. (Roemmich 1989; Bograd et al. 2001). Over these depths a mass balance does not require information on vertical upwelling velocities as the vertical extent of the upwelling cell does not generally reach this deep (Chhak and Di Lorenzo 2007).

For a mass budget calculated over a shallower region, e.g., the upper 50 m, the residual between the horizontal geostrophic convergence and Ekman divergence is the amount of water upwelled across 50 m. In this volume budget, knowledge of the horizontal geostrophic and Ekman flows gives insight into the vertical transport without direct measurement of the vertical velocity. Therefore, in this chapter a volume budget will be constructed over the upper 50 m for a control volume in southern California from the geostrophic and Ekman flow components. It will be shown that the geostrophic flow component in the volume budget can be reduced to using just sea level gradients from tide gauges along the coast to create a new upwelling index. The uncertainty in this new upwelling index is discussed in Appendix B. This new upwelling index will be assessed against other regional upwelling estimates and the new upwelling index will be investigated over multiple timescales including the annual cycle, interannual variability, and subseasonal upwelling. The last objective of this chapter is to approximate a heat budget over southern California. Anomalous advection during the 2014 marine heatwave and the 2015 - 2016 El Niño, as discussed in Chapter 1, motivate investigating how changes in advection impacted the advective heat fluxes over the control volume. The heat budget will use the transport from the volume budget to investigate changes in the advective heat flux terms during the years of large-scale climate phenomenon.

Section 2.2 describes the geographical region and lateral boundaries for the mass balance, introduces the data sets used in this chapter, and reviews the control box volume and heat budget calculations including the derivation of the new upwelling index. Section 2.3 compares the new upwelling index to other previously reported findings. Section 2.4 presents the results of the new upwelling index over several timescales of interest including the annual cycle, interannual

variability, and synoptic upwelling events. Section 2.5 inspects the southern California heat budget during the years of large-scale climate phenomena and Section 2.6 is the conclusion.

2.2 Data and Methods

This section introduces the control volume, describes the data sets used in this chapter, and reviews the volume and heat budget equations. It also presents the methods for approximating the terms in the budget equations and the simplifications that lead to constructing a new upwelling index. The last part of Section 2.2 addresses how synoptic upwelling events are detected, and the detected events will be examined as part of the upwelling analysis in Section 2.4.

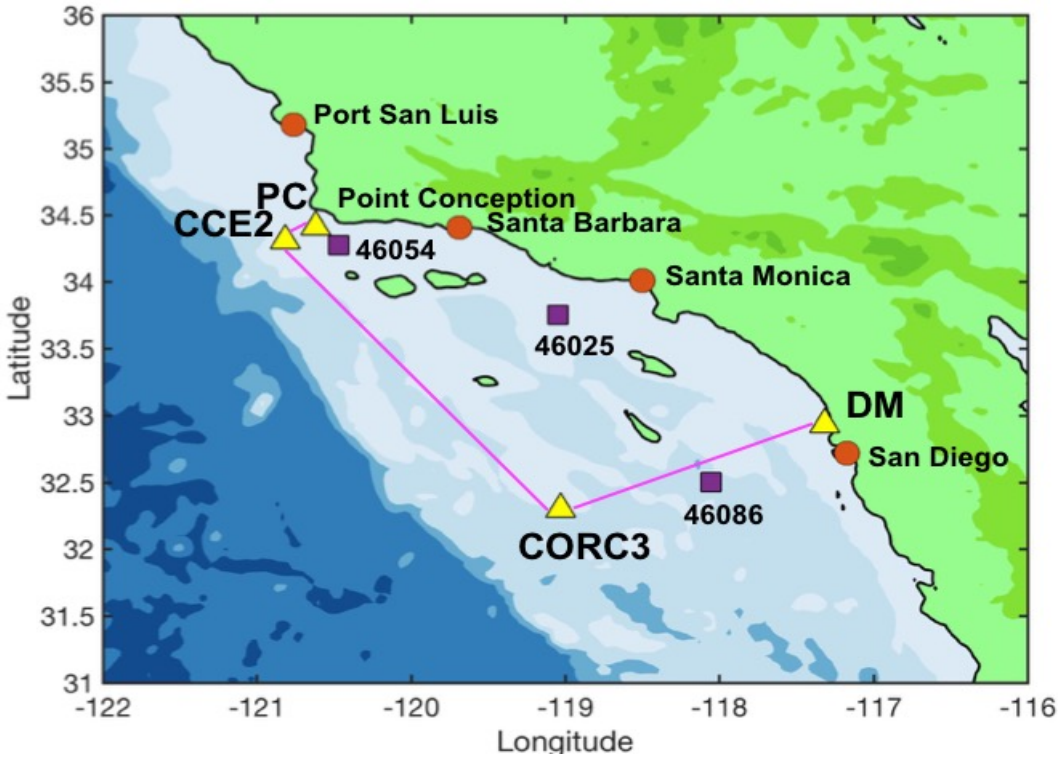

Figure 2.1: Southern California region of study. Moorings and gliders are denoted by yellow triangles, coastal tide gauges are represented by red circles, and NDBC buoys used in the study are indicated by purple squares. The magenta box denotes the area over which the volume budget is calculated.

2.2.1 Geographical Boundaries of Volume Budget

The southern California volume budget is executed over a defined region spanning the California coastline between Del Mar and Point Conception (Figure 2.1). This box extends over the upper 50 m of the ocean and is bounded by land on the east side. On the southern side, moorings CORC3 and DM mark the southwest and southeast corners of the box, respectively. DM is very close to the coast, about 3 km off of Del Mar. The west side follows the approximately 850 m depth bottom contour that extends from the CORC3 mooring to the northwest corner marked by the CCE2 mooring, and the north side is the segment between the CCE2 mooring and the northeast corner of the box, which is approximately 10 km off of the coast at Point Conception. With land constraining the east side of the box, no flow is permitted through this segment so horizontal transport is only measured for the other three sides.

The vertical extent of the control volume is the upper 50 m. This was chosen because 50 m is an estimated Ekman layer thickness in the CCS (Chereskin 1995) and regional model results show that in the time-mean, the offshore Ekman flow is within the upper 50 m (Zaba et al. 2020). Zaba et al. (2020) performed a volume budget over the upper 50 m, so for comparability this is the vertical extent of the control volume used in this study. The offshore boundary of the control box is set by the mooring locations used in this study and includes the region of maximum wind stress curl in the SCB (Winant and Dorman 1997; Di Lorenzo 2003). The inshore boundary of the control volume is the coastline, so it also includes the inshore region where upwelling occurs from a coastal divergence. The north and south sides are determined by the existing mooring sites.

One of the chapter's objectives is to analyze the volume budget. Non-divergence will be invoked in the volume budget to infer the vertical transport. To approximate vertical transport

through the bottom of the box, simultaneous measurements of horizontal transports are required through the three lateral sides. The horizontal transport is discussed in greater detail in Section 2.2.3 and the transport through the lateral sides of the box is decomposed into geostrophic and Ekman components. The geostrophic component is observed from multiple platforms (including moorings, gliders, PIES, and tide gauges), while the Ekman contribution is derived from a wind product. Section 2.2.2 presents these observations and the data products used for approximating the two components of transport, i.e., geostrophic and Ekman.

2.2.2 Data Sets

2.2.2.1 Geostrophic Data

The geostrophic transport through the box volume in Figure 2.1 is discussed further in Section 2.2.3 but has three separate components that are obtained from observations. These are the time-varying baroclinic shear, the depth-independent fluctuations, and the mean geostrophic transport. The observations that measure these components are presented next.

a.) Baroclinic Data Sets

At the southeast corner of the box (Figure 2.1), the DM mooring is anchored in 100 m of water and is equipped with temperature and salinity sensors that span the water column. The mooring was deployed in 2006 and has been maintained since. It is serviced 1 - 2 times a year, which requires the mooring to be completely removed and takes about one month to refurbish.

About 175 km offshore of the DM mooring is the subsurface CORC3 mooring (Figure 2.1), which lies in a water depth of 870 m. This mooring measures temperature and salinity between about 35 and 780 m depths. The mooring was first deployed in fall 2012 but failed after one year (Figure 2.2). In lieu of this mooring, Spray gliders performed dives at the CORC3 location. Gliders were active between fall 2013 and fall 2016, measuring temperature, salinity,

and pressure, and were programmed to dive down to almost the depth of the deepest mooring sensor (Figure 2.2). A failed sensor on a glider in the second half of 2014 leaves a large gap in the salinity timeseries. Following fall 2016, the mooring was redeployed and is still in operation to date. The overall data availability and the various gaps are summarized in Figure 2.2.

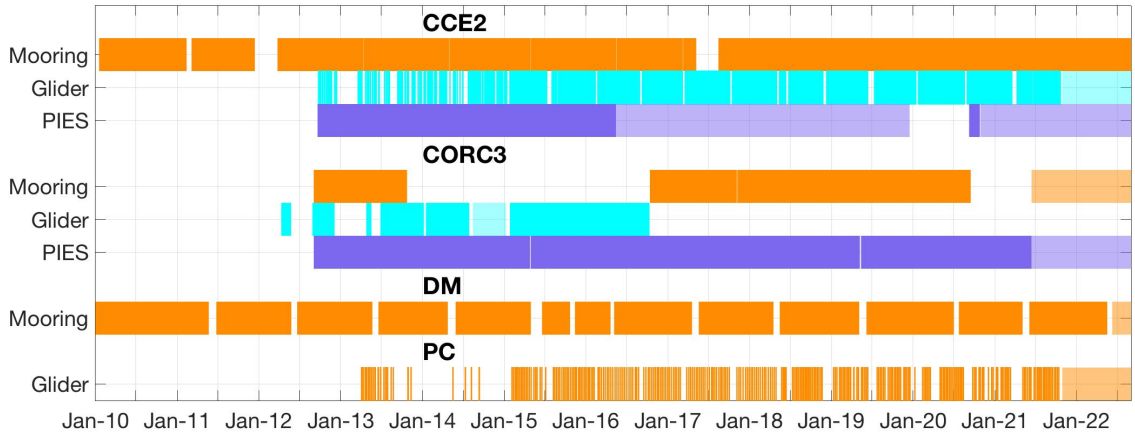

Figure 2.2: Active observations made by moorings, gliders, and PIES at CCE2, CORC3, and DM. Half-shaded deployments indicate that the platform is currently deployed or that only some of the data were recovered. For example, the most recent glider data block in the figure for CCE2/PC signifies that this glider is still underway, but data are expected to be retrieved. The DM data extend back to 2006 but deployments before 2010 are not shown.

CCE2 is the final mooring used from this region and it is situated in 840 m water depth and about 27 km off of Point Conception (Figure 2.1). The mooring is equipped with temperature and salinity sensors in the upper 80 m. Prior to 2015, only the upper 40 m were sampled. Separate measurements of temperature and salinity are made at CCE2 by a Spray glider. The glider serves two purposes. First, it enhances the vertical coverage of temperature and salinity at CCE2 by sampling the upper 600 m. The station-keeping glider data are used to determine dynamic height at CCE2 as discussed later in Section 2.2.3. Second, it transits the northern edge of the box between CCE2 and the coast about once a week, so it is not always present at CCE2. When the glider is inshore, these measurements are grouped to create data sets of temperature and salinity for the northeast corner of the box, referred to as PC (Figure 2.2).

These data sets are used for constructing dynamic height at this inshore corner of the northern side as reviewed in Section 2.2.3 and explained in Appendix A.

For the box region in Figure 2.1, the measurements made by the moorings and gliders on all sides enable calculations of the baroclinic component of the dynamic height profiles. These dynamic height calculations require density profiles over the water column. For some sides of the box, the in-situ observations do not measure temperature and salinity near the surface and/or near the bottom. Thus, at the offshore box endpoints these portions of the density profiles must be approximated. The procedure for estimating the temperature and salinity in these parts of the water column is reviewed in Section 2.2.3 but discussed in greater detail in Appendix A. For these processes, additional data products are used and are introduced as follows.

The World Ocean Atlas (WOA) 2013 provides climatological averages of vertical profiles of temperature and salinity. The climatological averages are computed over a period from 1955 - 2012. These objectively analyzed climatological fields incorporate several observational data sources (Locarnini et al. 2013; Zweng et al. 2013), and the climatological profiles aid in gridding the temperature and salinity fields at CCE2 and CORC3 as discussed in Appendix A.

The World Ocean Database (WOD) 2013 of hydrographic data is also used to create full water column profiles of density (Boyer et al. 2013). These data are downloaded in 0.3° x 0.3° boxes near CCE2 and CORC3, and help extrapolate salinity information at the bottom as discussed in Appendix A. Data selection was made using the WODselect tool (https://www.nodc.noaa.gov/OC5/SELECT/dbsearch/dbsearch.html).

At CORC3, near surface temperature and salinity must be approximated during mooring deployments (Figure 2.2) as the upper approximately 35 m are not sampled. To estimate

temperature near the surface, both sea surface temperature (SST) and mixed layer depth (MLD) are used. SST comes from the Group for High Resolution SST (GHRSST) product. This is a product by Remote Sensing Systems (REMSS) that utilizes remotely sensed SST including data from microwave and infrared sensors (Remote Sensing Systems 2017). This product provides daily global SST coverage using a 0.09° grid and data are downloaded over 2012 - 2020.

MLD data come from the Multi Observation Global Ocean ARMOR3D product from the Copernicus Marine and Environment Monitoring Service (CMEMS), which uses satellite and in-situ observations to deliver reprocessed weekly averaged mixed layer depths (Guinehut et al. 2012; Mulet et al. 2012). The spatial resolution is 0.25° and data are downloaded from 2012 - 2020. The weekly averaged data are linearly interpolated to a daily time step. The process for estimating temperature near the surface using the SST and MLD products is discussed in Appendix A along with the approximation of salinity near the surface.

b.) Depth-Invariant Data Sets

In addition to the baroclinic shear component of dynamic height, another component of dynamic height is the depth-invariant contribution. To measure the full dynamic height, the density-derived component of dynamic height is referenced with bottom pressure at CCE2 and at CORC3. At the CCE2 and CORC3 moorings, the bottom pressure measurements come from pressure inverted echo sounders (PIES), which are deployed for about 4 years at a time (Figure 2.2). The PIES bottom pressure data go through a series of data processing steps including de-spiking, de-tiding, and de-drifting the data. Lastly, a low-pass Butterworth filter is applied with a cutoff period of 3 days. During the PIES bottom pressure detrending procedure, the barotropic mean is removed and this must be accounted for in order to obtain the total dynamic height profiles. The process of referencing the baroclinic shear from the moorings and gliders to the

PIES bottom pressure fluctuations is discussed in Appendix A with an overview given in Section 2.2.3.

The PIES are also equipped with a temperature probe, but these temperature sensors are not calibrated and require some correction. This involves removing the temporal mean and replacing it with the WOA mean temperature at this depth. This is referred to as the adjusted temperature. The adjusted temperature aids in interpolating temperature from the deepest sensor on the moorings down to the depth of the PIES as described in Appendix A. Bottom pressure and temperature data are downloaded from the instrument when it is recovered, in addition to some of the data being telemetered throughout the deployment and thus available in near-real time. Telemetered data include the bottom pressure but not the temperature. The second CCE2 PIES deployment was not recovered, so there is only telemetered bottom pressure from this deployment and no temperature data. Additionally, the battery died during the second CCE2 PIES deployment so there are no data between December 2019 – September 2020 (Figure 2.2).

At the two inshore endpoints of the box, there are no PIES deployed so the depth-independent dynamic height fluctuations are derived from sea level data. Daily tide gauge data at Port San Luis (PSL), Santa Barbara (SB), Santa Monica (SM), and San Diego (SD) from the University of Hawaii Sea Level Center (1993 - 2019; Caldwell et al. 2015) and NOAA's Center for Operational Oceanographic Products (2020 – 2021) are used to reference the baroclinic component of dynamic height from the moorings and the gliders (Figure 2.1). Tide gauge data have the trend removed from 1993 – 2021. The detrended data are then corrected to remove atmospheric pressure influences on the sea level. This requires an inverse barometer correction to obtain the adjusted sea level. Daily surface pressure for this correction are gathered from the National Centers for Environmental Prediction North American Regional Reanalysis (Mesinger

et al. 2006). These tide gauges were selected based on their proximity to the moorings and reduced exposure to ocean swell. The error associated with the tide gauges and potential wave bias is reviewed in Appendix B. At DM, the sea level variability is taken to be the same as the sea level measurements by the SD tide gauge. For the northeast corner of the box, the depth-invariant fluctuations in dynamic height are approximated by linearly interpolating the tide gauge sea level measurements at the coast. Coastal tide gauges north, i.e., PSL, and south, i.e., SB, of the northeast box endpoint are interpolated at the latitude of the endpoint. The SSH fluctuations at this latitude on the coast are assumed to be the same as at the northeast box endpoint.

c.) Sea Level Mean

Since the processed PIES and tide gauge data do not include the dynamic height mean, this must be included to obtain the absolute dynamic height at each endpoint of the box. The time-mean comes from an altimetry product of absolute dynamic topography (ADT) published by CMEMS. The ADT is the sum of the mean dynamic topography and the sea surface height anomaly (SSHa). This product is on a 0.25° grid and provides data from 1993 to 2022. The temporally averaged ADT from this product gives the offset needed to adjust the vertical profiles of dynamic height for each endpoint of the box as described in Appendix A.

2.2.2.2 Ekman Data

To determine the amount of Ekman transport through the lateral sides of the box, surface wind data are needed over the region. The Cross-Calibrated Multi-Platform (CCMPv2) product from REMSS provides a gridded reanalysis wind product using satellite, buoy, and ERA Interim model wind data at a spatial resolution of 0.25° (Mears et al. 2022). Data are available every 6 hours, at a height of 10 m above sea level, and are extracted over 2000 – 2022. The choice for using this wind product is discussed in Appendix B.

To quantify the error in Ekman transport from the CCMPv2 product, CCMPv2 wind data are compared against buoy winds in Appendix B. Previous error estimates of the CCMPv2 product have been made on hourly timescales (Wang et al. 2019), but for the objective of resolving vertical transport on weekly timescales, the CCMPv2 error will be estimated on weekly timescales. The National Data Buoy Center (NDBC) operates a network of buoys that measure near surface ocean winds and report average wind speed every 10 minutes. Three NDBC buoys in southern California are selected for comparisons, namely buoys 46054, 46025, 46086, located within the north, central, and southerly regions of the box, respectively (Figure 2.1). The height of the anemometers is about 4 m above the sea surface, so buoy winds are estimated at 10 m height using the power law method (Hsu et al. 1994). Wind stress is calculated (this calculation is presented in Section 2.2.3), daily averaged, and weekly low-pass filtered. In addition to the NDBC buoys, the CCE2 buoy has a suite of meteorological instruments including an anemometer that measures wind at 3 m height. These data are processed in a similar fashion to the NDBC buoys to obtain weekly low-pass filtered wind stress.

2.2.2.3 Ancillary Data Sets

SSH is downloaded from the CMEMS GLORYS product for examining SSHa at CCE2 when no bottom pressure measurements were made over December 2019 – September 2020. The GLORYS product is an ocean reanalysis with 1/12˚ horizontal resolution and outputs daily averages (Lellouche et al. 2021). GLORYS SSHa are highly correlated with US west coast tide gauges suggesting this product is a reasonable alternative for the PIES data (Amaya et al. 2022; Chapter 1 Table 1.1). The GLORYS SSH data are available from 2000 - mid-2020 but this reanalysis is not run after mid-2020, so to extend sea level for a few more months another sea level product is used by CMEMS that comes from their forecasting product, the Global Ocean

Physics Analysis and Forecast. This product has the same spatial resolution as the GLORYS product and was compared to the GLORYS product and the tide gauge data in Chapter 1. As was done in Chapter 1, a site-dependent correction is made to account for the bias between the GLORYS and Forecast products. Despite the good correlation of these products to tide gauge data, the rms errors of the CMEMS products (Chapter 1 Section 1.2) are larger than the expected 1 - 2 cm rms error from the PIES (Watts and Kontoyiannis 1990; Hughes et al. 2013). Altimetry SSH data are another option to fill in this gap, but they do not capture fluctuations at a fixed site on the order of days to one week.

For the heat budget, surface heat fluxes into/out of the control volume must be estimated. ERA5 is a reanalysis from the European Centre for Medium-Range Weather Forecasts (ECMWF). It provides a record of climate variables for the atmosphere, land, and ocean. Surface heat flux data are downloaded from this product which includes net solar radiation, net thermal radiation, latent heat, and sensible heat. These data are hourly and on a 0.25° grid. Data are extracted over the box region in Figure 2.1, daily-averaged, and spatially-averaged over the box.

For the heat budget, temperature will be approximated over the control volume and the uncertainty in the temperature approximations is determined from hydrographic data. Bottle data collected during California Cooperative Oceanic Fisheries Investigations (CalCOFI) cruises include temperature measurements in the upper 50 m. These data are collected throughout southern California about four times a year. CalCOFI cruises have been ongoing since 1949. CalCOFI cruises follow a sampling pattern that is repeated quarterly, providing a long collection of data at these locations.

The upwelling index derived in Section 2.2.3 is compared to other regional estimates of upwelling including volume transport from a regional ocean model, the California State Estimate

(CASE). This assimilative model spans 27º – 40ºN and is forced at the boundaries by the Hybrid Coordinate Ocean Model (HYCOM). Atmospheric forcing comes from NCEP NARR, which is adjusted during the assimilation process. More information on the CASE model output is provided in Zaba et al. (2018) and Zaba et al. (2020), and a detailed validation of this model to observations in southern California is presented in Zaba et al. (2018). Other measures of upwelling used in this study are CUTI which was obtained from https://mjacox.com/upwelling-indices/ and the Bakun index which was downloaded at https://coastwatch.pfeg.noaa.gov/erddap/griddap/index.html. CUTI is derived from a data assimilating regional ocean model that spans 30º – 48ºN and encompasses multiple reanalysis products. Because of this, there are multiple products used for the wind field including the CCMP reanalysis, the ECMWF ERA 40 and ERA Interim reanalysis, and the Coupled Ocean/Atmosphere Mesoscale Prediction System (COAMPS; Jacox et al. 2018). The Bakun index depends on geostrophic alongshore winds computed from sea level pressure from an atmospheric model that is outputted by the US Navy's Fleet Numerical Meteorology and Ocean Center (FNMOC) and is available for latitudes between 21º – 60ºN. Appendix D explains in greater detail the upwelling estimates from CASE, CUTI, and the Bakun index.

2.2.3 Control Box Volume Budget Calculations

Vertical transport can be inferred through a volume budget analysis where the residual of the net horizontal transport is the vertical transport since mass must be conserved. For the box in southern California, the volume integral equation representing mass conservation is,

$$-\int_{N_1}^{N_2}\int_{-50}^{0} v\ dz\ dl\ +\ \int_{W_1}^{W_2}\int_{-50}^{0} u\,dz\,dl + \int_{S_1}^{S_2}\int_{-50}^{0} v\,dz\,dl\ +\ \int_{A}\ w\,dxdy = 0, \quad (1)$$

where N, W, and S represent the north, west, and south sides of the box, respectively, and subscripts specify the endpoints of a box side. The box is vertically bounded by the surface and

50 m depth. The along-box and cross-box velocity components are v and u respectively, while w is the vertical velocity integrated over the box area, A. The along-box direction is taken to be 30° west of true north and the cross-box direction is 36° north of due east. These directions are perpendicular to the box sides. The total flow field is assumed to be the sum of the geostrophic and Ekman components as,

$$v = v_G + v_E, \qquad u = u_G + u_E. \tag{2}$$

Subscripts G and E specify the velocity component due to geostrophic flow versus Ekman flow, respectively. Equation (1) is rewritten now as,

$$-\int_{N_1}^{N_2}\int_{-50}^{0}(v_G + v_E)\,dz\,dl + \int_{W_1}^{W_2}\int_{-50}^{0}(u_G + u_E)\,dz\,dl + \int_{S_1}^{S_2}\int_{-50}^{0}(v_G + v_E)\,dz\,dl$$

$$+\int_A w\,dxdy = 0. \tag{3}$$

The integrals are taken over the geostrophic and Ekman velocities separately to yield transport through a side due to geostrophic influences versus that from Ekman. For example, the transport through the north side is decomposed as,

$$\int_{N_1}^{N_2}\int_{-50}^{0}(v_G + v_E)\,dz\,dl = L_N\int_{-50}^{0}\overline{v_G}dz + \int_{N_1}^{N_2}\int_{-50}^{0}v_E\,dz\,dl, \tag{4}$$

where the overbar on the right-hand side denotes the mean geostrophic velocities. In estimating the geostrophic transport, i.e., the first term on the right-hand side of equation (4), the geostrophic velocity is averaged across a box side, multiplied by the length of the box side, L, and integrated over the upper 50 m. The calculations for the geostrophic and Ekman terms, like on the right-hand side of equation (4), are the focus in the next two sections.

2.2.3.1 Geostrophic Transport Calculations

The first term on the right-hand side of equation (4) is the geostrophic transport where the mean geostrophic velocity is defined as,

$$\overline{v_G(p)} = \frac{1}{fL}\int_{pref_p}^{p} \Delta D(p)dp, \quad (5)$$

where f is the Coriolis parameter, L is the length of the section of the box side, p_{refp} is the reference level of pressure below the surface, and ΔD is the difference in total dynamic height at the box endpoints as a function of pressure, p.

a.) Dynamic Height Calculations

The total dynamic height profile at an endpoint has three parts: the time-varying baroclinic contributions to the dynamic height, the barotropic fluctuations in dynamic height over the entire water column, and the temporal mean in dynamic height. The total dynamic height profile at a box endpoint is computed as,

$$D(p) = \int_{p_{refp}}^{p} \delta(p)dp + \frac{p'_{refp}}{\rho_{refp}} + \alpha. \quad (6)$$

Above, ρ is the density of seawater and δ is the specific volume anomaly at each of the box endpoints as a function of pressure. Specific volume anomaly is defined as,

$$\delta = \frac{1}{\rho_{s,t,p}} - \frac{1}{\rho_{35,0,p}}, \quad (7)$$

where the second term is the density of seawater at 0°C and 35 PSU. p' in equation (6) denotes the barotropic fluctuations in dynamic height, and α is an offset such that it adjusts dynamic height at an endpoint to agree with the time-mean dynamic height at the surface from CMEMS data. The three components that make up total dynamic height profiles are estimated separately from different observations. The first term in equation (6) is estimated from the moorings and the gliders, both of which measure the vertical changes in dynamic height over depth. These observations determine the contribution of the along isobar gradients in density to the total dynamic height profiles.

The second term in equation (6) describes the depth independent temporal changes in dynamic height that is exerted over the entire water column. This is essentially the fluctuation in reference pressure and is obtained from the PIES (offshore) and from the coastal tide gauges (inshore). The PIES directly measure pressure at the bottom of the seafloor, while tide gauges record the variability in sea level. For the tide gauges, the second term in equation (6) is,

$$p'_{refp} = \rho g SSH', \tag{8}$$

where g is the gravitational constant and SSH' are the sea level fluctuations observed by the tide gauges. The PIES and the tide gauges are different referencing levels, therefore, the direction that equation (6) is integrated depends on the referencing instrument. If the barotropic fluctuations are derived from the PIES, like at CCE2 and CORC3, then the specific volume is integrated upward from the bottom. In contrast, if the barotropic fluctuations come from the tide gauges, then the integration is downward from the surface.

The last term in equation (6) is based on the CMEMS ADT of the surface temporal mean. This is observed at the surface but is depth independent and is calculated as,

$$\alpha = \overline{D'(0)} - \frac{\overline{p_{refs}}}{\rho_{refs}}. \tag{9}$$

The first term on the right-hand side of equation (9) is the dynamic height at the surface based on the sum of the baroclinic and depth independent fluctuations from equation (6). The second term is the mean as represented by the CMEMS ADT data. This term is,

$$\overline{p_{refs}} = \rho g \overline{SSH}, \tag{10}$$

where $\overline{SSH}$ is the time-averaged CMEMS ADT. The time period taken for averaging dynamic height in equation (9) is over April 2013 – September 2020. This is the period for which there are overlapping observations at the box endpoints. This section presented the dynamic height

calculations and the next section gives an overview of how the dynamic height profiles are vertically and temporally gridded.

b.) Total Dynamic Height Profiles

Due to temporal and spatial gaps in observations of the time-varying baroclinic component and barotropic fluctuations in dynamic height, each side requires careful consideration in gridding the dynamic height profiles in order to compute the geostrophic velocities across each side. The technical details of this procedure are described in Appendix A, with the uncertainties in these estimates reviewed in Appendix B, and an overview is given below.

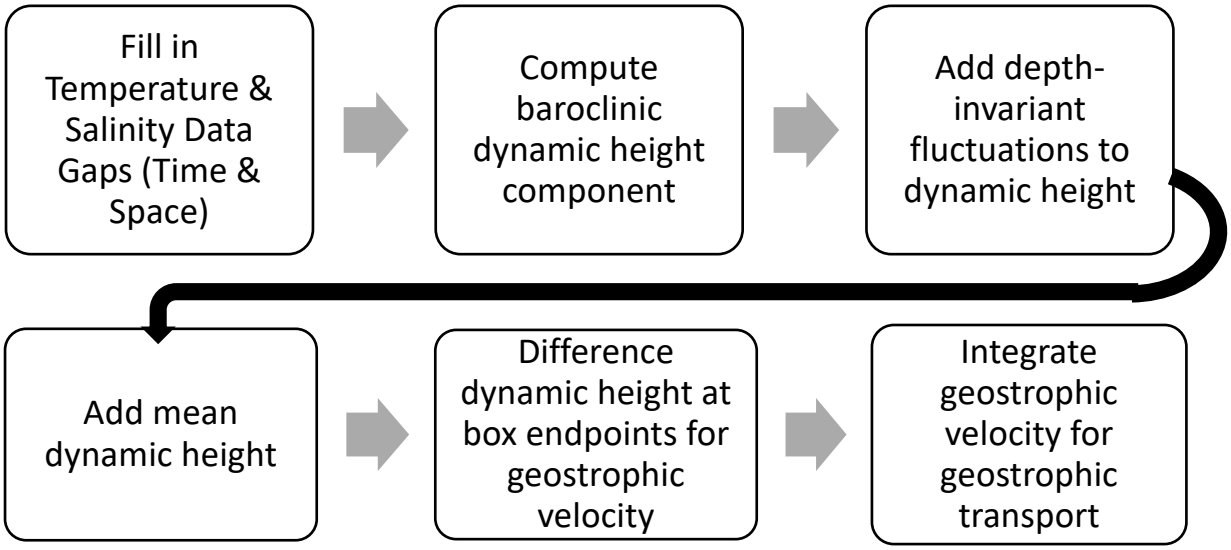

Figure 2.3: Flow chart illustrating the steps to compute geostrophic transport through the lateral box sides in Figure 2.1.

Figure 2.3 illustrates a flow chart that steps through the process of merging total dynamic height from the observations in order to estimate geostrophic transport. The first step is to have complete profiles of density in order to compute the time-varying baroclinic component. Since the inshore box endpoints reference dynamic height with SSH, the dynamic height profiles at these sites must be known for the upper 50 m for the volume budget. The offshore box endpoints

reference dynamic height with bottom pressure, so dynamic height profiles must be known over the whole water column.

To demonstrate how density information is gridded in time and space at two of the box endpoints, a few density approximations are mentioned below along with the uncertainty introduced in making these estimates. For a complete explanation of merging dynamic height at each box endpoint, the reader is referred to Appendix A, while the associated transport errors are listed in Appendix B. The upwelling signal is about 0.2 Sv over the area of the box based on the typical variability in vertical transport in the upper ocean (Jacox et al. 2018; Zaba et al. 2020), so the uncertainty in vertical transport must be less than this to resolve upwelling variability. The *absolute* vertical transport error depends on the errors in the dynamic height profiles from the time-varying baroclinic, time-varying barotropic, and time-independent components. However, the *time-varying* vertical transport error depends only on the baroclinic and barotropic dynamic height fluctuations.

The northeast box endpoint is periodically sampled by a glider. This requires temporally interpolating the glider measured temperature and salinity measurements to estimate these properties when the glider is not inshore. This approximation yields a geostrophic transport uncertainty of 0.03 Sv. Dynamic height is computed from the density profiles over the upper 50 m and these are referenced with SSH from the tide gauges. Then the mean surface dynamic height is adjusted to match the mean from ADT. Additional errors in geostrophic transport through the north side come from the glider sensor errors (0.001 Sv), transport inshore of the box endpoint not captured by the observational array (0.03 Sv), the tide gauge sensor error which accounts for error from the SB and PSL tide gauges (0.04 Sv), and the ADT error (0.12 Sv).

The northwest box endpoint is sampled by the same glider that measures the northeast box endpoint. As such, the temperature and salinity measurements must also be interpolated in time at this location. Since the glider spends more time at this location, there are more observations and the temporal interpolation error is smaller (0.01 Sv). The glider does not profile down to the PIES depth, so density is interpolated over the bottom layer resulting in a dynamic height error of about 0.004 Sv. Other errors in dynamic height at this site come from the glider sensor errors (0.02 Sv), the PIES sensor error (0.0612 Sv), and the ADT error (0.12 Sv).

The total dynamic height profiles at both northern endpoints are differenced, as in equation (5), to determine the geostrophic velocity, and then the velocity is integrated over the upper 50 m and multiplied by the length of the north side of the box to yield the geostrophic transport. The dynamic height profiles are determined for the other box endpoints as discussed in Appendix A with similar attention given to filling in gaps and estimating the error sources, and the geostrophic velocities are calculated through both the west and the south sides of the control volume. These velocities are integrated over the upper 50 m and multiplied by the respective box sides yielding the geostrophic transport, and this completes the geostrophic transport calculations.

2.2.3.2 Ekman Transport Calculations

This section explains how the Ekman transport in the volume budget is determined. The error in the Ekman transport is noted, but the reader is referred to Appendix B for the details of this estimate.

The second term on the right-hand side of equation (4) is the Ekman transport and this term is similarly evaluated over the box sides. This term is calculated from the two-dimensional Ekman transport, and for the north side this is expressed as,

$$\int_{N_1}^{N_2}\int_{-50}^{0} v_E \, dz \, dl = \int_{N_1}^{N_2} M^y \, dl. \tag{11}$$

Above, M^y is the along-box two-dimensional Ekman transport component in m^2/s over the Ekman layer. The same equation holds for the west and south sides of the box, where the west side uses the cross-box Ekman component, M^x. The Ekman transport is assumed to occur in the upper 50 m, which is a reasonable assumption given that Chereskin (1995) reported an Ekman layer thickness of 50 m in the CCS.

The two-dimensional Ekman transport is deduced as,

$$(M^x, M^y) = \frac{(\boldsymbol{\tau}^y, -\boldsymbol{\tau}^x)}{\rho f}. \tag{12}$$

In this equation, τ^y and τ^x are the along-box and cross-box wind stress components, respectively. The CCMPv2 wind data are extracted along the north, west, and south sides of the box and the wind stress is calculated from this data as,

$$\boldsymbol{\tau} = \rho_a c_d \mathbf{U}|\mathbf{U}|. \tag{13}$$

In equation (13), ρ_a is the density of air, c_d is the drag coefficient, and $\mathbf{U}$ contains the u and v components of the wind velocity. The drag coefficient is parameterized using the approach demonstrated in Edson et al. (2013) that was originally derived in Hersbach (2011), and this parameterization accounts for the influence of friction at lower and higher wind speeds based on empirical data. The error in the Ekman transport over the control volume is estimated to be about 0.09 Sv and the details of this calculation are reviewed in Appendix B.

2.2.4 CCUI Derivation

The requirement of contemporaneous measurements at all box endpoints and uncertainty in the baroclinic component of the dynamic height measurements motivate simplifying the geostrophic transport calculations where (1) the Coriolis parameter is assumed constant over the control volume and (2) the time-varying contribution of the geostrophic shear over the upper 50

m is neglected. For the latter, the uncertainty in the measurement of this term will be shown to be nearly the magnitude of its rms amplitude. These simplifications in the geostrophic transport calculations are incorporated into a new upwelling index, the Coastal California Upwelling Index (CCUI).

2.2.4.1 Coriolis Parameter Assumption

The geostrophic transport over the control volume requires making simultaneous measurements of transport through the lateral box sides. This can be difficult and if there is a missed measurement in the moorings, gliders, PIES, or tide gauges used in the volume budget, then the total geostrophic transport into the control volume cannot be determined. For example, a broken glider conductivity sensor in the second half of 2014 resulted in not being able to estimate the baroclinic component of dynamic height at CORC3 for several months (Figure 2.2). Likewise, the CORC3 mooring was not deployed over 2020 – 2021, and therefore the geostrophic transport through the west and south box sides cannot be determined in this period. This demonstrates how important it is to have simultaneous measurements at all box endpoints in order to compute the geostrophic transport for the volume budget.

The equation for the net geostrophic transport into the control volume is,

$$T_G = -\frac{1}{f_N}\int_{-50}^{0} \Delta D_N(p)dz + \frac{1}{f_W}\int_{-50}^{0} \Delta D_W(p)dz + \frac{1}{f_S}\int_{-50}^{0} \Delta D_S(p)dz. \quad (14)$$

This gathers the geostrophic terms in equation (1) and substitutes equation (5) for the geostrophic velocity. If the Coriolis parameter changes minimally over the control volume then,

$$f \approx f_N \approx f_W \approx f_S\,. \quad (15)$$

This Coriolis parameter approximation is inserted into equation (14) and the dynamic height differences are expanded yielding,

$$T_G = -\frac{1}{f}\int_{pref_p}^{p}\big(D_{N1}(p) - D_{N2}(p)\big)dp + \frac{1}{f}\int_{pref_p}^{p}\big(D_{W2}(p) - D_{W1}(p)\big)dp$$

$$+ \frac{1}{f}\int_{pref_p}^{p}\left(D_{S1}(p) - D_{S2}(p)\right)dp. \quad (16)$$

In equation (16), the dynamic heights at the endpoints of the west side, D_{W1} and D_{W2}, are the same as the dynamic heights at the offshore endpoints of the north and south sides of the box such that,

$$D_{N2}(p) = D_{W1}(p) \text{ and } D_{S2}(p) = D_{W2}(p). \quad (17)$$

Substituting this into equation (16) eliminates many of the terms and equation (16) reduces to,

$$T_G = \frac{d}{f}\Delta D_E(p), \quad (18)$$

where,

$$\Delta D_E(p) = D_{S1}(p) - D_{N1}(p). \quad (19)$$

In equation (18), d is the depth over which the volume budget is performed, i.e., 50 m, and ΔD_E(p) is the difference in dynamic height between the southeast and northeast box endpoints.

Equations (18) and (19) show that net geostrophic transport into the box can be determined from the total dynamic height profiles at the two inshore box endpoints alone. Under a constant Coriolis parameter, changes in the dynamic height profiles at the offshore endpoints drive transport into one side of the box which are compensated for by transport out through another side. For instance, an increase/decrease in dynamic height at CCE2 leads to less/more northward transport through the north side of the box that is balanced by less/more onshore transport through the west side. At CORC3, an increase/decrease in dynamic height yields more/less onshore transport through the west side in exchange with less/more northward transport through the south side.

Assuming that the Coriolis parameter is constant across all sides of the box increases the number of days for which geostrophic transport is estimated, thereby enhancing the temporal coverage of vertical transport (dashed line in Figure 2.4). For example, in the last years of the

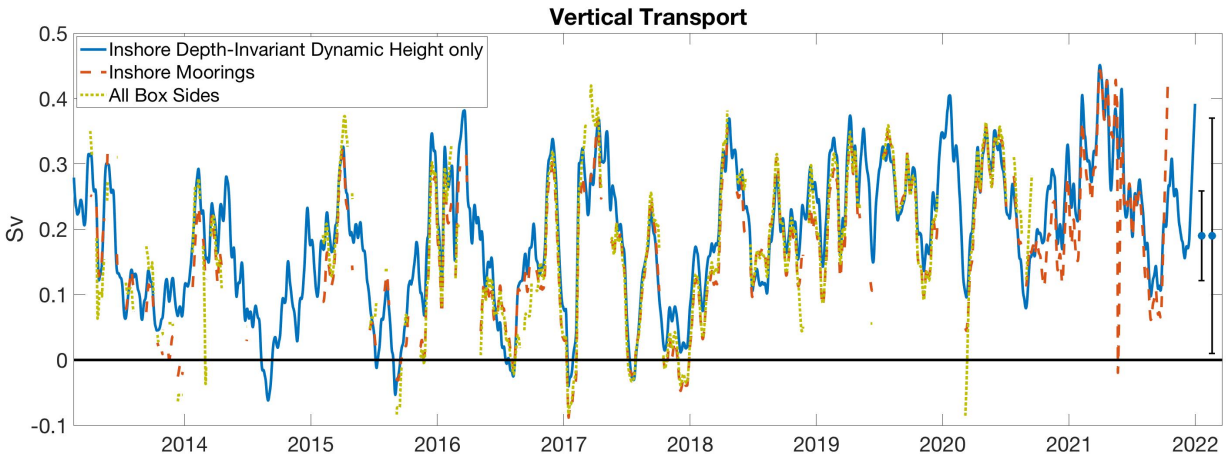

Figure 2.4: Weekly filtered vertical transport from (1) the volume budget that uses transport through the three lateral box sides (dotted line), (2) the assumption of a constant Coriolis parameter over the box region and using only the inshore moorings (dashed line), and (3) the inshore depth-independent measurements, i.e., the tide gauges and CMEMS data (solid line). There are two error bars shown for the vertical transport error in the solid timeseries. The smaller error bar does not include the time-mean error, while the larger error does (Appendix B).

record, i.e., 2020 – 2021, the CORC3 mooring could not be replaced and therefore vertical transport cannot be approximated in these years using the net geostrophic transport that is summed up from all three sides of the box (dotted line in Figure 2.4). In contrast, vertical transport is approximated in these years with equation (18; dashed line in Figure 2.4). The simplification from the Coriolis parameter assumption has an estimated transport error of 0.01 Sv, which is discussed in Appendix B. Thus, this approximation has relatively no influence on the total geostrophic transport error.

2.2.4.2 Depth-Dependence Assumption

This section shows that the depth-dependent geostrophic transport resulting from velocity shear over the upper 50 m makes a negligible contribution to the total transport, resulting in a second simplification. This section first shows the size of the baroclinic and barotropic fluctuations, then it argues that the uncertainty in the estimate of the baroclinic component of dynamic height is about the same size as the variability in this component, and lastly it presents

the mathematical simplifications in the geostrophic transport calculations that lead to the new upwelling index.

a.) Baroclinic versus Barotropic Transport Fluctuations

The dependence of the total geostrophic transport on the baroclinic and the barotropic components are examined, where the latter is the sum of the barotropic fluctuations and the time-independent part of the geostrophic transport, i.e., the sum of the second and third terms on the right-hand side of equation (6). The rms difference between the barotropic geostrophic transport and the total geostrophic transport is smaller than the rms difference between the baroclinic geostrophic transport and the total geostrophic transport (Table 2.1). This is true for all three lateral sides of the box. The percent variance explained, $100 \times r^2$ where r is the correlation, demonstrates that the barotropic geostrophic transport explains most of the variability in the total geostrophic transport (Table 2.1). Thus, in the upper 50 m of the box, the barotropic changes dominate the behavior of the total geostrophic transport.

Table 2.1: The rms difference between the geostrophic shear and the total geostrophic transport, as well as the rms difference between the sum of the depth-independent portion and the time-independent aspect of the geostrophic transport, i.e., the second and third terms on the right-hand side of equation (6), and the total geostrophic transport. The last column contains the percent variance explained in the geostrophic transport by the sum of the depth-independent portion and the time-independent aspect of the geostrophic transport.

	Rms Difference (Sv) between Baroclinic & Total Geostrophic Transport	**Rms Difference (Sv) between Depth-Independent & Total Geostrophic Transport**	**Percent Variance explained by the Depth-Independent Geostrophic Transport, $100 \times r^2$**
North Side	0.2472	0.0375	98%
West Side	0.2507	0.0865	97%
South Side	0.3904	0.0669	99%

b.) Geostrophic Shear Uncertainty versus Geostrophic Shear Fluctuations

Uncertainty in the geostrophic shear related to errors in the baroclinic component of dynamic height are assessed against the size of the geostrophic shear fluctuations. The transport error in the geostrophic shear is approximated as 0.04 Sv. This error estimate accounts for multiple sources of uncertainty in the baroclinic component of dynamic. At the southeast box endpoint these error sources include the DM mooring sensor error and the unmeasured geostrophic transport between DM and the coast. At the northeast box endpoint, the geostrophic shear error sources are the glider sensor error, the glider temporal interpolation, and the unmeasured geostrophic transport between this endpoint and the coast. The approximation of these error sources is discussed in Appendix B.

The magnitude of the contribution of the geostrophic shear fluctuations to the total transport is about 0.04 Sv; see Appendix B for an explanation of how this is determined. Thus, the shear fluctuations are about the same size as the uncertainty in the geostrophic shear. Since the uncertainty is about the size of the shear signal, there is negligible skill in estimating this component. Also, the percent variance explained by the barotropic component of dynamic height is large, so the shear component contributes very little to the overall variability. Therefore, the shear component can be omitted.

c.) Inshore Dynamic Height Simplification

Neglecting the baroclinic component of dynamic height is mathematically expressed as,

$$D(p) \approx \frac{p'_{refp}}{\rho_{refp}} + \alpha. \tag{20}$$

Substituting this into equation (18) yields,

$$T_G = \frac{d}{f}\left[\frac{p'_{refp_{S1}}}{\rho_{refp_{S1}}} + \alpha_{S1} - \left(\frac{p'_{refp_{N1}}}{\rho_{refp_{N1}}} + \alpha_{N1}\right)\right]. \tag{21}$$

Note that p'_{refp} is essentially the coastal sea level fluctuation. This third estimate of geostrophic transport increases the temporal coverage from the second estimate in Section 2.2.4.1 because it does not require both baroclinic and barotropic measurements at the same time. This results in increased temporal coverage of vertical transport (solid line in Figure 2.4) and extends the time series to include an earlier nearly 15 years of data. The uncertainty in the temporal variability of this geostrophic transport estimate depends on the tide gauge sensor error, which is about 0.003 m. This yields a transport error of 0.04 Sv for the temporal variability in the net geostrophic transport, which is much smaller than the geostrophic transport magnitudes, i.e., 0.2 Sv. This third estimate of geostrophic transport is the geostrophic component for the new upwelling index, i.e., the Coastal California Upwelling Index (CCUI).

The CCUI is the sum of the geostrophic and Ekman transports over southern California. The geostrophic transport is approximated from the barotropic fluctuations at the coast and the time-mean, i.e., the third geostrophic transport estimate, and the net Ekman transport is approximated from integrating the 2D Ekman transport around the perimeter of the control volume. The CCUI is a regional upwelling measure that represents the vertical volume flux at 50 m depth. This new upwelling index differs from other upwelling measures since it incorporates tide gauge sea level measurements to determine the cross-shore geostrophic influences, so it uses sea level measurements at the coast to account for the coastal APG. Additionally, the CCMPv2 wind product chosen for the CCUI has demonstrated that it provides reasonable wind estimates for the region (Wang et al. 2019; Appendix B). The method for calculating this new upwelling index is applicable for other EBUS and this will be demonstrated next for central California.

2.2.4.3 CCUI for Central California

The CCUI can be applied to other coastal upwelling regions and this is demonstrated for central California. The CCUI is approximated for central California in a similar fashion as to how it was derived for southern California. Coastal tide gauges are used to approximate the net horizontal geostrophic transport into or out of the central California box (Figure 2.5). The Monterey tide gauge captures sea level fluctuations for the northerly end of the central California box and this is combined with the mean CMEMS ADT (Figure 2.5). The coastal sea level measurements at the southeast box endpoint use the same sea level data set from the northeast endpoint of the southern California box. As with the southern California box, the CCMPv2 winds are integrated around the northern box in Figure 2.5 to determine the net Ekman transport. The combination of the geostrophic and Ekman transports gives the horizontal convergence/divergence in the box and thus the vertical transport through 50 m.

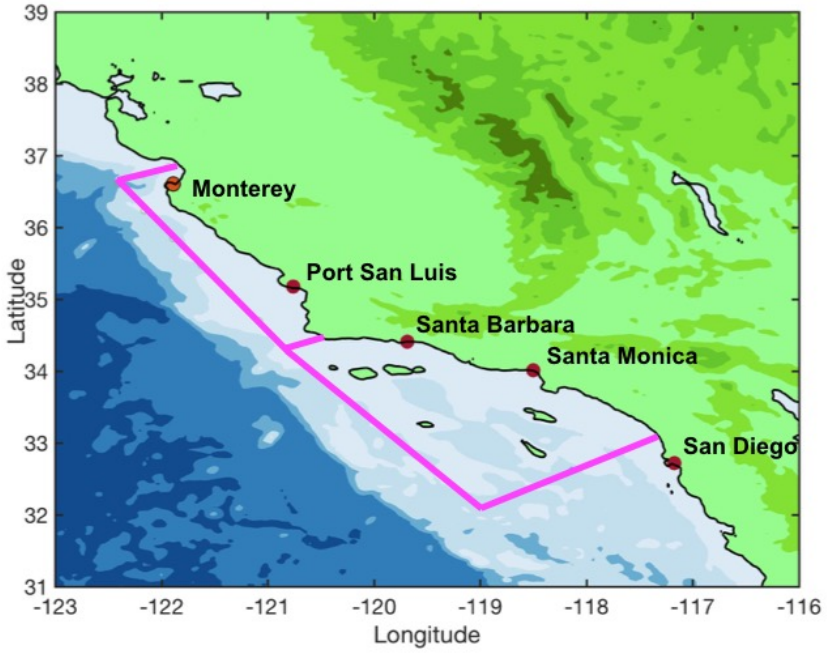

Figure 2.5: North and south boxes used for approximating upwelling in central and southern California, respectively, for CCUI. Purple circles are coastal tide gauges used in the upwelling estimates.

2.2.5 Control Volume Heat Budget Calculations

Like the volume budget, the heat budget is performed over the upper 50 m and this is approximated as,

$$\underbrace{\Delta T}_{(1)} = \Delta t \Big(\underbrace{-\frac{B_N}{b} T_N}_{(2)} + \underbrace{\frac{B_W}{b} T_W}_{(3)} + \underbrace{\frac{B_S}{b} T_S}_{(4)} + \underbrace{\frac{B_U}{b} T_U}_{(5)} + \underbrace{\frac{1}{d\rho c_p} Q_{net}}_{(6)} \Big). \quad (22)$$

Term (1) on the left-hand side of equation (22) is the change in temperature over the box and Δt is the time step, which is one day. Terms (2) – (4) are the temperature fluxes through the lateral sides of the box, with B denoting the volume transport through a box side which is then normalized by the volume of the box, b. Terms (2) – (4) are approximated using the averaged transport and averaged temperature across the box sides. The temperature for a box side, T, is the average upper 50 m temperature across the section and constructing the upper 50 m temperature field is explained in more detail below. Term (5) is the temperature flux through the bottom of the box and term (6) is the temperature flux through the air-sea interface. For this term, d is 50 m, c_p is the specific heat capacity of seawater, and Q_{net} is the net air-sea heat flux. The net air-sea heat flux is,

$$Q_{net} = Q_s + Q_l + Q_e + Q_h, \quad (23)$$

where the terms on the right represent the shortwave, longwave, latent, and sensible heat contributions, respectively. These components of the net air-sea heat flux are approximated from ERA5 data.

2.2.5.1 Control Volume Temperature Construction

Most of the terms in equation (22) require temperature estimates over some portion of the control volume and the method for approximating the temperature field over the upper 50 m in southern California is described in this section.

The southern California upper ocean temperature approximations are based on observations. In-situ measurements from the moorings and gliders are combined with satellite SST data and MLD information to grid temperature over the upper 50 m. This approach uses stratification, i.e., the vertical temperature gradient within the upper 50 m, $\frac{\partial T}{\partial z}$, from the moorings and gliders at the four endpoints of the box and interpolates this over the region. The location of the moorings and gliders capture the multiple dynamical regimes in southern California; namely, the upwelling area off of Point Conception, the inshore region along the coastline, and the more open ocean zones offshore. So, the coastal processes occurring within the box may be considered some combination of these regimes.

Satellite SST data over the box provides the surface temperature, which is combined with the stratification in order to integrate temperature downward, thereby obtaining the temperature field throughout the upper 50 m. Lastly, these temperature fields are modified based on the thickness of the mixed layer. Incorporating the MLD information accounts for local changes on the stratification that occur within the box.

2.2.5.2 Control Volume Temperature Change

The constructed temperature field is averaged over the control volume using the method in the previous section and the change in the box-average temperature is taken as the estimate of

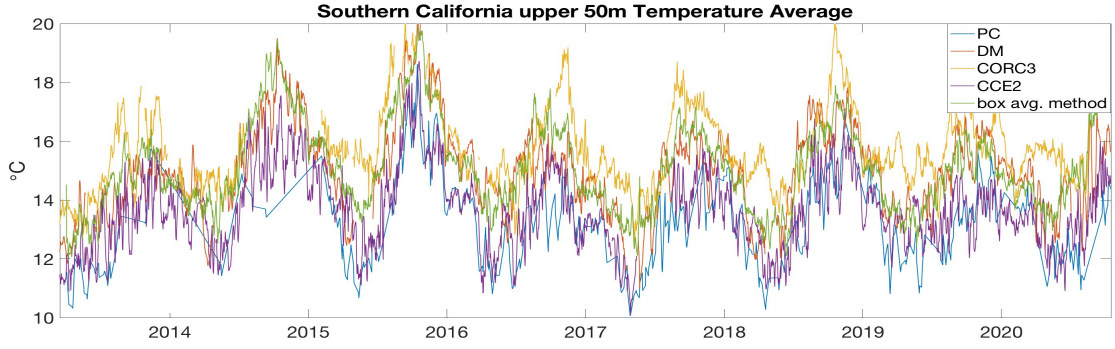

Figure 2.6: Upper 50 m temperature average at the endpoints of the southern California box along with the estimate of averaged temperature for the box over the upper 50 m.

term (1) in equation (22). Qualitatively, the averaged upper 50 m temperature over the box has similar values to those measured by the moorings and gliders (Figure 2.6). This is not a direct comparison as the in-situ measurements are only at select locations, but it provides a sense of the southern California temperature representation from the method outlined above.

2.2.5.3 Advected Heat Fluxes

Terms (2) – (4) in equation (22) are the horizontal temperature fluxes where the upper 50 m temperature average along each box side utilizes the in-situ temperature observations at the box endpoints and the constructed temperature field in between the endpoints. The average temperature for a lateral box side is multiplied by the total transport through that side, where the total transport is the sum of the geostrophic and Ekman transports in the upper 50 m. These transports are the same as those discussed in Section 2.2.3.

Since the temperature flux through a box side uses the average transport and temperature through the side, so along box variations in either of these properties are not considered. Such variations could alter the temperature flux through the side, so these temperature flux contributions were estimated and were shown not to significantly change the horizontal temperature fluxes (not shown).

The last advective term in equation (22), i.e., term (5), is the vertical temperature flux through the bottom of the box. Of the advective terms, term (5) is the most challenging term to approximate because the vertical transport is not directly measured, and neither is the temperature at 50 m depth, with the exception of this measurement at the box endpoints. Equation (22) is rewritten to separate term (5) on one side of the equation as follows,

$$\Delta t \frac{V_U}{b} T_U = -\Delta t \left(-\frac{V_N}{b} T_N + \frac{V_W}{b} T_W + \frac{V_S}{b} T_S + \frac{1}{d\rho c_p} Q_{net} \right) + \Delta T. \quad (24)$$

The temperature flux through the bottom of the box is calculated using the vertical transport from the volume budget in Section 2.2.3 along with the average temperature at 50 m depth over the box. The average 50 m temperature is approximated by taking the mean 50 m temperature from the constructed temperature field presented in Section 2.2.5.1. The approximation of the vertical temperature flux at 50 m depth will be assessed against the right-hand side of equation (24) in Section 2.3.3 to see how well the approximated 50 m temperature flux compares to the residual from the heat budget terms. The uncertainty in the 50 m vertical temperature flux is discussed in Appendix C.

2.2.6 Synoptic Upwelling Event Detection

One objective of this chapter is to study upwelling over multiple timescales including the subseasonal frequencies. The subseasonal frequencies are characterized by synoptic variability which includes intermittent upwelling events. To study the synoptic upwelling events, upwelling events must first be identified, and this section explains the event detection process followed by the event statistics that will be computed on the identified upwelling events.

2.2.6.1 Event Detection Process

Prior to identifying upwelling events, the CCUI timeseries is band-pass filtered between 7 – 100 days to focus on the variability on week-to-seasonal timescales. The upwelling events are detected based on the height of the upwelling *anomaly* amplitude, i.e., the height of the individual peaks in the anomaly timeseries (Figure 2.7). The height of a local peak must be above a particular threshold in order to be considered an upwelling event. The threshold is set to be about half the height of the band-passed vertical transport anomalies. Synoptic upwelling events are also examined in Chapter 3 and the influence of the threshold criteria on the event

statistics is assessed in Appendix A of that chapter. For those events that meet this criteria, the time during which the upwelling event peaks is referred to as the peak time.

Next, the upwelling and relaxation phases of the upwelling events are determined. The upwelling phase is the initial period when the event starts and reaches its peak intensity, while the relaxation phase is the period of time from the upwelling peak to the end of the event. The start of the upwelling phase and the end of the relaxation phase are determined based on the minima in the upwelling index before and after the peak, respectively. The time period encompassing both the upwelling and relaxation phases is referred to as the event window. Figure 2.7 exemplifies how upwelling events are identified over one year to demonstrate the technique utilized for event detection.

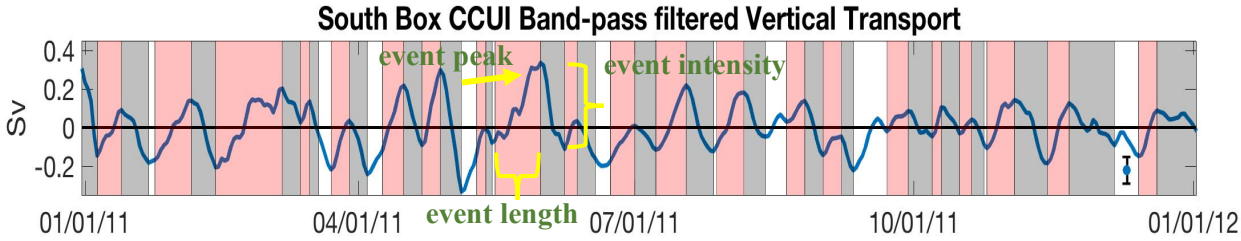

Figure 2.7: High-frequency upwelling event detection from the band-passed CCUI. Red periods denote the upwelling phase and gray periods are the relaxation phases of the upwelling events. The error bar in the top panel is the CCUI depth-independent time-varying geostrophic transport error based on rms errors from weekly filtered timeseries (Appendix B).

2.2.6.2 Event Statistics

Once the upwelling events are classified, statistics will be computed over the upwelling events to assess the synoptic variability in upwelling. The statistics used for this assessment are described here, while the results will be discussed in Section 2.4.3. There are three upwelling event statistics that will be calculated to analyze the synoptic variability. These statistics are upwelling intensity, upwelling duration, and the number of upwelling events per year, and they were selected because they characterize the physical forcing of upwelling.

Upwelling intensity is based on the height of the upwelling anomaly amplitude, and it is defined as the difference in upwelling between the maximum and minimum values during an event window. The upwelling intensity represents the magnitude of the wind forced anomalies and/or the alongshore propagating pressure gradient anomalies. Larger upwelling intensities signify stronger physical forcing of upwelling, and this is a factor that can drive more upwelled nutrients.

The second statistic is the length of the upwelling phase of the upwelling events, i.e., the elapsed time from the start of the upwelling event to the peak time. The significance of this statistic is that the duration of the upwelling phase may influence upwelling productivity and ocean acidification. Under the same upwelling intensity, longer events promote cumulatively more upwelled nutrients than shorter events. Both the intensity and the length of active upwelling can alter ocean acidification and may be accompanied by changes in pH and dissolved oxygen because these water properties are influenced by vertical heaving of isopycnals during upwelling events. Intense and/or prolonged upwelling can drive extreme acidic and hypoxic conditions that can be detrimental to calcareous organisms and benthic feeders (Chan et al. 2008; Fabry et al. 2008; Feely et al. 2008; Nam et al. 2011; Low et al. 2021).

The third event statistic is the number of upwelling events in a year and this captures the occurrence of synoptic upwelling. The number of events in a year indicates the number of incidents that may lead to an ecological upwelling response.

2.3 CCUI and Heat Budget Comparisons

Here the vertical transport from the CCUI is compared against other upwelling indices to provide confidence in the CCUI results, while the results themselves are analyzed in Section 2.4. Then, the estimated vertical temperature flux is evaluated against the residual of the terms on the

right-hand side of equation (24) to provide confidence is the vertical temperature flux estimate. The vertical temperature flux is of interest to study how changes in advection during the 2014 marine heatwave and the 2015 – 2016 El Niño impacted the heat budget.

2.3.1 CCUI Comparisons

The CCUI is compared against other measures of upwelling in both southern and central California to validate the vertical transport from the CCUI. The other measures of upwelling do not provide uncertainty estimates; however, if the errors in these other indices are comparable to the CCUI errors then this can suggest whether the vertical transport estimates agree with each other within the uncertainties. The three upwelling estimates used in the comparisons are CASE (Zaba et al. 2020), CUTI (Jacox et al. 2018), and the Bakun index (Bakun 1973). Appendix D reviews how vertical transport is derived in each of these indices and what wind products are used. The upwelling indices are compared statistically over 2007 – 2016 and shown for southern California for a 3-year duration that includes the 2014 marine heatwave and the 2015 – 2016 El Niño (Figure 2.8).

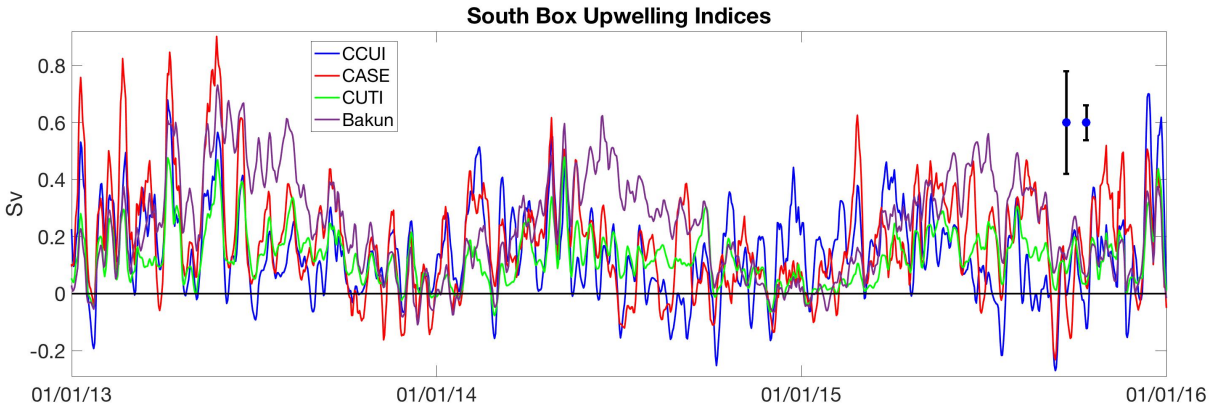

Figure 2.8: Weekly-filtered upwelling measures in the southern California box. The smaller error bar is for the time-varying CCUI transport error and the larger error bar is the CCUI error with the time-independent error. See Appendix B for the error discussion.

The southern California upwelling timeseries in Figure 2.8 include the seasonal cycle, low frequency variability, and synoptic upwelling events. All indices show variability at these

timescales of interest and the vertical transport from the CCUI will be filtered to inspect these timescales separately in Section 2.4. Two of the three years shown in Figure 2.8 contain large-scale climate events, i.e., the 2014 marine heatwave and the 2015 – 2016 El Niño. The error bars in Figure 2.8 demonstrate the uncertainty in the CCUI.

Statistics comparing the weekly-filtered upwelling indices for the north and south boxes (Figure 2.4) are given in Tables 2.2 and 2.3, respectively. The statistics are calculated over 2007 – 2016, since there is CASE data for these years. The upwelling index correlations in the south box are similar to their north box counterpart. Ranking the correlations from highest to lowest yields a similar order for both boxes with the CUTI - Bakun pair exhibiting the highest correlation and the CCUI - Bakun pair having the lowest correlation. For most of the index pairs, the rms difference is larger in the north box, and the highest rms differences in Tables 2.2 and 2.3 involve the Bakun index. Generally, the bias is small to moderate between index pairs. Calculations of bias that include CCUI as one of the upwelling indices are within the 0.17 Sv time-independent CCUI error.

The rms differences involving the CCUI are larger than the CCUI vertical transport error of 0.07 Sv. However, if the other indices have an error similar to the CCUI error, then the rms differences involving CASE and CUTI agree within these uncertainties. Likewise, CASE and CUTI agree with each other within these uncertainties. The statistics in Tables 2.2 and 2.3 show that the CCUI, CASE, and CUTI are moderately correlated with each other, have rms differences that are within the estimated uncertainty, and have bias values that are less than the time-independent error. Since the CCUI is consistent with the other upwelling indices and the time-varying error is small enough to resolve the upwelling variability, this index will be used to study upwelling at the timescales of interest in Section 2.4.

Table 2.2: North box correlation, rms difference, and bias between upwelling indices over 2007 - 2016. The 95% confidence interval is also given for the correlation. Negative bias means the second upwelling index in the first column is larger than the first upwelling index. The statistics are based on timeseries data that have a one-week low pass filter applied.

North Box Index Comparison	Correlation (95% CI)	RMS Difference (Sv)	Bias (Sv)
CCUI & CASE	0.67 ± 0.017	0.145	0.062
CCUI & CUTI	0.59 ± 0.014	0.148	-0.033
CCUI & Bakun	0.33 ± 0.019	0.220	-0.068
CASE & CUTI	0.72 ± 0.016	0.148	-0.094
CASE & Bakun	0.55 ± 0.20	0.212	-0.128
CUTI & Bakun	0.74 ± 0.15	0.135	-0.034

Table 2.3: South box correlation, rms difference, and bias between upwelling indices over 2007 - 2016. The 95% confidence interval is also given for the correlation. Negative bias means the second upwelling index in the first column is larger than the first upwelling index. The statistics are based on timeseries data that have a one-week low pass filter applied.

South Box Index Comparison	Correlation (95% CI)	RMS Difference (Sv)	Bias (Sv)
CCUI & CASE	0.62 ± 0.019	0.150	-0.014
CCUI & CUTI	0.63 ± 0.014	0.131	0.026
CCUI & Bakun	0.35 ± 0.018	0.207	-0.084
CASE & CUTI	0.71 ± 0.017	0.134	0.040
CASE & Bakun	0.56 ± 0.020	0.177	-0.070
CUTI & Bakun	0.74 ± 0.013	0.160	-0.110

2.3.2 Vertical Temperature Flux

To gain confidence in the vertical temperature flux through the bottom of the control volume, i.e., across 50 m depth, this term is compared to the residual of the terms on the right-hand side of equation (24). Figure 2.9 shows the 50 m vertical temperature flux scaled by the volume of the box and applied over 1 day to yield units of temperature change (blue) and the sum of the terms on the right-hand side of equation (24; red). The two curves compare well with one another and have a correlation of 0.84 and a rms difference of 0.09ºC. In Figure 2.9, the sum of the terms on the right-hand side of equation (24) lie mostly within the error bounds of the 50

m vertical temperature flux, emphasizing good agreement between the two curves. The similarity of the two curves in Figure 2.9 is partly related to the volume budget. Volume is conserved, so the vertical transport at 50 m depth is the residual of the net horizontal transport into/out of the box, as designated by equation (1). So, the volume transport on the left-hand side of equation (24) is dependent on the volume transports on the right-hand side of equation (24). Additionally, the data sets used to estimate the two curves in Figure 2.9 are not independent of each other. The temperature estimated at 50 m depth over the box uses the mooring and glider vertical temperature gradients, i.e., $\frac{\partial T}{\partial z}$, at the box endpoints and these temperature data are also used for averaging the temperature across the lateral box sides (Section 2.2.5). So, the temperature data used to estimate the curves in Figure 2.9 both contain mooring and glider data.

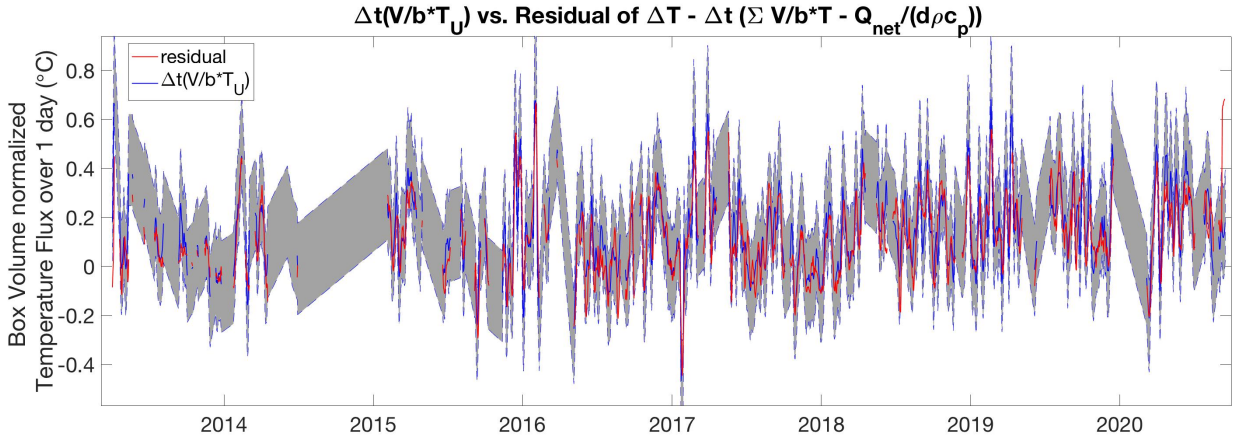

Figure 2.9: Vertical temperature fluxes at 50 m depth scaled by the volume of the box and applied over 1 day to yield units of temperature change (blue). Also shown is the residual of the horizontal temperature fluxes, the temperature fluxes through the surface, and the box-averaged temperature, i.e., the right-hand side of equation (24; red). Error bars of the temperature flux at 50 m depth use the geostrophic transport error (see Appendix B) and the temperature error at 50 m depth (see Appendix C).

In the 50 m vertical temperature flux estimate, it is assumed that all of the upwelling occurs uniformly throughout the box. Temporally averaged alongshore wind stress in southern California increases offshore (Figure 2.10; Winant and Dorman 1997). This implies that while upwelling occurs next to the coast, the increased upwelling favorable winds offshore drive

additional upwelling in other parts of the box away from the coastline. This suggests that the vertical velocities are somewhat distributed over the box, allowing us to use a horizontally averaged temperature at 50 m as a first approximation.

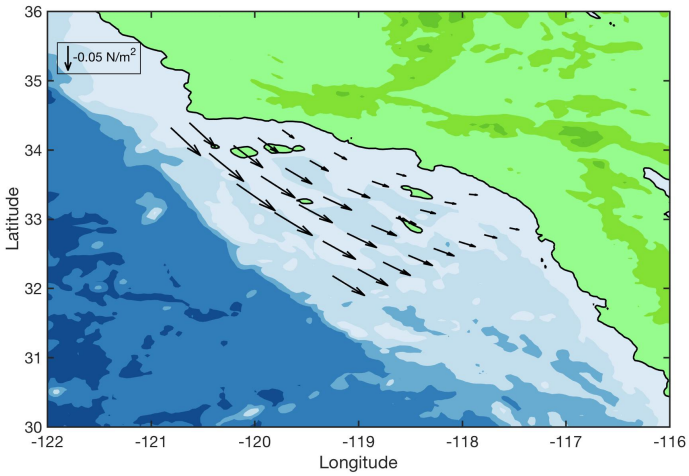

Figure 2.10: CCMPv2 wind stresses averaged over 2000 – 2021.

However, some modeling studies indicate that most of the upwelling in EBUS occurs close to the coast (Marchesiello and Estrade 2010; Jacox et al. 2011). To see if the spatially averaged temperature has an impact on the vertical temperature flux, the 50 m temperature is averaged over only the inshore region, i.e., within ~10 km from the coast. The inshore averaged temperature at 50 m depth is very similar to the 50 m box temperature average (not shown). Given the similarities between the two temperature time series, the vertical temperature flux through the bottom of the box using the inshore averaged temperature is insignificantly different from the blue curve in Figure 2.9.

2.4 CCUI Results and Discussion

The consistency of the CCUI against other upwelling measures in Section 2.3 along with the advantage that the CCUI offers in estimating the coastal APG from coastal tide gauges motivates using the CCUI as the estimate of upwelling going forward, i.e., for the vertical

transport at 50 m depth. The vertical transport from the CCUI will be analyzed over the annual cycle, interannual variability, and on synoptic timescales to characterize regional upwelling for both central and southern California. For these timescales of interest, the influence of the wind-driven forcing and the cross-shore geostrophic flows on the vertical transport will be assessed. It will be shown that over the timescales of interest, upwelling is largely driven by wind forcing, but upwelling is at times substantially modulated by cross-shore geostrophic flows and this is examined for the different timescales.

2.4.1 Annual Cycle

The annual cycle of vertical transport is inspected for central and southern California to assess the seasonal variability in upwelling. Then, the annual cycles of the geostrophic and Ekman contributions to this are analyzed to understand how these influences drive and modify seasonal upwelling. The annual cycles in this section are computed from 2000 – 2021.

2.4.1.1 Vertical Transport Annual Cycle

In both California regions, upwelling is year-round and the annual cycle in vertical transport shows a pronounced peak in upwelling in the spring with a relaxation in summer – early fall (Figure 2.11). The maximum upwelling value is larger off of central California than in southern California. The spring upwelling peak in early April in the north box is nearly contemporaneous with the spring upwelling peak in the south box. After the spring upwelling season, the CCUI has a minimum in vertical transport in July for both boxes. In the last two months of the calendar year, vertical transport increases in both boxes forming a secondary upwelling maximum.

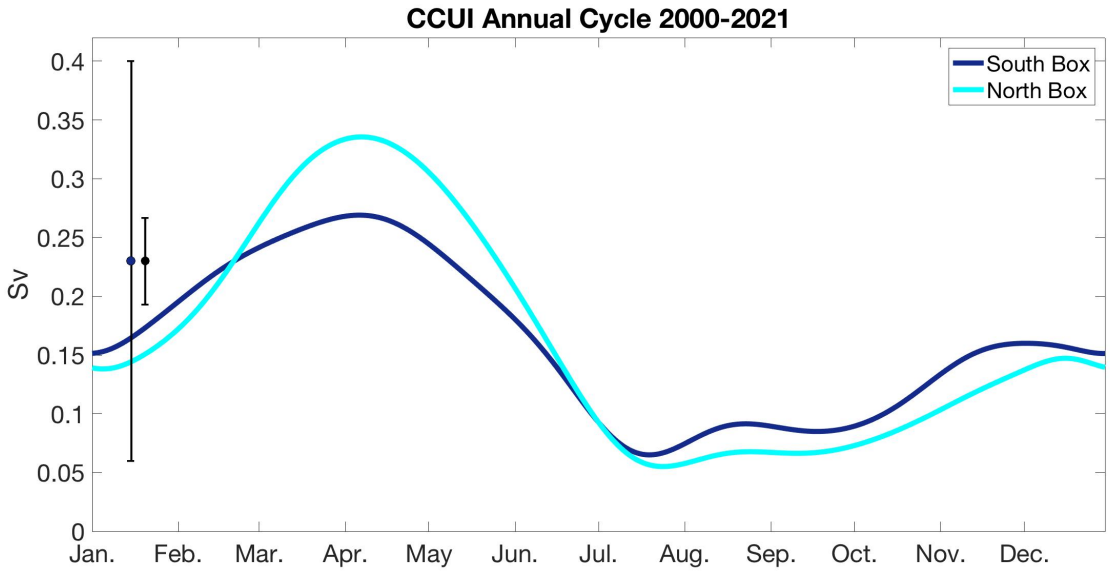

Figure 2.11: CCUI upwelling annual cycles, i.e., the vertical volume flux at 50 m depth. The smaller error bar does not include the error from the CMEMS data, which incorporates the time-mean depth-invariant component of dynamic height, while the larger error does. See Appendix B for a discussion on the error calculations.

Year-round upwelling that is strongest in spring is expected, as other regional upwelling measures have also reported this for southern California (Bakun 1973; Jacox et al. 2018; Zaba et al. 2020). It is also anticipated that upwelling is greater in central California than in southern California based on previous climatological transport estimates (Bakun 1973; Jacox et al. 2018). Unlike other climatological estimates for California, the results shown here exhibit a wintertime increase in vertical transport, whereas other upwelling measures indicate vertical transport is weakest in this time of the year (Bakun 1973; Jacox et al. 2018; Zaba et al. 2020). To further understand the behavior in the vertical transport annual cycle, the geostrophic and Ekman transport annual cycles are inspected.

2.4.1.2 Geostrophic Transport Annual Cycle

The annual cycles of the CCUI net geostrophic transport into the control volumes (i.e., negative values indicate geostrophic convergence, implying downwelling) are shown in Figure 2.12. For the south box the annual cycle remains negative throughout the year with greater

geostrophic transport between late-March and early-November (Figure 2.12). For the north box, the CCUI geostrophic annual cycle is negative from May – November and positive for the other months of the calendar year. Geostrophic convergence is relatively uniform in summer and the geostrophic transport is nearly the same for both regions in this season. Both annual cycles increase in fall – winter, with the north box annual cycle indicating geostrophic divergence between December and April. Geostrophic divergence is strongest in March and of nearly the same magnitude as the peak in the summertime geostrophic convergence. In southern California, the annual cycle remains negative but it is very low in January – early March and near 0 Sv in February. It is worth mentioning that within the margin of error, this annual cycle could be positive for the first 1 - 3 months of the year.

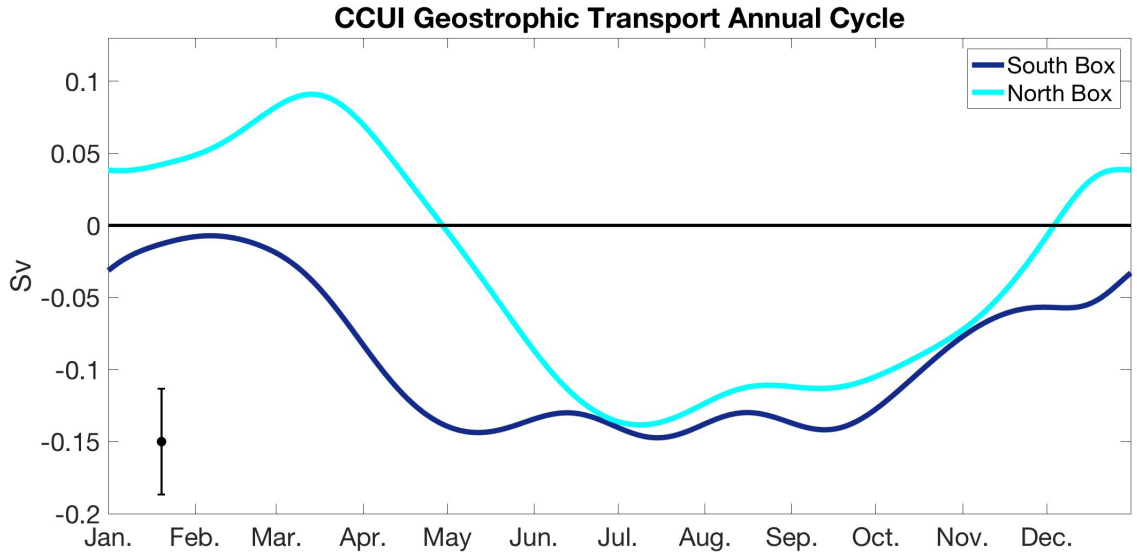

Figure 2.12: CCUI geostrophic transport convergence annual cycles for both California boxes. Negative values denote net geostrophic transport into the box, which implies downwelling. The CCUI error bar is constructed from the rms errors based on seasonally filtered data in Appendix B, which does not include the error from the CMEMS data, i.e., the product used to incorporate the time-mean depth-invariant component of dynamic height.

The wintertime behavior in the CCUI geostrophic component for central and southern California requires more attention. The sign of the calculated geostrophic transport is such that net negative geostrophic transport means geostrophic convergence, which is downwelling or a

weakening of any upwelling transport. In contrast, positive net geostrophic transport drives geostrophic divergence that results in greater upward vertical transport. Under this scenario, there is larger transport through the bottom of the box in order to balance the horizontal flows out of the box. The sign of the net geostrophic transport is important because of how it modifies upwelling, and in central California positive net geostrophic transport occurs for a third of the year (Figure 2.12).

The wintertime geostrophic divergence in central California implies a southward APG force, such that coastal sea level is higher at the northern of this box and lower at the southern end. Monthly mean absolute sea levels for the US west coast from tide gauges show a change in the alongshore sea level difference in the winter months over central and southern California (Hickey and Pola 1983). Typically, coastal sea level is higher in the south driving a poleward APG force, but in the winter months, i.e., January and February, the sea level over central California drives an equatorward APG force. This also happens in southern California but for a shorter period of time and with a weaker equatorward APG force. This wintertime weakening of the APG force, i.e., a more equatorward APG force, agrees with the more positive values in winter in the geostrophic transport annual cycles (Figure 2.12). This supports the results presented here in winter with positive or near 0 Sv geostrophic transport values in the annual cycles.

The positive geostrophic transport in the north box annual cycle lasts about twice as long as the reversal in the APG in Hickey and Pola (1983). The number of years over which the APG climatology in Hickey and Pola (1983) is constructed over is similar to the number of years used in the CCUI geostrophic annual cycle, but the record in Hickey and Pola (1983) began in 1950. The CCS has been shown to exhibit significant decadal variability in its physical and ecological

systems, and some of the differences in the duration and magnitude of the seasonal reversal in the APG may be due to this variability (Mantua et al. 1997; Di Lorenzo et al. 2005; Chhak and Di Lorenzo 2007).

Previous results of geostrophic convergence in central California indicate year-round geostrophic convergence that is strongest in late spring - summer (Jacox et al. 2018; Zaba et al. 2020). Some of the results presented here disagree with these previous studies because this study shows wintertime geostrophic divergence in central California, which suggests that there is a reversal in the wintertime APG in central California. This behavior is also possible in southern California, within the uncertainties of geostrophic transport. The wintertime dissimilarities between the observation and model results indicate differences in the coastal APG. Tide gauges used in this study and in Hickey and Pola (1983) are stationed *at* the coast, whereas the models used in Jacox et al. (2018) and Zaba et al. (2020) assimilate altimetry data that is *near* the coast. Thus, the differences in the coastal sea level estimates may explain the wintertime differences in geostrophic transport.

2.4.1.3 Ekman Transport Annual Cycle

The Ekman transport annual cycles show year-round Ekman divergence for both California coastlines consistent with other findings (Figure 2.13; Bakun 1973; Jacox et al. 2018; Zaba et al. 2020). The Ekman divergence in southern California is generally greater than that in central California, despite more vertical transport in central California during the spring upwelling season (Figure 2.11). If vertical transport was only dependent on Ekman transport, then the vertical transport annual cycle in southern California would be greater than that in central California during the upwelling season. The offshore Ekman transport in Figure 2.13 peaks in late-April and mid-May for southern and central California, respectively. A later peak in

the Ekman transport annual cycle in central California is expected based on previous investigations which found that upwelling may peak up to 1 – 2 months later in central California than in southern California (Bakun 1973; Jacox et al. 2018). The Ekman transport peak timing differs from the vertical transport peak timing by about 1.5 months for central California and by about 3 weeks for southern California. For both boxes, the vertical transport leads the Ekman transport. This shows that the geostrophic transport not only modifies the strength of upwelling, but also the seasonality.

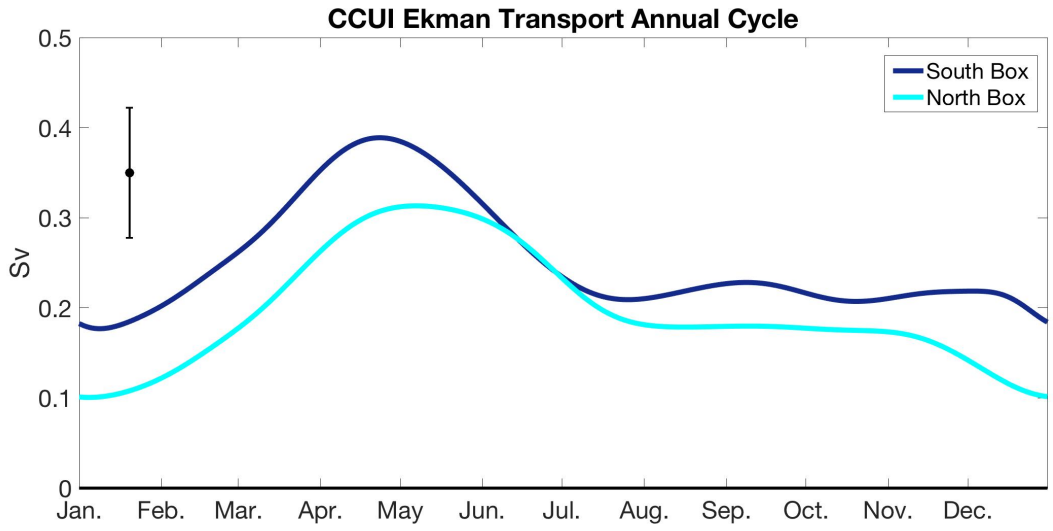

Figure 2.13: CCUI Ekman transport annual cycles for both boxes. Positive values denote Ekman transport out of the box, which implies upwelling. The CCUI Ekman transport error bar uses the rms errors from seasonally filtered data (Appendix B).

In southern California, the sign in the Ekman and geostrophic transport annual cycles oppose one another, but the larger magnitudes in the Ekman annual cycle over the geostrophic annual cycle result in positive vertical transport throughout the calendar year. In central California, the vertical transport annual cycle is also always positive, but both the Ekman and geostrophic components drive upwelling for the first four months of the calendar year. The annual cycles of the vertical, geostrophic, and Ekman transport showed that upward transport is largely due to Ekman divergence, while the geostrophic component mostly has an opposing

effect. Thus, on seasonal timescales the presence of upwelling is caused largely by the wind, but the magnitude and timing of upwelling is modified substantially by the geostrophic transport.

2.4.2 Interannual Variability

Interannual variability in upwelling is inspected for central and southern California to assess year-to-year changes in upwelling. Then, the low-frequency variability in the geostrophic and Ekman contributions are analyzed to understand how these influences drive and modify interannual changes to upwelling. For this section, the low-frequency signals in the vertical, geostrophic, and Ekman transport are assessed by removing the annual cycle and low-pass filtering the anomalies over 100 days.

2.4.2.1 Vertical Transport Anomalies

The low-frequency vertical transport anomalies show significant variability over the last 20 years and there are differences at times in this variability between the north and south boxes (Figure 2.14a). A notable period in the interannual variability is 2011 – 2018 when the vertical transport anomalies in central California are mostly negative and the annual averages are also negative. In southern California this is over a shorter period of time with negative annual averages persisting from 2014 – 2017.

This notable period includes the 2014 marine heatwave and the 2015 – 2016 El Niño. The negative vertical transport anomalies are some of the largest in the record for central California, and in southern California the anomalies remain persistently negative from fall 2013 – fall 2015. The transition in late 2015 from negative to positive upwelling anomalies occurs in both boxes. Weaker upwelling in 2014 - 2015 was also reported by Zaba et al. (2020) for both central and southern California, but this was less persistent and lasted for a shorter period of time. Zaba et al.

(2020) found that the transition to unusually strong upwelling favorable conditions during the El Niño occurred in summer 2015, while in Figure 2.14a this took place several months later.

Both 2014 and 2015 contained anomalous poleward flow in southern California that was discussed in Chapter 1. Some of the poleward flow anomalies were attributed to less upwelling

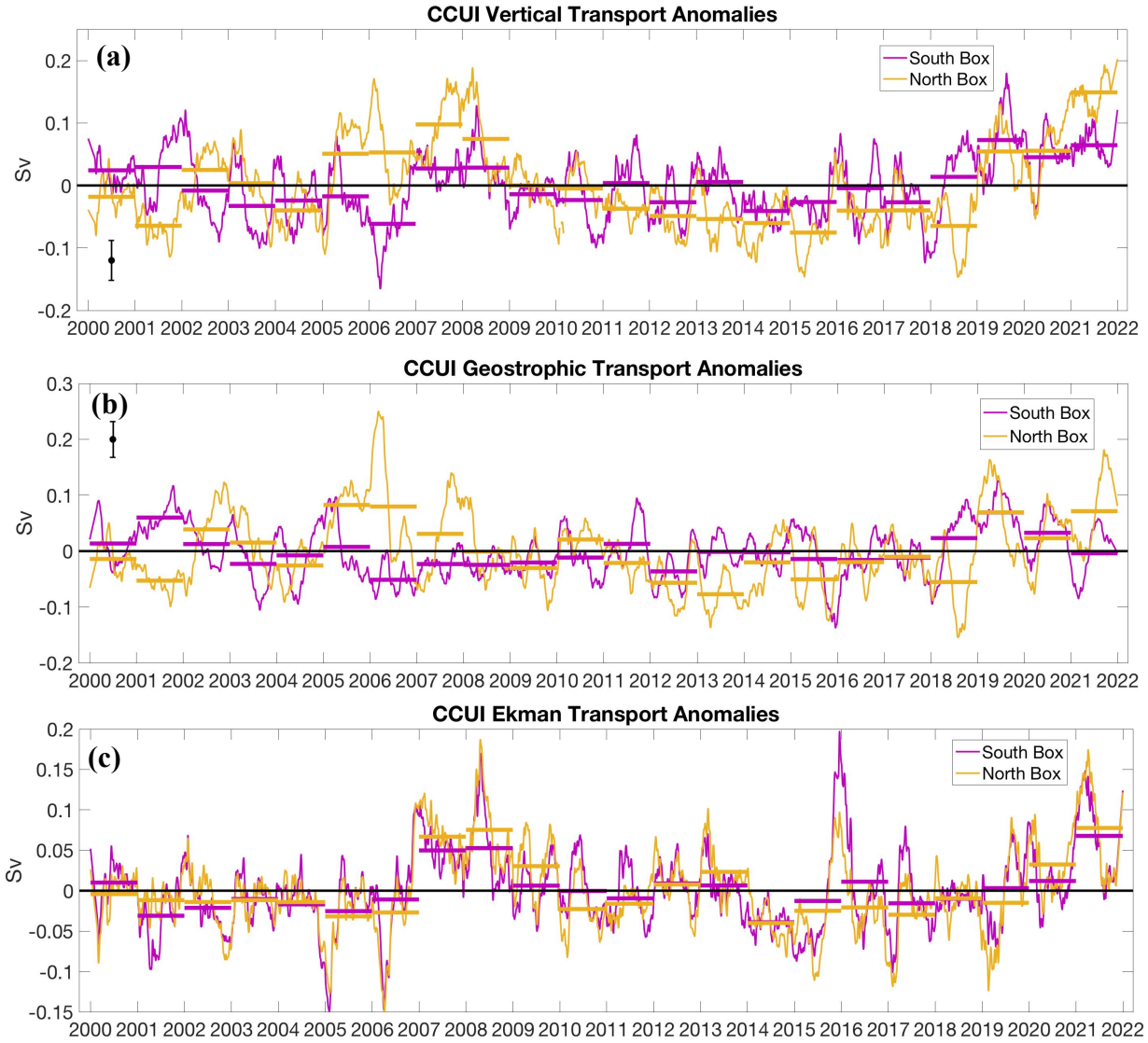

Figure 2.14: CCUI (a) vertical, (b) geostrophic, and (c) Ekman transport anomalies for the north and south boxes. Horizontal bars denote annual averages over the calendar year. Anomalies are based on removing the annual cycle that is calculated over 2000 – 2021 and the anomalies are low-pass filtered over 100 days. Positive vertical transport anomalies in (a) denote more upwelling into the box, positive geostrophic transport anomalies in (b) indicate more geostrophic transport out of the box which means upwelling, and positive Ekman transport anomalies in (c) are associated with more Ekman transport out of the box which means upwelling. Error bars in (a) and (b) show the depth-independent time-varying geostrophic transport error using the rms errors based on data that was low-pass filtered over 100 days (Appendix B).

favorable winds, while in late 2015 a large increase in the poleward APG force was responsible for the poleward flow and the northward advection of more tropical waters. It is suspected that both weaker upwelling favorable winds and at times an enhanced poleward APG force contributed to weaker vertical transport in the years of the large-scale climate phenomena. The weaker vertical transport at this time motivates investigating the interplay of the geostrophic and Ekman contributions to the reduced upwelling.

2.4.2.2 Geostrophic Transport Anomalies

The lower annual averages in the vertical transport anomalies between 2011 and 2018 in the north box can be explained by the geostrophic transport anomalies (Figure 2.14b). In this period, the geostrophic anomalies are persistently negative, i.e., more geostrophic convergence into the box, from 2011 – mid 2014, and the annual averages are negative for all years in this period. The south box also has negative annual averages for most years in this period, but the averages tend to be smaller and the anomalies are not persistently negative. During the marine heatwave and the El Niño, the magnitude of the geostrophic, i.e., downwelling, anomalies are largest in fall 2015 for both boxes. Results from Chapter 1 revealed that there was a stronger poleward APG force at this time that reflected the heightened equatorial activity causing poleward propagating CTWs.

Table 2.4: CCUI statistics for the 100-day low-pass filtered net geostrophic and Ekman transport anomalies between the north and south boxes. The anomalies are constructed by removing the annual cycle, where the annual cycle is computed over 2000 – 2021. The correlation is at a lag of 0 days and this is provided along with the 95% confidence interval. The rms differences are reported between the geostrophic/Ekman anomalies.

	Correlation ± 95% CI	**RMS Difference (Sv)**
Geostrophic Transport Anomalies	0.09 ± 0.01	0.079
Ekman Transport Anomalies	0.85 ± 0.01	0.028

Over the record, the geostrophic transport anomalies in the north and south boxes show differences in the low-frequency variability, despite sharing SSH off of Point Conception in the CCUI construction. The geostrophic anomalies in the California boxes are not correlated with each other and the rms difference is large (Table 2.4). Despite the agreement in the geostrophic anomalies at the end of 2015 when both boxes were influenced by remote forcing, the low correlation between the north and south box geostrophic anomalies suggests that the two sections of coastline are also influenced by more local changes in the APG.

The geostrophic and vertical transport anomalies in central California are well correlated with each other, while in southern California the correlation is moderate (Table 2.5). About 56% percent of the variance in vertical transport in central California can be explained by the geostrophic anomalies. This indicates the importance of the geostrophic transport in moderating the low-frequency upwelling variability off of California.

Table 2.5: CCUI statistics for the 100-day low-pass filtered net geostrophic and Ekman transport anomalies with the vertical transport anomalies. The anomalies are constructed by removing the annual cycle where the annual cycle is computed over 2000 – 2021. The correlation is at a lag of 0 days and this is provided along with the 95% confidence interval. The rms differences between the geostrophic/Ekman and vertical transport anomalies are included.

	Correlation ± 95% CI	**RMS Difference (Sv)**
North Box Geostrophic Transport Anomaly	-0.74 ± 0.01	0.051
North Box Ekman Transport Anomaly	0.44 ± 0.02	0.068
South Box Geostrophic Transport Anomaly	-0.54 ± 0.02	0.048
South Box Ekman Transport Anomaly	0.58 ± 0.02	0.047

2.4.2.3 Ekman Transport Anomalies

In both boxes, Ekman transport anomalies and the annual averages of these anomalies also contributed to reduced upwelling at times between 2011 and 2018 (Figure 2.14c). Weaker,

i.e., more negative, Ekman anomalies are most apparent from late 2013 – fall 2015. The persistently less Ekman divergence in this period coincides with the persistently weaker vertical transport. Not only did the weaker upwelling favorable winds drive less upwelling, the results from Chapter 1 showed that they also drove poleward flow anomalies. The negative vertical transport anomalies change sign in late 2015 contemporaneously with the transition from negative to positive Ekman anomalies. Thus, this transition to greater upwelling was driven by upwelling favorable winds.

Unlike the geostrophic record, the Ekman anomalies in the two California boxes indicate similar variability over the record. The Ekman anomalies are highly correlated with each other and the rms difference is small (Table 2.4). This suggests that the decorrelation scale in the low frequency wind field is larger than the alongshore length over the two boxes.

The vertical transport anomalies and the Ekman transport anomalies in central California are not well correlated with each other, with the Ekman anomalies explaining only about 20% of the variance in the vertical transport anomalies and the rms difference is higher between the two anomaly records (Table 2.5). In southern California, the Ekman anomalies are moderately correlated with the vertical transport anomalies. For this box, the Ekman and geostrophic anomalies explain nearly the same amount of variance in low frequency upwelling. Thus, the year-to-year changes in upwelling are dominated by the geostrophic signal in central California, and in southern California the geostrophic and Ekman flows are nearly equally influential.

2.4.3 Synoptic Upwelling Events

Synoptic upwelling events are inspected for central and southern California to characterize upwelling on synoptic timescales. The method for upwelling event detection was described in Section 2.2.6 and the event statistics computed from these identified events will be

presented with respect to the long-term means and interannual variability during the 2014 marine heatwave and the 2015 – 2016 El Niño. Then, the relative roles of the wind-driven forcing and the APG on synoptic timescales are discussed.

2.4.3.1 Long-Term Averages

The upwelling event statistic calculations were explained in Section 2.2.6, and the three statists calculated are event intensity, event duration, and the number of upwelling events in a year. The first statistic, event intensity, is fairly similar across both California boxes (Table 2.6). Likewise, the event intensity standard deviations are similar for both boxes. The record-long mean in the event duration, i.e., the length of the upwelling phase, for both boxes is a little more than one week and most events last between 4 and 12 days long. The average number of upwelling events in a year is nearly the same in both central and southern California. The spreads in the number of events in a year are small, namely, the standard deviations are less than two events per year for both boxes.

Table 2.6: CCUI high-frequency statistics over 2000 – 2021 for the north and south boxes. σ is the standard deviation.

	Average Event Intensity, ± 1 σ	**Average Event Duration, ± 1 σ**	**Average Number of Events per Year, ± 1 σ**
North Box	0.242 ± 0.15 Sv	8.4 ± 3.5 days	18.6 ± 1.9
South Box	0.273 ± 0.16 Sv	8.3 ± 3.8 days	20.4 ± 1.6

2.4.3.2 Interannual Variability

The low-frequency interannual variability in the upwelling event statistics is assessed for 2014 and 2015 when there were the large-scale climate phenomena. In central California, the annual averages of event intensity are below the long-term mean in 2014 and 2015, as well as all of the annual averages between 2011 and 2018 (Figure 2.15a). The weaker event intensities in these years coincide with the weaker low frequency variability in vertical transport that was

presented in Section 2.4.2a. This decrease in the event intensities is not seen in the south box. The other two event statistics, event duration and the number of events in a year, are not anomalous in 2014 and 2015 for either of the boxes. It is emphasized that in this analysis, all upwelling events in a year were considered for the event statistics. Chapter 3 also investigates synoptic upwelling events, but Chapter 3 only uses events that occur during the upwelling season, i.e., February – June. Event statistics calculated on these upwelling events indicate weaker and shorter synoptic upwelling events in 2014 and 2015. Thus, on synoptic timescales

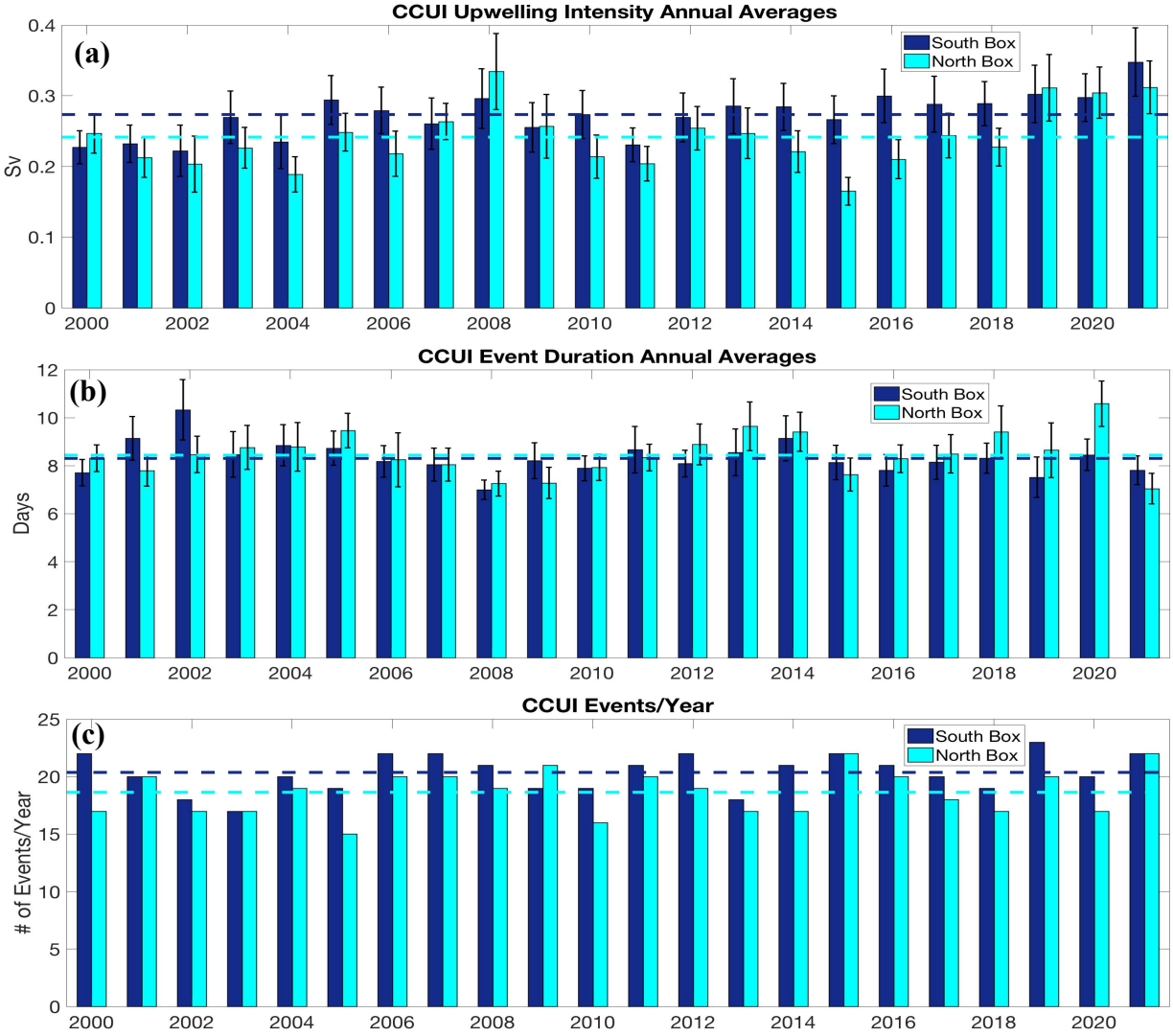

Figure 2.15: CCUI annual averages of upwelling event statistics for (a) the event intensity, (b) the event duration, and (c) the number of events per year. Horizontal dashed lines are the mean over 2000 – 2021. Error bars in (a) and (b) denote the standard error of the mean.

upwelling was altered more so during the upwelling season than in the relaxation season during the 2014 marine heatwave and the 2015 – 2016 El Niño.

2.4.3.3 Wind-Driven Forcing vs. Pressure Gradients

For synoptic upwelling, intermittency in the wind field and propagating pressure gradients can both generate and modify upwelling events. Both mechanisms can shoal or suppress isopycnals and alter the local circulation as part of the upwelling-relaxation cycle. In both California regions, intermittency in the wind field has a smaller rms difference and accounts for a much larger amount of percent variance in the upwelling events than propagating pressure gradients (Table 2.7).

Table 2.7: Rms difference and percent variance from r^2 using the band-pass filtered CCUI. Positive lag means geostrophic/Ekman transport leads vertical transport. The band-pass filter is over 7 – 100 days.

	Rms Difference (Sv)	**Percent Variance**	**Lag (days)**
North Box Geostrophic & Vertical Transport Anomalies	0.158	21%	4
North Box Ekman & Vertical Transport Anomalies	0.083	64%	1
South Box Geostrophic & Vertical Transport Anomalies	0.174	7%	1
South Box Ekman & Vertical Transport Anomalies	0.076	71%	0

In central California, there is a marginal decrease in the rms difference and a slight increase in the percent variance explained by propagating pressure gradients, i.e., the geostrophic component of vertical transport, than in southern California. Unlike the Ekman term, which has no lag with the vertical transport in southern California, the geostrophic component has a minimal lag in southern California that increases by 3 days in central California. This suggests that the APG field is modified south of the southern box, i.e., off of Baja California, and these pressure gradients are generated close enough to southern California where they only take a day

to reach the south box. Based on this lag information, the speed at which these propagating pressure gradients reach central California is ~124 - 186 km/day, which is consistent with CTW phase speeds for southern California and Baja California (Enfield and Allen 1980; Enfield and Allen 1983; Hickey et al. 2003). Propagating pressure gradients account for a small fraction of the variance in synoptic upwelling, with most of the fluctuations in vertical transport due to wind-driven changes.

The band-passed geostrophic transport anomalies over the two boxes are not well correlated with each other (Table 2.8). While this correlation is higher than the correlation at low frequencies, even at synoptic timescales there are local influences on the coastal APG in each of the California regions altering the net geostrophic transport. In contrast, the band-passed Ekman transport anomalies are well correlated across the two boxes indicating that wind-driven synoptic upwelling events tend to have alongshore spatial scales encompassing the lengths of the two boxes.

Table 2.8: CCUI statistics for the 7 – 100 days band-pass filtered net geostrophic and Ekman transport anomalies between the north and south boxes. The correlation is at a lag of 0 days and this is provided along with the 95% confidence interval. The rms differences are reported between the north and south box geostrophic/Ekman anomalies.

	Correlation ± 95% CI	**RMS Difference (Sv)**
Geostrophic Transport Anomalies	0.43 ± 0.02	0.085
Ekman Transport Anomalies	0.81 ± 0.01	0.083

The upwelling event statistics showed similar statistical mean values of upwelling strength, upwelling length, and the number of events in both California boxes. Upwelling events are largely driven by forcing from the wind field, but remote forcing such as off of Baja California can modify synoptic upwelling.

2.4.4 CCUI Summary

A key result of examining vertical transport off of central and southern California over multiple timescales was the respective roles of wind-driven upwelling and coastal APGs at the different timescales of interest. The Ekman transport is responsible for driving the seasonality of upwelling, but the geostrophic transport shifts the upwelling season to occur earlier and weakens the vertical transport magnitudes during the upwelling season. The geostrophic transport explains much of the percent variance on interannual timescales in central California, whereas in southern California both the geostrophic and Ekman transport anomalies nearly equally explain the same amount of percent variance. Lastly, the wind-driven forcing explained most of the variance in the vertical transport on synoptic timescales.

2.5 Heat Budget Results and Discussion

The DM and CCE2 ADCP data measured more poleward flow close to the coast in the years of large-scale climate phenomena, as reported in Chapter 1. Did the poleward flow anomalies during the 2015 - 2016 El Niño drive a greater alongshore temperature flux? If so, was the temperature flux going into the box through the south side matched by the temperature flux exiting the box through the north side or was there an alongshore convergence into the box? To address these questions, the horizontal advective temperature fluxes are examined in relation to the large-scale climate phenomena followed by the vertical heat flux. Then, the net advective temperature flux, i.e., the sum of terms (2) – (5) in equation (22), is assessed alongside the change in temperature over the box, i.e., term (1) in equation (22).

2.5.1 Horizontal Heat Fluxes

The 2014 and 2015 anomalous poleward flow presented in Chapter 1 is expected to have caused a greater poleward temperature flux. If there was a greater temperature flux through the

south side than through the north side of the control volume, then this would have encouraged warming over the box, i.e., a larger term (1) in equation (22). To test this, the horizontal temperature fluxes, which are scaled by the volume of the box and applied over 1 day to yield units of temperature change, are inspected in the years of the large-scale climate phenomena (Figure 2.16). The sign of the horizontal temperature fluxes in Figure 2.16 are dependent on the sign of the volume transport, since transport is multiplied with an always positive temperature value. Generally, northward temperature fluxes through the north and south sides are strongest in summer, and this is when the temperature flux through the west side is strongest offshore.

During the years of the large-scale climate phenomena, a broken glider conductivity sensor in the second half of 2014 limits coverage of the horizontal temperature fluxes. In winter 2013/2014, there is evidence of an enhanced onshore temperature flux through the west side despite intermittent sampling (Figure 2.16). Zaba et al. (2020) also report anomalous onshore heat advection that peaks in January 2014. In this winter, there is a poleward temperature flux through the north and south sides. In the second half of 2014, there are large amplitudes in the poleward temperature flux through the north side causing heat advection out of the box.

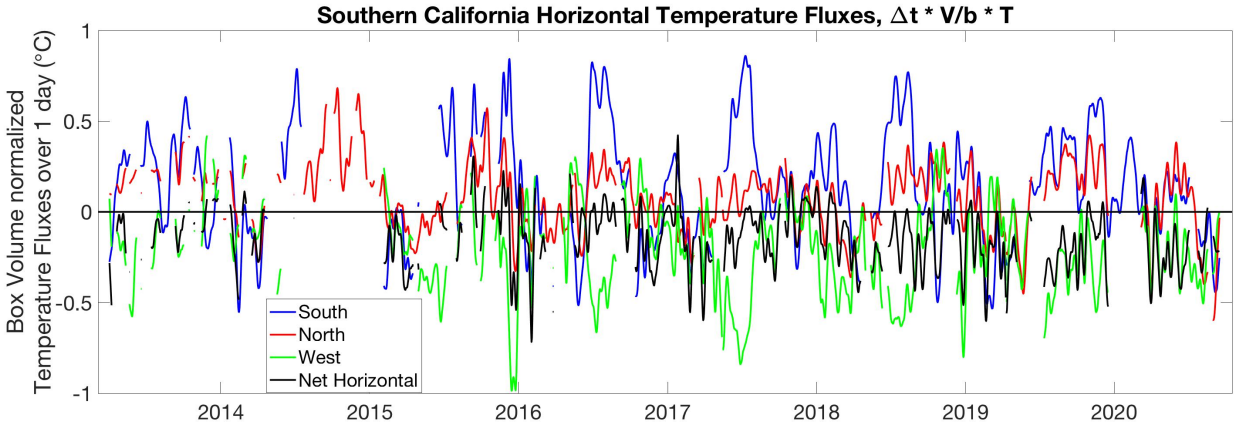

Figure 2.16: Horizontal temperature fluxes scaled by the volume of the box and applied over 1 day to yield units of temperature change. Positive values in the north (red) and south (blue) sides timeseries denote a poleward temperature flux, while positive values in the west (green) side timeseries represent an onshore temperature flux. Negative values in the net horizontal temperature flux (black) act to decrease temperature over the box.

However, due to the sensor failure it is unknown if this is compensated for by lateral temperature fluxes into the box through the other two sides. The horizontal temperature flux timeseries in 2015 illustrates multiple episodes of large poleward temperature flux through the south side and an increased northward temperature flux through the north side. The alongshore temperature fluxes show an alongshore convergence into the box. This is similarly seen in Zaba et al. (2020) over summer – fall 2015. The greater onshore temperature flux through the west side during the marine heatwave and the more northward temperature flux during the El Niño were also seen off of central California (Chao et al. 2017).

The net horizontal temperature flux, i.e., the horizontal flux convergence, is determined as the sum of the horizontal advective terms in the heat budget (black line in Figure 2.16). Positive values in this curve indicate that the horizontal temperature fluxes accumulate heat in the control volume. The net horizontal temperature flux is typically negative with largest magnitudes in spring during the upwelling season. The negative net horizontal temperature flux is expected since upwelling is year-round, i.e., there is a horizontal volume flux divergence (see Section 2.4.1), and the volume fluxes are multiplied by positive temperatures. By design the volume budget balances, so the horizontal volume flux divergence, and hence the horizontal temperature flux divergence, is compensated by a vertical volume flux convergence, and hence a vertical temperature flux convergence at 50 m depth. This vertical temperature flux is discussed more in the next section. In summer/fall, there can be heat advected into the box, but these magnitudes are small and these positive values in Figure 2.16 are largely due to poleward heat advection through the south side. In general, the horizontal temperature fluxes act to reduce the box-averaged temperature.

2.5.2 Vertical Temperature Flux

The 50 m vertical temperature flux scaled by the volume of the box and applied over 1 day to yield units of temperature change is positive most of the time due to typical year-round upwelling (Figure 2.17). Generally, this term has larger magnitudes during the upwelling season when vertical transport is strongest. Since the vertical transport relies on contemporaneous observations at all of the box endpoints, the vertical temperature flux in 2014 and 2015 cannot be approximated during much of this time. Starting in winter 2015/2016, the temporal coverage in the vertical temperature flux improves and the vertical temperature flux changes sign several times in this winter. This behavior is analyzed on event timescales with the horizontal temperature fluxes and is related to remote, i.e., equatorially-driven CTWs, and local, i.e., wind-driven, forcing.

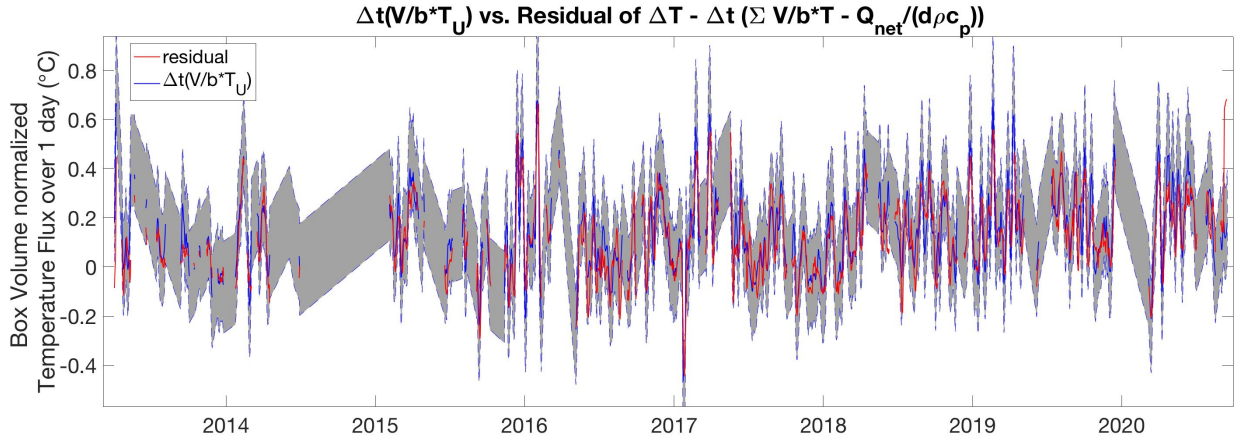

Figure 2.17: Vertical temperature fluxes at 50 m depth scaled by the volume of the box and applied over 1 day to yield units of temperature change (blue). Also shown is the residual of the horizontal temperature fluxes, the temperature fluxes through the surface, and the box-averaged temperature, i.e., the right-hand side of equation (24; red). Error bars of the temperature flux at 50 m depth use the geostrophic transport error (see Appendix B) and the temperature error at 50 m depth (see Appendix C).

When there is downward and near 0 temperature fluxes in fall 2015 (Figure 2.17), these periods coincide with large northward temperature fluxes through the north and the south sides of the box (Figure 2.16). In fall 2015, there were multiple CTWs that caused positive SSHa as they propagated poleward from the equator (Figure 1.11). These coastally trapped signals raised

sea levels near the coastline and drove poleward geostrophic flow due to the cross-shore sea level difference. As these downwelling CTWs propagate through the control volume they subduct isopycnals and this drives a poleward baroclinic flow. This explains the northward temperature fluxes through the north and south sides of the box. As the CTW events enter the control volume and propagate through the *south side,* this causes more poleward barotropic and baroclinic flows that lead to more of a horizontal volume flux convergence. The increased horizontal volume flux convergence is compensated by a larger vertical volume flux divergence, and hence there is a greater downward temperature flux at 50 m depth.

As the CTWs propagate through the box and exit through the *north side*, this causes higher SSH at the northeast box endpoint than at the southeast box endpoint. Thus, there is an equatorward APG force driving geostrophic divergence, i.e., more geostrophic transport out of the box. So, as the CTWs enter the control volume through the *south side* they drive geostrophic convergence and as the CTWs exit through the *north side* they drive a geostrophic divergence. The geostrophic divergence drives a greater offshore temperature flux through the west side of the box (Figure 2.16) and a larger upward temperature flux through the bottom of the box (Figure 2.17). This demonstrates how the remote forcing influences the vertical temperature flux during the 2015 – 2016 El Niño.

2.5.3 Volume-Averaged Temperature Change Anomalies and Net Advective Anomalies

Several studies have reported unusually warm conditions along the US west coast persisting over 2014 and 2015 during the marine heatwave and the El Niño (Bond et al. 2015; Di Lorenzo and Mantua 2016; Robinson 2016; Zaba and Rudnick 2016; Chao et al. 2017; Gentemann et al. 2017). The warming in these years could be due to surface heating, advective

processes, or both. The temperature changes over southern California are examined alongside net heat advection, i.e., both the horizontal and vertical advective components, into the control volume for the years of the large-scale climate phenomena. As a reminder, the volume flux is balanced exactly prior to computing the advective terms in the heat budget equation.

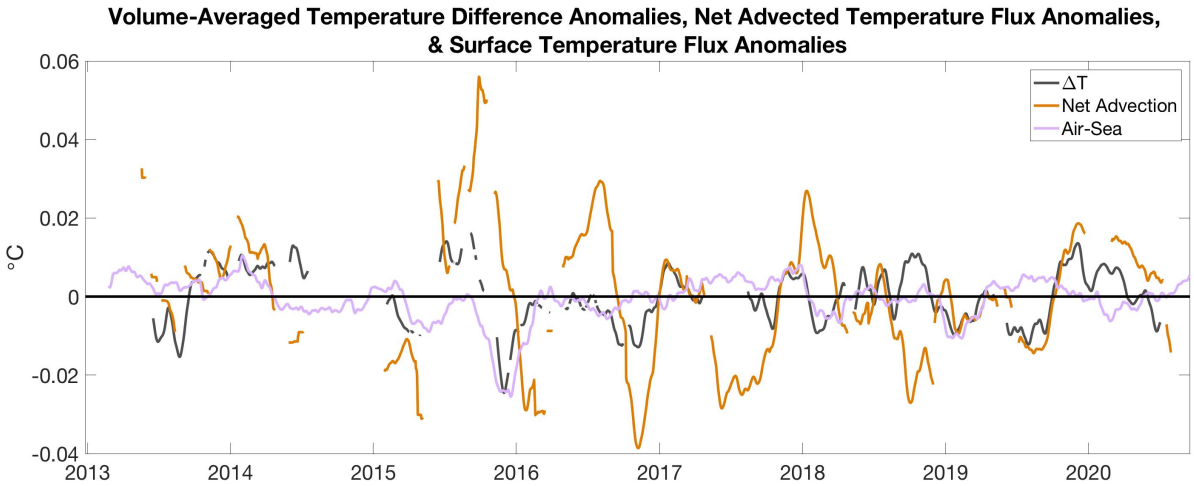

Figure 2.18: Anomalies of the volume-averaged temperature change over the box along with the net advected temperature anomalies and the air-sea temperature flux anomalies. Anomalies are constructed based on removing the annual cycle which is computed over 2013 – 2020 and the anomalies are low-pass filtered over 80 days.

Overlapping observations in time at the multiple sites are sparse in 2013 – 2015, with only short periods of information available from the analysis of the temperature fluxes into southern California (Figures 2.16 and 2.17). However, some notion of warming is apparent by the positive ΔT anomalies in winter 2013/2014 alongside positive anomalies in the net heat advection (Figure 2.18). Onshore absolute temperature fluxes through the west side contribute to the warming in the box at this time (Figure 2.16). There is also an anomalous downward temperature flux through the surface (Figure 2.18). These results agree with model data in southern California that found that the warming in winter 2013/2014 was due to the air-sea temperature flux in addition to advection from the west (Zaba et al. 2020). Off of central California, model data also showed anomalous warming in winter 2013/2014 and this was

equally due to atmospheric forcing and advection of warmer waters from the west (Chao et al. 2017).

Another notable period of warming during the large-scale climate phenomena is in summer - fall 2015/2016. The increase in average temperature over the box is forced by large positive anomalies in the net advected temperature fluxes, and the net advected temperature fluxes are caused by enhanced poleward temperature fluxes through the south side (Figure 2.16). This was attributed to remote forcing from poleward propagating CTWs (Figure 1.10). Model data revealed advection from the south caused the winter warming off of central California (Chao et al. 2017), whereas model data in southern California suggest both atmospheric forcing and advection from the south drove increased changes in temperature (Zaba et al. 2020).

Observations of the volume-averaged temperature changes and advected temperature fluxes in southern California are not continuous, but brief periods were captured during the 2014 – 2016 warming containing the 2014 marine heatwave and the 2015 – 2016 El Niño and these periods reveal warming in agreement with other studies. Warming during the marine heatwave was associated with atmospheric forcing and onshore temperature fluxes through the west side of the box, while warming during the El Niño was driven by larger poleward temperature fluxes through the south side of the box. When temperature changes over the box are anomalously positive, these anomalies are often associated with increased temperature fluxes into the box demonstrating that advection is an important mechanism for causing warming in southern California.

2.6 Conclusion

This chapter introduced a new upwelling index for southern California that utilizes in-situ measurements. This work expanded upon previous efforts of approximating upwelling in

southern California from observations (Roemmich 1989; Bograd et al. 2001) where here we include high-frequency variability in the vertical transport. The method for constructing the upwelling index was applied for the coast off of central California to compare upwelling from two regions of California and this method can be tried in other EBUS. The CCUI was shown to be a promising new upwelling index that can be a useful tool for scientists in evaluating the physical forcing in coastal upwelling regions. The volume transport was also an important part of the southern California heat budget, and the heat budget identified the drivers of the anomalous warming in southern California during the years of large-scale climate phenomena.

First, this chapter computed the volume budget over the upper 50 m layer for southern California, quantified the uncertainty in the vertical transport, and derived a new upwelling index. Observations in southern California were used to perform a volume budget and the error analysis on the vertical transport derived from the volume budget were carefully considered in order to quantify the various sources of error. The error analysis warranted making the Coriolis parameter the same over the box and simplifying the dynamic height calculations at the inshore box endpoints to use only the inshore depth-independent fluctuations from tide gauges and the mean CMEMS ADT for computing net geostrophic transport. This geostrophic transport estimate was used with the Ekman transport to construct the new upwelling index, the CCUI. The CCUI provided a more complete timeseries of vertical transport through the 50 m level in southern California with a longer upwelling estimate and fewer gaps in the temporal coverage. The upwelling index proposed here utilizes already existing data products that provide data at near real time. This does not require running a model and this method is capable of capturing upwelling events on weekly timescales.

Prior to analyzing the CCUI timeseries, this new upwelling index was validated against other upwelling measures. The CCUI was moderately correlated with CASE and CUTI in both California regions (Tables 2.2 and 2.3), and like the CCUI, both CASE and CUTI account for cross-shore geostrophic influence and alongshore gradients in the cross-shore wind stress on the vertical transport. If the CASE and CUTI uncertainties are similar to the CCUI uncertainty, then these other upwelling estimates generally agree with the CCUI within the uncertainties in the vertical transport based on the rms differences.

The CCUI and its geostrophic and Ekman constituents were assessed over different timescales. In the annual cycle, there was year-round upwelling, where upwelling was defined by the volume flux across 50 m depth. Upwelling intensified in March – May with a secondary upwelling increase over the winter months. Qualitatively, the spring upwelling was forced by the wind stress, whereas the wintertime increase in upwelling was related to more geostrophic divergence. Weaker upwelling occurred during the 2014 marine heatwave and the 2015 - 2016 El Niño as a result of persistently weaker upwelling favorable winds. There were significant onshore geostrophic transport anomalies in late 2015 related to the large poleward APG from remotely-forced CTWs, but this was countered by a wind switch to greater upwelling favorable winds. The synoptic upwelling event statistics were very similar for both central and southern California. Upwelling event intensities, i.e., the range of vertical transport during upwelling, were about 0.26 Sv on average over the record, the upwelling phase of upwelling events typically lasted 8 days long, and generally there were 20 upwelling events in a year.

The vertical transport annual cycle was largely driven by the seasonality in the Ekman transport, but the strength of the vertical transport annual cycle and the timing of the upwelling season were substantially modified by the geostrophic transport. At low frequencies, the

geostrophic transport in central California explained 55% of the vertical transport variance, while in southern California both the geostrophic and Ekman transport explained nearly equal amounts of the percent variance. The difference in the variance explained by the geostrophic transport in central and southern California demonstrates the importance of local influences on the coastal APG on interannual timescales. On synoptic timescales, upwelling was largely forced by Ekman transport with the wind forcing explaining about 70% in the vertical transport variance. Remotely forced propagating pressure gradients, e.g., generated off of Baja California, accounted for about 20% or less of the variance in vertical transport, and the implied phase speeds of these disturbances agreed with known coastal trapped wave speeds from this region. At the multiple timescales of interest, the results showed that both the wind field and the coastal pressure gradients are important for driving and modifying coastal upwelling and that both of these factors should be considered when approximating upwelling.

Lastly, the heat budget was examined for the years of large-scale climate phenomena. Temperature changes in southern California associated with the 2014 marine heatwave were driven by onshore advection of heat through the west side of the box as well as increased surface heating. Temperature changes in southern California during the 2015 - 2016 El Niño were driven by northward heat advection through the south side of the box that was not matched by the poleward heat transport through the north side of the box. The heat budget results signified the pathways for how warmer waters entered southern California during the 2014 marine heatwave and the 2015 – 2016 El Niño.

The results of this chapter emphasized the roles of the physical processes that drive upwelling. This includes the wind-driven upwelling and cross-shore geostrophic transport which are important factors controlling physical, biogeochemical, and ecological variability in EBUS.

Monitoring these fluctuations at higher frequencies, i.e., daily - weekly, and over long periods of time is useful for understanding long-term variability of upwelling while also capturing time scales of interest that stimulate biological responses like recruitment and retention. Furthering our understanding of upwelling through its physical drivers and utilizing observational records addresses many of the objectives and priorities of Climate and Ocean: Variability, Predictability and Change (CLIVAR), which has a research focus specifically on EBUS. The highly productive ecosystems fostered by EBUS coupled with their close proximity to coastal human populations makes them a societally relevant research topic. Modeling of these systems is important for their impact on climate simulations (Large and Danabasoglu 2006), but large biases in the models persist and argue the need for a better understanding of the physical processes in EBUS (Toniazzo and Woolnough 2014; Balaguru et al. 2021; Farneti et al. 2022). The work presented here addresses some of these concerns by examining the role of geostrophic convergence on upwelling and helps further the knowledge needed to improve upwelling models.

2.7 Acknowledgements

Support for the CCE2 mooring, the CORC3 mooring, and the CCE2 gliders come from the NOAA Ocean Observing and Monitoring Division and Ocean Acidification Program (NA15OAR4320071). Data from the CCE2 mooring is collected and made freely available by the international OceanSITES project at ftp://data.ndbc.noaa.gov/data/oceansites/DATA/CCE2/. CORC3 mooring data are publicly available through the data archive at NOAA NCEI. CCE2 glider data which are part of the CORC project are online at https://spraydata.ucsd.edu/projects/CORC/. The Instrument Develop Group at Scripps Institution of Oceanography is thanked for operating the gliders used in this chapter and for processing the glider data. CCMP Version-2.0 vector wind analyses are produced by Remote Sensing Systems and data are available at www.remss.com. NDBC winds are made publicly available by NOAA at https://www.ndbc.noaa.gov/. Tide gauge data from the UHSLC can be obtained at https://uhslc.soest.hawaii.edu/. CMEMS products used in this chapter can be found at https://data.marine.copernicus.eu/products. NCEP NARR surface pressure is downloaded from https://psl.noaa.gov/thredds/catalog/Datasets/NARR/monolevel/catalog.html. GHRSST used in this chapter can be found at https://podaac.jpl.nasa.gov/GHRSST. World Ocean Database data are available at https://www.nodc.noaa.gov/OC5/SELECT/dbsearch/dbsearch.html and World Ocean Atlas data used in this study can be found at https://www.ncei.noaa.gov/products/world-ocean-atlas. CalCOFI data can be downloaded at https://calcofi.org/ and ERA5 data were obtained from https://cds.climate.copernicus.eu/.

Thank you to Kasia Zaba, Ganesh Gopalakrishnan, and Bruce Cornuelle for sharing output from the CASE model to use for comparisons against the CCUI. CASE model data can be downloaded from http://ecco.ucsd.edu/case.html. CUTI estimates were downloaded from

https://mjacox.com/upwelling-indices/ and timeseries of the Bakun index were obtained from the ERDDAP server, https://coastwatch.pfeg.noaa.gov/erddap/griddap/index.html, and provided by the NOAA Southwest Fisheries Science Center Environmental Research Division.

Chapter 2, in part is currently being prepared for submission for publication of the material. Lowcher, Caroline; Send, Uwe; Lankhorst, Matthias. The dissertation author was the primary researcher and author of this material.

2.8 Appendix A: Constructing the Total Dynamic Height

2.8.1 Total Dynamic Height

Total dynamic height is constructed for each of the box endpoints. This includes an explanation of how the time-varying baroclinic, time-varying barotropic, and time-independent data sets are used, and the uncertainties associated with merging the dynamic height. For all error estimates, the reader is referred to Appendix B for a description of these calculations.

2.8.1.1 North Side Dynamic Height

a.) North Side Inshore Endpoint Dynamic Height

On the north side of the box, gliders transit between CCE2 and inshore which takes about 3 - 4 days one way. When the glider is inshore, the temperature and salinity measurements are collected and used as a pseudo inshore mooring. This creates a dataset similar to a mooring platform but with intermittent sampling that is linearly interpolated in time between glider visits. Prior to 2015, gliders were programmed to mostly stay near the CCE2 site with very irregular inshore transits (Figure 2.2). Dynamic height is computed from the temporally interpolated data set. The geostrophic transport error associated with the glider temperature and salinity sensor measurements and the error from temporally interpolating the glider data are 0.001 Sv and 0.03 Sv, respectively. Additionally, the glider does not travel all the way to the coast and the magnitude of the transport inshore of the pseudo mooring is approximated as 0.03 Sv.

The barotropic fluctuations are added to the dynamic height profiles from SSH spatially interpolated from the Port San Luis (PSL) and Santa Barbara (SB) tide gauges. These are the closest tide gauges north and south, respectively, of the pseudo mooring. The error in the tide gauge sea level measurements is 0.02 Sv per site. Between 2000 – 2005, there were no sea level measurements at SB, so the Santa Monica (SM) tide gauge (Figure 2.1) is utilized instead.

Lastly, the mean from ADT is added to the dynamic height profiles and the error in the estimate of the mean is 0.12 Sv.

b.) North Side Offshore Endpoint Dynamic Height

At the offshore endpoint on the north side, glider profiles of temperature and salinity measure the upper ~600 m of water, whereas mooring temperature and salinity measurements only span the upper 80 m. Since the glider measures at deeper depths than the mooring, the glider data are used for computing the time-varying baroclinic contributions to dynamic height at CCE2. When the glider is station-keeping at CCE2, i.e., not transiting inshore, the temperature and salinity data are temporally interpolated to fill in the periods when the glider is not at CCE2. Interpolating the glider data yields a transport error of 0.01 Sv, while the transport error from the glider temperature and salinity sensors is 0.02 Sv. This error is larger at CCE2 than at the northeast endpoint of the box because dynamic height at CCE2 is referenced with the PIES bottom pressure, which involves integrating density over the water column as oppose to only

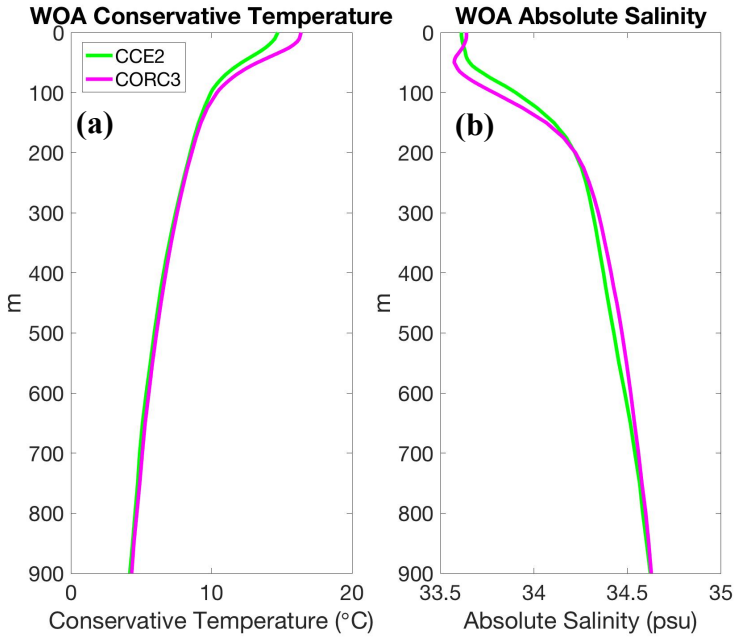

Figure 2.19: WOA profiles of (a) temperature and (b) salinity at CCE2 and CORC3.

over the upper 50 m like at the northeast box endpoint. The details of this step are explained next.

The bottom mounted CCE2 PIES lies at 870 m depth, so density must be estimated down to this depth. Temperature anomalies from the deepest glider measurement and at the depth of the PIES are linearly interpolated over the ~270 m vertical gap. These anomalies are the residuals after the WOA mean temperature (Figure 2.19a) is removed from the temperature at the depths of the deepest glider measurement and the PIES. The interpolated temperature anomalies between ~600 – 870 m depth then have the WOA temperature mean added back in. Interpolating the temperature anomalies in this fashion accounts for the curvature in the WOA profile (Figure 2.19a).

As mentioned in Section 2.2.2, the second CCE2 PIES deployment was not recovered and temperature data were not telemetered. During this PIES deployment, glider temperature anomalies from the deepest measurement are assumed constant and extrapolated down to the PIES depth. Then the mean WOA temperature profile is added to the extrapolated anomalies. This same procedure is used for the most recent PIES deployment since the PIES is still deployed.

The PIES do not include conductivity sensors, so salinity at the PIES depth is approximated based on the PIES adjusted temperature, i.e., the PIES temperature sensor mean is replaced by the WOA temperature mean at this depth, and from the fitted temperature-salinity curve to WOD data (Figure 2.20a). The pink circles in Figure 2.20a show the predicted salinity at the PIES depth based on the PIES adjusted temperature. The uncertainty in density at the PIES depth produces a transport error of 0.003 Sv. Like temperature, salinity fluctuations are linearly interpolated between the PIES depth and the deepest glider measurement, and then the WOA

mean salinity (Figure 2.19b) is added. The transport error associated with estimating temperature and salinity in the bottom layer from interpolating the anomalies is 0.002 Sv.

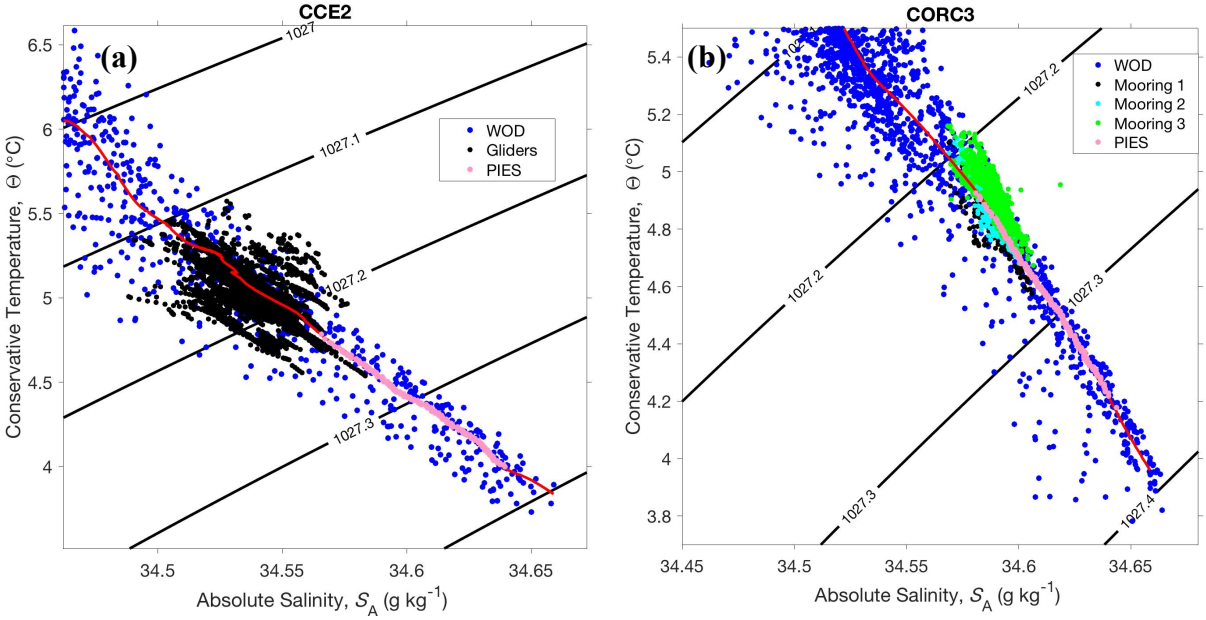

Figure 2.20: Temperature-salinity diagrams at (a) CCE2 and (b) CORC3. WOD data are the blue circles, the red line is a temperature-salinity (T-S) fit to the WOD data, the pink circles on top of the red line are approximations of salinity at the depth of the PIES based on the T-S fit, and the other colored circles denote observations of temperature and salinity from gliders and moorings. Moorings 1, 2, and 3 in (b) reference the mooring deployment.

For the second CCE2 PIES deployment there are no temperature data, so glider salinity anomalies from the deepest measurement are assumed constant and extrapolated down to the PIES depth. Then the WOA mean salinity is added to the salinity anomalies. This is similar to how the glider temperature anomalies are handled. For the currently deployed PIES, where the telemetered data do not include temperature measurements, the salinity anomalies from the deepest glider measurement are also assumed constant and extrapolated down to the bottom, where the WOA mean is then added. This resultant transport error from extrapolating the anomalies is 0.003 Sv.

Dynamic height is computed from the complete profiles of temperature and salinity from the surface down to the depth of the PIES and this is referenced with the bottom pressure

fluctuations. The PIES have an approximated sensor error that when integrated over 50 m is 0.06 Sv. There is a gap in the bottom pressure measurements between late 2019 – mid 2020 (Figure 2.2), which is filled by GLORYS and CMEMS Forecast SSH data. Since SSH provides the barotropic fluctuations in this period, the baroclinic component of dynamic height is referenced to the surface. Next, the dynamic height mean is added from the offset in equation (9) using CMEMS ADT data at the surface.

2.8.1.2 West Side Dynamic Height

a.) West Side Northern Endpoint Dynamic Height

For the west side of the box, the northern endpoint is the same as the offshore endpoint on the north side of the box. Thus, the construction of the total dynamic height field at this location was explained in Section 2.8.1.1b.

b.) West Side Southern Endpoint Dynamic Height

At CORC3, mooring measurements of temperature and salinity at fixed depths require interpolating temperature and salinity between the sensor depths. The mean temperature and salinity are removed for each sensor, and the resulting temperature and salinity anomalies are vertically interpolated from the shallowest sensor to the deepest sensor on the mooring. These property anomalies then have the WOA mean added to account for the curvature in the temperature and salinity profiles (Figure 2.19). When the mooring was broken (Figure 2.2), gliders served as a replacement mooring performing repeated dives at the site. The transport error from the glider baroclinic measurements is 0.02 Sv and the transport error from the mooring temperature and salinity sensor errors is 0.01 Sv.

The gliders and mooring do not sample all the way down to the bottom-mounted PIES at 840 m depth and there is ~100 m between the deepest density measurement and the PIES depth.

Like at CCE2, temperature is approximated over the bottom layer by interpolating the PIES and the deepest mooring/glider temperature anomalies, and then adding in the WOA mean temperature profile (Figure 2.19a). The CORC3 PIES temperatures are used to estimate salinity at the bottom based on WOD data (Figure 2.20b). Figure 2.20b shows that some of the deeper mooring measurements overlap in temperature-salinity space with the PIES temperature and agree with the estimated salinity at the PIES depth. The transport error from the density uncertainty at the PIES depth is 0.001 Sv, and the transport error from the interpolation of temperature and salinity anomalies in the bottom layer is 1.16×10^{-4} Sv.

Since this is a subsurface mooring, the upper ~35 m are not sampled and require approximating density in this layer. Gliders do profile the upper ocean so when they are active, the upper 35 m are sampled. During mooring deployments, satellite SST from the GHRSST product and MLD information from the CMEMS ARMOR3D product aid in approximating temperatures in the upper ~35 m. If the mixed layer is deeper than 35 m, then temperature in the *upper ~35 m* is assumed to be the same as the SST. If the mixed layer is shallower than ~35 m, then temperature *throughout the mixed layer* is assumed to be the same as the SST. Between the mixed layer and the shallowest mooring instrument, the temperature anomalies from the shallowest sensor are assumed constant and extrapolated upward to the bottom of the mixed layer. These anomalies then have the WOA mean added to them.

To estimate salinity in the upper ~35 m, salinity from the shallowest mooring sensor have the mean removed and the anomalies are assumed constant and extrapolated up to the surface. Then the WOA mean is added to the anomalies. If the MLD is deeper than ~35 m, then the salinities derived from the extrapolation process are averaged in the *upper ~35 m* and this value is assumed to be homogenous over the upper ~35 m. If the MLD is shallower than ~35 m, then

the salinities *within the mixed layer* are averaged and it is assumed that this average is the salinity over the mixed layer. The transport error associated with estimating temperature and salinity near the surface at CORC3 is 0.02 Sv, and this error was smaller than the error when extrapolating the temperature and salinity fluctuations from ~35 m depth upward and adding in the WOA mean temperature and salinity, respectively.

Using the complete profiles of temperature and salinity over the water column, dynamic height is calculated and is referenced with the PIES bottom pressure. Then the mean absolute dynamic height from the CMEMS data is incorporated.

2.8.1.3 South Side Dynamic Height

a.) South Side Offshore Endpoint Dynamic Height

For the south side of the box, the offshore endpoint is the same as the southern endpoint on the west side of the box. Thus, the construction of the total dynamic height field is the same as that discussed in Section 2.8.1.2b.

b.) South Side Inshore Endpoint Dynamic Height

At DM the vertical sampling is dense, where instruments on the mooring span the entire water column. This provides the time-varying baroclinic component of dynamic height and the associated transport error from the sensors is 0.001 Sv. There is a small segment between DM and the coast that does not get measured by the mooring and the transport missed near the coast is approximated as 0.01 Sv.

The dynamic height profiles from the mooring are referenced with the San Diego (SD) tide gauge SSH. Next, the mean signal is added from the CMEMS ADT.

2.9 Appendix B: Volume Budget Errors

In the volume budget, there are uncertainties in both the geostrophic and Ekman transports. The geostrophic transport errors are discussed first in Section 2.9.1 followed by the Ekman transport errors in Section 2.9.2. Many of the error bars shown in this chapter represent the geostrophic transport error. In the upwelling comparisons, i.e., Section 2.3, all of the upwelling indices use a wind product that has some uncertainty. So, the CCMPv2 Ekman transport error is not included in many of these error bars and instead the vertical transport error is the geostrophic transport error. However, an error estimate for the Ekman transport is discussed in Section 2.9.2.

2.9.1 Geostrophic Transport Errors

The geostrophic transport errors stem from using the multiple observational platforms and products for determining the dynamic height. These errors are assumed to be statistically independent from one another and are combined as,

$$\sigma = \sqrt{\sigma_1^2 + \sigma_2^2 + \cdots + \sigma_N^2}, \tag{B.1}$$

where N denotes the different contributors to the total geostrophic transport error. Many of the inshore box endpoint geostrophic transport errors are associated with approximating CCUI and these are discussed in Section 2.9.1.1, while the errors in the dynamic height profiles at the offshore box endpoints are described in Section 2.9.1.2. The latter group does not contribute to the vertical transport error in CCUI since it does not incorporate the offshore box endpoint dynamic height profiles.

2.9.1.1 Inshore Endpoint Errors

The errors in the dynamic height profiles from the inshore box endpoints are presented in this section and many of these errors factor into the vertical transport error in CCUI. These errors

include the errors in the baroclinic component of the dynamic height profiles, the time-varying depth-independent aspect of dynamic height, and the mean dynamic height. The errors are given for weekly, monthly, and seasonally filtered data as the transport figures in Sections 2.3 and 2.4 show data filtered at these time scales.

a.) DM Mooring Sensor Error

At DM, the instruments on the mooring induce an error in the baroclinic component of the dynamic height profiles. This error is due to the sensor errors in measuring temperature and salinity. These are fixed point measurements on the mooring with five instruments in the upper 50 m and the instrument errors are independent of each other. For temperature, a sensor error is assumed to be 0.003ºC and for salinity the conductivity sensor error is assumed to be 0.01 psu. This is based on a mooring post-calibration analysis by Kanzow et al. (2006) with a modification made to the salinity error. Since the study area in this chapter is a region of high upwelling, biofouling accumulates more rapidly and in practice the salinity error is larger than the 0.003 psu reported by Kanzow et al. (2006). Sensors are calibrated before and after each deployment which is then used to remove a linear drift over the deployment period. This mitigates instrument error induced by the mooring sensors and details of this calibration technique are described in Kanzow et al. (2006). Using the temperature and salinity sensor errors given above, a transport error is approximated for the DM mooring based on the error in the dynamic height profile from the baroclinic contribution.

To ascertain the error in dynamic height at DM from the instruments, 10,000 profiles are created for temperature and salinity that use the mean DM temperature and salinity profile for the upper 50 m. Then a randomly generated sensor offset of ± 0.003ºC for temperature and ± 0.01 psu for salinity is added to the temperature and salinity profiles, respectively. Each of the

five instruments in the upper 50 m on the mooring have an error that is independent from the other instruments, which gets reflected in the random error generation by making it independent with depth. Once the 10,000 profiles for temperature and salinity are simulated, dynamic height is computed and evaluated against the dynamic height calculated from the mean temperature and salinity profiles. The rms error is deduced from the difference in the dynamic height profiles from the randomly simulated profiles and the mean dynamic height profile. This error when integrated over the upper 50 m gives a transport error of 0.0006 Sv (Table 2.9).

Table 2.9: Transport errors at the inshore endpoints of the southern California box in Figure 2.1. Those errors which get smaller at lower frequencies due to a smaller noise signal are also listed. Transport errors are based on integrating over the upper 50 m.

	Weekly Filtered (Sv)	**Monthly Filtered (Sv)**	**Seasonally Filtered (Sv)**
DM Mooring Sensors	0.0006		
PC Glider Sensors	0.0013		
PC Temporal Interpolation	0.0321	0.0224	0.0164
Baroclinic Contribution	0.0396	0.0379	0.0245
DM Inshore Transport	0.0110	0.0095	0.0075
PC Inshore Transport	0.0264	0.0228	0.018
Coriolis error	0.0122	0.0108	0.0093
Tide Gauge	0.0206	0.0127	0.0061
CMEMS Mean	0.1212		
Total CCUI Error (Mean Included)	0.1854	0.1804	0.1756
Total CCUI Error (Mean Excluded)	0.0706	0.0561	0.0381

b.) PC Glider Sensor Error

Off of Point Conception, the pseudo inshore mooring also contributes an error to the baroclinic component of the dynamic height profiles. To attain an error for this platform, a similar approach is employed that was used in the previous section with the DM mooring, but with a few additional considerations. The dynamic height measurements at this location are made

by a glider with similar temperature and salinity instruments, so the sensor error is the same. For assessing the error due to the glider sensors, 10,000 profiles are created using the record-long glider mean temperature and salinity in the upper 50 m and a random error is added to the profiles. The random errors are constrained to be within the sensor errors, as stated in the previous section. Unlike at DM, the sensor errors at this endpoint of the box do not change with depth, i.e., the same sensor measures at all depths in the upper 50 m, so each randomly generated error is held the same over the upper ocean. The rms error in dynamic height from the glider sensors corresponds to a geostrophic transport error of 0.0013 Sv (Table 2.9).

c.) PC Glider Temporal Sampling Error

A second error is introduced by the inshore pseudo mooring which deals with the intermittent glider sampling inshore. The glider is programmed to make cross-shore transects so it only resides inshore part of the time. The dynamic height at this endpoint is linearly interpolated over the period when the glider is not present which introduces a temporal sampling error. The temporal error is estimated based on mooring data at CCE2. To approximate this error, a subset of the mooring data is extracted which includes only the days for which the glider is located inshore. This subset of temperature and salinity data is linearly interpolated between gaps in time. This mimics the handling of the intermittent glider data inshore. Dynamic height is then computed on the interpolated dataset and this is compared to the dynamic height from the full mooring record. The resultant rms error from the differences in the dynamic height profiles yields a weekly filtered transport error of 0.0321 Sv (Table 2.9).

d.) Baroclinic Contributions to Total Geostrophic Transport

The difference between the second and third upwelling indices in Section 2.2.4 is the inclusion of the baroclinic component of the dynamic height profiles in the second index. Not

using the baroclinic contribution as in the third index allows for a longer upwelling timeseries with fewer gaps. However, neglecting the baroclinic component comes with an associated error for approximating the vertical transport. To determine the error by not using the baroclinic portion of the dynamic height profiles as in the third upwelling index, the baroclinic component is considered to be the difference in net geostrophic transport that is utilized in the constructions of the second and third upwelling indices. The rms error for these two timeseries has a resultant weekly filtered transport error of 0.0396 Sv which represents the size of the baroclinic contribution to the total geostrophic transport (Table 2.9).

e.) Alongshore Transport Inshore of the Box

The DM mooring and the pseudo mooring off of Point Conception are not at the coast. The DM mooring contains a downward looking ADCP that measures the currents in the upper 50 m, so these data are used to approximate the transport inshore of the DM site. It is assumed that the upper 50 m averaged alongshore velocity measured by the ADCP is constant across the shelf. The magnitude of the alongshore velocity averaged in this layer is shown in Figure 2.21 and this is integrated across the shelf, a distance of about 5 km, to yield a transport of 0.0110 Sv. To estimate the transport inshore of the northeast endpoint of the box, the velocity fluctuations in the

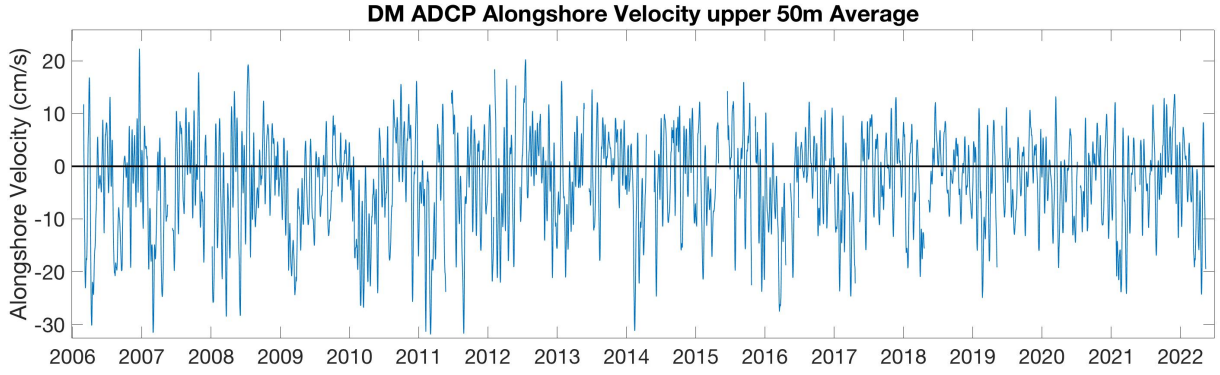

Figure 2.21: DM ADCP alongshore velocity averaged over the upper 50 m and weekly low-pass filtered. The alongshore velocity is taken as the north-south direction.

upper 50 m inshore of the pseudo mooring are assumed to be similar to those measured by the DM ADCP. This is then integrated across a shelf width of about 12 km to yield a transport of 0.0264 Sv. The approximated transports inshore of the northeast and southeast endpoints of the box are listed in Table 2.9 for multiple time filters.

f.) Latitudinal Variations in the Coriolis Parameter

In Section 2.2.4, the geostrophic component is assumed to have a constant f over the box. The error in assuming that the Coriolis parameter remains constant over the box is deduced by recomputing the geostrophic velocity through each of the box sides using the box-averaged Coriolis parameter. The net geostrophic transport from these velocities is compared to the net geostrophic transport that uses f values dependent on the latitude of the box side. This yields a weekly filtered transport error of 0.0122 Sv (Table 2.9).

g.) Tide Gauge Error

Another contribution to the geostrophic transport error is the sea level measurement error from coastal tide gauges. Previous studies have published these errors for sea level sensors at higher frequencies, e.g., 6-minutely and hourly (Woodworth and Smith 2003; Boon et al. 2012). For week-long timescales, it is expected that this error is reduced as some of the instrument noise is averaged out. To ascertain the tide gauge errors at this frequency, acoustic and radar data are acquired at several tide gauge locations along the US west coast. These sites are at Crescent City, Point Reyes, Santa Monica, San Diego, and La Jolla (Figure 2.22). These tide gauges are part of

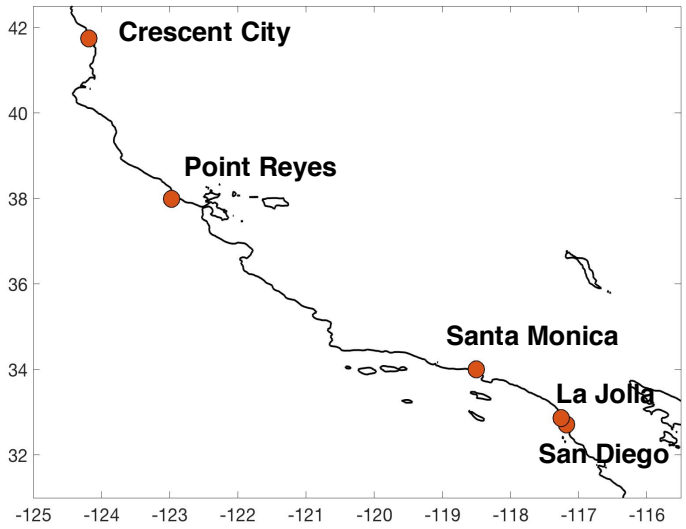

Figure 2.22: Tide gauge locations used for determining the tide gauge sensor error.

the National Water Level Observation Network (NWLON) and are operated by NOAA's Center for Operational Oceanographic Products and Services (CO-OPS; https://tidesandcurrents.noaa.gov/). Tide gauges were transitioned from acoustic to radar sensors at various times between 2013 and 2018 and while these data are public, they were retrieved via personal communication. Some overlap exists between the installations of the acoustic and radar sensor that is long enough to determine the sea level measurement error on weekly timescales.

Table 2.10: Tide gauge daily and weekly rms errors using acoustic and radar sensors at each site.

Tide Gauges	RMS Error – Daily (m)	RMS Error – Weekly (m)
Crescent City	0.0024	0.0017
Point Reyes	0.0066	0.0038
Santa Monica	0.009	0.006
San Diego	0.0022	0.0017
La Jolla	0.0364	0.0232

The acoustic and radar sea level data are 6-minute averages and are initially de-tided using t_tide.m. This is software is publicly available by Rich Pawlowicz (https://www.eoas.ubc.ca/~rich/index.html). This software does not remove all of the tidal signal, so data are low-pass filtered with a 36-hour Butterworth filter. Then data are daily averaged and

weekly filtered, and most of the time the acoustic and radar timeseries are nearly indistinguishable from each other (Figures 2.23 and 2.24a). The rms errors were computed between the acoustic and radar timeseries for both daily-averaged and weekly-filtered timeseries (Table 2.10). As expected, the rms errors decrease for the weekly-filtered data with more instrument noise removed. Notably, the La Jolla tide gauge has a much larger error in comparison to the other sites (Table 2.10). Since this tide gauge has an anomalously larger error and it is the closest tide gauge to the DM mooring, this tide gauge data is investigated further to determine whether it is suitable for incorporating into the coastal alongshore sea level difference as part of the volume budget calculations.

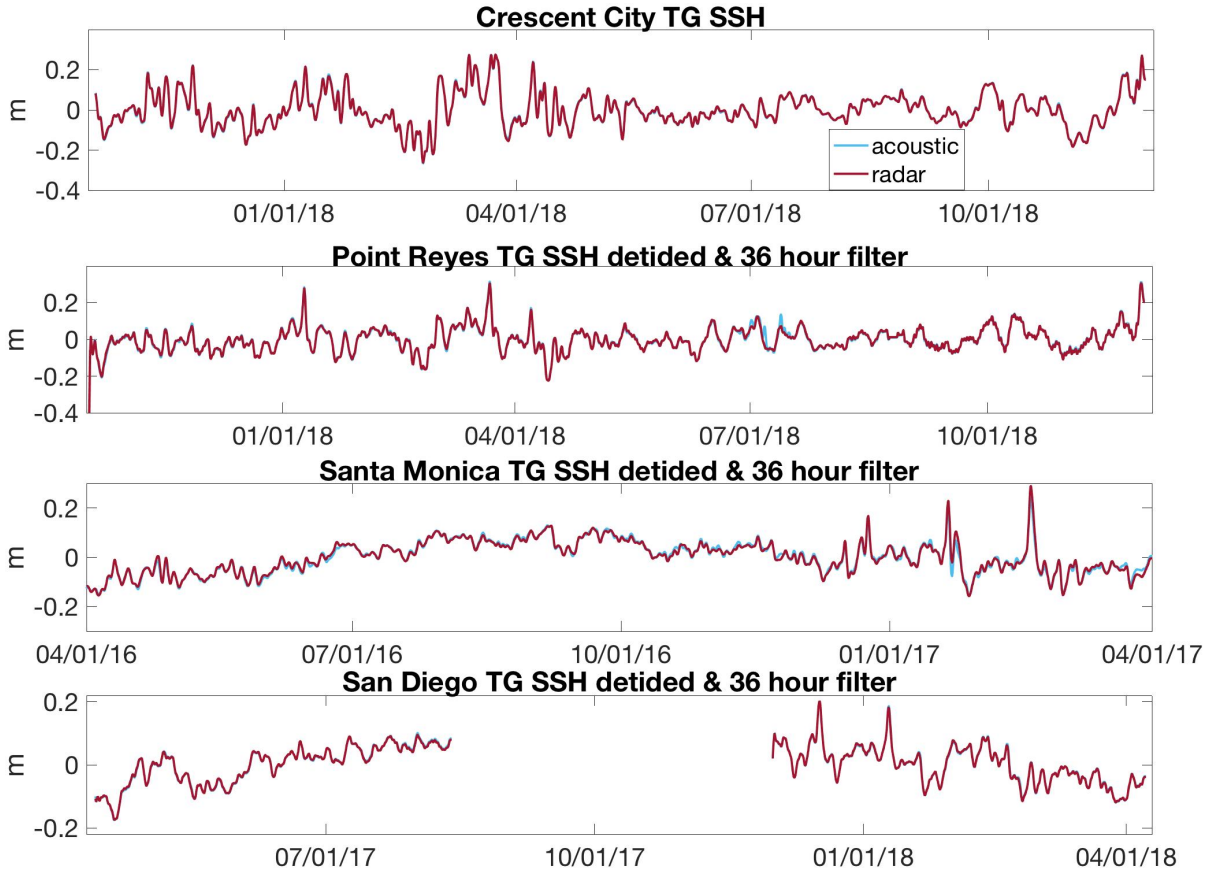

Figure 2.23: Tide gauge SSH from both acoustic and radar sensors.

The time-varying nature in the sensors' discrepancy of sea level is shown in Figure 2.24b, where positive differences denote that the acoustic sensor measures a higher sea level than the

radar. These differences are compared against wave height (Figure 2.24c) where swell measurements come from the NDBC LJPC1 platform that is located near the end of the Scripps pier. For reference, the La Jolla tide gauge is also mounted at the end of the Scripps pier, so these measurements are nearly co-located. The events of poor agreement in Figure 2.24b occur when the swell exceeds approximately 1 m. Previous studies have reported that tide gauge sensors that are exposed to larger swells, e.g., swells that exceed 1 m in height, make larger measurement errors during these higher sea states (Parke and Gill 1995; Haines et al. 2003; Boon et al. 2012; Park et al. 2014). This affects the acoustic sensor more than the radar as there tends to be a wave-induced water level draw down in the acoustic protective well and this underestimates sea level during larger swell activity (Park et al. 2014). The other tide gauge sites in Figure 2.23 are suspected to be exposed to less swell than the La Jolla tide gauge, e.g., installed in a harbor where not as much swell penetrates through or are topographically protected from many swell angles. This is also true for the tide gauges used in providing the depth-invariant fluctuations of dynamic height, i.e., Port San Luis and Santa Barbara, which are shielded more from larger swells. This does not imply that these sites are completely protected from swell activity, as there are infrequent disagreements between the radar and acoustic sensors in Figure 2.23, but these influences are included in the rms errors in Table 2.10.

The larger SSH error at La Jolla coincides with larger swell conditions and the exposure of swell appears to be less significant at the other tide gauge sites in Figure 2.23. Therefore, the La Jolla tide gauge is not included in evaluating the error for sea level measurements as it does not seem to be representative of the other tide gauges used in the analysis nor is it used for the barotropic fluctuations in the dynamic height profiles at DM. The representative error of coastal

SSH data averages the weekly rms errors in Table 2.10 from the other tide gauge locations. This error translates into a weekly filtered transport error of 0.0206 Sv (Table 2.9).

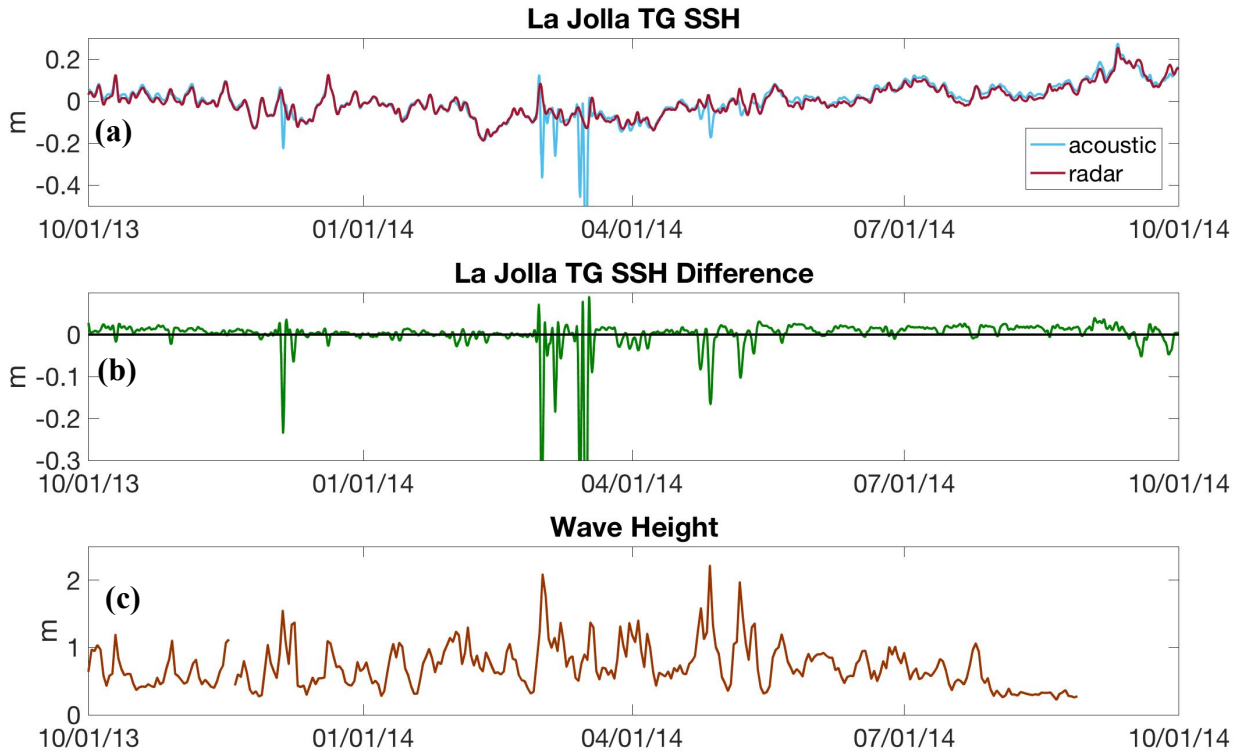

Figure 2.24: (a) La Jolla tide gauge SSH from acoustic and radar sensors. (b) SSH difference between the acoustic and radar sensors. (c) Wave height recorded near the La Jolla tide gauge.

h.) Dynamic Height Mean Error Total

In constructing total dynamic height, the mean is obtained from the CMEMS ADT product. The error in the mean of dynamic height stems from the error in the estimate of the mean dynamic topography, i.e., the non-fluctuating component of ADT. In this region, this error is anticipated to be less than 2 cm (Mulet et al. 2019), which is a transport error of 0.1212 Sv (Table 2.9).

i.) Total CCUI Error

The CCUI vertical transport error is determined by combining the errors in this section as in equation (B.1). The CCUI error is computed from the rms errors derived over weekly,

monthly, and seasonally filtered data as some of the analysis in Sections 2.3 and 2.4 are over these time scales. This error is shown in Table 2.9 with and without the time-mean error from the CMEMS product (Section 2.9.1.1h). The time-mean error is the largest off all the geostrophic transport errors. Since the CMEMS data provide the mean at both box inshore endpoints, this error is accounted for at both locations in equation (B.1) and this error source significantly raises the transport error. Showing the total transport error with and without the mean in Table 2.9 demonstrates the smaller uncertainty in the time-varying aspect of CCUI and that this time-dependent component is known better than the mean in the absolute transport.

2.9.1.2 Offshore Endpoint Errors

The errors in the dynamic height at the offshore box endpoints are presented. These errors do not contribute to the vertical transport error in the CCUI, but they do reflect how sources of uncertainty are introduced at the offshore box endpoints when gridding dynamic height.

a.) CORC3 Mooring Sensor Error

The instruments on the CORC3 mooring contribute an error in the baroclinic shear of the dynamic height profiles. There are eight sensors on the CORC3 mooring that span the water column from about 35 m down to 780 m depth. Since the mooring references dynamic height with the PIES, all instruments on the mooring contribute to the error in dynamic height when approximating dynamic height in the upper 50 m. The dynamic height error from the sensors is approximated in the same fashion as was done at DM in Section 2.9.1.1a. This error is then integrated over the upper 50 m to yield a transport error of 0.0118 Sv (Table 2.11).

b.) CCE2 and CORC3 Glider Sensor Errors

The temperature and conductivity sensors of the gliders that profile at CCE2 and CORC3 contribute an error to the baroclinic shear in the dynamic height profiles. The gliders make measurements of temperature and salinity from the surface down to about 600 m. Since both of these sites reference dynamic height with the bottom-mounted PIES, the sensor errors from the glider as it profiles the water column are estimated. This error is approximated in a similar fashion as the glider sensor errors at the northeast box endpoint in Section 2.9.1.1b. The sensor errors are integrated over the upper 50 m which results in a transport error of 0.0204 Sv (Table 2.11).

Table 2.11: Transport errors at the offshore endpoints of the southern California box in Figure 2.1. Those errors which get smaller at lower frequencies due to a smaller noise signal are also listed. Transport errors are based on integrating over the upper 50 m.

	Weekly Filtered (Sv)	**Monthly Filtered (Sv)**	**Seasonally Filtered (Sv)**
CORC3 Mooring Sensors	0.0118		
CCE2/CORC3 Glider Sensors	0.0204		
CCE2 Temporal Interpolation	0.0092	0.0092	0.0092
CCE2 PIES Density	0.0034		
CORC3 PIES Density	0.0013		
CCE2 Bottom Layer Density	0.0016/0.0034		
CORC3 Bottom Layer Density	$1.16 * 10^{-4}$		
CORC3 Upper Layer Density	0.0218	0.0199	0.0168
PIES Bottom Pressure	0.0612		

c.) CCE2 Glider Temporal Interpolation

The glider on the north side of the box is programmed to make cross-shore transects, so it only resides at the CCE2 site part of the time. The dynamic height profiles at this endpoint are

linearly interpolated over the period when the glider is not present, which introduces a temporal sampling error. The temporal error is estimated based on mooring data at CCE2. To approximate this error, a subset of the mooring data is extracted which includes only the days for which the glider is located near the CCE2 mooring. This subset of temperature and salinity data is linearly interpolated between gaps in time. This mimics the handling of the glider data when it is at CCE2. Dynamic height is then computed on the interpolated dataset and these dynamic height profiles are compared to the dynamic height profiles from the full mooring record. The resultant rms error from the differences in the dynamic height profiles yields a transport error of 0.009 Sv (Table 2.11).

d.) PIES Density Approximations

The PIES measure bottom pressure which is the reference for the baroclinic component of the dynamic height profiles, so density must be known at the depth of the PIES. The PIES do not contain a conductivity sensor, so salinity at the PIES depth is approximated based on the PIES temperature as outlined in Appendix A. The typical spread in salinity over the PIES temperature ranges (Figure 2.20) is used to create a second salinity dataset at the PIES depth that includes this potential offset in salinity values. Dynamic height profiles computed from this dataset are compared to dynamic height profiles that uses the salinity from the temperature-salinity fit in Figure 2.20 for CCE2 and CORC3, respectively. The difference in the dynamic height profiles is integrated over the upper 50 m resulting in a transport error of 0.0034 Sv and 0.0013 Sv for CCE2 and CORC3, respectively (Table 2.11).

e.) Bottom Layer Density Approximations

At CCE2, the glider dives down to about 600 m depth and the PIES is located at the bottom which is approximately 872 m depth. Thus, over the nearly 300 m between the glider and

PIES sampling, density is interpolated as described in Appendix A. To test the error associated with this interpolation, WOD data are used near CCE2. To mimic the missing glider data over this gap, data in the approximately 300 m above the bottom are removed from the WOD data set except for the density data near the bottom. Temperature and salinity fluctuations are then interpolated over this gap as explained in Appendix A and dynamic height profiles are computed. The rms error between these dynamic height profiles and the dynamic height profiles that include the complete set of observations yields a transport error of 0.0016 Sv when integrated in the upper 50 m (Table 2.11).

Data from the second CCE2 PIES deployment (2016 - 2020, see Figure 2.2) were retrieved via telemetry, since the PIES failed to release off the bottom. Telemetered data include bottom pressure but not temperature, so another approach involving extrapolating glider temperature and salinity fluctuations down to the bottom was implemented for estimating dynamic height between the bottom and the deepest depth the glider reaches as explained in Appendix A. The error in dynamic height from this procedure is assessed by using WOD data, i.e., hydrographic profiles near CCE2, and replicating the extrapolation of temperature and salinity fluctuations from about 600 m depth down to the bottom. Repeating this approach with WOD data gives a transport error of 0.0034 Sv when integrated over the upper 50 m depth (Table 2.11).

Similar to CCE2, CORC3 has a gap below the deepest mooring/glider measurement and the bottom. This vertical gap is about 100 m which is smaller than the gap at CCE2. WOD data are used to approximate the error associated with interpolating density over this gap. Like at CCE2, WOD data is removed over the gap and temperature and salinity fluctuations are interpolated over these depths. Dynamic height profiles calculated from this interpolated data are

compared against dynamic height profiles using the WOD observations over this layer, which when integrated over the upper 50 m gives an error of 1.16×10^{-4} Sv (Table 2.11).

f.) CORC3 Near Surface Density Approximations

CORC3 temperature and salinity timeseries are a mixture of subsurface mooring measurements and glider profiles. The subsurface mooring was designed to measure baroclinic changes in the dynamic height profiles, with the shallowest sensor at approximately 35 m depth. Thus, during the mooring deployments (Figure 2.2), the upper ocean is not sampled, and temperature and salinity must be estimated. The approach for estimating these properties uses MLD and SST and was discussed in Appendix A. To assess the error in dynamic height related to the approximation of temperature and salinity near the surface, the procedure for approximating these properties during the mooring deployments is implemented during the time period when gliders were active (Figure 2.2). The dynamic height profiles over this period are then compared to the dynamic height profiles from the gliders, and the rms error for dynamic height in the upper 50 m is determined. This rms error in the dynamic height profile is integrated over the upper 50 m which gives a weekly filtered transport error of 0.0218 Sv (Table 2.11).

g.) PIES Bottom Pressure Fluctuations

Bottom pressure measurements made by the PIES provide depth-invariant fluctuations in dynamic height at CCE2 and CORC3. Previous studies have estimated errors from the PIES bottom pressure measurements to be about 1 – 2 cm (Watts and Kontoyiannis 1990; Hughes et al. 2013). To evaluate the error in dynamic height related to the PIES bottom pressure measurements, an error of 1 cm yields a transport error of 0.0612 Sv when integrated over the upper 50 m (Table 2.11).

2.9.2 Ekman Transport Error

Selecting the CCMPv2 wind product for computing the Ekman transport was based on a previous analysis of wind products for California. Wang et al. (2019) demonstrated a reasonable performance of the CCMPv2 product in their analysis of wind products covering a region in California that overlaps with the southern California box. While scatterometers performed best in their analysis, they lack the spatiotemporal resolution that is needed for this analysis, thereby motivating the choice of using the CCMPv2 product for its better spatial coverage. Additional comparisons of the CCMPv2 product are made with buoy winds to further validate this product and assess the error on weekly timescales.

Table 2.12: Alongshore wind stress statistics. All correlations are significant at 95% and the 95% confidence interval is given. Negative bias means CCMPv2 data is more positive than buoy data. Statistics are computed over 2013 – 2015 and with weekly filtered data.

	Correlation (95% CI)	**RMS Error (N/m^2)**	**Bias (N/m^2)**
CCE2	0.79 ± 0.023	0.0315	0.0097
NDBC 46025	0.87 ± 0.014	0.0116	0.0042
NDBC 46086	0.97 ± 0.004	0.0071	-0.0047
NDBC 46054	0.83 ± 0.018	0.0874	-0.0729
CCMPv2 Alongshore Wind Stress Error		0.0261 N/m^2	

Table 2.13: Cross-shore wind stress statistics. All correlations are significant at 95% and the 95% confidence interval is given. Negative bias means CCMPv2 data is more positive than buoy data. Statistics are computed over 2013 – 2015 and with weekly filtered data.

	Correlation (95% CI)	**RMS Error (N/m^2)**	**Bias (N/m^2)**
CCE2	0.42 ± 0.051	0.0150	-0.0041
NDBC 46025	0.70 ± 0.029	0.0103	0.0022
NDBC 46086	0.95 ± 0.006	0.0071	0.0052
NDBC 46054	0.57 ± 0.039	0.0241	0.0192
CCMPv2 Cross-shore Wind Stress Error		0.0123 N/m^2	

Wind data were extracted from four buoys over southern California, and the buoys are located in the northern, central, and southern portions of southern California (Figure 2.1). The

northernmost wind buoy is the CCE2 mooring, while the other three buoys (46054, 46025, and 46086) are part of the NDBC network. CCMPv2 wind data were interpolated at the four buoy sites and comparisons are made over 2013 – 2015 for weekly filtered, monthly filtered, and seasonally filtered alongshore wind stress and cross-shore wind stress. The statistics of these comparisons are in Tables 2.12 and 2.13 and quantify the good agreement of the CCMPv2 product over southern California. One distinction is the larger rms error at the 46054 site. Previous work documents an expansion fan off of Point Conception, where wind speeds accelerate within the expansion fan (Dorman and Winant 1995; Winant and Dorman 1997; Dorman and Winant 2000). This feature may be responsible for the larger rms error and this is investigated further.

Both the NDBC 46054 buoy and the CCE2 site have moderate-to-high correlations but larger rms errors and biases, more strongly so for the 46054 buoy in the alongshore wind stress (Tables 2.12 and 2.13). These statistics indicate that the CCMPv2 product underestimates the magnitudes of upwelling favorable wind stresses off of Point Conception. This discrepancy is larger near the core of the expansion fan, i.e., NDBC 46054, and decreases in the peripheral of the fan, i.e., CCE2. The underestimated winds in the CCMPv2 product may be due to the proximity of this location to the coastline where satellite wind measurements cannot be retrieved and thus the CCMPv2 product is the background field of ERA-Interim winds. The background wind field is a mix of land and ocean winds and likely underestimates the actual wind speeds at this part of the expansion fan (REMSS communication). The differences in the comparisons of CCMPv2 reanalysis data with buoy observations at CCE2 and at NDBC 46054 indicates that the wind field on the inshore portion of the north side of the box is under represented in the CCMPv2 data.

To determine the overall error in using the CCMPv2 wind product, the rms errors in Tables 2.12 and 2.13 are averaged to yield a single value for each of the wind stress components. Prior to averaging for the whole region, the performance of the CCMPv2 product in the northern end of the box is addressed by averaging the rms errors at CCE2 and NDBC 46054. This establishes a regional representation of the wind error for the northern portion of the box where there is an expansion fan. Then the regional average uses this value for the northern region of the box and the rms errors in the central, i.e., NDBC 46025, and southern, i.e., NDBC 46086, regions of the box. This is done for both the alongshore and the cross-shore wind stresses, which gives a weekly filtered alongshore wind stress error of 0.0261 N/m^2 and a cross-shore wind stress error of 0.0123 N/m^2 for the CCMPv2 reanalysis (Tables 2.12 and 2.13). These errors are computed into the 2D Ekman transport error where the perpendicular component is integrated over the box side, σ_E^2. The Ekman transport error over the box is given in Table 2.14 for multiple time scales.

Table 2.14: Ekman transport error for the southern California box in Figure 2.1 for multiple time scales. The transport error is based on the alongshore and cross-shore wind stress rms errors in Tables 2.12 and 2.13 and the perpendicular component of the 2D Ekman transport error is integrated over the length of each box side. The combined Ekman transport error in the table is computed as $\sqrt{\sigma_{E_N}^2 + \sigma_{E_W}^2 + \sigma_{E_S}^2}$.

Weekly Filtered	Monthly Filtered	Seasonally Filtered
0.0922 Sv	0.0775 Sv	0.0720 Sv

2.10 Appendix C: Heat Budget Errors

In Section 2.3, the estimate of the vertical temperature flux through the bottom of the control volume is compared against the sum of the terms on the right-hand side of equation (24). A challenge in estimating the vertical temperature flux is approximating the box-averaged 50 m temperature. The 50 m temperature throughout the control volume is determined as described in Section 2.2.5 and the uncertainty in the vertical temperature flux at 50 m depth is approximated from the uncertainty in the vertical transport and the uncertainty in the 50 m temperature over the box. The sources of error in the vertical transport were presented in Appendix B and the uncertainty in the approximated 50 m temperature is discussed below.

Table 2.15: CalCOFI stations used in Figures 2.25 and 2.26, and the rms errors between the CalCOFI data and the approximated temperature for the temperature at 50 m depth.

CalCOFI Line	CalCOFI Station	Station Longitude (º)	Station Latitude (º)
80	55	-120.802	34.317
81.8	46.9	-120.025	34.467
83.3	42	-119.509	34.178
86.7	55	-120.007	33.156
86.7	40	-118.974	33.656
90	45	-118.936	32.918
90	30	-117.906	33.418
93	55	-119.233	32.013
93	45	-118.554	32.346
93	26.7	-117.305	32.956
50 m Temperature Rms Error (ºC)			0.62

To quantify the uncertainty in the box-averaged 50 m temperature, the errors are approximated based on a comparison with CalCOFI data. CalCOFI data is extracted at several locations throughout the box. These locations are listed in Table 2.15 and shown in Figure 2.25. The selected CalCOFI stations are spread uniformly throughout the box to check for spatial errors resulting from the method of approximating the 50 m temperature. Figure 2.26 compares

CalCOFI cruise data at 50 m depth alongside the estimated 50 m temperature that is averaged over the same CalCOFI locations. The CalCOFI 50 m temperature is averaged from the boxed stations in Figure 2.25 and the estimated 50 m temperature is also averaged over these locations. The rms error between the CalCOFI temperature measurements and the estimated temperature are reported in Table 2.15. This error along with the vertical transport error are used to determine the uncertainty in the vertical temperature flux at 50 m depth.

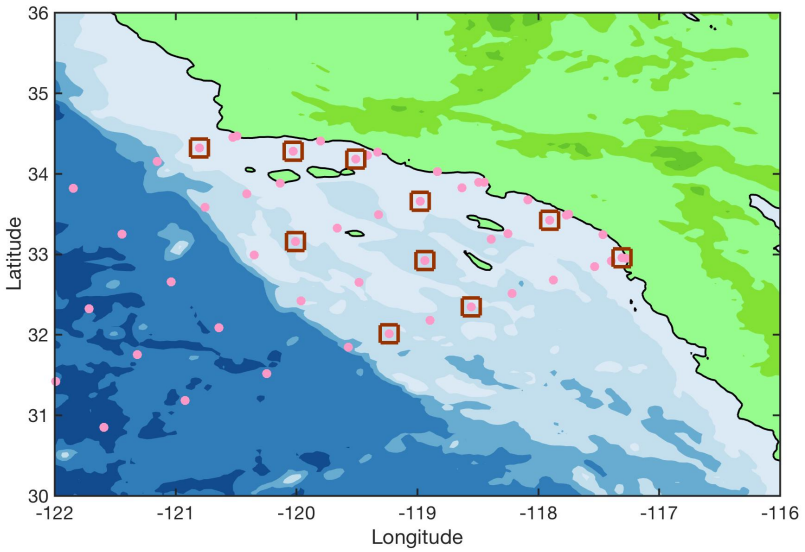

Figure 2.25: Southern California with CalCOFI stations as pink circles. Stations that are included for the temperature comparisons are designated by a box.

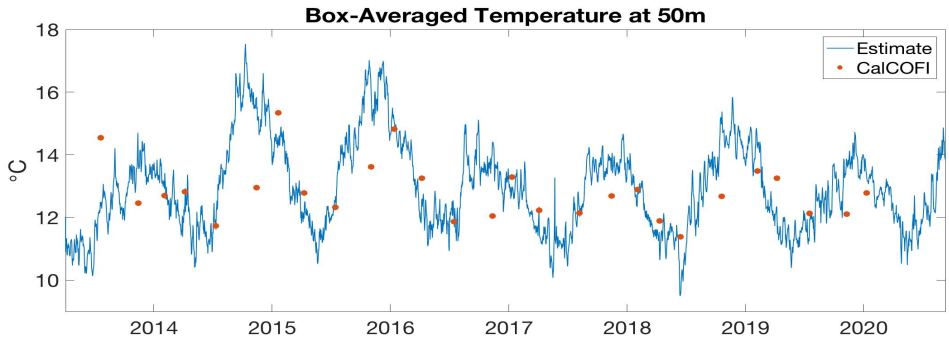

Figure 2.26: Temperature comparisons between CalCOFI data and approximated temperature for the southern California box at 50 m depth. CalCOFI stations used for the averaging are listed in Table 2.15 and boxed in Figure 2.25.

2.11 Appendix D: Additional California Upwelling Indices

Three additional upwelling measures are used in Section 2.3 in the comparisons with the CCUI. These upwelling measures are the Bakun index, the Coastal Upwelling Transport Index (CUTI), and the California State Estimate (CASE). Below, each measure of upwelling is described including the wind data sets used and how vertical transport is computed, followed by how vertical transport is determined from each index.

2.11.1 Bakun Index

The Bakun index was presented and elaborated on in Section 2.1. It uses the US Navy Fleet Numerical Meteorological and Oceanographic Center (FNMOC) model data of sea level pressure to compute geostrophic winds. In calculating wind stress, the traditional 3° Bakun index uses a constant drag coefficient, while the 1° Bakun index issues a drag coefficient that is a function of wind speed and tries to capture changes in the drag coefficient due to the strength of the wind field. This procedure is outlined in Large and Pond (1981) with a modification in the low wind speed parameterization by Trenberth et al. (1990). Once wind stress is derived, the alongshore component of the wind stress is the Bakun index. With the traditional Bakun index, a constant drag coefficient may underestimate or overestimate the frictional effects depending on the speed of the wind. Even with the improvement in handling the drag coefficient in the 1° product, the parameterization of the drag coefficient at high/low wind speeds underestimates/overestimates empirical evidence of the drag coefficient (Edson et al. 2013). These older parameterizations of the drag coefficients are drawbacks of the Bakun index, in addition to those disadvantages that were outlined in Section 2.1. Namely, these were the larger spatial resolution of the FNMOC model, the exclusion of the alongshore gradients in the cross-shore wind stress, and the omission of the influence of the cross-shore geostrophic flow.

2.11.2 CUTI

More recently, a newer upwelling index has been derived to improve upon the Bakun index. The daily CUTI timeseries is derived from the California Current System (CCS) Regional Ocean Modeling System (ROMS) reanalysis (Jacox et al. 2018). Multiple products are used for atmospheric forcing depending on the reanalysis and the time period of interest. Surface forcing includes the CCMP winds (an earlier version of the CCMPv2 product used in Section 2.2), the European Center for Medium-Range Weather Forecasts (ECMWF) ERA40 and ERA Interim projects, and the Naval Research Laboratory's Coupled Ocean Atmosphere Mesoscale Prediction System (COAMPS; Moore et al. 2013; Neveu et al. 2016). The spatial resolution of the wind forcing products range from ~3 - 250 km, with the ERA40 being the least spatially resolved. The ERA40 was used from 1980 - 2001 and for most of these years it was combined with the CCMP winds which have a higher resolution of ~25 km.

CUTI offers estimates of vertical transport for each degree of latitude for the US west coast (see Figure 2 in Jacox et al. 2018). For each 1° latitude bin, vertical transport is estimated as the sum of net Ekman transport and cross-shore geostrophic transport over the mixed layer. Net Ekman transport is the integrated Ekman transport through each side, i.e., the sum of the alongshore Ekman transport through the north and south sides of each bin and the cross-shore Ekman transport through the offshore side. This is similar to the procedure implemented in the CCUI and inherently accounts for spatial changes in the wind field thereby incorporating Ekman transport from the alongshore wind stress, e.g., coastal divergence, and wind stress curl, e.g., Ekman suction.

The cross-shore geostrophic transport in CUTI uses SSH from the model at the coastal northernmost and southernmost points of each 1° bin to calculate the cross-shore geostrophic

velocity. The CCS ROMS reanalysis are data assimilating and include altimetry SSH, but they do not incorporate tide gauge sea level data. The geostrophic velocity is assumed constant over the mixed layer and the product of the cross-shore geostrophic velocity and the MLD yields the layer transport. This is added to the net Ekman transport to deliver the vertical transport for each 1° bin.

2.11.3 CASE

Another regional model, CASE, has been previously used for studying the physical variability in southern California (Zaba et al. 2018) and for performing a volume budget analysis (Zaba et al. 2020). CASE is a regional implementation of the Massachusetts Institute of Technology general circulation model (MITgcm) and of the Estimating the Circulation and Climate of the Ocean (ECCO) 4D variational assimilation. The temporal coverage of the model is from 2007 – 2016 and the model is constrained by governing physical equations and assimilated observations. One of the assimilated data products in CASE is satellite SSH, but not tide gauge data. Atmospheric forcing comes from the National Centers for Environmental Prediction National Center for Atmospheric Research (NCEP NCAR) reanalysis. This product has a 2° resolution and wind stress calculations use the method from Large and Pond (1981). The wind forcing is adjusted in the assimilation process. CASE is a closed budget so the volume transport between the horizontal and vertical sides of the box balance. Thus, vertical transport includes the effect of cross-shore geostrophic flows and alongshore Ekman currents from the cross-shore wind stress.

2.11.4 Vertical Transport

The CCUI reports upwelling as vertical transport (Sv), so for the comparisons in Section 2.3 vertical transport over southern and central California is determined from CASE, CUTI, and

the Bakun index. CASE reports vertical velocities for southern and central California and these velocities are integrated over the boxed areas (Figure 2 in Zaba et al. 2020) to produce vertical transport timeseries. CUTI and the Bakun index report upwelling in m^2/s, so they are integrated along the length of the coastline to determine the transport in Sv of upwelled waters. CUTI outputs upwelling estimates every 1° latitude, so these latitudinal changes in upwelling are accounted for when determining the vertical transport over southern and central California. The Bakun index used for southern and central California is the 6-hourly timeseries at 33°N and 36°N, respectively, from the 1° FNMOC atmospheric product. The Bakun index does not report upwelling estimates between these two latitudes, so there are no latitudinal variations in the Bakun upwelling estimates within southern and central California. Once vertical transport is determined for all of the upwelling indices for both southern and central California, each upwelling estimate is low-pass filtered over one week. The comparisons in Section 2.3 use these weekly low-pass filtered vertical transport timeseries from all four upwelling indices.

CHAPTER 3

Physical and Biogeochemical Upwelling Characteristics and Interannual Variability of Synoptic and Low-Frequency Upwelling off Southern California

Abstract

Eastern boundary upwelling systems (EBUS) are coastal regions of prolific productivity. This places a significant socioeconomic value on them and attracts societal and scientific interest for understanding these systems and how they will respond to future changes in climate. High-frequency physical and biogeochemical observations along the coast sustained over the last decade monitored the oceanic response to upwelling on synoptic and low frequency timescales. The synoptic oceanic upwelling responses during the 2015 – 2016 and the 2018 – 2019 El Niños were weaker in comparison to other years in the last 1 - 2 decades. This change in the synoptic upwelling was due to weaker upwelling favorable winds. The low frequency oceanic upwelling response in the El Niño years, in addition to 2014, i.e., the 2014 marine heatwave, were also reduced. In general, the processes contributing to the change in the background upwelling in these years were reduced upward vertical transport related to weaker upwelling favorable winds, shallower source water depth, deeper nutricline depth, and a water mass composition that favored a lower nutrient supply.

3.1 Introduction

Eastern Boundary Upwelling Systems (EBUS) are some of the most productive waters in the ocean accounting for approximately 10% of global primary production and around 20% of global fish catches; yet they occupy less than 2% of the global ocean surface (Chavez and

Toggweiler 1995; Pauly and Christensen 1995). This production is fueled by the vertical circulation during upwelling that carries cool, nutrient-rich water up from below; thereby bringing new nutrients into the euphotic zone that are taken up by relatively larger phytoplankton. This process creates short food chains and large *f*-ratios (the fraction of new production to old production); thus, more energy is transferred to top predators in the food web (Ryther 1969; Moloney et al. 1991). The ecological significance of these systems has drawn attention to how they will respond to climate change and other extreme events, e.g., El Niño and marine heatwaves. In order to understand how they will be impacted, it is desirable to have long-term observations of the physical and biogeochemical properties (Sievanen et al. 2018). The observations presented in this chapter address this objective by providing long-term physical and biogeochemical measurements. These data are collected in near real time which is beneficial for monitoring the coastal ocean during recent regional events, e.g., upwelling, hypoxia, harmful algal blooms (HABs), etc.

Upwelling events are processes that occur on timescales of days to weeks and are characterized by synoptic events, e.g., atmospheric systems, which can drive upwelling winds and/or cause downwelling coastal trapped waves (CTWs; Hill et al. 1998). These processes have significant impacts on ecosystems such as enhancing primary production, influencing biological transport and recruitment, altering ocean chemistry, and creating upwelling fronts. Upwelling events provide the nutrients for primary production, which in turn fuels zooplankton and supports lower trophic levels (Lasker 1975; Wilkerson et al. 2006). Upwelling must be intense enough to fuel productivity, but if there is too much upwelling with rapid offshore advection of nutrients then this may limit nutrient uptake (Cury and Roy 1989). The episodic nature of upwelling events alters the cross-shore and alongshore flows, and along with bathymetry, are

essential to larvae dispersal and retention (Roughgarden et al. 1988; Farrell et al. 1991; Barth et al. 2005; Roughan et al. 2006). Upwelling events also impact ocean chemistry such that the upwelled waters often have a lower pH and dissolved oxygen content. Multiple studies have observed benthic and demersal organisms exposed to corrosive and hypoxic waters during upwelling (Chan et al. 2008; Feely et al. 2008; Chan et al. 2017). Under some circumstances, this process can cause dissolution of calcareous skeletal structures and mass die-offs of fish and invertebrates (Grantham et al. 2004; Fabry et al. 2008). Additionally, upwelling events can form upwelling fronts that promote biological activity. Such fronts are significant to the ecosystem because they increase the ecosystem biomass and channel nutrients through multiple trophic levels (Landry et al. 2012; Woodson and Litvin 2015). These examples demonstrate how upwelling events are critical to the coastal ocean ecosystem.

A key component of upwelling events is the alternation between intensification and relaxation in the wind field. The marine boundary layer interacts with topography such that off Point Conception in southern California the winds accelerate in an expansion fan (Dorman and Winant 1995; Dorman and Winant 2000). Approximately every two weeks the winds relax, and weaker winds may last for 2 – 4 days or even longer (Halliwell and Allen 1987; Dorman and Winant 1995; Dorman and Winant 2000; Melton et al. 2009). These relaxation events can be attributed to an offshore extension of the desert heat atmospheric low pressure. This can occur off central California and can weaken or reverse the upwelling favorable winds (Halliwell and Allen 1987; Mass and Bond 1996; Fewings et al. 2016). Secondly, in the atmosphere Catalina eddies form off the southern California coast and these cyclonic systems cause poleward winds in the SCB (Skamarock et al. 2002). While the smaller spatial scales of this atmospheric circulation do not directly extend as far north as Point Conception, they can potentially lead to

coastally-trapped disturbances that propagate poleward and indirectly weaken the winds off Point Conception (Skamarock et al. 2002). Such episodic fluctuations in the wind field are critical for retaining upwelled nutrients so that the nutrients are not advected offshore faster than biological uptake, and it is suggested that relaxations need to be 3 - 7 days to enable nutrient uptake (Dugdale and Wilkerson 1989; Dugdale et al. 1990; Botsford et al. 2006; Dugdale et al. 2006; Wilkerson et al. 2006).

One aspect of the wind-driven coastal circulation is cross-shore transport. The cross-shore transport is a significant process in the coastal ocean, exchanging waters on the shelf with those farther offshore. One way this happens is during upwelling when waters in the upper ocean are advected offshore and are replaced by upwelled waters on the shelf. At depth, onshore flow supplements the upwelled waters. The depth at which onshore flow occurs, and subsequently the source waters used in upwelling, can differ depending on the strength and vertical extent of the upwelling cell (Chhak and Di Lorenzo 2007; Song et al. 2011). The depths over which the source waters are drawn are important, as the composition of regional water masses and their associated biogeochemical content vary with depth. The upwelling source water depth depends on the stratification, bottom slope, and intensity of the wind field (Jacox et al. 2011; Jacox et al. 2012; He and Mahadevan 2021).

The latter of these criteria, wind intensity, is often used as a proxy for the strength of upwelling. Upwelling indices, like the Bakun index, are based on the alongshore wind stress and have been used to evaluate the strength of upwelling (Bakun 1973; Schwing et al. 1996). This is useful in evaluating the strength of the wind field, but it does not incorporate the ocean's response to upwelling and the resulting ecological productivity. EBUS are of interest because of their biological productivity, so monitoring these regions is important. Limited long-term

measurements of these high-frequency properties exist, and often other assumptions are made to infer the ecological response to upwelling. For example, one practice to assess potential biological productivity is to approximate nitrate from temperature based on an empirical relationship between these two properties (Kamykowski and Zentara 1985; Kudela and Dugdale 1996; McGowan et al. 2003, Palacios et al. 2013; García-Reyes et al. 2014; Jacox et al. 2018). This is a suitable method when there are quality data to derive a temperature - nitrate relationship and when water masses are not complex. However, under climate change, decadal variability, and extreme events, advection or other physical processes may become anomalous resulting in changes in regional water masses and/or temperature which may break down the temperature - nitrate relationship (Kim and Miller 2007; Palacios et al. 2013). While nutrient availability is an important factor in governing primary production, there are other factors that influence this like irradiance, temperature, and phytoplankton population and composition (Sverdrup 1953; Lewis and Smith 1983; Antoine and Morel 1996; Behrenfeld et al. 2002). Given these considerations, nitrate and temperature proxies of nitrate should be understood as the nutrients available for primary production, since there are other factors that influence the amount of chlorophyll fluorescence. Jacox et al. (2018) address some of these bottom-up drivers of productivity in generating the Biologically Effective Upwelling Transport Index (BEUTI). BEUTI estimates the vertical nitrate flux and aims to account for the nutrient content in the upwelled waters. The mooring observations in southern California measure both nitrate and chlorophyll-*a* fluorescence to help evaluate the productivity of upwelling events.

This chapter analyzes synoptic and low frequency upwelling from high-frequency physical and biogeochemical measurements, e.g., density, oxygen, pH, ΔpCO_2, nitrate, made in the coastal ocean off southern California. On synoptic timescales, the oceanic upwelling

response, i.e., changes in the physical and biogeochemical variables, and the upwelling forcing, i.e., 2D Ekman transport and vertical transport, are studied to investigate year-to-year changes in synoptic upwelling. In addition to the aforementioned physical and biogeochemical variables, the cross-shore currents are part of the oceanic upwelling response and the cross-shore currents are averaged over synoptic upwelling events to characterize the mean vertical structure in the cross-shore flow, and then the upper 50 m 2D ADCP transport is inspected for year-to-year changes. On interannual timescales, the oceanic upwelling response, i.e., the physical and biogeochemical properties as well as cross-shore flows, and the processes that govern low frequency variability in upwelling are examined. Throughout the investigations of upwelling at the different timescales, there will be a particular emphasis on the interannual variability of synoptic and low frequency upwelling during the years of large-scale climate phenomena, i.e., the 2014 marine heatwave, the 2015 – 2016 El Niño, and the 2018 – 2019 El Niño.

The observations used in this chapter are unique because (1) they provide comprehensive coverage of the physical and biogeochemical properties in the coastal ocean and (2) they have been ongoing for over a decade with continued operations. Section 3.2 describes the data that have been collected over the last 10 years. Additionally, this section presents the method for how upwelling events are detected for the analysis on synoptic upwelling, discusses how the cross-shore velocity profiles are averaged to characterize the flow field on synoptic and seasonal timescales along with deriving 2D cross-shore transport from the ADCP data, and reviews the Burger number for how this scalar and a steady state theory relate to the cross-shore velocity profiles. Section 3.2 also explains how the source water depth is determined as part of the analysis presented in Section 3.3 on low frequency modulators of upwelling and this section

presents the method for how nitrate is predicted for comparison against observed nitrate in Section 3.3.

In Section 3.3, synoptic and low frequency upwelling are examined with respect to the oceanic upwelling responses and the factors that alter upwelling. First, upwelling event statistics are computed to understand changes in the synoptic oceanic upwelling response and in the upwelling forcing particularly during the 2014 marine heatwave, the 2015 – 2016 El Niño, and the 2018 – 2019 El Niño. Cross-shore currents are characterized during synoptic upwelling events and interannual variability in the 2D ADCP derived cross-shore transport is investigated. Then, the low frequency variability in the oceanic upwelling response including the 2D cross-shore transport are assessed. Processes that govern the background variability in upwelling are studied and how these vary in the years of the large-scale climate phenomena. Section 3.4 concludes this chapter with a review of the results presented in Sections 3.3.

3.2 Data Sets and Methods

3.2.1 Upwelling Data Sets

3.2.1.1 Mooring Measurements

For the analysis on upwelling, data come from the CCE2 mooring (Figure 3.1). CCE2 has been in operation since 2010, and it is located 25 km offshore and lies in ~840 m water depth. This mooring is positioned off Point Conception which is a region of high upwelling. Regarding the physical properties observed, the mooring measures temperature and salinity in the upper 80 m. For the first several years, there are no temperature and salinity data below 40 m depth. So, temperature and salinity are linearly regressed between 40 and 80 m depth prior to 2014 using the 40 m temperature and salinity observations over 2014 – 2021 with the 80 m temperature and salinity observations in these years. The CCE2 mooring is equipped with an ADCP, and the

north-south and east-west velocity components are rotated into the alongshore and cross-shore directions. This angle of rotation is 60° west of true north based on the decorrelation between the two velocity components.

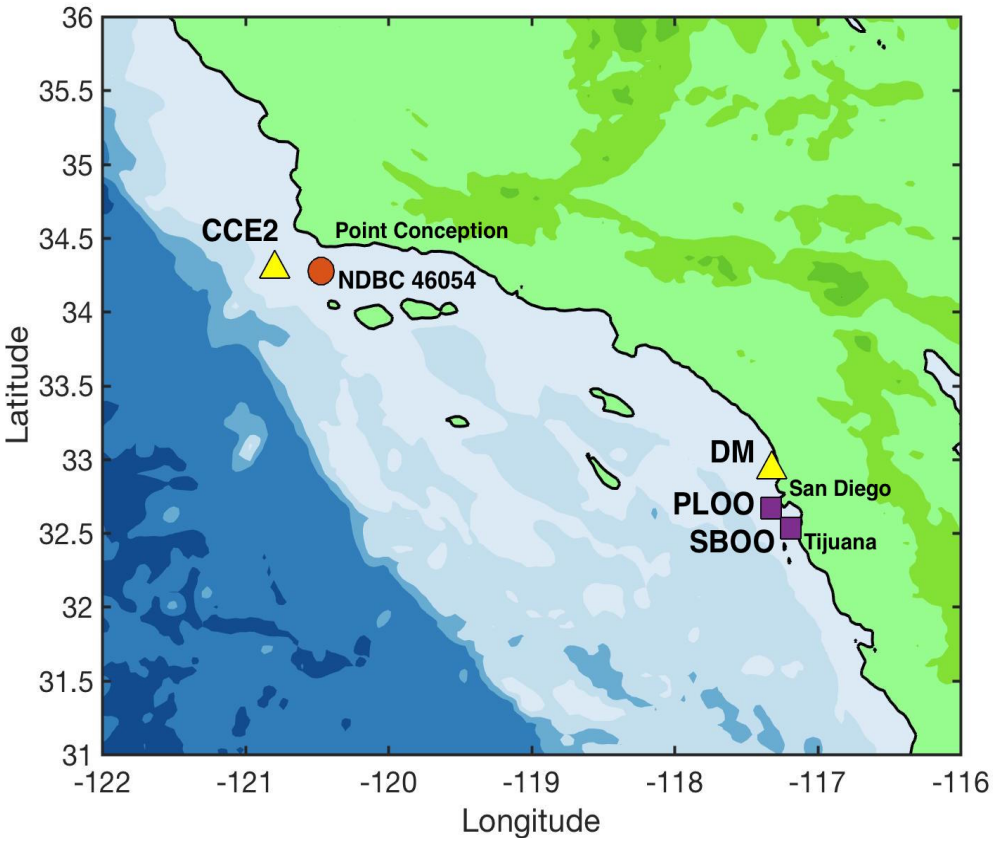

Figure 3.1: Map of southern California with the CCE2 mooring (yellow triangle) and the NDBC 46054 buoy (orange circle) near CCE2.

The CCE2 mooring has a package of biogeochemical sensors at 15 m depth that measure dissolved oxygen, pH, nitrate+nitrite, and Chl-*a* fluorescence. At 75 m depth there is an additional oxygen sensor. At the surface the mooring has an array of sensors, including xCO_2 measurements in the ocean and in the air. Mooring sensors sample hourly or faster, and the data are daily-averaged for the analysis presented in Section 3.3.

The CCE2 temperature and salinity sensors are calibrated with water samples before and after deployment to remove instrument drift. The details of this processing procedure are outlined in Chapter 2 and in Kanzow et al. (2006). Oxygen data are also processed in a similar

manner with water samples collected pre- and post-deployment for validating the sensor. The CCE2 oxygen measurements are also compared against CalCOFI data from Line 80 Station 55, i.e., the same CalCOFI location as the CCE2 site, and an adjustment factor is applied if needed. The CCE2 pH data are calibrated based on calibrations at the start and end of each deployment from water samples evaluating carbon content. Moreover, throughout the deployment additional calibration coefficients are determined during times when the mixed layer extends down to the depth of the pH sensor. This allows for a more comprehensive calibration by comparing subsurface pH measurements to pH calculated at the surface (Bresnahan et al. 2014).

The surface pH is calculated based on a regional empirical relationship and is estimated from pCO2 and total alkalinity, the latter of which is calculated from temperature and salinity based on a regional empirical relationship as described in Alin et al. (2012). The CCE2 pCO_2 data are derived from xCO_2, the mole fraction of CO_2 which is measured for both seawater and air. The details of these measurements and the determination of pCO_2 from xCO_2 are provided in Sutton et al. (2014). The difference in pCO_2 from seawater and the air is positive when there is an uptake of CO_2 by the ocean.

The nitrate+nitrite (hereafter "nitrate") data at CCE2 is measured with a SUNA uv-optical nitrate sensor. Data are processed using a baseline correction that adjusts for sensor drift during deployments. The SUNAs are calibrated in the laboratory with known nitrate standards before and after each mooring deployment and also at sea, immediately before and after deployment using Niskin bottle samples. For the CCE2 deployments in 2015 and 2016, the nitrate sensor failed, and reconstructed nitrate is used which is determined from the temperature data and a regionally derived temperature-nitrate relationship (see Lilly et al. 2019 for a complete discussion). Chlorophyll-*a* fluorescence data likewise have a baseline correction

applied, are converted to Standard Fluorescence Units (SFU) based on the relationship between the fluorometer voltages and laboratory prepared chlorophyll-*a* samples, and are compared

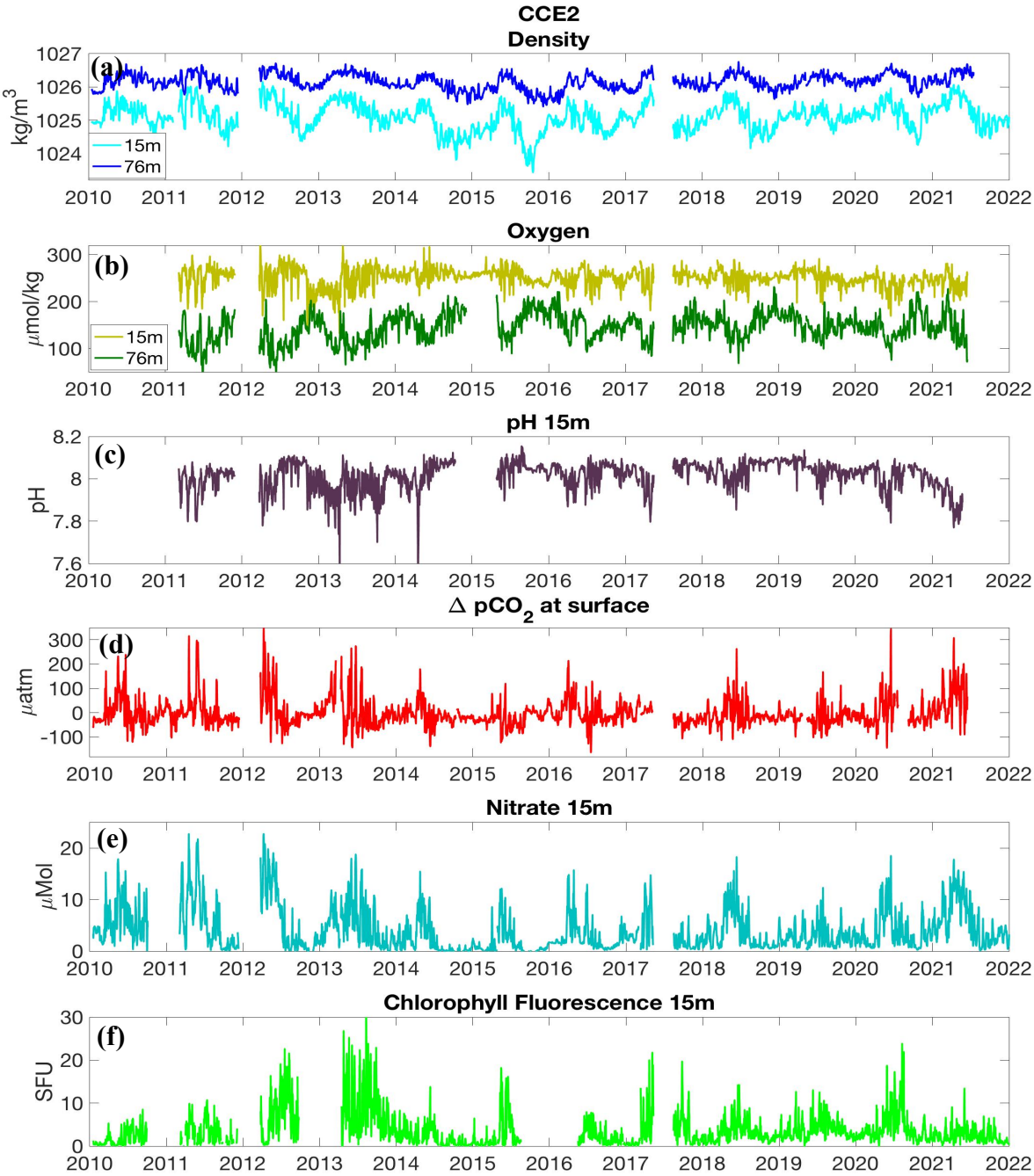

Figure 3.2: CCE2 timeseries of in-situ measurements which include (a) density at 15 and 75 m depths, (b) oxygen at 15 and 75 m depths, (c) pH at 15 m depth, (d) ΔpCO_2 between the ocean and the air, (e) nitrate at 15 m depth, and (f) chlorophyll fluorescence at 15 m depth.

against CalCOFI data to make any additional adjustments. A review of the calibration procedure for nitrate and fluorescence is given in Lilly et al. (2019).

The processed data shown in Figure 3.2 illustrate the long timeseries of multiple co-located physical and biogeochemical measurements at the CCE2 mooring. In Figure 3.2 there are a few data gaps. Notably, at CCE2 there are no oxygen and pH data at 15 m depth and no oxygen data at 76 m depth in 2010. As mentioned above, the deepest temperature and salinity instrument at 76 m depth was not implemented until 2014, so prior to this time density information is reconstructed based on density data at 40 m depth, i.e., the next deepest sensor. The reconstructed density at 76 m depth correlates well with the measured density at this depth over 2014 - 2021 and has a correlation of 0.90 and a rms error of 0.106 kg/m^3. Both winter 2011/2012 and summer 2017 contain months when the CCE2 mooring was not deployed, so no measurements were made at these times. This may have some impact on the upwelling event statistics presented in Section 3.3 as 2012 and 2017 may be underrepresented.

The World Ocean Atlas (WOA) 2013 provides climatological averages of vertical profiles of temperature and salinity. The climatological averages are computed over a period from 1955 - 2012. These objectively analyzed climatological fields incorporate several observational data sources (Locarnini et al. 2013; Zweng et al. 2013), and the climatological profiles aid in gridding the temperature and salinity fields at CCE2 as discussed in Section 3.2.4.2.

3.2.1.2 Wind Measurements and Upwelling Index

To assess the strength of the upwelling forcing, hourly-averaged wind measurements near the CCE2 mooring are obtained to calculate wind stress. The wind data come from NDBC buoy 46054 (Figure 3.1) and wind stress is calculated as,

$$\boldsymbol{\tau} = \rho_a c_d \boldsymbol{U}^2. \quad (1)$$

In equation (1), ρ_a is the density of air, c_d is the drag coefficient, and $\boldsymbol{U}$ contains the u and v components of the wind velocity. The drag coefficient is parameterized using the approach demonstrated in Edson et al. (2013) that is originally derived in Hersbach (2011). Wind stress is daily-averaged and projected into the alongshore and cross-shore components, where the alongshore direction is taken to be 60° west of true north.

Two gaps occur in the NDBC buoy 46054 timeseries which are over February – September 2010 and August 2018 – October 2019. These gaps are filled in with CCMPv2 wind data that have been interpolated at the NDBC buoy location. Prior to filling in the NDBC wind data gaps, the CCMPv2 wind data are regressed to better agree with the NDBC buoy winds. As discussed in Chapter 2 Appendix B, the CCMPv2 wind product underestimates alongshore winds immediately off Point Conception, so the regression reduces the rms error between NDBC 46054 winds and CCMPv2 winds.

The 2D Ekman transport is then calculated from the NDBC alongshore wind stresses as,

$$\mathrm{M^x} = \frac{-1}{\rho \mathrm{f}} \tau^{\mathrm{y}}. \quad (2)$$

In equation (2), ρ is the seawater density, f is the Coriolis parameter, and τ^y is the alongshore component of the wind stress.

In Chapter 2, an upwelling index was constructed, the CCUI, that approximates vertical transport across the 50 m layer over southern California. The index, which accounts for both wind stress and alongshore pressure gradients, is a regional representation of the physical upwelling strength, which is assessed as a measure of the upwelling forcing alongside the local NDBC wind stress. The vertical transport from the CCUI is in Sv and for much of the analysis in

this chapter the CCUI is normalized by the length along the coastline to yield the 2D transport in m^2/s.

3.2.2 Upwelling Event Detection

The procedure for detecting synoptic upwelling events is presented first, followed by a description of the event statistics that will be calculated on the detected upwelling events.

3.2.2.1 Upwelling Event Detection Procedure

A chapter objective is to analyze upwelling on event timescales, so to assess synoptic upwelling the physical and biogeochemical properties will be used to detect upwelling events. Upwelling events are oftentimes defined when the wind reaches a certain speed and blows persistently over a particular number of days (Cury and Roy 1989; Roughan et al. 2006; Wilkerson et al. 2006; García-Reyes et al. 2014; Aguirre et al. 2021). Here, a new method is developed for identifying upwelling events on timescales of days to weeks. Rather than relying on wind speed for event determination, upwelling events are detected using a suite of physical and biogeochemical components based on the mooring observations. Upwelling events that occur during the upwelling season, i.e., February – June, are used for analysis. Generally, wind forcing is the primary driver of upwelling events, but CTWs may account for some fraction of the observed changes (Chapter 2). Since the wind field is not used in classifying the upwelling events, CTWs that modify the in-situ properties in a manner similar to the effect of upwelling favorable winds are inherently included using this method for event detection.

The set of physical and biogeochemical variables used to detect upwelling events are listed in Table 3.1. Using multiple variables facilitates detecting common occurrences of upwelling-like fluctuations. For example, during upwelling isopycnals heave, and a stationary sensor in the upwelling zone will measure increased density as denser waters are displaced

upward. These denser waters are generally less oxygenated, more acidic, and contain higher nutrient concentrations than the overlying less dense waters. Table 3.1 lists the expected direction, i.e., increase or decrease, of a property change during the upwelling phase of an event. As upwelling relaxes, properties that increased during the upwelling phase will decrease and properties that decreased during upwelling will increase. Including both physical and biogeochemical responses of upwelling takes into account the ecosystem impact for the definition and the detection of events.

Table 3.1: CCE2 mooring in-situ measurements used for upwelling event detection. Inc. stands for Increase and Dec. is abbreviated for Decrease.

Measured Property	Density	Oxygen	pH	ΔpCO2	Nitrate	Density	Oxygen
Sensor Depth (m)	15	15	15	surface	15	76	76
Upwelling (Relaxation) Response	Inc. (Dec.)	Dec. (Inc.)	Dec. (Inc.)	Inc. (Dec.)	Inc. (Dec.)	Inc. (Dec.)	Dec. (Inc.)

The routine for detecting upwelling events begins with inspecting each timeseries for localized peaks. A localized peak is considered to be a local maximum or a local minimum depending on the variable of interest and its anticipated response to upwelling (Table 3.1). For example, density is expected to increase at a fixed point as observed by a stationary sensor during the upwelling phase so local maxima values in density are noted. In contrast, dissolved oxygen levels are anticipated to decrease during the upwelling phase so local minimum values are recorded. For each variable, a particular amplitude threshold is implemented such that the local maximum or minimum value must meet this criterion in order to be considered a potential upwelling event. The threshold for each variable is a subjective choice based on the timeseries of the data. The thresholds are selected to yield a similar number of localized peaks across all variables. The influence of this threshold selection on the upwelling event statistics is examined

in Appendix A and is shown to not significantly alter the interannual variability of the event statistics. When multiple variables capture upwelling-like fluctuations, then this is classified as an upwelling event.

The times of the local maxima/minima are grouped, and they must be within five days of each other. The mean of these times is termed the peak time. The peak time distinguishes the

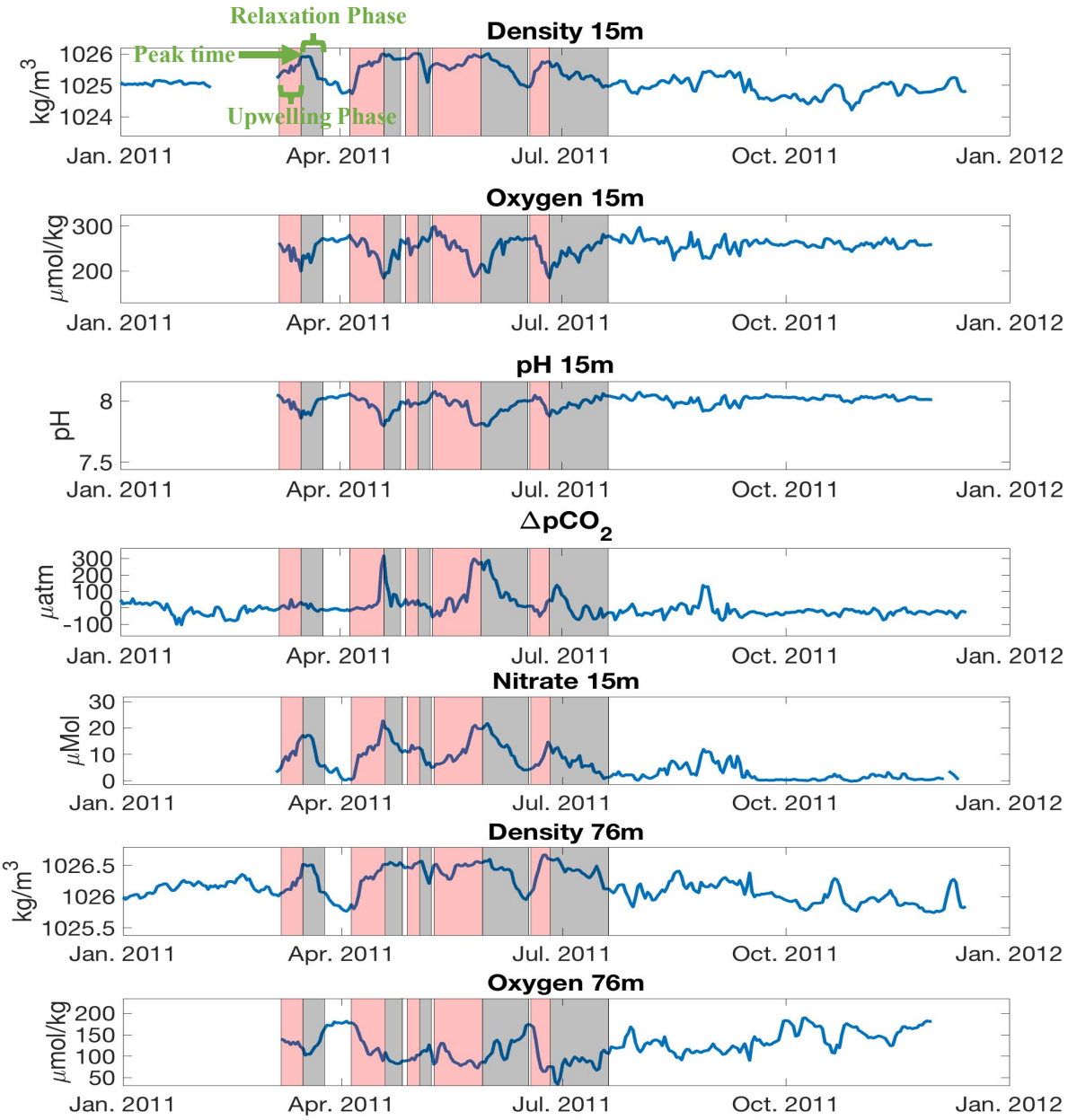

Figure 3.3: CCE2 physical and biogeochemical properties used for upwelling event determination. Red shading represents the upwelling phase and gray shading illustrates the relaxation phase.

upwelling phase from the relaxation phase of the upwelling event. The start of the upwelling phase is defined as the average of the variable times which mark the beginning of a property increase (for density, ΔpCO2, and nitrate) or the beginning of a property decrease (for oxygen and pH). Similarly, the end of the relaxation phase is determined as the average of times denoting the end of a property decrease (for density, ΔpCO2, and nitrate) or increase (for oxygen and pH). Figure 3.3 demonstrates this approach for determining upwelling events and the classification of the start and end times.

3.2.2.2 Event Statistics Calculated

Event statistics are computed on the detected upwelling events to assess year-to-year changes in upwelling at synoptic time scales. The event statistics computed are event intensity, event duration, and the number of upwelling events in the upwelling season from February - June. These statistics are analyzed because they help characterize upwelling strength and are suggestive of the potential for biological productivity. Another event statistic calculated is the cumulative intensity. Unlike the other three event statistics, this statistic is calculated on the upwelling forcing data sets as oppose to the physical and biogeochemical data.

A.) Upwelling Response Event Statistics

The event intensity is the magnitude of the difference between the maximum and minimum values during an upwelling event. The intensity for any variable is thus always positive regardless of the upwelling behavior of a variable listed in Table 3.1. This statistic characterizes the range of values occurring within an upwelling event and is suggestive of the strength of the ocean's response to wind-driven and pressure gradient forcing. Larger upwelling intensities in the physical and biogeochemical properties signify stronger physical forcing of upwelling.

The second statistic assessed is the event duration, which investigates separately the length of the upwelling and relaxation phases as defined in Section 3.2.2.1 and shown in Figure 3.3. The length of the upwelling phase is calculated as the number of days between the start of the upwelling period up until the peak time. The duration of the upwelling phase can impact upwelling productivity and ocean acidification. Without changes in the upwelling intensity, longer events promote cumulatively more upwelled nutrients than shorter events. So, both the intensity and the length of active upwelling can modify ocean acidification. This may be accompanied by changes in pH and dissolved oxygen since these water properties are influenced by vertical heaving of isopycnals during upwelling events. Strong and/or persistent upwelling can cause acidic and hypoxic conditions harmful to calcareous organisms and benthic feeders (Chan et al. 2008; Fabry et al. 2008; Feely et al. 2008; Nam et al. 2011; Low et al. 2021).

The third statistic evaluated is the number of upwelling events in the upwelling season and this captures the occurrence of synoptic upwelling. The number of events during the upwelling season indicate the number of incidents that may lead to an ecological upwelling response.

B.) Upwelling Forcing Event Statistic

The event cumulative intensity is the sum of the 2D transport over the upwelling phase of the upwelling events. This statistic accounts for both the strength of the upwelling forcing and the duration of the event upwelling phase. The event cumulative intensity is calculated from the NDBC 2D Ekman transport and the CCUI normalized by coastline length.

3.2.3 Cross-shore Velocity Profiles and Cross-shore Transport

The cross-shore currents are part of the oceanic upwelling response. The vertical structure in the cross-shore velocities is an important component of the wind-driven overturning

upwelling circulation, and this is expected to vary from year-to-year based on the wind-driven forcing. The vertical structure in the horizontal velocity fields is characterized for synoptic and seasonal upwelling, and these mean velocity profiles will be studied in Section 3.3. Year-to-year changes in the 2D ADCP cross-shore transport will be assessed in Section 3.3 as part of the emphasis on the interannual variability in upwelling during the 2014 marine heatwave, the 2015 – 2016 El Niño, and the 2018 – 2019 El Niño. In addition to the ADCP estimate of cross-shore transport, there are two other estimates of the 2D cross-shore transport. These two other estimates are the 2D Ekman transport derived from local wind stress and the CCUI which is normalized by the length along the coastline.

3.2.3.1 Cross-shore Velocity Profiles

The mean cross-shore velocity profiles are determined from the CCE2 ADCP data to characterize the cross-shore velocity fields during synoptic and seasonal upwelling. For both timescales of interest, the cross-shore velocity profiles are constructed over the upwelling and relaxation periods. For synoptic upwelling events, the upwelling and relaxation periods are the upwelling and relaxation phases of the upwelling events. For seasonal upwelling, the upwelling and relaxation periods are the upwelling and relaxation seasons. The procedure for determining the mean upwelling and relaxation velocity profiles for both timescales of interest are described below.

For synoptic upwelling, the cross-shore CCE2 ADCP velocities are band-pass filtered over 3 – 100 days. The cross-shore velocity anomalies are then temporally averaged over the upwelling and relaxation phases for each upwelling event. For each upwelling event, the depth-averaged velocity is removed to suppress barotropic fluctuations unrelated to overturning

upwelling. The velocity profiles are annually averaged, i.e., averaged over all upwelling events during the upwelling season, which is defined to be from February – June.

For seasonal upwelling, the band-passed cross-shore velocities described above are removed from the total cross-shore velocity field and these residual velocities are averaged over the upwelling season, i.e., February – June. This creates the cross-shore upwelling velocity profiles for each year where the depth average mean is removed to suppress barotropic fluctuations unrelated to overturning upwelling. The cross-shore velocity profiles representative of the relaxation season are determined in a similar manner. For the relaxation profiles, the residual horizontal velocities are averaged over the relaxation season, i.e., July – December, for each year. This creates the cross-shore relaxation velocity profiles for each year where the depth average mean is removed.

3.2.3.2 2D Cross-shore Transport

Interannual variability in the 2D cross-shore transport will be examined as part of the oceanic upwelling response on both synoptic and seasonal timescales. There are three ways for calculating the 2D cross-shore transport and the results will be shown in Section 3.3. Below, the three different methods for calculating the cross-shore transport are discussed.

On synoptic timescales, the first way the 2D cross-shore transport is calculated uses the CCE2 ADCP data. The band-passed filtered cross-shore velocity anomalies derived in the previous section that are averaged over the event upwelling phases and then annually averaged are integrated over the upper ADCP bins from 14 – 50 m depth. This yields the 2D ADCP cross-shore transport. In addition to the 2D ADCP transport, the second way 2D cross-shore transport is determined is from the NDBC 2D Ekman transport. The NDBC 2D Ekman transport is band-passed filtered over 3 – 100 days and these anomalies are averaged over the upwelling phase of

the upwelling events and then averaged over all events in a year. The third estimate of the 2D transport comes from the CCUI. As with the 2D Ekman transport, the CCUI is band-pass filtered and the anomalies are averaged in the same manner as the 2D Ekman transport. The CCUI annual averages are normalized by a coastline length of 100 km to give the 2D transport.

On seasonal timescales, the 2D ADCP cross-shore transport is determined from the seasonal averages, i.e., the upwelling season, of the cross-shore velocity data derived in the previous section. These velocities are vertically integrated over the upper 50 m, however, for the interannual variability in 2D cross-shore transport, the depth-average velocities are not removed from the seasonal averages. The cross-shore transport from the NDBC 2D Ekman transport and the CCUI data are handled similarly as the CCE2 ADCP data, where the synoptic component is removed from the total signal and the residuals are averaged over the upwelling season, i.e., from February – June.

3.2.4 Steady State Theory and Burger Number

The vertical structure in the cross-shore flow is important for the depth of upwelled waters, and consequentially the nutrient supply, as well as for the upper ocean 2D cross-shore transport. The physical flow regime at CCE2 may be governed by a topographic Burger number, as previously reported for other EBUS (Lentz and Chapman 2004). A steady state theory presented in Lentz and Chapman (2004) will be reviewed and the Burger number calculation will be presented. The calculated CCE2 Burger number will be reported in Section 3.3 and the steady state theory will be tested with the CCE2 ADCP data in Section 3.3.

3.2.4.1 Steady State Coastal Upwelling Theory

In a theory presented by Lentz and Chapman (2004), the depth of the onshore Ekman return flow reflects which term in the alongshore momentum equation balances the alongshore

wind stress. Onshore return flow in the interior indicates a balance between the wind stress and the divergence of the cross-shore momentum flux, while onshore return flow in the bottom boundary layer signifies that the wind stress is balanced largely by bottom friction.

In the steady state theory for two-dimensional coastal upwelling presented by Lentz and Chapman (2004), the depth of the onshore return flow is qualitatively proxied as the magnitude of the topographic Burger number,

$$S = \frac{\alpha N}{f}. \tag{3}$$

In equation (3), α is the bottom slope and N is the stratification, which is calculated as the buoyancy frequency as,

$$N^2 = -\frac{g}{\rho_0}\frac{\partial \rho}{\partial z}. \tag{4}$$

As part of the steady state theory, a larger Burger number indicates that the return flow occurs in the interior, i.e., a balance between wind stress and the divergence of the cross-shore momentum flux, and a smaller Burger number signifies that the return flow is in the bottom boundary layer, i.e., a balance between wind stress and bottom friction.

3.2.4.2 CCE2 Burger Number Calculations

A.) Calculation Overview

The Burger number will be calculated for synoptic upwelling events, the upwelling season, and the relaxation season at CCE2. For calculating the Burger number, the bottom slope is estimated to be 0.01 from the ETOPO global relief model. The stratification used in equation (4) is the buoyancy frequency averaged over the upper 125 m. This layer is similar to the layer thickness over which stratification is averaged at other EBUS sites (Lentz 1992). For each timescale of interest, the upper 125 m buoyancy frequency is temporally averaged to obtain a

representative stratification value. For synoptic upwelling events, the upper 125 m averaged buoyancy frequency is averaged over the upwelling phase of the upwelling events. Then the record-long mean buoyancy frequency is averaged over all events and this value is used in equation (3). For the upwelling season, the upper 125 m averaged buoyancy frequency is averaged over the upwelling season, i.e., February – June. The record-long mean is the averaged buoyancy over all upwelling seasons. For the relaxation season, the upper 125 m averaged buoyancy frequency is averaged over the relaxation season, i.e., July – December. The record-long mean is the averaged buoyancy over all relaxation seasons.

B.) Upper 125 m Averaged Buoyancy Frequency

The Burger number calculations use the buoyancy averaged in the upper 125 m. The CCE2 mooring only measures density in the upper 80 m, so density must be approximated between 80 and 125 m depths. Gliders periodically profile at the CCE2 mooring site starting in 2013 (see Chapter 2 Section 2.2.2.1 for a full description) and they do sample density in the upper ~600 m. The gliders do a mixture of station keeping and cross-shore transects, so they are not always at CCE2, and they do not provide measurements of density before 2013. To approximate density over the upper 125 m, both the mooring and the glider observations are utilized as follows.

Temperature and salinity fluctuations at the deepest mooring sensor are assumed constant and are extrapolated down to 125 m. The fluctuations are determined based on removing the WOA mean temperature and salinity at the depth of the deepest sensor. The extrapolated temperature and salinity fluctuations then add the WOA mean temperature and salinity over 80 – 125 m depths. This procedure is similar to how temperature and salinity were estimated at CCE2 in the bottom layer in Chapter 2 (see Chapter 2 Appendix A). With these approximations of

temperature and salinity, density is computed and the buoyancy frequency is calculated. Before mid-2014 and after mid-2021, the deepest mooring sensor was at 40 m depth, so temperature and salinity fluctuations in these times come from the 40 m sensor.

To assess this approach in approximating the layer averaged buoyancy frequency over the upper 125 m, the glider derived upper 125 m averaged buoyancy frequency is compared to the layer averaged buoyancy from the mooring data (Figure 3.4). The averaged buoyancy from the mooring data is well correlated, i.e., a correlation of 0.90, with the glider averaged buoyancy and the rms error is 1.30×10^{-5} $1/s^2$. This demonstrates that this approach for approximating the upper 125 m averaged stratification is reasonable.

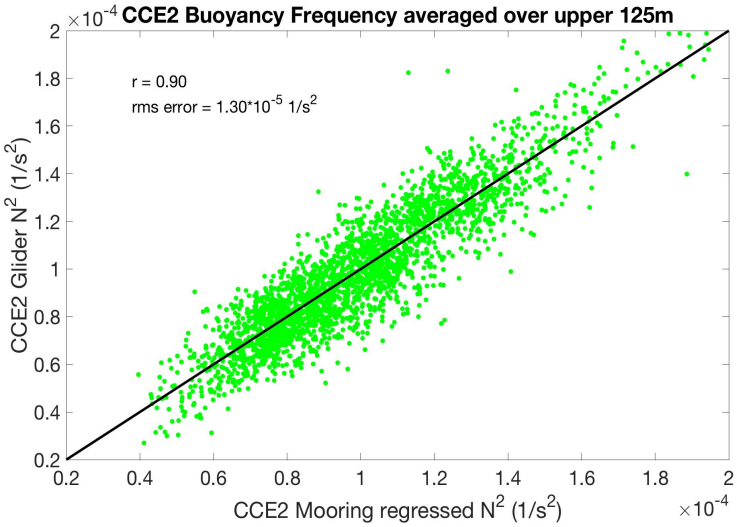

Figure 3.4: CCE2 upper 125 m averaged buoyancy from the glider data against the upper 125 m averaged buoyancy estimated from the extrapolated mooring data set. The black line shows the 1-1 fit. The correlation and the rms error are reported in the figure.

3.2.5 Source Water Depth

The cross-shore velocity profiles discussed in Section 3.2.3 are one proxy of the source water depth. On seasonal timescales and longer, the source water depth will also be estimated from a source water depth parameterization. Both approaches for estimating the source water depth will be used to assess typical source water depths at CCE2 in Section 3.3.

3.2.5.1 Source Water Depth Scaling

The source water depth is the depth from which water originates when it is brought to the surface during the upwelling process. Many physical and biogeochemical properties in the ocean change with depth, so the characteristics of the water upwelled to the surface depend on the depth from which the water came. The source water depth is influenced by both wind stress and stratification. Greater upwelling-favorable wind stresses enhance wind-driven overturning, cause mixing, and decrease buoyancy in the ocean. The wind stress may directly influence source water depth by modifying the overturning upwelling circulation and indirectly through its effect on the stratification, e.g., wind-driven mixing decreasing the stratification in the upper ocean. A weaker stratification is less inhibitory to the vertical fluxes of properties, thereby facilitating upwelling processes such as the uplifting of cooler, denser waters from below and the mixing of nutrients upwards (Roemmich and McGowan 1995; Bograd and Lynn 2003).

Recent work by He and Mahadevan (2021) used both the wind stress and the buoyancy frequency to parameterize the depth of source waters based on a nonlinear relationship as follows,

$$D_s = \left(\frac{4\tau}{C_e \rho_0 N f}\right)^{1/2}. \quad (5)$$

In this equation C_e is an efficiency factor set to 0.06 as in He and Mahadevan (2021) and N is the stratification that is determined by the buoyancy frequency. Equation (5) for the source water depth represents the opposing influences of wind stress and buoyancy on the depth of source waters. On seasonal timescales and longer, this parameterization from He and Mahadevan (2021) is applicable to any EBUS including southern California.

3.2.5.2 CCE2 Source Water Depth Calculations

To compute the source water depth as in equation (5), both the wind stress and the buoyancy frequency must be known. Local wind stresses from the NDBC 46054 buoy near the CCE2 mooring are used, and the stratification is determined from equation (4) where the buoyancy frequency is averaged over the upper 125 m.

The annual cycle of the source water depth was computed based on data over 2010 – 2021 (not shown) and compared to a source water depth climatology for California from a regional ocean model (Figure 3 in Jacox et al. 2015). The annual cycle of the source water depth estimated from equation (5) is about 35 m deeper than the source water depth climatology from Jacox et al. (2015), therefore the source water depth is shifted to be 35 m shallower to agree better with Jacox et al. (2015). The source water depth is examined in Section 3.3 as part of the analysis on the processes that modify low frequency upwelling variability and will be qualitatively compared against the mean seasonal cross-shore velocity profile discussed in the previous section.

3.2.6 CCE2 Nitrate Prediction

As part of the analysis on interannual variability in upwelling, nitrate is predicted and compared to the observed nitrate. Two processes that govern year-to-year changes in upwelling are the nutricline depth and the regional source waters. The nutricline depth is strongly related to the depth of isopycnals in the range of 1025.8 - 1026 kg/m^3 (Collins et al. 2003; Jacox et al. 2015; Jacox et al. 2016; Zaba and Rudnick 2016), so changes in the nutricline depth reflect isopycnal heaving. Both the nutricline depth and the regional source waters will be discussed in Section 3.3. By comparing the predicted nitrate to the observed nitrate at CCE2 15 m depth, the nutricline depth, i.e., isopycnal shoaling, and the regional source waters are tested to see how

well they can explain the interannual variability in nitrate concentrations. Nitrate is predicted using the mean water mass composition on isopycnals, the CCE2 along isopycnal water mass anomalies, and nitrate content representative of the regional source waters. The nutricline depth, i.e., isopycnal shoaling, is accounted for by incorporating the isopycnal mean water mass composition, and changes in the regional source waters are included in the nitrate prediction through the along isopycnal water mass anomalies.

Regional water masses have different nutrient properties and the composition varies with density, so the fractional amounts of the source waters are important as they influence the nutrients available for biological productivity. This demonstrates that the water mass composition and the nitrate content of the regional water masses are two important criteria for predicting nitrate. First, the water mass composition is determined. The nitrate observations at CCE2 are at 15 m depth, so to compare predicted nitrate to the observed nitrate, the water mass composition must be determined at 15 m. The water mass analysis from Chapter 1 cannot be executed at this depth because it is within the mixed layer and temperature is not conserved. Therefore, the water mass composition at 15 m depth is estimated as follows.

The water mass composition at 15 m depth is determined as the sum of the mean isopycnal water mass composition and the along isopycnal anomalies. The mean isopycnal water mass composition is evaluated from the CCE2 water mass analysis that was performed at 76 m depth in Chapter 1. The fractional composition of water masses is averaged on isopycnals to calculate the mean isopycnal composition. As isopycnals heave, i.e., changes in the nutricline depth, this causes changes in the water mass composition. So, the isopycnal mean water mass composition accounts for variability in the nutricline depth.

The second component in computing the 15 m water mass composition is the along isopycnal anomalies. This accounts for changes in the fractional amounts of regional waters due to advection. This information is gathered from the water mass anomalies at 76 m depth, where the anomalies are assumed to be constant upward, i.e., the anomalies at 76 and 15 m depths are the same. For each day, these anomalies are added to the mean isopycnal composition, where the mean composition depends on the daily density. One limitation of this procedure for evaluating the 15 m water mass composition is that the mean water mass composition for the densities measured at 15 m depth is not always known. Lighter densities are not measured at the 76 m depth, so the mean composition for these shallower isopycnals is not known from the 76 m water mass analysis. Specifically, this method can only estimate the 15 m water mass composition when the 15 m density is 1025.5 kg/m^3 or greater.

Table 3.2: Nitrate content of the regional water masses from Bograd et al. (2019) on select isopycnals.

	PSUW	**PSUW**	**PEW**	**PEW**
Density (kg/m^3)	1025.6	1026.4	1026.2	1026.8
Nitrate (μM)	10.33	22.21	28.38	36.41

The nitrate content of the regional water masses is the second criteria needed for predicting nitrate. Bograd et al. (2019) estimated the nitrate content of the regional source waters on specific isopycnals (Table 3.2). To extend the characterization of nitrate on isopycnals from Bograd et al. (2019), the nitrate content is assumed to vary linearly between isopycnals. The approximated nitrate on an isopycnal is multiplied by the estimated 15 m water mass composition, i.e., the sum of the mean isopycnal composition and along isopycnal anomalies, to determine the predicted nitrate and this is reported in Section 3.3.

3.3 Upwelling Variability Results and Discussion

Upwelling is examined from observations made off Point Conception, CA at synoptic and low frequency timescales. At both timescales of interest, the oceanic response is studied

followed by an investigation of factors that influence upwelling. A particular emphasis is placed on changes in upwelling during the 2014 marine heatwave, the 2015 – 2016 El Niño, and the 2018 – 2019 El Niño.

3.3.1 Synoptic Upwelling Events

To characterize synoptic upwelling in southern California, the oceanic upwelling response and the upwelling forcing are examined. The oceanic upwelling response is the change in the physical and biogeochemical properties related to upwelling. To analyze the upwelling response, upwelling statistics are calculated on the detected upwelling events, where the event detection procedure was described in Section 3.2.2. The upwelling response also includes the cross-shore currents, so these are assessed as well. Then, the upwelling forcing is examined and these are the drivers of upwelling, i.e., wind stress and pressure gradients. The statistics on the upwelling forcing will be presented. A particular emphasis will be placed on the interannual variability in synoptic upwelling, i.e., upwelling response and upwelling forcing, in the years of the large-scale climate phenomena.

3.3.1.1 Oceanic Response

The oceanic upwelling response is assessed on synoptic timescales beginning with the correlation amongst the physical and biogeochemical parameters. This demonstrates that upwelling events are a significant process that influence the temporal variability in the in-situ conditions and motivates investigating upwelling at this timescale. Event statistics characterize synoptic upwelling, and year-to-year changes in the statistics are evaluated. The oceanic upwelling response also includes the cross-shore currents. The cross-shore flow is characterized for synoptic upwelling, and the synoptic 2D upper 50 m cross-shore transport is investigated for

changes during the years of the large-scale climate phenomena, i.e., the 2014 marine heatwave, the 2015 – 2016 El Niño, and the 2018 – 2019 El Niño.

A.) Property Correlations

To demonstrate that the subseasonal variability is largely due to synoptic upwelling events, the CCE2 physical and biogeochemical timeseries are band-pass filtered over 3 - 100 days. This filter removes the low-frequency variability and the annual cycle. Table 3.3 reports the correlations between the different CCE2 physical and biogeochemical properties at a lag of 0 days. There is generally moderate to good agreement between the physical and biogeochemical properties over the duration of the record, particularly with those located at the same depth. The physical and biogeochemical measurements are also compared to the local wind stress with the max lagged correlation reported in Table 3.3. Maximum correlation occurs when the wind stress leads by 2 - 3 days. Overall, the correlations demonstrate a relationship between the properties,

Table 3.3: CCE2 correlations amongst in-situ measurements of physical and biogeochemical properties. Correlations are computed over the band-passed data. The 95% confidence interval is listed. For wind stress, values in parentheses are the number of days at which the maximum correlation occurs.

	Oxygen 15m	**pH 15m**	**ΔpCO_2 surface**	**Nitrate 15m**	**Density 76m**	**Oxygen 76m**	**Wind Stress**
Density 15m	-0.43 ± 0.03	-0.52 ± 0.02	0.30 ± 0.03	0.72 ± 0.01	0.65 ± 0.02	-0.50 ± 0.03	-0.30 (4)
Oxygen 15m		0.80 ± 0.01	-0.60 ± 0.02	-0.68 ± 0.02	-0.33 ± 0.03	0.33 ± 0.03	0.31 (3)
pH 15m			-0.63 ± 0.02	-0.72 ± 0.02	-0.33 ± 0.03	0.29 ± 0.03	0.31 (3)
ΔpCO_2 surface				0.66 ± 0.02	0.03 ± 0.03	0.40 ± 0.03	-0.42 (2)
Nitrate 15m					0.46 ± 0.03	-0.34 ± 0.03	-0.36 (3)
Density 76m						-0.82 ± 0.01	-0.17 (7)
Oxygen 76m							0.12 (6)

and some of this variability is related to synoptic wind forcing. The good correlation suggests that upwelling events are a significant process occurring in the coastal ocean that influence the temporal variability in the in-situ conditions and motivates inspecting year-to-year changes in subseasonal upwelling through the interannual variability of upwelling events.

B.) Event Statistics

To assess interannual variability in the oceanic upwelling response, three statistics are computed on the detected upwelling events. The statistics computed are event intensity, event duration, and the number of upwelling events in the upwelling season. The calculations of these statistics were described in Section 3.2.2 and the results are presented below.

B1.) Upwelling Event Intensity

Annual averages of the event intensity for the 3 - 100 day band-pass filtered physical and biogeochemical variables demonstrate substantial interannual variability (Figure 3.5). The 2011 and 2012 event intensity averages are above the long-term mean for all of the variables in Figure 3.5. Most of these averages are statistically different from the long-term mean, and this supports a stronger oceanic response on event time scales in these upwelling seasons.

In the years encompassing the large-scale climate phenomena, both the 2014 and 2016 seasonal averages of event intensity display mixed behavior regarding the relative strength of the oceanic response to synoptic upwelling. For example, the 2014 and 2016 15 m oxygen, ΔpCO_2, and nitrate seasonal averages are below normal indicative of reduced upwelling. In contrast, other variables, e.g., the 2014 15 m pH, the 2014 and 2016 76 m oxygen, and the 2016 15 and 76 m density, imply near normal synoptic upwelling conditions. During the 2014 marine heatwave and in the upwelling season after the 2015 – 2016 El Niño, the oceanic response to synoptic upwelling may have been slightly weaker. It is clear though that both the 2015 and the 2019

event intensity averages all suggest weaker upwelling events in these two upwelling seasons. Thus, the years associated with the El Niños report weaker synoptic oceanic upwelling responses.

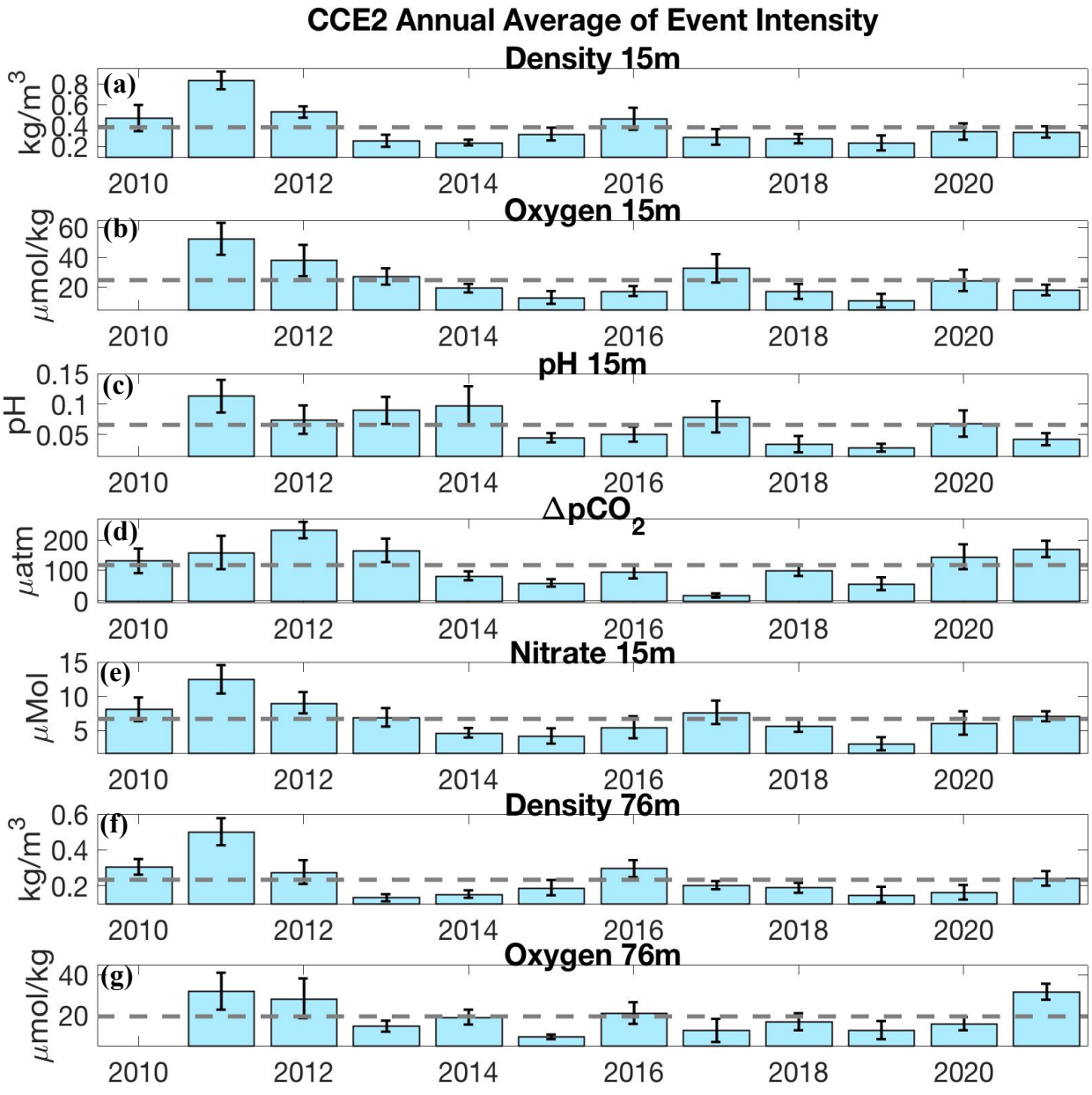

Figure 3.5: CCE2 averages of event intensity over the upwelling events using the band-pass filtered anomalies of (a) density at 15 m depth, (b) oxygen at 15 m depth, (c) pH at 15 m depth, (d) ΔpCO_2 between the ocean and the air, (e) nitrate at 15 m depth, (f) density at 76 m depth, and (g) oxygen at 76 m depth. Error bars show the standard error. Gray dashed lines denote the average over all years.

B2.) Upwelling Event Duration

On average, the upwelling phase lasts for about one week (Figure 3.6). This agrees with other studies that have investigated the duration of wind intensification driving synoptic upwelling (Dorman and Winant 1995; Austin and Barth 2002; Aguirre et al. 2021). The longer upwelling phase in 2011 is a factor contributing to the large event intensity averages for this upwelling season in Figure 3.5. The near normal upwelling phase length in 2012 suggests that the event intensity averages in this year that favor stronger upwelling in Figure 3.5 are not due to a longer amount of time spent in the upwelling phase. This implies that the magnitude of the upwelling forcing, e.g., wind stress, is greater in these years.

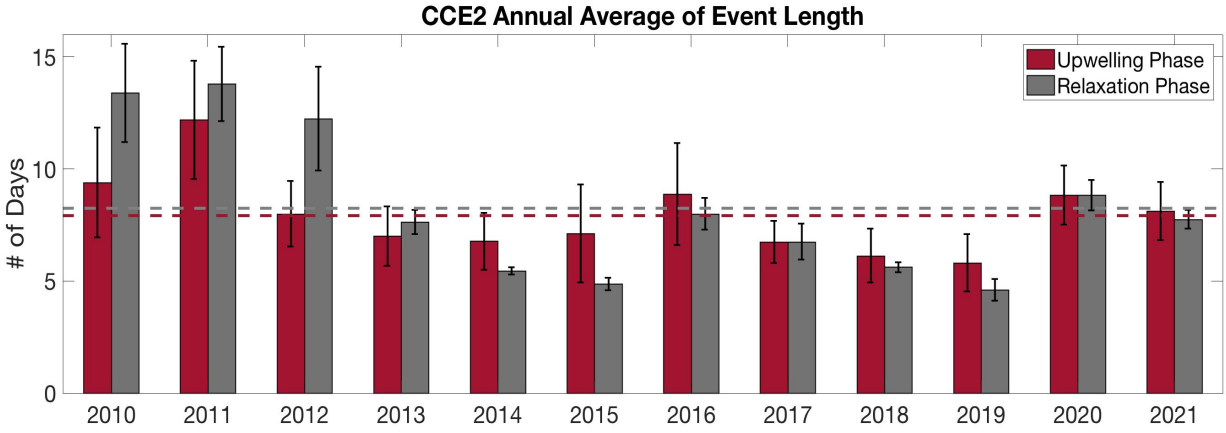

Figure 3.6: Annual averages of the upwelling and relaxation phase lengths from the detected upwelling events at CCE2 that occur between February - June. Horizontal dashed lines are the mean upwelling and relaxation phase lengths averaged over all years. Error bars show the standard error.

The seasonal average upwelling phase lengths in 2014, 2015, and 2019 are below the long-term average, significantly so for 2019 (Figure 3.6). The shorter amount of time spent in the upwelling phase in these seasons contributes to the smaller event intensities in Figure 3.5. The average upwelling phase length in 2016 is slightly longer than the long-term average, which may explain why some of the event intensity averages in Figure 3.5 for this year are near normal or just above the long-term mean. In the years of large-scale climate phenomena, there are shorter

upwelling phase lengths except for in 2016. The shorter amount of time spent under upwelling would have limited the opportunity for water to be upwelled from below, and thereby not drive large changes in the water mass properties at a fixed depth, as evident in Figure 3.5.

Also shown in Figure 3.6 are the seasonal averages of the relaxation phase duration. The record-long average of the relaxation phase lengths shows that generally relaxations in southern California are about a week long. The relaxation length can be an important criterion for biological productivity as previous investigations report an optimal relaxation time frame of 3 – 7 days to enable nutrient uptake (Dugdale and Wilkerson 1989; Dugdale et al. 1990; Botsford et al. 2006; Dugdale et al. 2006; Wilkerson et al. 2006). Thus, amongst the upwelling events detected in this chapter, these events relax long enough to facilitate productivity. The year-to-year changes in the lengths of the upwelling and relaxation phases generally follow each another. However, the amount of time spent in the upwelling versus the relaxation phase can differ given the asymmetry in upwelling.

B3.) Upwelling Events Per Season

The third statistic evaluated is the number of upwelling events in the upwelling season (Figure 3.7). The long-term average in the number of upwelling events detected within the

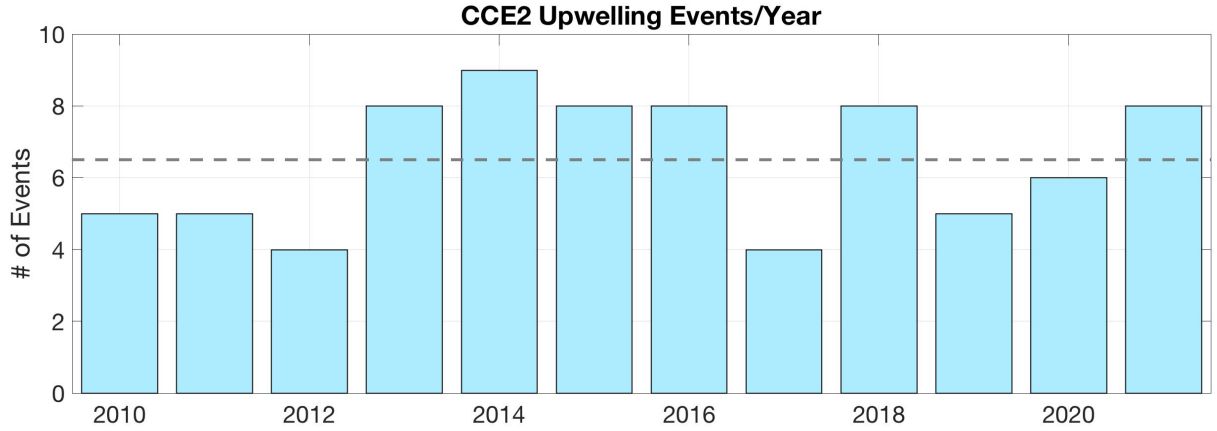

Figure 3.7: The number of upwelling events during the upwelling season at CCE2. Horizontal dashed line is the average over all years.

upwelling season is about 7. Note that the smaller value in 2017 at CCE2 is biased by the limited time the mooring was in the water (Figure 3.2). There is a casual association between the number of upwelling events in a season and the durations of the upwelling and relaxation phases. Years that have a greater number of events typically last for a shorter period of time in the upwelling and/or relaxation periods, as expanded on below (Figures 3.6 and 3.7).

In the years of stronger oceanic upwelling responses prior to the 2014 marine heatwave, i.e., 2011 and 2012 (Figure 3.5), the number of events during these upwelling season are lower in 2011 and 2012. While there were fewer events in 2011 and 2012, the total length of these events, i.e., the sum of the upwelling and relaxation phases, persisted longer than the typical 16 day duration (Figure 3.6). The near normal to longer event upwelling phases in these seasons encourage a greater upwelling response due to the cumulative effect of the upwelling forcing, e.g., wind stress. Meanwhile, the longer relaxation periods allow the coastal ocean to relax back to baseline conditions so that when the subsequent upwelling event begins, the event intensity is calculated over a large range by including neutral, more stratified conditions. These conditions favor larger event intensities, which is apparent in 2011 and 2012 (Figure 3.5).

During the 2014 marine heatwave and the 2015 – 2016 El Niño, there were slightly more events (Figure 3.7) that lasted for a slightly shorter period of time (Figure 3.6). Despite the occurrence of more upwelling events, the shorter event durations may be associated with a cumulatively less significant upwelling forcing, which will be investigated in a later section. In the upwelling season after the 2018 – 2019 El Niño, there are fewer upwelling events (Figure 3.7) and the events are shorter as well (Figure 3.6).

C.) Cross-shore Velocity Profiles and 2D Cross-shore Transport

The cross-shore transport in upwelling regions is significant for influencing how much water gets upwelled and the depth at which the upwelled water comes from. The significance of the cross-shore circulation on upwelling motivates investigating the cross-shore velocity to characterize the cross-shore flow regime during upwelling over synoptic time scales. The characteristic cross-shore velocities will be studied from the detected upwelling events, and these velocities are used to study the interannual variability in the upper 50 m synoptic 2D cross-shore transport.

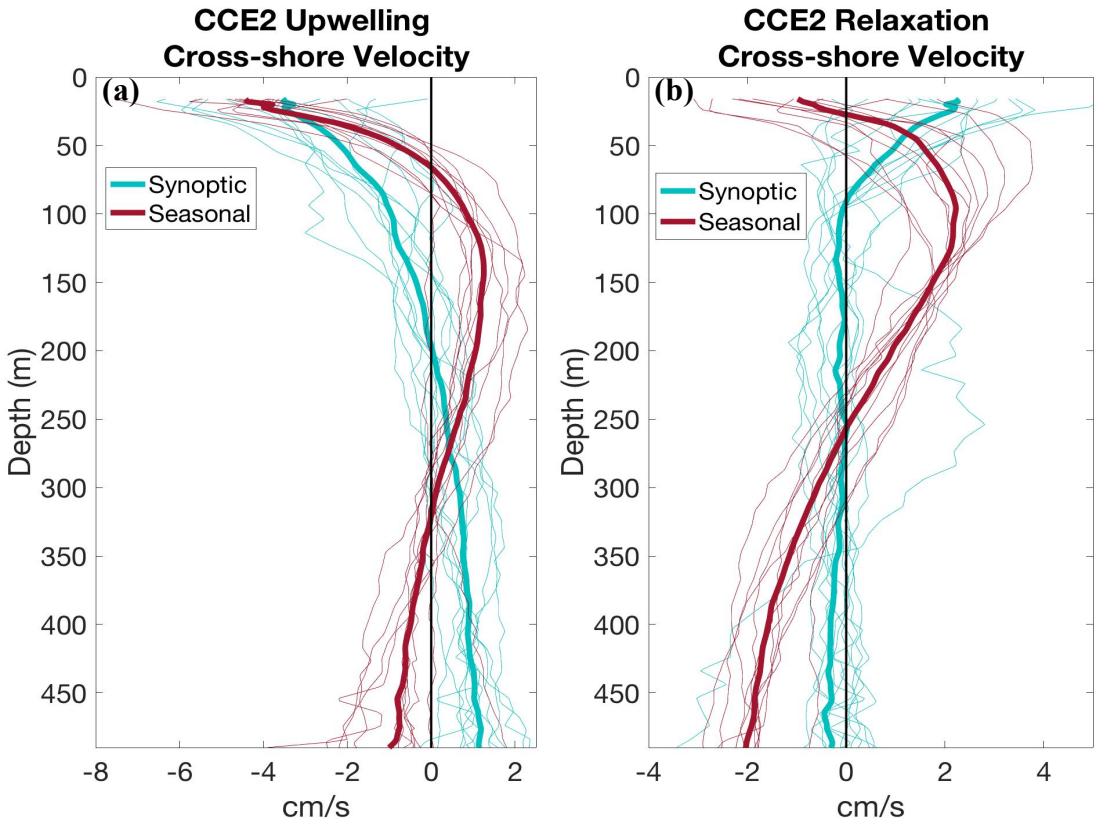

Figure 3.8: CCE2 cross-shore velocity anomalies averaged over the upwelling phases of upwelling events in (a) and averaged of the relaxation phases of upwelling events in (b). Also shown in (a) are the seasonally averaged cross-shore velocities over the upwelling season, i.e., February – June, while the seasonally averaged cross-shore velocities during the relaxation season, i.e., July – December, are shown in (b). The thin lines in (a) and (b) are the annual averages and the thick lines are the averages over all years.

C1.) Upwelling Cross-shore Velocity Profile

The averaged cross-shore flow typical during the upwelling phase of the upwelling events is offshore in the upper ocean with an offshore maximum at the shallowest bin measured, i.e., ~14 m (Figure 3.8a). Just below 200 m depth, the offshore flow becomes onshore and the cross-shore velocity continues to be onshore at least down to 500 m depth. Over the depth range measured by the ADCP, onshore flow is a maximum at 500 m depth. Since the depth-averaged cross-shore velocity has been removed, the offshore 2D transport in the upper approximately 200 m is balanced by onshore transport between 200 and 500 m depth, so that the net cross-shore transport in the upper 500 m is 0 m^2/s. The shape of the synoptic upwelling profile differs from other cross-shore velocity profile results averaged over long periods of time, but these other results do not isolate synoptic variability (Zaba et al. 2020). The shape of the mean synoptic upwelling profile in Figure 3.8a can be explained by a steady state theory.

Table 3.4: CCE2 buoyancy frequency using equation (4) and the corresponding Burger number using equation (3) for the upwelling periods of synoptic upwelling events, the upwelling season, and the relaxation season. In equation (3), α is estimated to be 0.01 from the ETOPO global relief model.

	Buoyancy Frequency (1/s)	**Burger Number**
Synoptic Upwelling	1×10^{-3}	0.12
Upwelling Season	9.2×10^{-3}	1.12
Relaxation Season	10×10^{-3}	1.22

In the upwelling event profile, the onshore maximum occurs in the deepest ADCP bins and the cross-shore flow increases with depth. Under the assumption of a 2D balance, the depths at which the onshore return flow occurs suggests the balance of terms in the alongshore momentum equation. Using this theory published by Lentz and Chapman (2004), Figure 3.8a shows that on synoptic time scales the wind stress is balanced more by the bottom friction. Table 3.4 contains representative values of the synoptic stratification and the corresponding Burger

number, with these calculations described in Section 3.2.4. The weaker stratification during synoptic upwelling yields a smaller Burger number.

This Burger number and the mean cross-shore velocity profile are compared to Burger numbers and cross-shore velocity profiles from other upwelling regions. The Burger numbers from other upwelling regions published by Lentz and Chapman (2004) are listed in Table 3.5. NW Africa's Burger number is most similar to the CCE2 synoptic Burger number and the NW Africa cross-shore flow profile (Figure 3.9) is similar to the CCE2 synoptic profile with offshore flow strongest at the surface, onshore flow greatest near the bottom, and a 0 cm/s crossing at mid-depth. This comparison shows qualitative similarities between the synoptic cross-shore circulation at CCE2 and upwelling off NW Africa.

Table 3.5: Burger numbers for multiple upwelling regions. Values at locations other than the CCE2 mooring and central California are from Lentz and Chapman (2004). The central California Burger number is approximated from the values in Table 2 of Davis (2010).

Upwelling Region	NW Africa	Northern California	Oregon	Peru	Central California
Burger Number	0.19	0.43	0.95	1.35	2

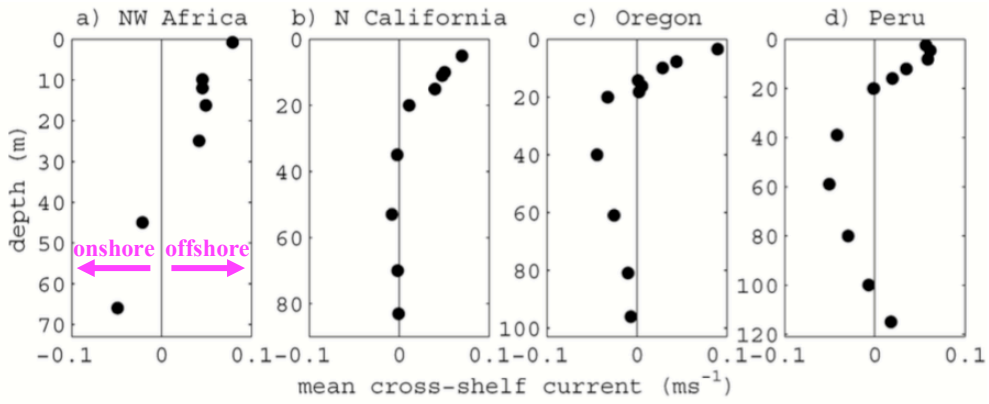

Figure 3.9: Cross-shore velocity profiles at multiple upwelling sites. Positive values in the cross-shore velocities are offshore. Figure is modified from Lentz and Chapman (2004).

C2.) Relaxation Cross-shore Velocity Profile

The cross-shore velocity anomalies averaged over the relaxation phase of upwelling events are shown in Figure 3.8b. As upwelling relaxes, it is expected that the wind-driven cross-shore flow in the surface layer becomes less offshore and may even become onshore (Winant et al. 1987; McCabe et al. 2015). This behavior is apparent in the mean synoptic cross-shore velocity profile in Figure 3.8b. The cross-shore currents are onshore and strongest near the surface with weak nearly constant offshore flow at depths deeper than about 100 m. Onshore flow during relaxation periods can be important for facilitating larval retention near the coastline demonstrating why periodic reversals in the offshore flow are important for biological processes (Farrell et al. 1991; Roughan et al. 2006).

C3.) Interannual variability in the 2D Cross-shore Transport

The physical and biogeochemical properties in Sections 3.3.1.1b demonstrated changes in the synoptic oceanic upwelling response during the 2015 – 2016 El Niño and the 2018 – 2019 El Niño. Given the weaker oceanic upwelling response in 2015 and 2019, it is anticipated that there

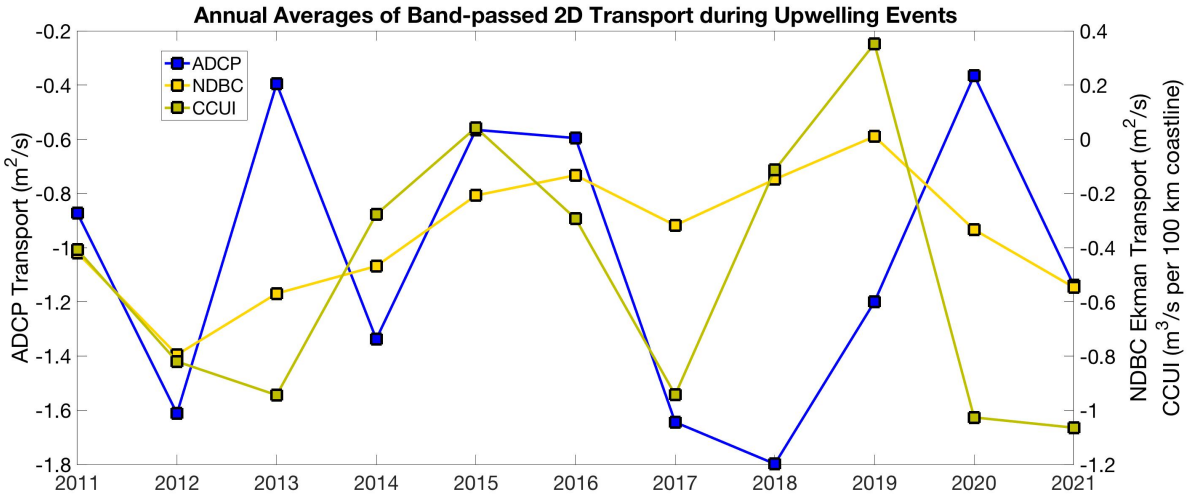

Figure 3.10: CCE2 ADCP annual averages of the band-passed cross-shore transport anomalies when integrated over 14 – 50 m depths during event upwelling phases. Also shown are the annual averages of the local 2D Ekman transport anomalies from the NDBC 46054 buoy and the CCUI anomalies normalized by 100 km coastline length.

may also be weaker offshore 2D transport in the upper 50 m. This layer is strongly wind-driven, so changes in the alongshore winds, i.e., upwelling forcing, are expected to result in changes in the 2D cross-shore transport over the upper 50 m. The interannual variability in the synoptic cross-shore 2D transport is investigated to inspect changes in offshore Ekman transport during the El Niños beginning with the ADCP velocities evaluated in the previous section.

The annual averages of the ADCP 2D cross-shore transport in the upper ocean reveal weaker offshore transport in 2015 and 2016, however these are not the weakest years in the record (Figure 3.10). In another estimate of the 2D cross-shore transport, the NDBC 2D Ekman transport has less offshore annual averages in 2015 and 2019, as well as in 2016. Locally, this indicates weaker upwelling favorable winds off Point Conception on synoptic timescales in these years. The third estimate of cross-shore transport is the normalized CCUI, and the normalized CCUI annual averages in 2015 and 2019 are the least offshore over the record. Thus, off Point Conception and regionally in the SCB, there were weaker upwelling winds on synoptic timescales in the years of the El Niños, and there was also relatively weaker offshore ADCP transport in these years.

3.3.1.2 Upwelling Forcing

The in-situ measurements describe the ocean's response to upwelling, but it is also of interest to see how the oceanic upwelling response relates to the strength of the upwelling forcing. To assess the interannual variability of upwelling strength on event timescales and how similar it is to the in-situ observations, both the local wind stress and the CCUI are analyzed to understand the variability in the upwelling forcing.

Annual averages of the event cumulative intensity calculated on the 3 - 100 day band-pass filtered 2D NDBC Ekman transport and the 3 - 100 day band-pass filtered CCUI normalized

by coastline length are higher in 2011 and 2012 for the local Ekman transport and in 2012 for the CCUI (Figure 3.11). The larger cumulative intensity in these years is consistent with the larger event intensities in the physical and biogeochemical properties (Figure 3.5). The larger cumulative forcing is related to the longer upwelling phase lengths (Figure 3.6) and above average values in the upwelling forcing. For 2011 and 2012 the local wind stress is above average, whereas in 2012 the CCUI is above average (not shown).

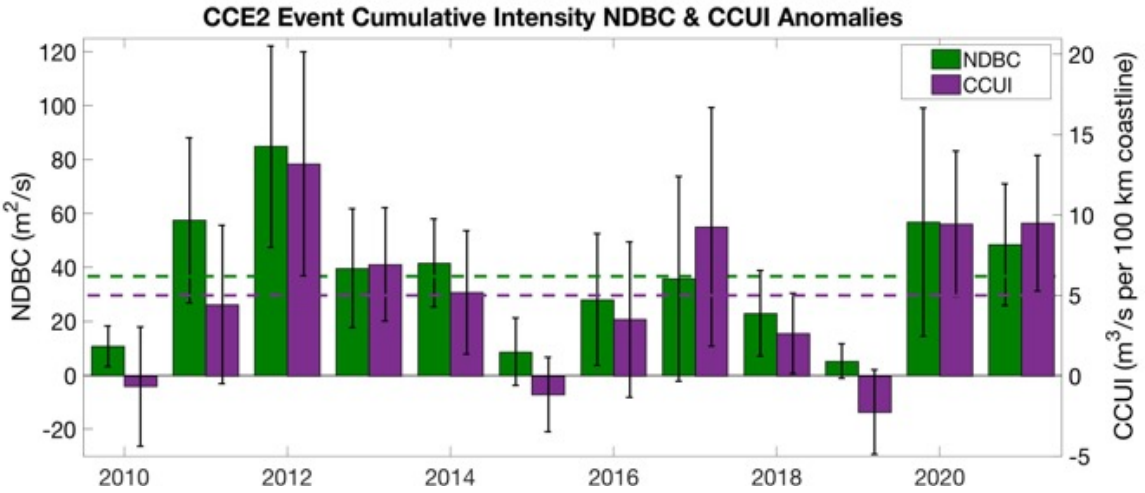

Figure 3.11: Annual averages of event cumulative intensity for the local NDBC Ekman transport anomalies near CCE2 and the CCUI anomalies. Horizontal dashed lines are the record-long averages of event cumulative intensity for the Ekman transport anomalies and the CCUI anomalies. Error bars show the standard error. CCUI anomalies have been normalized by a 100 km coastline length.

While the annual average of cumulative event forcing in 2014 during the marine heatwave is near normal, the NDBC and CCUI annual averages in 2015 and 2016 during the 2015 – 2016 El Niño are below the long-term average in Figure 3.11, significantly so for 2015. The shorter upwelling phase in 2015 (Figure 3.6) contributed to the lower cumulative Ekman and vertical transport (Figure 3.11), while in both 2015 and 2016 weaker magnitudes in the upwelling forcing averaged over the upwelling phases contributed to the lower cumulative forcing in these years (not shown). Thus, the reduced oceanic response on synoptic time scales in the years associated with the 2015 – 2016 El Niño (Figure 3.5) is attributed to the weaker

cumulative wind forcing related to changes in the upwelling phase length for 2015 and in the strength of the upwelling forcing in 2015 and 2016.

In the following 2018 – 2019 El Niño, the 2019 average in the local Ekman transport and CCUI anomalies are substantially lower than the decadal average. As with the earlier El Niño, the weaker cumulative upwelling forcing is related to the shorter duration of upwelling events (Figure 3.6) and the smaller magnitudes in the upwelling forcing during event upwelling periods (not shown). These two effects on the cumulative event intensity are responsible for the subdued oceanic response in the 2019 upwelling season (Figure 3.5).

In this section, qualitative comparisons showed that greater event cumulative forcing drove a larger response in the oceanic properties, i.e., 2011 and 2012, while years exhibiting a weaker oceanic upwelling response were associated with weaker event cumulative intensity, i.e., 2015 and 2019. As expected, this reflects that in general greater upwelling forcing, i.e., longer upwelling length or larger magnitudes, drives a stronger oceanic upwelling response.

3.3.1.3 Summary of Synoptic Scale Upwelling during the 2014 Marine Heatwave, the 2015 – 2016 El Niño, and the 2018 – 2019 El Niño

In this section, the variability of synoptic upwelling was assessed to investigate if there were changes in upwelling in the years of the large-scale climate phenomena. An overview is given of the results from Section 3.3.1 pertaining to years associated with the large-scale climate phenomena.

Many of the event intensity averages for the multiple CCE2 physical and biogeochemical properties are lower in 2014 – 2016 and 2019 (Figure 3.5). These weaker averages are most notable in 2015 and 2019 when nearly all of the event intensity averages are significantly

reduced. The weaker synoptic upwelling response, particularly in 2015 and 2019, demonstrates the anomalous changes in upwelling in these years.

The averaged event cumulative intensity from the local 2D Ekman transport and the CCUI showed that the weaker synoptic upwelling response in the years affiliated with climate phenomena were due to weaker synoptic upwelling forcing (Figure 3.8). The event cumulative intensity, which considers both the length of upwelling phase and the magnitude of the upwelling forcing, demonstrated that one or both of these factors contributed to weaker synoptic upwelling in the years of climate phenomena. In the years of large-scale climate phenomena aside from 2016, synoptic upwelling events were shorter limiting the time in which heightened upwelling winds acted on the ocean (Figure 3.6). Furthermore in 2015, 2016, and 2019 the upwelling forcing when averaged over the event upwelling periods were weaker, thereby reducing the cumulative intensity in these years (not shown).

These results indicate that both the upwelling drivers and the oceanic responses were altered in the years of large-scale climate phenomenon at synoptic timescales. These results agree with other studies that have investigated the impacts of El Niño on upwelling in the CCS. For example, multiple model results demonstrated decreased upwelling productivity during the 2015 – 2016 El Niño (Frischnecht et al. 2015; Jacox et al. 2015; Jacox et al. 2016; Frischnecht et al. 2017). Additionally, Zaba and Rudnick (2016) report weakened upwelling and deepening of the chlorophyll fluorescence maximum that began in 2014 during the marine heatwave and continued into the 2015 – 2016 El Niño.

3.3.2 Low Frequency Upwelling Variability

To assess the low frequency interannual variability in upwelling, first the upwelling response is investigated followed by an examination of the processes that govern the low-

frequency upwelling variability. In the analysis on the low frequency oceanic upwelling response, the multiple CCE2 physical and biogeochemical observations are assessed, along with the cross-shore currents.

In the analysis on the processes that modify interannual variability in upwelling, there are several factors considered including the vertical transport, the depth of the upwelled source waters, the nutricline depth, and the composition of the source waters. To assess how some of these processes influence upwelling, i.e., nutrient concentration at a fixed depth, nitrate is predicted and compared to observed nitrate. The predicted nitrate considers isopycnal heaving, i.e., nutricline depth, and along isopycnal source water variability.

3.3.2.1 Oceanic Response

The seasonal variability in the oceanic upwelling response is assessed from the physical and biogeochemical properties. The oceanic upwelling response also includes the cross-shore

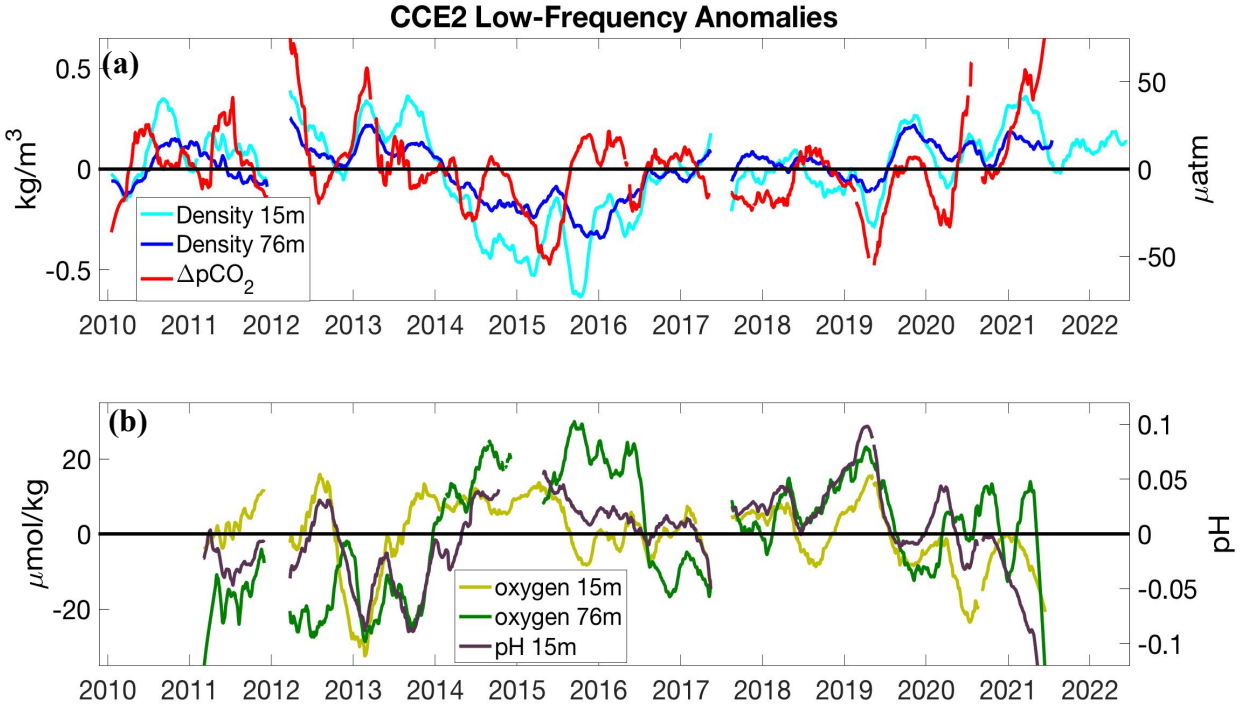

Figure 3.12: CCE2 seasonally low-pass filtered density at 15 and 76 m depths and ΔpCO_2 with the annual cycle removed in (a) and the same for oxygen at 15 and 76 m depths and pH at 15 m depth in (b).

currents, so the cross-shore flow is characterized for seasonal upwelling and the 2D cross-shore transport is inspected in the years of large-scale climate phenomena.

A.) Low pass filtered physical and biogeochemical timeseries

The assessment of low frequency upwelling begins with analyzing the physical and biogeochemical properties at this time scale. The first several variables investigated at low frequencies are density, oxygen, pH, and ΔpCO_2 (Figure 3.12). To inspect the lower frequencies excluded by the band-passed data in Section 3.3.1, the timeseries data are low-pass filtered over 100 days and the annual cycle is removed. The annual cycle is computed over 2010 – 2021.

Many of the variable properties exhibit anomalies characteristic of greater upwelling in the first several years of the record, i.e., 2010 – 2013. This includes positive density anomalies at both depths, positive ΔpCO_2 anomalies at the surface, negative pH anomalies at 15 m depth, and negative oxygen anomalies at 76 m depth. Thus, not only were there stronger synoptic upwelling responses in some of these years, e.g., 2011 and 2012 (Figure 3.5), but the low frequency oceanic response also suggests stronger background upwelling. In winter 2013/2014, the anomalies of the aforementioned variables that were supportive of greater upwelling from 2010 - 2013 switch signs signifying a change in upwelling that persists for the next few years (Figure 3.12).

During the 2014 marine heatwave and the 2015 – 2016 El Niño, all of the physical and biogeochemical properties in Figure 3.12 indicate reduced upwelling. The anomalies largely maintain the same sign up until approximately mid-2016. This persistency in the anomaly behavior sets apart the upwelling seasons in these years from other years in the record. The change in the properties during the El Niños reveal that there was a weakened oceanic response in the low frequency upwelling as well as on event timescales.

The other notable period of reduced upwelling in Figure 3.12 is in spring 2019 following the 2018 – 2019 El Niño. Beginning in winter 2018/2019, negative anomalies appear in density at both depths, which is contemporaneous with positive anomalies in oxygen at both depths and pH. The magnitude of the oxygen and pH anomalies reach similar values to those that occurred during the 2014 marine heatwave and the 2015 – 2016 El Niño. Despite the positive ΔpCO_2 anomalies during winter 2018/2019, the ΔpCO_2 anomalies switch sign to become negative, i.e., indicative of reduced upwelling, by early spring 2019. The reduced upwelling oceanic response lasts until about mid-2019 and the low frequency fluctuations imply that in addition to the weakened synoptic upwelling in spring 2019, the background upwelling signal is also anomalously low.

The 2021 low frequency upwelling response implies stronger upwelling in spring 2021. The upwelling response suggests there may be stronger upwelling in this year and that upwelling in this year may be comparable to the years before the 2014 marine heatwave, i.e., 2010 – 2013. The greater upwelling over these two different periods will be examined in the next several sections.

B.) Cross-shore Velocity Profiles and Cross-shore Transport

The cross-shore flow is also part of the oceanic upwelling response and this section examines the cross-shore velocities over the upwelling and relaxation seasons. The procedure for averaging the cross-shore velocities was described in Section 3.2.3, and the cross-shore velocities are studied for interannual variability in the seasonal 2D cross-shore transport over the upper 50 m.

B1.) Upwelling Cross-shore Velocity Profile

The seasonal cross-shore velocity in the upper ocean is offshore with an offshore maximum at about 20 m depth (Figure 3.8a). The seasonal cross-shore velocity profile has a 0 cm/s crossing at about 70 m depth which is much shallower than the 0 cm/s crossing in the synoptic profile. Onshore velocity in the seasonal velocity profile is a maximum at about 125 m depth and the cross-shore flow goes offshore at depths below approximately 325 m. The cumulative cross-shore transport is 0 m^2/s at about 150 m depth signifying that the onshore transport between 70 and 150 m depth balances offshore Ekman transport in the upper layer. These results will be useful for validating the source water depth estimate, and they will be revisited in Section 3.3.2.2.

An important distinction in the seasonal velocity profile is that the subsurface onshore maximum is just below the Ekman layer, whereas in the synoptic upwelling profile this maximum is closer to the bottom. In the steady state theory presented by Lentz and Chapman (2004), the onshore return flow in the interior indicates a balance between the wind stress and the divergence of the cross-shore momentum flux, suggesting that these terms balance on seasonal time scales. Consistent with this theory, the Burger number for seasonal upwelling is large, and it is greater than the Burger number that was found for synoptic upwelling (Table 3.4).

The Oregon and Peru Burger numbers are most alike the CCE2 seasonal Burger number (Table 3.5) and both of these regions have onshore return flow immediately below the Ekman layer (Figure 3.9). The CCE2 seasonal profile has a shallower onshore peak like Oregon but contains offshore flow closer to the bottom like Peru. The cross-shore velocity profile off central California shares similar features to the seasonal CCE2 profile (Figure 8 in Davis 2010).

Onshore return flow off central California is more pronounced and occurs over a thinner layer and this may be attributed to the larger Burger number approximated for this region (Table 3.5).

Under the theory proposed by Lentz and Chapman (2004), the relatively stronger stratification during the upwelling season promotes a shallower onshore return flow, while during upwelling events the weaker stratification favors a deeper onshore return flow. This illustrates how upwelling on different timescales impacts the cross-shore circulation. The upwelling cross-shore velocity profiles are similar to other upwelling sites with comparable Burger numbers (Smith 1981; Lentz and Chapman 2004; Davis 2010). Lentz and Chapman (2004) examined the role of the divergence of the cross-shore momentum flux on the cross-shore circulation by supporting return flow in the interior, but the APG can also influence the cross-shore velocity profile by promoting interior onshore return flow (Pringle and Dever 2009; McCabe et al. 2015) and the pronounced presence of APGs in EBUS may be an important mechanism in modifying the circulation (Hickey and Pola 1983; Connolly et al. 2014).

B2.) Relaxation Cross-shore Velocity Profile

The mean seasonal profile of cross-shore flow during the relaxation season has weak offshore flow in the upper ocean that becomes onshore at ~30 m depth with an onshore maximum at 100 m depth (Figure 3.8b). At depths below 250 m, the cross-shore flow returns offshore. The weak offshore Ekman flow near the surface with a shallower 0 cm/s crossing is consistent with the results in Chapter 2 (see Figure 2.11). Namely, the annual cycle for vertical transport in southern California remains positive throughout the year signifying that upwelling occurs even in months outside of the upwelling season, but it is weaker than upwelling during the spring season. These results will be useful for validating the source water depth estimate, and they will be revisited in Section 3.3.2.2.

Another feature of the mean relaxation season profile is the shallower depth of the maximum onshore velocity. Stratification is larger in summer and fall during the relaxation season, and consequentially the calculated Burger number is bigger (Table 3.4). The relaxation season cross-shore velocity profile is like Peru's cross-shore velocity profile (Figure 3.9) where there is greater offshore flow closer to the bottom. Additionally, the Burger number representative of Peru is similar to the Burger number at CCE2 during the relaxation season (Tables 3.4 and 3.5).

B3.) Interannual variability in the 2D Cross-shore Transport

Interannual variability in the cross-shore transport during the upwelling season is examined to assess changes that may have occurred during the years of large-scale climate phenomena (Figure 3.13). The cross-shore flow in the upper ocean is strongly wind-driven, so changes in the alongshore winds, i.e., upwelling forcing, are expected to result in changes in the 2D cross-shore transport over the upper 50 m. The unusually low ADCP transport value in 2017 is due to the limited data in this season with only about two months of observations. The ADCP

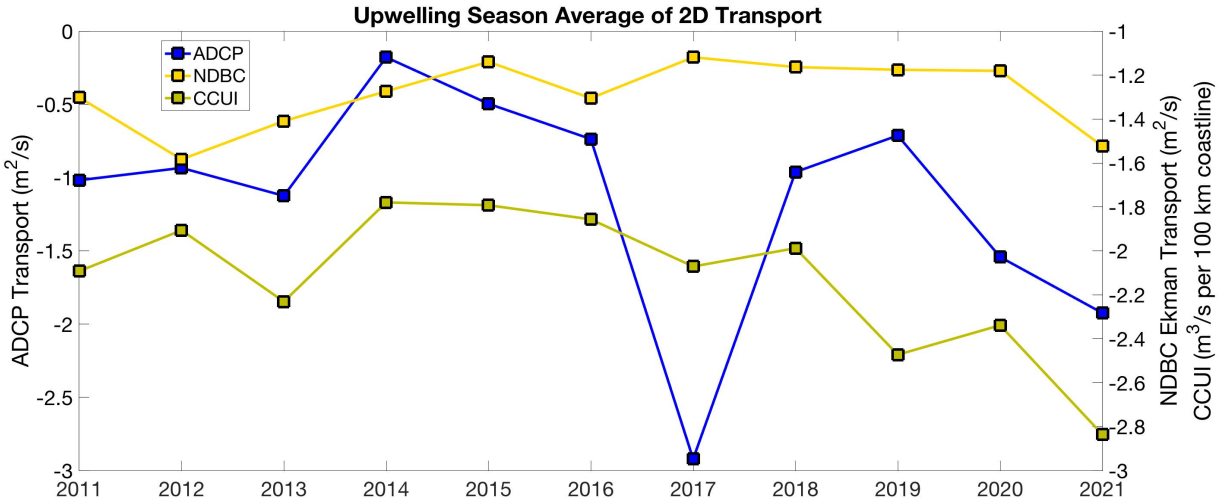

Figure 3.13: CCE2 ADCP annual averages of the cross-shore transport when integrated over 14 – 50 m depths during the upwelling season, i.e., February - June. Also shown are the annual averages of the local 2D Ekman transport from the NDBC 46054 buoy and the CCUI normalized by 100 km coastline length where both are averaged over February - June.

data reveal reduced offshore transport in 2014 – 2016 and 2019 during the years of large-scale climate phenomena. Thus, not only were the physical and biogeochemical properties anomalous in these years, but the strength of the coastal divergence was also altered on seasonal time scales.

The less offshore ADCP transport in 2014 may have been assisted by more onshore geostrophic transport, in addition to the weaker upwelling favorable wind forcing, as will be shown in Section 3.3.2.2, and this would have facilitated the less negative average in 2014 in Figure 3.13. While in 2015 the less onshore geostrophic transport, which will be shown in Section 3.3.2.2, would have been in favor of more offshore flow, thereby reducing the anomalous behavior in the 2D ADCP transport. This opposes the weaker upwelling favorable wind forcing that is suggested by the NDBC 2D Ekman transport, and the 2D ADCP transport would be expected to have been less offshore in this season had the cross-shore geostrophic transport been near normal.

The NDBC 2D Ekman transport does not clearly indicate anomalously less offshore transport in the years of large-scale climate phenomena aside from 2015. The 2D cross-shore transport from the normalized CCUI shows some weakening in the 2014 – 2016 annual averages. The 2D Ekman transport and normalized CCUI transport generally suggest there was weakening in the seasonal upwelling winds in the 2014 marine heatwave and the 2015 – 2016 El Niño.

The 2D ADCP cross-shore transport is relatively less offshore in 2019 after the 2018 – 2019 El Niño. However, a more positive annual average is not apparent in either the NDBC 2D Ekman transport nor in the CCUI averages. It will be suggested in a later section that there was a delay in the 2019 upwelling season. Thus, the averages over February – June may not comprehensively represent upwelling in this year. A change in the averaging period for this year

would reveal a less offshore annual average in the Ekman transport and normalized CCUI transport, like the change with the more positive ADCP cross-shore transport.

With the exception of 2017 and 2019, there is a decreasing trend in the ADCP data, i.e., increased offshore transport, from 2014 onwards. This is also a general feature in the CCUI seasonal averages but not in the NDBC Ekman transport indicating that the general trend in increased offshore transport over the last several years is related to a decreased poleward APG force in these seasons. The seasonal transport averages captured reduced ADCP transport during the 2014 marine heatwave, the 2015 – 2016 El Niño, and the 2018 – 2019 El Niño. Of these years, the upwelling forcing was weaker in 2014 and 2015.

3.3.2.2 Processes Governing the Low Frequency Upwelling Variability

The low frequency variability from the in-situ measurements in Section 3.3.2.1 demonstrated interannual changes in the low frequency oceanic upwelling response. These observations showed anomalous changes during the 2014 marine heatwave, the 2015 – 2016 El Nino, and in the upwelling season after the 2018 – 2019 El Nino indicative of less upwelling. There are multiple processes that alter low frequency changes in upwelling including vertical transport, source water depth, depth of the nutricline, and source water composition. These processes are examined over the CCE2 mooring record. Some of these processes are closely associated with nitrate concentrations, and nitrate is predicted to determine how well these processes explain interannual variability in the observed nitrate.

A.) Vertical Transport

The interannual variability in upwelling is assessed by studying the low frequency variability in the vertical transport from CCUI. The CCUI anomalies are constructed based on removing the annual cycle and low-pass filtering the anomalies over 100 days (Figure 3.14). The

annual cycle is computed over 2010 – 2021. The CCUI Ekman and geostrophic components are also investigated, where the Ekman and geostrophic anomalies are determined in the same fashion as the CCUI anomalies. Additionally, the 2D Ekman transport anomalies derived from the local wind stresses near CCE2 are handled similarly.

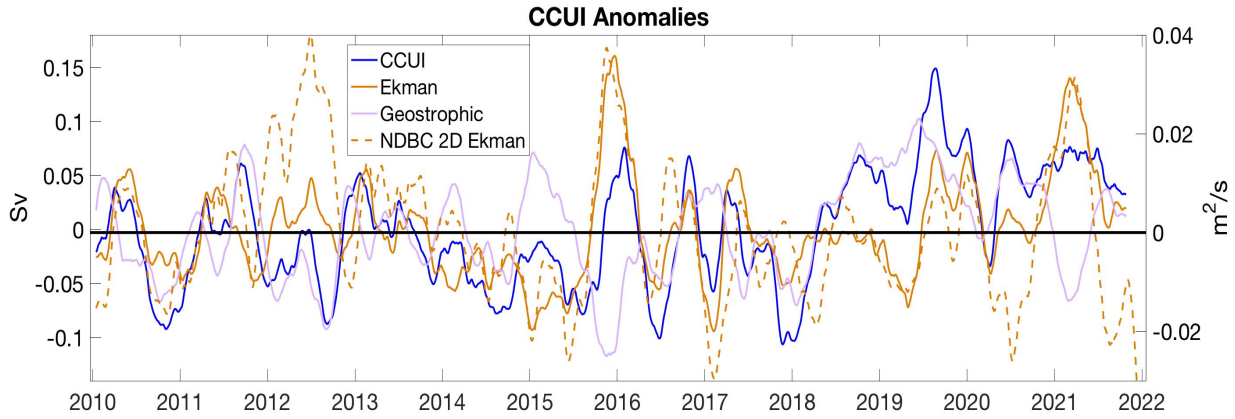

Figure 3.14: CCUI anomalies that have the annual cycle removed and are low-pass filtered over 100 days. The annual cycle is computed over 2010 – 2021. The Ekman and geostrophic transport components that compose the CCUI are also shown where the annual cycle is removed and the anomalies are low-pass filtered over 100 days. The last timeseries shown is the 2D Ekman transport anomalies derived from the NDBC 46054 buoy alongshore wind stress anomalies. Positive anomalies are in favor of more upwelling.

The CCUI anomalies illustrate mildly above average values in vertical transport in the 2011 and 2013 upwelling seasons, i.e., positive anomalies in Figure 3.14 in February - June. To assess whether the positive CCUI anomalies are related to a strengthening in the upwelling favorable winds or to the APG, the Ekman and geostrophic transports that contribute to the CCUI are examined. The sign convention of the anomalies in Figure 3.14 are arranged such that positive Ekman transport anomalies signify greater upwelling favorable winds, while positive geostrophic transport anomalies represent less onshore geostrophic transport. The CCUI Ekman transport anomalies and 2D Ekman transport anomalies are largely positive, i.e., upwelling favorable, in the 2010 – 2013 spring upwelling seasons indicating that the larger oceanic response in these years (Figure 3.12) coincided with greater upwelling favorable winds. The CCUI geostrophic transport anomalies are not consistently in favor of upwelling throughout

these upwelling seasons, so the greater vertical transport and oceanic upwelling response in the 2010 – 2013 upwelling seasons are forced primarily by the alongshore winds.

After these years, the CCUI anomalies are negative from 2013 – fall 2015 and again in spring 2016. While these anomaly magnitudes are not particularly unusual, the persistency of the negative anomalies over 2014 and 2015 is noteworthy. In the 2014 - 2016 upwelling seasons, the 2D Ekman transport anomalies and the CCUI Ekman transport anomalies are generally negative, while the geostrophic transport anomalies are near normal or negative in spring 2014 and 2016. These results demonstrate that upward vertical transport was reduced in the years of large-scale climate phenomena, and this was a result of weakened upwelling favorable winds and more onshore geostrophic transport in some seasons. Thus, the reduced vertical transport forced less of an oceanic response (Figure 3.12). The weakened background upwelling signal in 2015 occurred alongside decreased synoptic upwelling in this year.

Interestingly, in the upwelling season after the 2018 – 2019 El Niño the CCUI anomalies are positive, and vertical transport is greater in this year. In spring 2019, the CCUI Ekman transport anomalies and the 2D Ekman transport anomalies are negative denoting weakened upwelling favorable winds. The CCUI geostrophic transport anomalies are positive in this upwelling season, which has an effect of reducing onshore geostrophic transport and facilitating more coastal divergence. This influence opposes the behavior in the wind field and drives the positive CCUI anomalies at this time. While there is a greater approximated amount of upwelling in the 2019 upwelling season, other processes may have influenced the weaker oceanic response in Figure 3.12, and these will be explored in the next few sections.

In spring 2021, a stronger oceanic upwelling response was shown in Figure 3.12. The low frequency CCUI anomalies in Figure 3.14 demonstrate an enhanced background upwelling

signal that contributed to the increase in upwelling in spring 2021. The positive CCUI anomalies were forced by the positive CCUI Ekman transport anomalies with positive 2D Ekman transport anomalies also present at the time.

The results in this section demonstrate that there is a qualitative association between the low frequency fluctuations in vertical transport (Figure 3.14) and the low frequency variability in the physical and biogeochemical measurements (Figure 3.12). Upwelling seasons with stronger/weaker vertical transport anomalies occur alongside anomalies in the in-situ measurements that indicate a stronger/weaker oceanic upwelling response, except in spring 2019. This relationship is expected as a stronger upwelling forcing is thought to drive greater vertical shoaling of isopycnals and hence the change in water mass properties. In spring 2019 when this relationship does not appear to hold, the weaker upwelling favorable wind stress may have modified other processes, e.g., source water depth, which could have caused the reduced ocean upwelling response in Figure 3.12, and this is investigated next.

B.) Source Water Depth

The time series of approximated source water depth using the parameterization by He and Mahadevan (2021) shown in Figure 3.15a is low-pass filtered over 100 days and the source water depth anomalies are displayed in Figure 3.15b. The anomalies have the annual cycle removed, where the annual cycle is computed over 2010 – 2021. The source water depth estimate using the Burger number and the steady state theory presented by Lentz and Chapman (2004) suggests a region within the water column where the source water depth occurs, e.g., interior or bottom boundary layer; while the source water depth estimate using the He and Mahadevan (2021) parameterization calculates a value for the source water depth. Therefore, low frequency changes in source water depth are examined based on this parameterization.

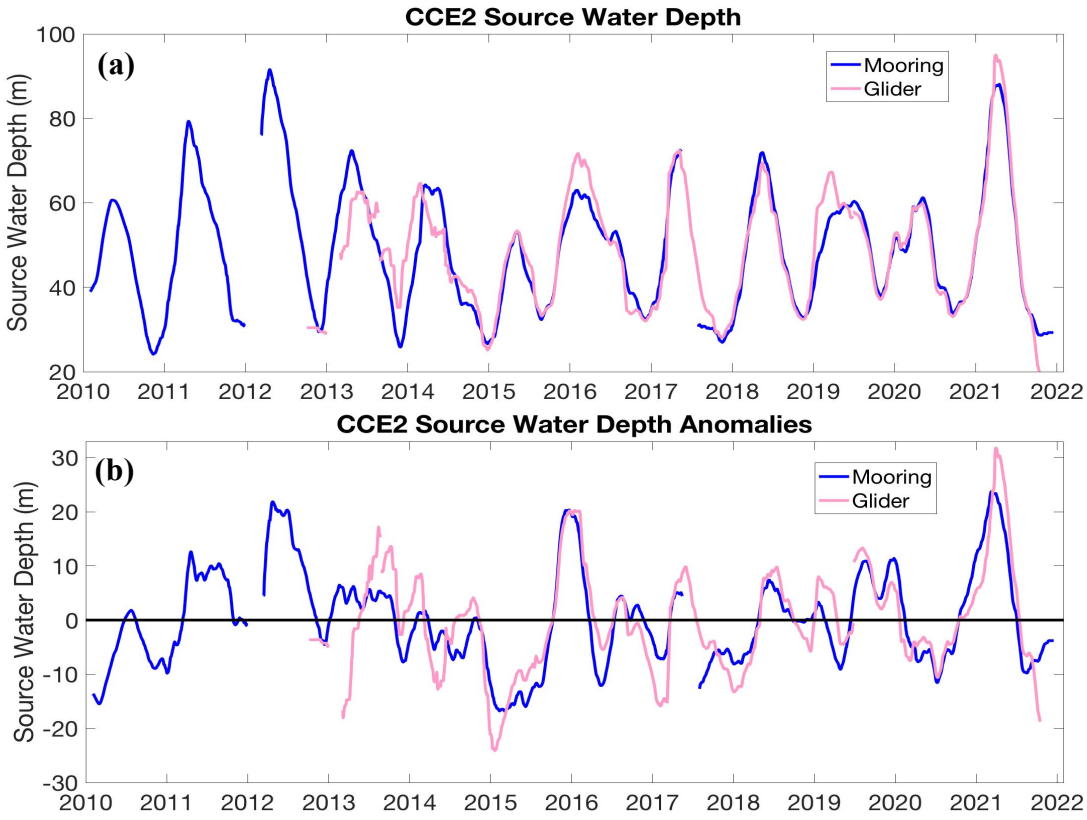

Figure 3.15: (a) Seasonally low-pass filtered source water depth approximated at CCE2 from both mooring and glider data from the parameterization by He and Mahadevan (2021; equation 5). The buoyancy frequency is averaged over the upper 50 m. (b) Source water depth anomalies where the annual cycle is computed over 2010 – 2021 and removed from

The mean source water depth during the upwelling season, i.e., February – June, is about 75 m depth and the mean source water depth during the relaxation season, i.e., July – December, is about 35 m depth (Figure 3.15a). These characteristic values of the source water depth are just below the depth of the 0 m/s crossing in the upwelling and relaxation season mean cross-shore velocity profiles (Figure 3.8). The source water depth should be below the 0 m/s crossing in the cross-shore velocity profile, so this check on the parameterization provides some confidence in the source water depth approximation in Figure 3.15.

The deeper source water depth estimated in the 2011 – 2013 upwelling seasons reflects the stronger upwelling favorable winds in these years, i.e., negative anomalies in Figure 3.16, as well as the weaker stratification, i.e., negative anomalies in Figure 3.16. In addition to the larger

vertical transport in these years (Figure 3.14), the deeper depth of upwelled waters implies greater isopycnal shoaling, which suggests larger changes in water properties that contribute to the larger oceanic upwelling response in Figure 3.12.

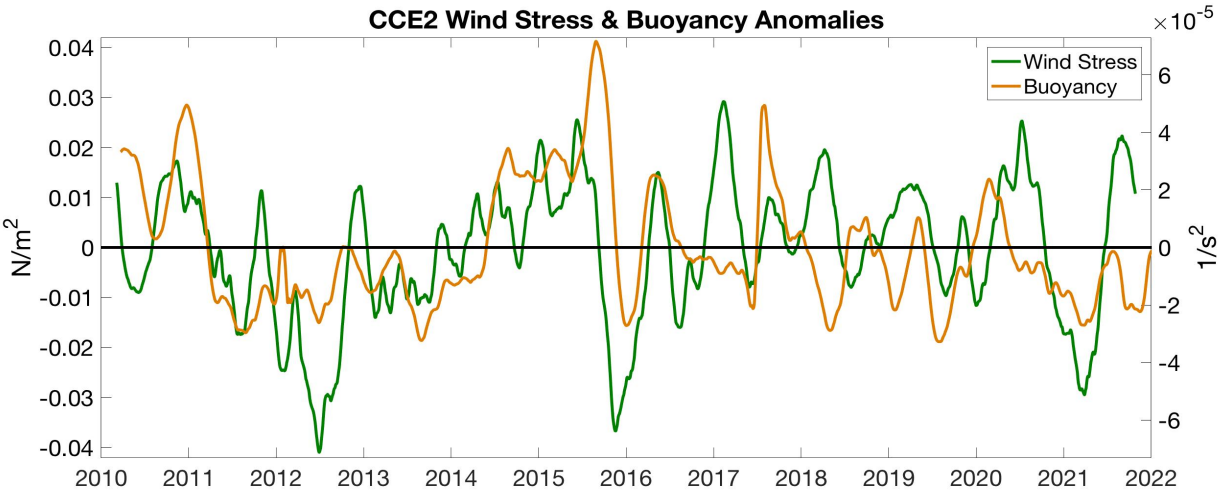

Figure 3.16: NDBC 46054 wind stress anomalies and the upper 50 m averaged buoyancy frequency anomalies using the mooring data low-pass filtered over 100 days.

In the 2014 – 2016 upwelling seasons, the source water depth is shallower (Figure 3.15b), with source waters approximated to originate from about 50 - 60 m depth (Figure 3.15a). Starting in spring 2014 and persisting through fall 2015, both the wind stress and the stratification anomalies support shallower source water depths in these upwelling seasons (Figure 3.16). These features return again in spring 2016. Thus, in the years of the 2014 marine heatwave and the 2015 – 2016 El Niño, the shallower source water depth suggests less shoaling of isopycnals, and this along with the reduced vertical transport (Figure 3.14) prompted weaker upwelling and the weaker oceanic upwelling response (Figure 3.12). Uncharacteristic of previous strong El Niños like in 1982 – 1983 and 1997 - 1998, the upwelling favorable winds increase in fall/winter 2015 (negative anomalies in Figure 3.16; Frischknecht et al. 2017). Despite the increase in the poleward APG force, the stronger equatorward winds drive anomalously larger vertical transport (Figure 3.14) outside of the upwelling season and deepen the source water depth (Figure 3.15). During this period, the CCE2 nitrate measurements are low (Figure 3.17) implying that one

possible scenario was the occurrence of a deeper upwelling cell of less dense, nutrient-poor waters. The depth of the nutricline will be examined in the next section.

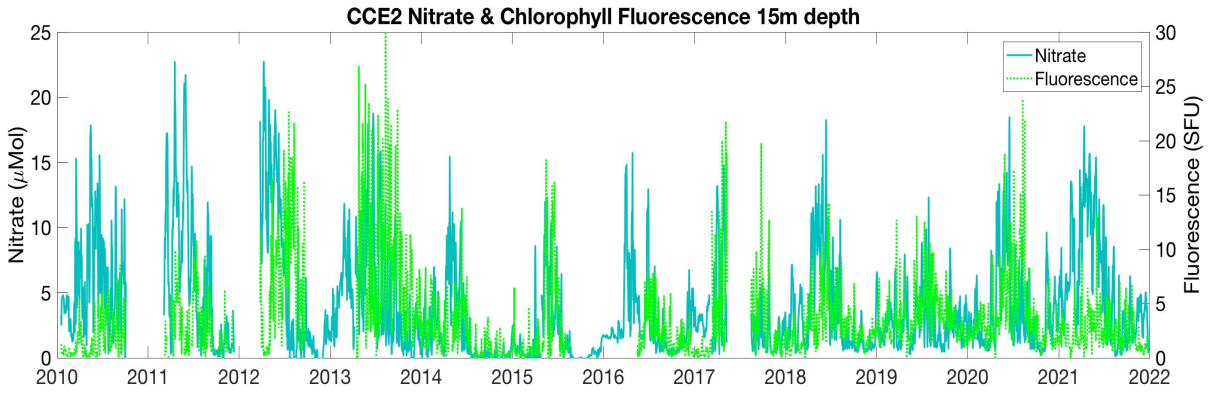

Figure 3.17: CCE2 nitrate and chlorophyll fluorescence at 15 m depth, the same as in Figures 3.2e and 3.2f.

In spring after the 2018 – 2019 El Niño, the negative source water depth anomalies denote a shallower upwelling depth (Figure 3.15). The negative source water depth anomalies in spring result from weaker southward wind stresses and greater stratification (Figure 3.16). By summer, the source water depth anomalies are positive with magnitudes similar to those that occurred in mid-2011 (Figure 3.15). Despite these positive anomalies, the absolute source water depths in this year have typical magnitudes for when the upwelling season peaks. The transition to positive source water depth anomalies in summer coincide with negative anomalies in both the wind stress and the stratification (Figure 3.16). Thus, both of these factors support the positive source water depth anomalies. These results indicate that there was a delay in the upwelling season that peaks in summer similar to the observed nitrate (Figure 3.17). Even though vertical transport was larger in this upwelling season, in response to the positive APG anomalies (Figure 3.14), the shallower source water depth in spring may have limited the extent of isopycnal heaving, and thus drawn up waters in a shallower layer where the nutrient supply was lower. In summer, the deepening of the source water depth would have upwelled waters closer to the

nutricline. The nutrient content of the upwelled waters depends on the source water depth, but also on the depth of the nutricline, which will be explored in the next section.

Over the entire record, one of the deepest estimated source water depths occurs in spring 2021, when the depth is estimated to be about 120 m (Figure 3.15a). Negative anomalies are present in both the wind stress and the stratification records (Figure 3.16) indicating that both of these processes support the deeper source water depth. The greater vertical transport in this upwelling season (Figure 3.14) and the vertical extent of the overturning upwelling circulation drive stronger upwelling that sources waters from deeper depths. These conditions support the stronger upwelling response in spring 2021 that was similar to the response in the 2011 – 2013 upwelling seasons (Figure 3.12).

Both the source water depth approximation in equation (5) from He and Mahadevan (2021) and the CCUI calculation (see Chapter 2) rely on the wind stress. Hence, it is expected that the source water depth and the vertical transport would not be independent of each other. However, as was demonstrated in spring 2019, the low frequency variability in the APG can modify the vertical transport to enhance upwelling despite the reduction of upwelling favorable winds. This influence of the APG illustrates how other coastal processes aside from the wind stress can be important for modulating coastal upwelling. This section focused on the vertical extent of the overturning upwelling circulation, and it is suspected that in general a deeper upwelling cell is conducive for upwelling larger nutrient concentrations (Chhak and Di Lorenzo 2007; Song et al. 2011; Bonino et al. 2019; Rosales Quintana et al. 2021). A deeper upwelling cell is more likely to reach the nutricline resulting in upwelled waters that have a larger nutrient content. However, the nutricline depth does vary over time and this will be examined next.

C.) Nutricline Depth

Another factor that influences upwelling is the nutricline depth. The nutricline depth is modulated by alongshore winds and remote forcing from poleward propagating CTWs. As with the pycnocline, alongshore winds can shoal/suppress the nutricline during upwelling/downwelling (Simpson 1983; Lynn et al. 2003), while CTWs also alter the nutricline depth (Bograd and Lynn 2001; Frischknecht et al. 2015). In the CCS, the depth of isopycnals in the range of 1025.8 - 1026 kg/m^3 are closely tied to the nutricline (Collins et al. 2003; Jacox et al. 2015; Jacox et al. 2016; Zaba and Rudnick 2016). Based on these previous findings, the depth of the 1026 kg/m^3 isopycnal is examined at CCE2 to infer changes in the nutricline depth.

The depth of the 1026 kg/m^3 isopycnal, i.e., a proxy of the nutricline depth, is noticeably shallower in spring of 2011 and 2012 (Figure 3.18). The shallower depth in these years suggests that the nutricline is also shallower placing the nutrient supply closer to the surface. Like the increased vertical transport (Figure 3.14) and the deeper source water depth (Figure 3.15) in these upwelling seasons, the approximated shallower nutricline would have also contributed to the higher nitrate measured at CCE2 (Figure 3.17). Despite the higher nitrate in 2011, chlorophyll fluorescence is relatively low in 2011 but high in 2012. This may be due to other

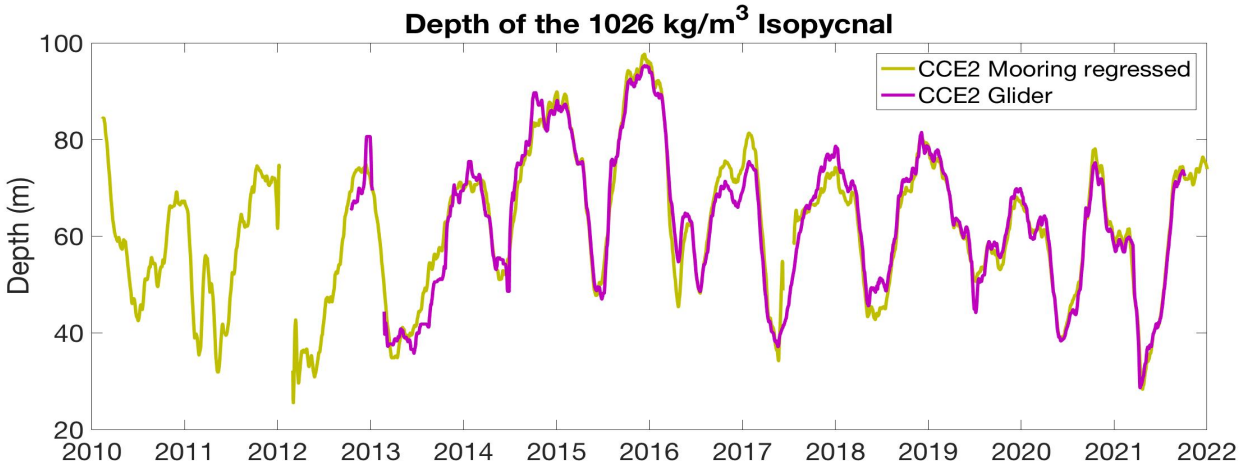

Figure 3.18: Depth of the 1026 kg/m^3 isopycnal at CCE2 from both the mooring and the glider data sets.

biotic and/or abiotic factors governing primary production and limiting the chlorophyll fluorescence in 2011.

In the years of the climate events, i.e., the 2014 marine heatwave and the 2015 – 2016 El Niño, the depth of the 1026 kg/m^3 isopycnal in spring is deeper relative to other upwelling seasons (Figure 3.18). The deeper isopycnal extends for the rest of the time in these calendar years. Nitrate content is lower in the 2014 – 2016 upwelling seasons and so is chlorophyll fluorescence, with the exception of a brief approximately 2-month window in 2015 which has a notable uptick in chlorophyll fluorescence values (Figure 3.17). The decreased chlorophyll in these years reflects the less upwelling favorable conditions set up by the reduced vertical transport (Figure 3.14), the shallower source water depth (Figure 3.15), and the suspected deeper nutricline (Figure 3.18). The deeper nutricline in these years may have encouraged the deeper chlorophyll fluorescence maximum that was reported by Zaba and Rudnick (2016) from glider data.

In spring of 2019 after the 2018 – 2019 El Niño, the 1026 kg/m^3 isoypycnal depth is anomalously deep for this time of year and is at a depth similar to what was found in spring 2014 and 2015 (Figure 3.18). The suggested deeper nutricline in spring 2019, along with the shallower source water depth (Figure 3.16), may explain some of the lower nitrate (Figure 3.17) at the fixed depth of the CCE2 sensor. However, the chlorophyll fluorescence in this season is not particularly low in comparison to other years in the record. Previous studies have shown that the wintertime depth of the 1026 kg/m^3 isopycnals during El Niño years can be used to forecast lower biological productivity in the following spring upwelling season (Jacox et al. 2015; Jacox et al. 2016). This may be due to poleward propagation or advection of tropically generated phenomena that may take 1 – 2 months to reach California and thus arrive at the onset of the

upwelling season (Jacox et al. 2015). This behavior holds for both the 2015 – 2016 and the 2018 – 2019 El Niños where the wintertime 1026 kg/m^3 isopycnal is deep followed by a less biologically productive upwelling season. For both of these El Niños, in winter/early spring there are poleward propagating sea level fluctuations extending as far south as the equator (Chapter 1 Figure 1.14).

The shoaling of the 1026 kg/m^3 isopycnal in spring 2021 reaches depths similar to those found in spring 2011 and 2012, and this is nearly 20 m deep at CCE2 (Figure 3.18). The implied shallower nutricline depth in this upwelling season combined with a deeper source water depth (Figure 3.15) and more upward vertical transport (Figure 3.14) would have facilitated a larger nutrient flux into the upper ocean, which is supported by the higher nitrate (Figure 3.17). However, chlorophyll fluorescence is low in this year suggesting other influential factors were important in determining the biological productivity.

The nutricline depth qualitatively agrees with the nitrate measured by the fixed sensor at CCE2, namely shallower approximated nutricline depths correspond to higher nitrate measurements. The correlation between nitrate at 15 m depth and the depth of the 1026 kg/m^3 isopycnal is -0.7, which reflects the relationship between nitrate near the surface and shoaling of isopycnals/the nutricline. This section demonstrated that the nutricline depth is a factor governing the nutrient supply of upwelled waters. Other factors can also influence this, one of which includes the water mass composition which is investigated next.

D.) Source Waters

Another mechanism that influences upwelling is the source water present. The source water is the water that gets upwelled, and it depends on the source water depth and the water mass composition. The regional water masses in southern California have various water mass

characteristics. For instance, subsurface waters in southern California, e.g., water advected poleward by the CU, have greater amounts of PEW. This spicier water mass is low in dissolved oxygen and low in pH but high in nutrients (Wyrtki 1967; Nam et al. 2011; Meinvelle and Johnson 2013; Bograd et al. 2015; Bograd et al. 2019). The nutrient content differs amongst the water masses with PEW containing higher amounts of nitrate than PSUW (Bograd et al. 2019), so the relative ratio of these water masses modifies the nutrients available for upwelling. Alongside the vertical transport, source water depth, and nutricline depth, the source waters may also contribute to interannual variability in upwelling. The source water composition is the final consideration on the variability of upwelling during the 2014 marine heatwave, the 2015 – 2016 El Niño, and the 2018 – 2019 El Niño.

The water mass composition is approximated using the results from the water mass analysis in Chapter 1, which was performed at 76 m depth at CCE2. Thus, the water mass composition is not known at all depths, so this is a limitation if the water mass composition at the source depth differs from the water mass analysis performed at 76 m depth. The details of determining the fractional composition of the regional water masses are explained in Chapter 1, and the reader is referred to Section 1.2 for a complete discussion on calculating the composition of the regional water masses.

The two ways the water mass composition varies at a fixed depth are by (1) vertical heaving of isopycnals and (2) anomalous advection of water masses on an isopycnal. In the first way, the stratification in the ocean tends to exhibit vertical gradients in the water mass properties. This leads to a density-dependent composition of regional water masses. As isopycnals heave vertically either from alongshore winds or propagating pressure gradients, the isopycnal shoaling causes changes at a fixed depth in the density and therefore the fractional

composition of regional water masses. This behavior was briefly described in Chapter 1, where denser waters have more PEW (less PSUW) than less dense waters (Figure 1.18). Therefore, as isopycnals shoal, such as during upwelling, it is expected that PEW concentrations increase at a fixed depth.

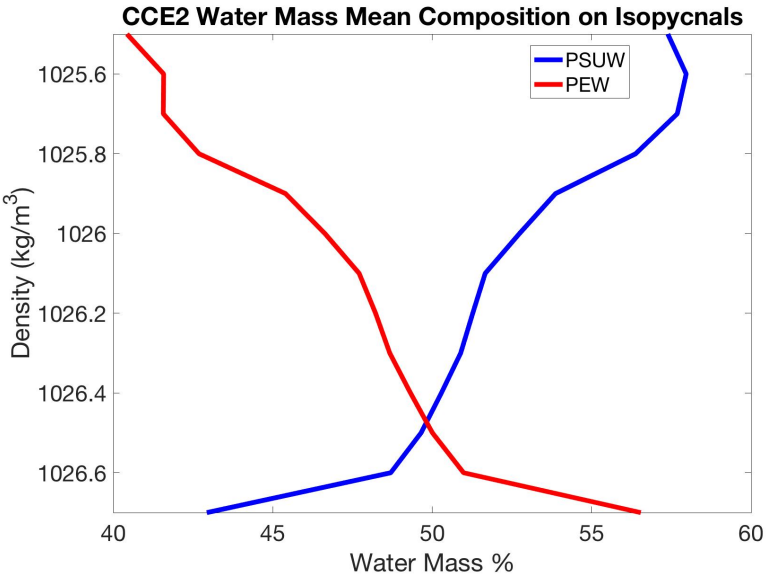

Figure 3.19: CCE2 mean water mass composition along isopycnals from the water mass analysis at 76 m depth in Chapter 1.

Figure 3.19 shows the mean composition of PEW and PSUW on isopycnals at CCE2. The increase/decrease of PEW/PSUW over the density range in Figure 3.19 reflects a transition in the horizontal circulation from near surface flows, e.g., CC, to subsurface flows, e.g., CU. The CU is characterized by the 1026 kg/m^3 isopycnal, with the CU core flowing along ~1026.6 kg/m^3 (Lynn and Simpson 1987; Lynn and Simpson 1990; Bray et al. 1999; Gay and Chereskin 2009). In the isopycnal outcropping of the CU, the increase in PEW signifies a shift to spicier waters with a lower latitude origin. This demonstrates the density-dependence of the water mass composition such that when isopycnals shoal this can alter the water mass ratios at a fixed depth.

Much of the variability in the water mass result is expected to be related to vertical displacement of isopycnals. Figure 3.20a shows the 100 day low-pass filtered water mass results

at CCE2 76 m depth. The water mass composition is predominately made up of PSUW and PEW. A third regional water mass, ENPCW, minimally contributes to the fractional composition at CCE2 so it is not included in this analysis. Seasonal changes in the fractional composition in Figure 3.20a are apparent with increasing/decreasing PEW/PSUW in spring-summer and decreasing/increasing PEW/PSUW in summer-fall. This seasonality in the water mass results is related to vertical heaving of isopycnals. However, as stated earlier the fractional composition can also change due to anomalous horizontal advection along isopycnals.

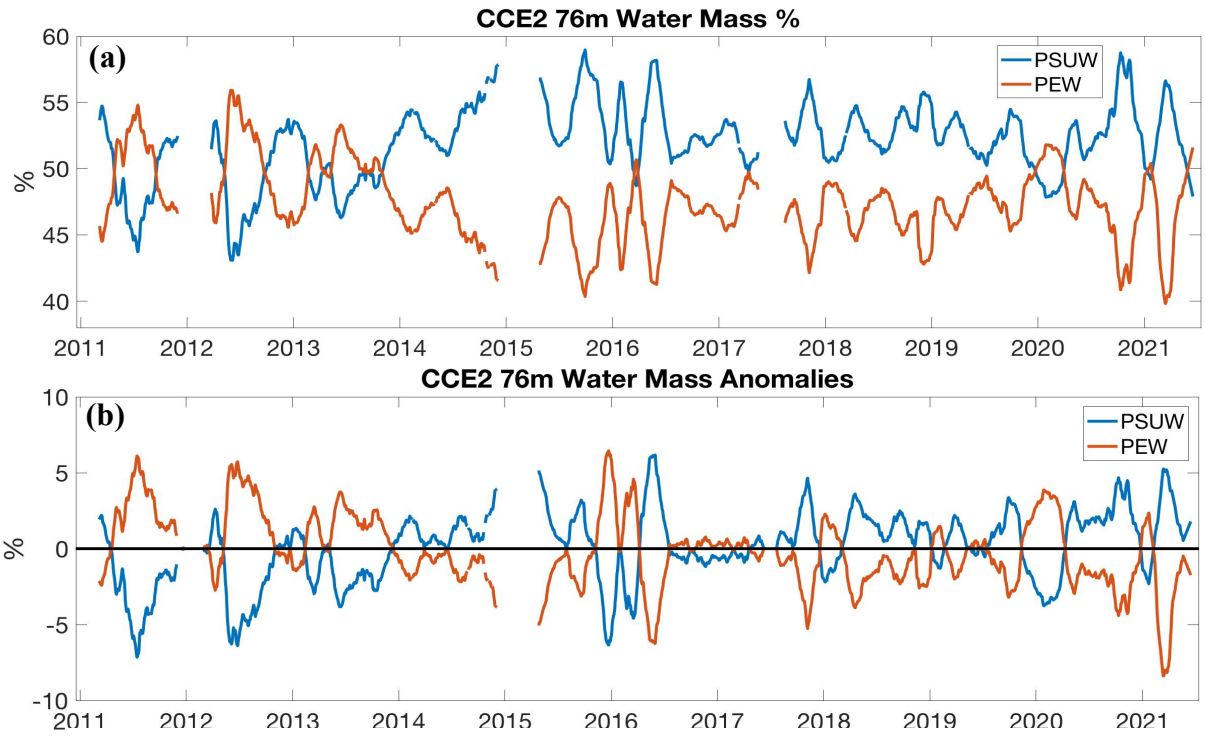

Figure 3.20: (a) Fractional composition of PSUW and PEW at CCE2 76 m water depth and (b) the along isopycnal anomalies.

In this second way for altering the water mass ratios, changes in the circulation can modify the fractional composition of water masses on an isopycnal. This was a focus in Chapter 1 where the water mass anomalies were analyzed. These anomalies have the isopycnal mean water mass composition removed, so they represent anomalous along-isopycnal advection and this was described in Chapter 1 Section 1.4. The 100 day low-pass filtered water mass anomalies

on an isopycnal are shown in Figure 3.20b. Interannual variability in both the total percentage of each water mass (Figure 3.20a) and the water mass anomalies (Figure 3.20b) are investigated to assess how they may have altered upwelling over the last decade, particularly during the 2014 marine heatwave, the 2015 – 2016 El Niño, and the 2018 – 2019 El Niño.

In the first three years in the record, 2011 – 2013, the dominance in the fractional composition alternates between PSUW and PEW (Figure 3.20a). The larger amount of PEW in spring-summer occurs over the upwelling season. This is partly attributed to isopycnal shoaling (Figure 3.18) where the larger densities, i.e., 1026.6 kg/m^3, at the sensor depth (Figure 3.2a) have a mean composition of PEW that would be about half of the total water composition (Figure 3.19). This accounts for much of the PEW in these seasons (Figure 3.20a), but there is some additional PEW fraction above 50%. The water mass anomalies indicate that the additional few percentages in these seasons are due to anomalous horizontal advection (Figure 3.20b). Thus, there is both considerable heaving of isopycnals and anomalous horizontal advection contributing to the elevated PEW fraction in these years. In these upwelling seasons, the presence of more PEW in the upper ocean (Figure 3.20a) is expected to influence the nutrient concentration (Figure 3.17) which is explored later.

Throughout 2014 and 2015, PSUW is the dominant water mass at CCE2 (Figure 3.20a) with positive PSUW anomalies for these years up until fall 2015 (Figure 3.20b). Again in spring 2016, large PSUW values (Figure 3.20a) are contemporaneous with positive PSUW anomalies (Figure 3.20b). The amount of PSUW in the composition reach some of their highest values over the record. The less dense waters in these upwelling seasons (Figure 3.12a) are expected to yield more PSUW due to the suggested reduction in isopycnal shoaling (Figure 3.18). Additionally, along isopycnal advection also contributed to the greater proportion of PSUW (Figure 3.20b).

The generally lower nitrate measured in these upwelling seasons (Figure 3.17) was associated with a deeper nutricline depth (Figure 3.18), but the lower nitrate at the 15 m sensor depth may have also been influenced by positive PSUW anomalies (Figure 3.20b). The variability of source waters during the 2014 marine heatwave and the 2015 – 2016 El Niño indicate that the less dense waters, which have a higher proportion of PSUW to PEW in the mean composition (Figure 3.19), contributed to the higher amounts of PSUW (Figure 3.20a), and also that these waters contained some anomalous amounts of PSUW (Figure 3.20b) due to advective processes.

In the upwelling season after the 2018 – 2019 El Niño, the water mass results show a larger proportion of PSUW to PEW, but the PSUW magnitudes in this year are not as high as in the previous years of large-scale climate phenomena (Figure 3.20a). There are mild positive PSUW anomalies with a very weak reversal in the PSUW and PEW anomaly signs mid-year (Figure 3.20b). The density anomaly changes from negative to positive (Figure 3.12a) when the 1026 kg/m^3 isopycnal, i.e., proxied nutricline, is at its shallowest (Figure 3.18) and when nitrate peaks at 15 m depth (Figure 3.17). This behavior is consistent with an upwelling season that occurred later in the year. The largely negative PEW anomalies through the spring and summer seasons (Figure 3.20b) with the less dense waters in spring (Figure 3.12a) would have supported source waters (Figure 3.20a) with lower nitrate levels (Figure 3.17).

The larger oceanic upwelling response in spring 2021 coincides with predominantly more PSUW in this year (Figure 3.20a) and positive PSUW anomalies (Figure 3.20b). The larger proportion of PSUW to PEW in this year contrasts 2021 from earlier years of strong upwelling, e.g., 2011 and 2012. All three of these years were characterized by greater vertical transport (Figure 3.14), deeper source water depths (Figure 3.15), and strong vertical heaving of

isopycnals (Figures 3.18). The differences in the water mass fractions for these years may explain the differences in the observed nitrate (Figure 3.17) and this is examined next.

E.) Nitrate Prediction

To assess the influence of vertical heaving, i.e., nutricline depth, and source water composition on nitrate, predicted nitrate is compared to observed nitrate. The predicted nitrate demonstrates year-to-year changes similar to the observed nitrate, with predicted nitrate larger in 2011 – 2013 and 2021 and predicted nitrate lower in 2014 – 2016 and 2019 (Figure 3.21).

In the 2011 – 2013 upwelling seasons, the predicted nitrate magnitudes are similar to the observed nitrate values. There are many days in these years when the density threshold is met, and in 2011 and 2012 the density is relatively denser in comparison to other upwelling seasons. The predicted nitrate reveals that the larger nitrate values in these years are attributed to the larger shoaling of isopycnals (Figure 3.20) and the anomalous PEW (Figure 3.20), since PEW contains higher nitrate than PSUW (Table 3.2). The predicted nitrate magnitudes in the 2011, 2012, and much of the 2013 upwelling seasons demonstrate that the method for estimating nitrate is successful in these years.

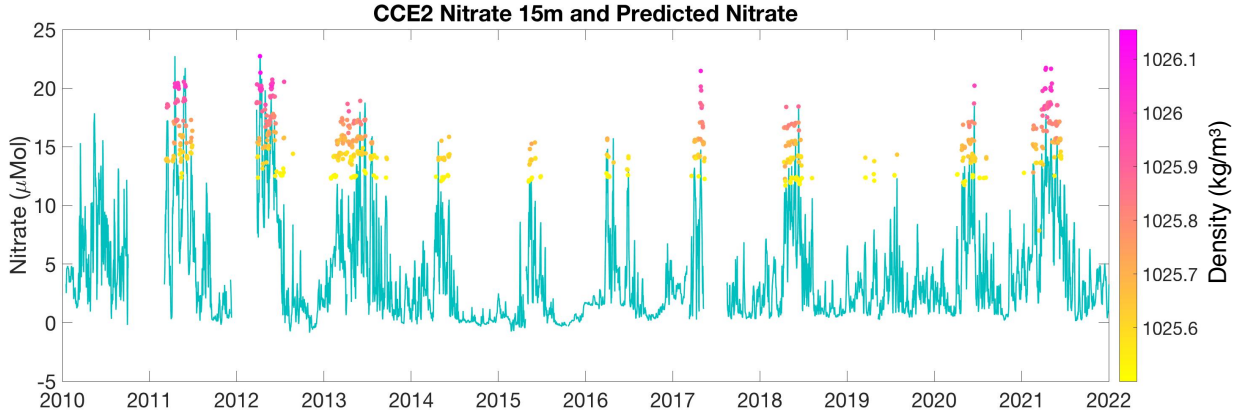

Figure 3.21: CCE2 observed nitrate (timeseries) at 15 m depth along with predicted nitrate (circles). The color of the predicted nitrate signifies the density at 15 m for that day.

In the 2014 – 2016 upwelling seasons, there are only a few days when the density reaches 1025.5 kg/m^3. i.e., the density threshold. For some of the days in these years, the predicted nitrate exceeds the observed nitrate, more so in 2015. The mismatch between predicted and observed nitrate at times during the marine heatwave and the El Niño could be explained by variability in the nitrate content of the regional water masses. Variability in water mass properties like temperature, salinity, and oxygen were shown in Chapter 1 (Figure 1.5), and it is likely that nitrate also varies from the single isopycnal value reported by Bograd et al. (2019). Furthermore, biological consumption of nitrate at 15 m depth demonstrates that nitrate is not conservative at this depth, and nitrate drawdown is not accounted for in the nitrate predictions.

Another cause of the discrepancy between the observed and predicted nitrate in these years may be due to the assumption that the water mass anomalies at 76 m depth are the same at 15 m depth. This assumption may underestimate the PSUW anomalies at 15 m depth since the wind-driven horizontal circulation drives stronger currents near the surface which become sheared with depth. The stronger surface currents can advect more water and be responsible for larger water mass anomalies at shallower depths than at deeper depths. If this applies and the positive PSUW anomalies at 15 m depth are larger, then the larger fractional amount of PSUW would lower the predicted nitrate estimate. This estimate would then be in closer agreement with the observed nitrate.

In the upwelling season after the 2018 - 2019 El Niño, the predicted nitrate overestimates the observed nitrate (Figure 3.21). As in the 2014 – 2016 seasons, there are only about a week's worth of days in 2019 when the density criterion is met. The discrepancy in observed and predicted nitrate in this year may be caused by some of the processes listed above for the previous years of large-scale climate phenomena.

In the 2021 upwelling season, the number of days when the density criteria are met is similar to 2011 – 2013, and the 15 m density is larger in this year like in 2011 and 2012. The predicted nitrate lies within but also above the range of observed nitrate. This upwelling season coincided with positive PSUW anomalies, unlike the 2011 and 2012 upwelling seasons (Figure 3.20b). As expressed above, an explanation for the larger predicted than observed nitrate in many of the days in 2021 is the assumption that water mass anomalies at 76 and 15 m depths are the same. If the water mass anomalies at 15 m depth had greater magnitudes than that at 76 m depth, then this may account for some of the disagreement between the observed and predicted nitrate.

In general, the results in Figure 3.21 indicate that the predicted nitrate magnitudes are reasonable approximations of the in-situ nitrate, more so when the waters at 15 m depth are denser than about 1025.8 kg/m^3. There are some seasons when the predicted nitrate overestimates the observed nitrate, i.e., those seasons when density does not reach 1025.8 kg/m^3. This could be due to assuming that the water mass anomalies at 76 m depth are the same at 15 m depth or from variability in the water mass nitrate content (i.e., deviations from the values listed in Table 3.2 for an isopycnal). However, this simplified estimate for predicting nitrate is a test of the water mass composition and validates the results from the water mass analysis presented in Chapter 1.

3.3.2.3 Summary of Low Frequency Upwelling during the 2014 Marine Heatwave, the 2015 – 2016 El Niño, and the 2018 – 2019 El Niño

During the 2014 marine heatwave and the 2015 – 2016 El Niño, background variability in the vertical transport was reduced (Figure 3.14), the suspected source water depth was shallower (Figure 3.15), the inferred nutricline was deeper (Figure 3.18), and the water mass composition favored PSUW (Figure 3.20a). All of these conditions are less favorable for

biogeochemical upwelling responses and influenced the less upwelling favorable physical and biogeochemical low-frequency anomalies in Figure 3.12 as well as the lower nitrate in Figure 3.17. In the cross-shore circulation, there was generally less offshore 2D transport in the upper 50 m (Figure 3.13). The same oceanic upwelling response was true for the ADCP cross-shore transport during the 2018 – 2019 El Niño. Ultimately, the changes in the low-frequency upwelling in the 2014 – 2016 and 2019 seasons impacted the biological productivity as chlorophyll fluorescence was reduced (Figure 3.17). These impacts propagated through the ecosystem with geographical changes in species (Leising et al. 2015; McClatchie et al. 2016; Peterson et al. 2017), changes in marine mammal foraging behavior (Elorriaga-Verplancken et al. 2016), and die-offs of sea birds (Welch 2015).

In comparing the two El Niños, both events were associated with weakened upwelling favorable winds, but differences in the APG drove less/more coastal divergence in the 2015 – 2016/2018 – 2019 El Niño causing less/more vertical transport. However, the weaker upwelling favorable winds and the increased stratification in both El Niños are suggestive of shallower source water depths. The shallower source water depths along with the suspected deeper nutricline in these upwelling seasons resulted in similar oceanic upwelling responses for both El Niños.

The results from this section showed that the low frequency variability in upwelling was significantly altered in 2014 – 2016 and 2019. Section 3.3.2.1 also revealed that at synoptic timescales, upwelling in 2015 and 2019 was reduced. Thus, weaker upwelling occurred at both synoptic and seasonal timescales during the two El Niños.

3.4 Conclusion

This chapter was dedicated to investigating upwelling in southern California. Upwelling is studied at synoptic and low frequency time scales. On synoptic timescales, event statistics were computed to study the interannual variability in upwelling events in southern California. The event intensity demonstrated stronger synoptic upwelling responses in 2011 and 2012 and weaker synoptic upwelling responses in 2014 – 2016 and 2019 during the 2014 marine heatwave, the 2015 – 2016 El Niño, and the 2018 – 2019 El Niño (Figure 3.5).

As part of the synoptic oceanic upwelling response, the cross-shore currents were examined and on average offshore Ekman transport in the surface layer was balanced by onshore transport in the near bottom layer. The smaller Burger number reported for synoptic upwelling agreed with the Lentz and Chapman (2004) theory, where bottom friction balances the wind stress in the alongshore momentum equation and onshore Ekman return flow is in the bottom layer. Interannual variability in the 2D cross-shore transport showed less offshore transport in 2015 and 2016 (Figure 3.10).

Stronger synoptic biogeochemical responses (Figure 3.5) coincided with greater cumulative upwelling forcing (Figure 3.11) due to longer event lengths (Figure 3.6) and/or larger upwelling forcing magnitudes (Figure 3.10). The weaker upwelling responses (Figure 3.5) were associated with weaker cumulative upwelling forcing (Figure 3.11), where the length of the upwelling phase was shorter in these years (Figure 3.6) and/or the averaged upwelling forcing during the upwelling phase was weaker (Figure 3.10). On synoptic timescales, upwelling was anomalously weak during the 2015 – 2016 El Niño and the 2018 - 2019 El Niño.

Low-frequency changes in the physical and biogeochemical properties indicated a greater upwelling response at CCE2 over 2010 – 2013 and 2021 (Figure 3.12). For many of these

upwelling seasons, alongshore winds were more favorable for upwelling (Figure 3.14), approximated source water depths were deeper (Figure 3.15) due to the greater upwelling favorable winds and weaker stratification (Figure 3.16), the nutricline depth was shallower (Figure 3.18), and the water mass composition contained greater amounts of PEW (Figure 3.20a). The higher fractional amount of PEW was due to the shoaling of isopycnals (Figures 3.2a and 3.18), where denser waters have a larger fraction of PEW (Figure 3.20), and from anomalous horizonal advection of PEW (Figure 3.20b). These upwelling favorable conditions in the 2010 – 2013 and 2021 upwelling seasons increased the nitrate concentration at 15 m depth, and in the 2012 and 2013 upwelling seasons this supported more ecological productivity (Figure 3.17).

Significant changes occurred in the 2014 – 2016 upwelling seasons. There was a weaker oceanic response to upwelling (Figure 3.12), reduced vertical transport resulting from weakened equatorward winds (Figure 3.14), shallower source water depths (Figure 3.15) that were supported by both the weaker upwelling winds and the stronger stratification (Figure 3.16), a deeper nutricline (Figure 3.18), and a greater fraction of PSUW (Figure 3.20a) given the less dense waters (Figure 3.12a) and positive PSUW anomalies (Figure 3.20b). In late 2015, there was a disruption in the weaker upwelling conditions. While this was outside of the upwelling season, the change in conditions in late 2015 implied a deeper upwelling cell with upwelling of less dense waters. The upwelling season after the 2018 - 2019 El Niño also exhibited many of these same features that were present during the 2014 marine heatwave and the 2015 – 2016 El Niño, but the upwelling season occurred in summer than in spring for this year. The less upwelling favorable conditions during the 2014 marine heatwave, the 2015 – 2016 El Niño, and the 2018 – 2019 El Niño resulted in lower nitrate concentrations at 15 m depth and generally supported less ecological productivity in 2014 and 2015 (Figure 3.17). Previous studies have

noted the impacts of large-scale climate phenomena on upwelling in 2014 - 2016, and the results in Section 3.3.2 are consistent with those findings (Jacox et al. 2015; Jacox et al. 2016; Zaba and Rudnick 2016; Frischknecht et al. 2017).

As part of the oceanic upwelling response, the offshore Ekman transport in the surface layer was balanced by onshore transport just below the Ekman layer. The larger Burger number found during the upwelling season agreed with the Lentz and Chapman (2004) theory where the divergence in the cross-shore momentum flux balances the wind stress in the alongshore momentum equation and onshore Ekman return flow is in the interior. Interannual variability in the 2D cross-shore transport showed less offshore ADCP transport in 2014 – 2016 and 2019. This behavior was generally true in the normalized CCUI transport, but not in the 2D Ekman transport. On low frequency timescales, upwelling was anomalously weak during the 2014 marine heatwave, the 2015 – 2016 El Niño, and the 2018 - 2019 El Niño.

EBUS are coastal regions of prolific productivity with significant socioeconomic value. As such, the anticipated effect of climate change on these systems is of particular interest. Projected future changes for EBUS include modifications in the upwelling favorable winds and increased stratification. Bakun (1990) proposed that stronger horizontal pressure gradients between the land and sea which would drive intensified alongshore winds and promote coastal upwelling. Changes in either the oceanic high- and continental low-pressure systems or latitudinal migrations in atmospheric high-pressure cells may be responsible for the stronger pressure gradients (García-Reyes et al. 2015; Rykaczewski et al. 2015). Consequences of this may include alterations in the seasonal timing of the upwelling season, latitudinal effects on upwelling intensity such that higher latitude regions in EBUS will experience more upwelling

while lower latitudes will have less, and upwelling events may become stronger and longer in duration (Iles et al. 2012; Rykaczewski et al. 2015; Wang et al. 2015; Xiu et al. 2018).

Potential increases in stratification attributable to global warming are another consideration of how EBUS will be impacted. Global warming is expected to cause wide spread warming of the oceans and thereby strengthen the stratification (Palacios et al. 2004; Roemmich and McGowan 1995; McGowan et al. 1998). In EBUS, there are mixed results as to how stratification will be influenced with respect to climate change. Stronger upwelling favorable winds may induce greater mixing, cool SST, and reduce stratification, while increased global ocean temperature would increase stratification (Bakun et al. 2015; García-Reyes et al. 2015; Xiu et al. 2018; Seabra et al. 2019). The environmental impacts of these changes may affect the vertical nutrient flux, community composition, and ocean acidification (Illes et al. 2012; Bakun et al. 2015; Xiu et al. 2018). Given the complexities of how EBUS will be impacted by future climate change, much more needs to be understood as to how these systems will fare in the future and this motivates the need for long-term monitoring. The observations presented in this chapter contribute to this goal.

3.5 Acknowledgements

We would like to thank Jeff Sevadjian for providing quality control on the ADCP data. Support for the CCE2 mooring comes from the NOAA Ocean Observing and Monitoring Division and Ocean Acidification Program (NA15OAR4320071) and indirectly from the NSF-supported California Current Ecosystem LTER site. The CCE2 mooring is a part of the OceanSITES program where quality controlled data are available online at ftp://data.ndbc.noaa.gov/data/oceansites/DATA/CCE2/. CCE2 glider data which are part of the CORC project are online at https://spraydata.ucsd.edu/projects/CORC/. The Instrument Develop Group at Scripps Institution of Oceanography is thanked for operating the gliders used in this chapter and for processing the glider data. We would like to thank Todd Martz and Taylor Wirth for assistance in processing the pH data, Adrienne Sutton for sharing the pCO_2 data, and Mark Ohman for sharing the nitrate and chlorophyll fluorescence data. NDBC winds are made publicly available by NOAA at https://www.ndbc.noaa.gov/. CCMP Version-2.0 vector wind analyses are produced by Remote Sensing Systems and data are available at www.remss.com. World Ocean Atlas data used in this study can be found at https://www.ncei.noaa.gov/products/world-ocean-atlas.

Chapter 3, in part is currently being prepared for submission for publication of the material. Lowcher, Caroline; Send, Uwe; Lankhorst, Matthias. The dissertation author was the primary researcher and author of this material.

3.6 Appendix A: Upwelling Event Detection Threshold Test

The event detection method described in Section 3.2 identifies upwelling events based on a threshold where local peaks that were larger than this threshold were considered possible upwelling events. A threshold is specified for each variable used in the detection of high-frequency upwelling events. Here, the sensitivity of this threshold is examined for its impact on generating event statistics.

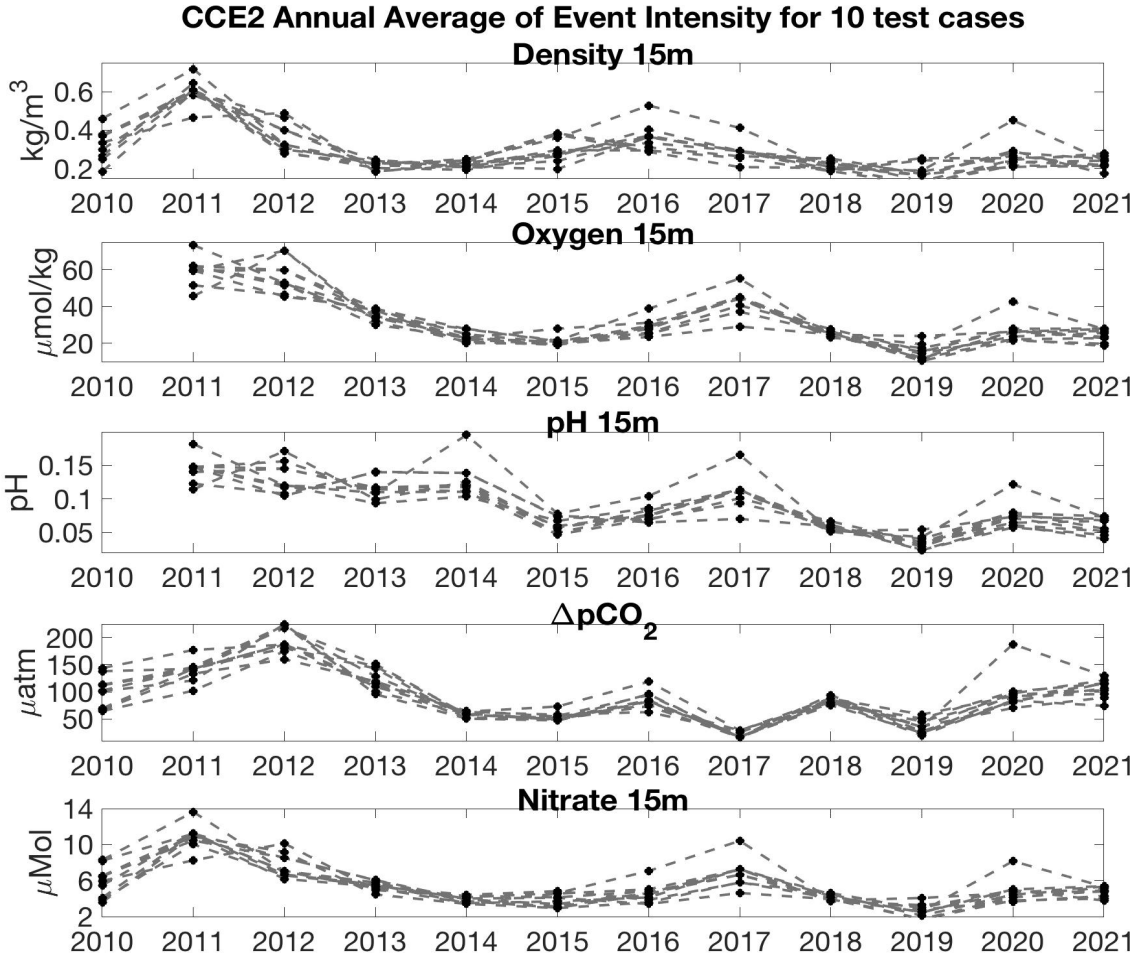

Figure 3.22: CCE2 annual averages of event intensity for the ten different test cases where each test case has a different parameter threshold for the physical and biogeochemical properties used in the upwelling event detection procedure.

To assess the influence of the property thresholds on event determination, a set of ten test cases are run where the criteria for peak significance is varied for all physical and biogeochemical variables. Then the event statistics (event intensity, length of the upwelling

phase, and number of upwelling events in a year) are computed based on the upwelling events determined in each test case. Figure 3.22 shows the annual averages of event intensity for all test cases for the physical and biogeochemical properties at 15 m depth or shallower. Density and oxygen at 76 m depth are not shown, but the interpretation of the results is similar and thus not shown for redundancy. Some variability is present amongst the magnitudes of the event intensity annual average in a given year for all properties. However, the trends in the annual averages

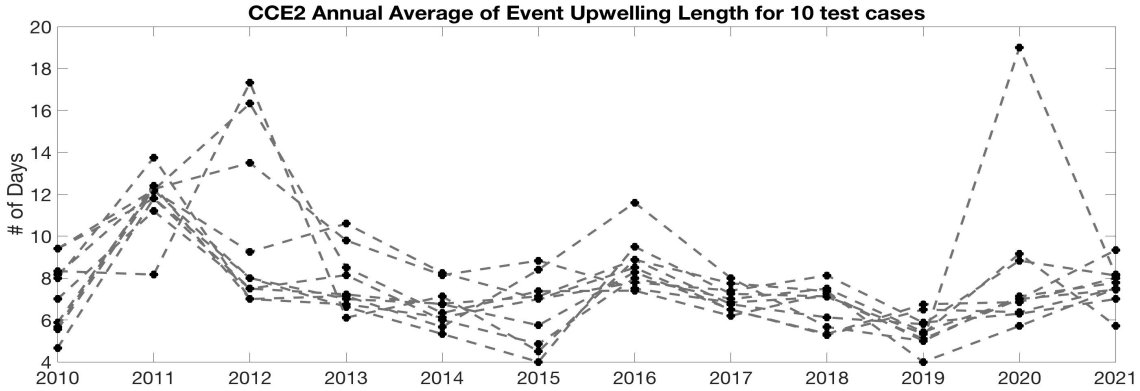

Figure 3.23: CCE2 annual averages of event upwelling length for the ten different test cases where each test case has a different parameter threshold for the physical and biogeochemical properties used in the upwelling event detection procedure.

across the test cases are comparable. Likewise, for the length of the upwelling phase of upwelling events and the number of upwelling events in a year, the annual values vary some amongst the test cases but interannual variability is quite similar regardless of the parameter thresholds incorporated (Figures 3.23 and 3.24). These results demonstrate the robustness of the event statistics and shows that there is minimal dependence on the thresholds used for event detection and this robustness provides confidence that the computed statistics are representative of the ocean upwelling response.

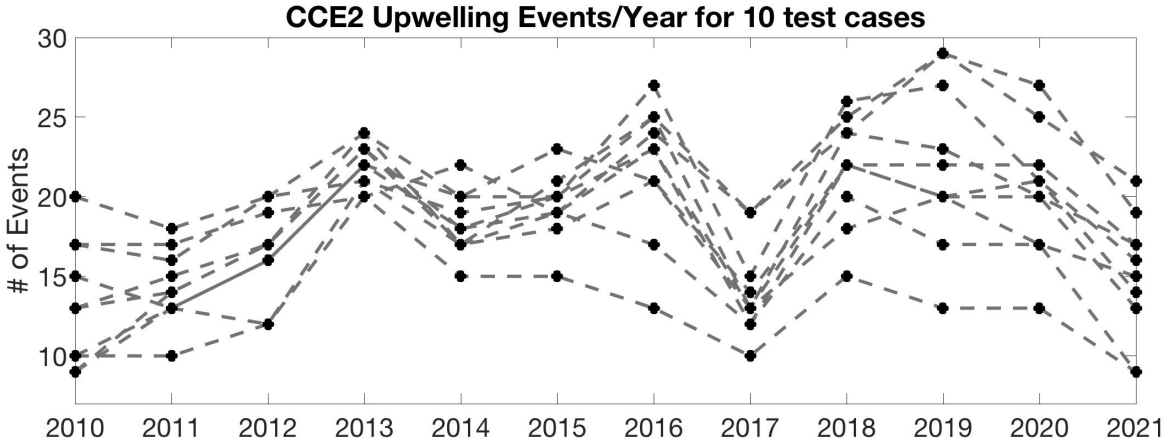

Figure 3.24: CCE2 the number of upwelling events per year for the ten different test cases where each test case has a different parameter threshold for the physical and biogeochemical properties used in the upwelling event detection procedure.

CHAPTER 4

Physical Processes Influencing the 2020 Red Tide in Southern California

Abstract

In spring 2020, a red tide event occurred in southern California comprised of the dinoflagellate species, *Lingulodinium polyedra*. This red tide event was significant in that it contained an incredibly high biomass and had a long bloom duration. Observations from coastal moorings measured the oceanic conditions prior to, during, and after the red tide. Using these in-situ observations, the physical processes that led to the initiation, continuation, and termination of the red tide are examined. Unusually strong stratification, onshore transport, and synoptic upwelling events initiated and sustained the oceanic conditions favorable for the growth of the red tide species. The strengthened stratification was initially driven by decreased surface salinity from an atmospheric event, and this was followed by elevated surface temperatures that maintained the enhanced stratification. Meanwhile, there was persistent onshore transport that spanned from Santa Monica to northern Baja California, and the onshore transport was driven by the seasonal spin up of the Southern California Eddy that appeared alongside an anticyclonic eddy. Over the course of the red tide, there were multiple upwelling events that periodically elevated the nutrient supply below the surface layer of strengthened stratification. The synoptic upwelling events, stronger stratification, and onshore flows appeared to be important for establishing and supporting the red tide making the coastal ocean conditions favorable for *L. polyedra*. The red tide terminated as the near surface stratification decreased to below climatological values. The

decreased near surface stratification was due to decreased surface temperatures and increased surface salinity.

4.1 Introduction

Eastern boundary upwelling systems (EBUS) are biologically productive coastal regions that support fisheries industries and are subject to multiple coastal processes including harmful algal blooms (HABs). HABs are a bloom of a particular toxic species, and some species may actually make the water appear red or brown; hence the name red tide. Red tides are common in EBUS, and California has experienced several blooms over the last couple of decades (Anderson et al. 2006; Sekula-Wood et al. 2011; Baron et al. 2013). In southern California, red tide events oftentimes include the dinoflagellate species *Lingulodinium polyedra.* Not only does this species make the ocean appear red or brown, but this species also produces bioluminescence at night (Allen 1946; Omand et al. 2011; Kahru et al. 2021). In late March 2020, a red tide event began in the SCB and in-situ measurements revealed *L. polyedra* was the planktonic species responsible. The red tide peaked between the end of April and the beginning of May, and the spatial range of the event extended from northern Baja California to Santa Monica (Kahru et al. 2021). The red tide was persistent, lasting over several weeks, when typically blooms last between one and two weeks (Moorthi et al. 2006; Omand et al. 2011). Coastal moorings operated before, during, and after the 2020 red tide, and made high-frequency measurements of the oceanic conditions throughout this time. These observations will be examined to assess the sequence of events that led up to the 2020 red tide and the physical processes that contributed to the bloom.

There are multiple physical processes that may condition the coastal ocean favorable for HABs. Synoptic upwelling events uplift nutrients during the upwelling phase, and as upwelling relaxes, the ocean restratifies and the horizontal circulation adjusts to the decreased upwelling

favorable winds. Synoptic upwelling events were assessed in Chapter 3, and these conditions can facilitate the aggregation of species known to cause HABs. Onshore and poleward currents retain planktonic species and may cause a build-up of high biomass along the coast encouraging the possibility of a HAB (Donaghay and Osborn 1997; Lucas et al. 1999). The more stratified conditions during relaxations are advantageous for some species of phytoplankton like dinoflagellates. The reduced mixing and turbulence make it easier for dinoflagellates to swim vertically in the water column. Their motility allows them to reach deeper depths of higher nutrient concentrations, and in places like southern California their vertical migration can be enhanced by internal waves (Kamykowski 1974/1981; Smayda 1997; Smayda and Trainer 2010). In southern California, HABs have been commonly reported nearshore and over the shelf (Caron et al. 2010; Omand et al. 2011; Seubert et al. 2013; Kudela et al. 2015).

This chapter uses in-situ measurements from multiple sensors at three different moorings in the coastal ocean off San Diego. These moorings are equipped to monitor several physical and biogeochemical properties. The moorings make measurements throughout the water column, and were deployed before, during, and after the red tide. These observations will be used to assess the physical processes that contributed to the initiation, continuation, and termination of the red tide.

Section 4.2 presents the data sets used in this chapter and Section 4.3 reviews a timeline of events encompassing the time period of the red tide. This section also analyzes the physical processes that created favorable conditions for initiating and sustaining the red tide, followed by changes in the coastal ocean that coincided with the decline in the red tide. Section 4.4 concludes this chapter with a summary of the results.

4.2 Data Sets and Methods

4.2.1 Data Sets

To analyze the chronology of events encompassing the 2020 red tide, observations from three different coastal moorings are used. The three moorings are Del Mar (DM), Point Loma Ocean Outfall (PLOO), and South Bay Ocean Outfall (SBOO). The DM mooring is stationed 5 km offshore of Del Mar in 90 m water depth and has been maintained since 2006 (Figure 4.1). The PLOO mooring is deployed about 8 km off Point Loma and in 100 m water depth, while the SBOO mooring site is approximately 8 km off of the US-Mexico border and in 30 m water depth (Figure 4.1). The latter two of these moorings are owned by the City of San Diego.

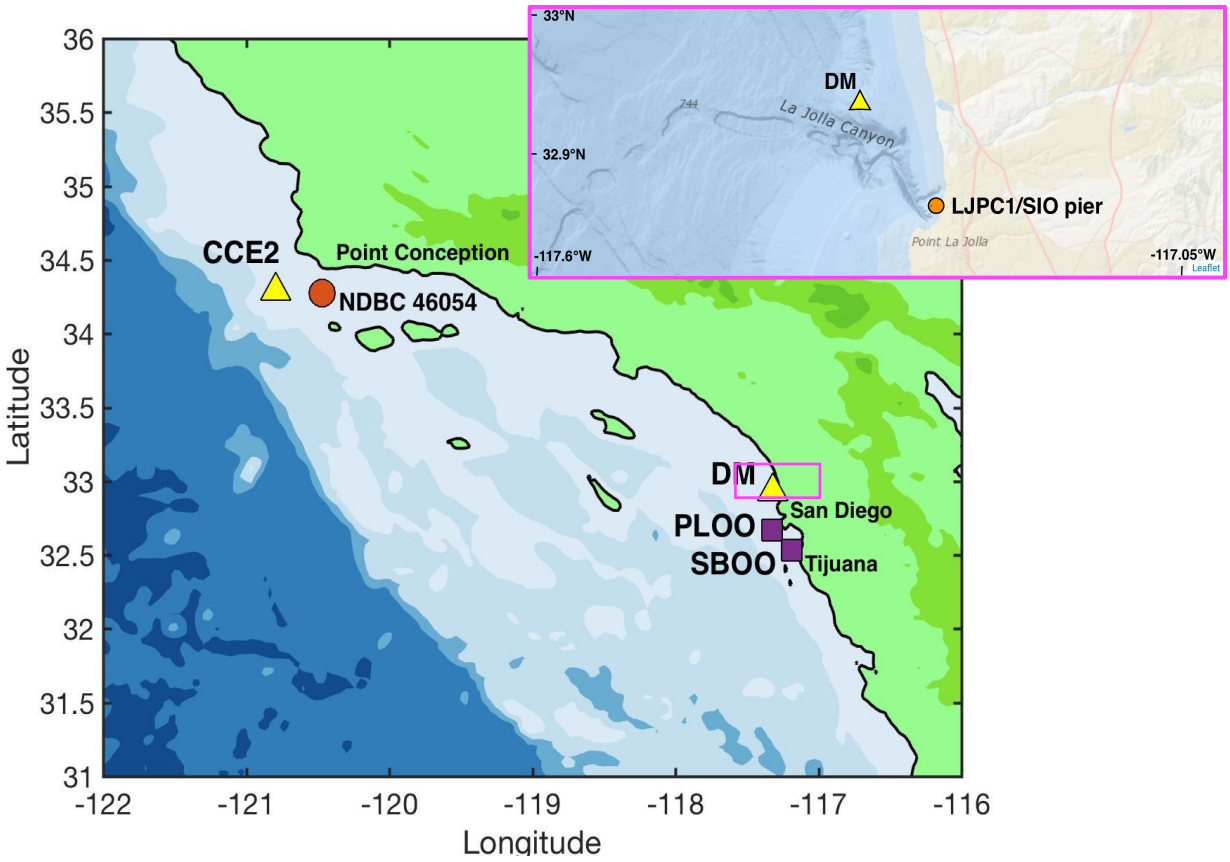

Figure 4.1: Map of southern California with the DM mooring (yellow triangle) and the PLOO and SBOO moorings (purple squares). The subset in the upper right-hand corner is a close up of the region off San Diego which shows the close proximity of the DM mooring to local wind measurements made from the NDBC LJPC1 buoy and from the SIO pier.

The DM mooring measures temperature and salinity in the upper 90 m and is equipped with a downward looking ADCP. The mooring also has oxygen sensors at 35 and 90 m depths and a fluorometer is deployed on the mooring at 1 m depth. This platform is outfitted with an Imaging FlowCytobot (IFCB; Olson and Sosik 2007) at 5 m depth, which is a flow cytometer that images multiple phytoplankton and microzooplankton species. Data from the IFCB are available at https://ifcb-data.whoi.edu/timeline?dataset=SIO_Delmar_mooring. The PLOO and SBOO moorings are also equipped with a variety of physical and biogeochemical sensors. The measurements made by these moorings include temperature, salinity, velocity, oxygen, nitrate, and Chl-*a* fluorescence.

Other measurements used for the red tide analysis include wind data and rainfall data. There are two sets of wind data used in Section 4.3. The first wind data set is from NDBC buoy LJPC1, which is southeast of the DM mooring and is located near the Scripps Institution of Oceanography (SIO) pier (Figure 4.1). The second wind data set comes from the Tijuana River estuary (Figure 4.1). There are also two sets of rainfall data. The first data set is provided by the National Weather Service using observations at Lindbergh Field in San Diego (https://w2.weather.gov/) and the second data set is from the Tijuana River National Estuarine Research Reserve (http://cdmo.baruch.sc.edu/).

To assess the regional horizontal circulation in southern California in the months encompassing the red tide, SSH and geostrophic currents are downloaded from the Copernicus Marine and Environment Monitoring Service (CMEMS) absolute dynamic topography (ADT) product. This product is on a 0.25° grid with daily output.

4.2.2 Upwelling Event Detection

Synoptic upwelling events are detected from the physical and biogeochemistry measurements. The process for determining these upwelling events is similar to the event detection procedure implemented in Chapter 3 at the CCE2 mooring. The reader is referred to Chapter 3 Section 3.2.2 for a description on how upwelling events are detected from the in-situ measurements.

4.3 Physical Processes Results and Discussion

Coastal moorings operated before, during, and after the 2020 red tide and made high-frequency measurements of the oceanic conditions. These observations are examined to assess the sequence of events leading up to the 2020 red tide followed by the physical processes that may be responsible for or contributed to initiating, sustaining, and terminating the red tide.

4.3.1 Timeline of Events

Beginning in late March, observations reveal an upwelling event taking place off San Diego. The upwelling event is near normal, e.g., equatorward winds, southward flow, and decreased temperatures during the upwelling phase (Figures 4.2a, 4.2b, and 4.2c). However, there is a decrease in the near surface salinity that causes the buoyancy frequency to increase (Figures 4.2d and 4.2e). In the biogeochemical measurements, nitrate and chlorophyll fluorescence increase during the upwelling phase (Figures 4.3a and 4.3b). The increase in chlorophyll fluorescence is due to a mixed assortment of plankton, e.g., diatoms and dinoflagellates, as revealed by images from the IFCB on the DM mooring (not shown). At the surface, dissolved oxygen increases marginally, while at depth dissolved oxygen decreases due to upwelling of less oxygenated water (Figure 4.3d).

In between the first and second upwelling events, heavy rainfall accumulates at multiple sites in southern California (Figure 4.2f). A rare occurrence of storm activity involving a cutoff

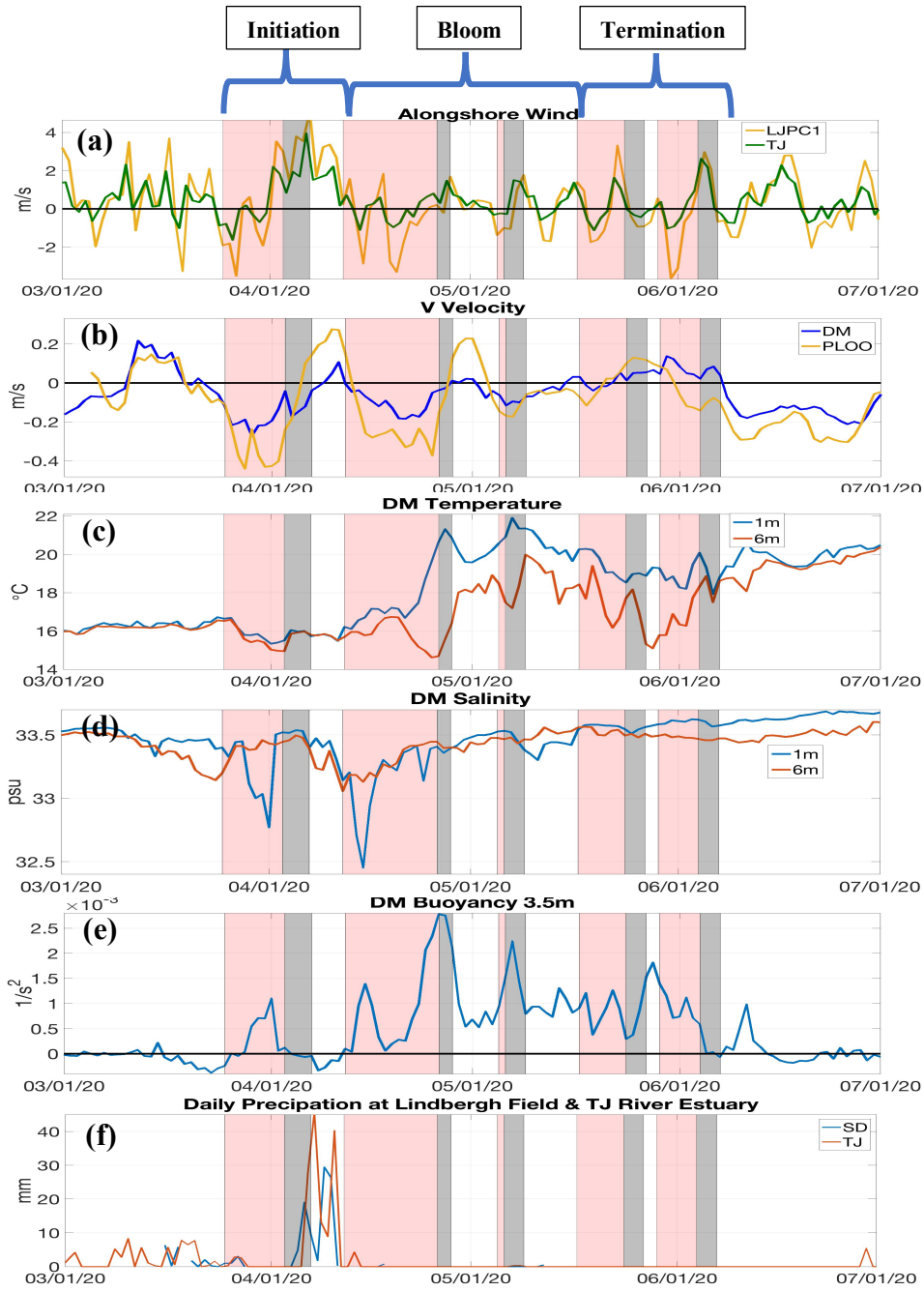

Figure 4.2: Daily averaged (a) north-south wind velocity component from LJPC1 and in Tijuana, (b) north-south velocity component averaged over the upper 35 m depths at DM and PLOO, DM (c) temperature and (d) salinity at 1 and 6 m depths, (e) DM buoyancy just below the surface, and (f) rainfall in San Diego and Tijuana. Red shading denotes upwelling phases of upwelling events while gray shading indicates the relaxation phases of upwelling events. At the top of panel (a) are markers signifying the initiation, bloom, and termination of the 2020 red tide.

low, i.e., a low pressure that separates from the Jet Stream, combined with an atmospheric river which caused record-setting rainfall throughout California (Oakley et al. 2020). This atmospheric event brought persistent rainfall to southern California which lasted for about a week. The two peaks in cumulative rainfall in San Diego and Tijuana in Figure 4.2f reflect the trajectory of the system as it moves east, i.e., the first peak, and then the system meanders west returning over southern California, i.e., the second peak (Oakley et al. 2020).

During this week, salinity at the 1 and 6 m sensors decreased to 33 psu (Figure 4.2d). Given these in-situ salinity measurements and cumulative rainfall from nearby locations (Figures 4.2d and 4.2f), the mixed layer thickness can be approximated. Since the salinity decreased from 33.5 to 33 psu, the mixed layer was nearly 10 m thick (yellow circle in Figure 4.4). From this information, fresher water during the rainfall event mixed down over this relatively thicker mixed layer with only a small change in buoyancy between April 5 and April 12 (Figure 4.2e).

During the second upwelling event and immediately following the atmospheric event, salinity in the upper ocean continues to decline causing increased stratification near the surface (Figures 4.2d and 4.2e). Increases in the upper ocean stratification coincide with higher concentrations of chlorophyll fluorescence (Figures 4.2e and 4.3b). This begins during the upwelling phase, continues through the relaxation phase, and persists into the third upwelling event. Data from the IFCB capture high levels of *L. polyedra* signifying much of the composition in the plankton bloom is due to this particular species (Figure 3.25c; Kahru et al. 2021). During the upwelling phase of the second upwelling event, surface temperatures and dissolved oxygen increase around April 19 (Figures 4.2c and 4.3d). These changes in the water properties are unexpected since they oppose the typical upwelling response. Typically, during upwelling isopycnals shoal bringing cooler, less oxygenated water upward. This behavior is reported at the

deeper sensor depths (Figures 4.2c and 4.3d), and the difference in the oceanic response between the surface and subsurface layers suggests that biological changes in the surface layer are altering these water properties.

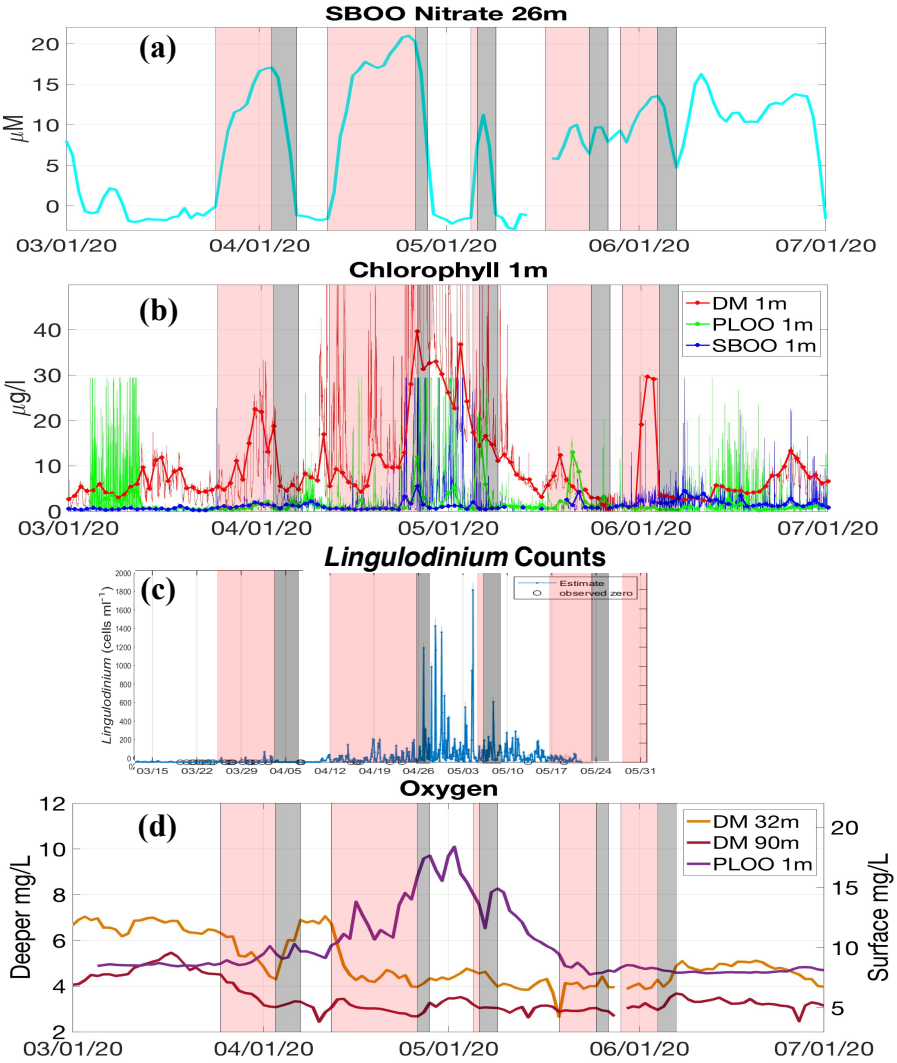

Figure 4.3: (a) Nitrate at SBOO, (b) surface chlorophyll fluorescence at DM, PLOO, and SBOO, (c) *L. polyedra* counts from the IFCB at DM, and (d) oxygen at DM and PLOO. Red shading denotes upwelling phases while gray shading indicates the relaxation phases. In (d), the left y axis is for the 32 and 90 m sensors at DM and the right y axis is for the PLOO sensor.

The combination of upwelled nutrients and stronger stratification in the upper ocean are oceanic conditions advantageous for *L. polyedra* (Figures 4.2e and 4.3a). Their flagella enable them to swim down to reach the upwelled nutrients and return to the surface to photosynthesize

(Smayda 1997; Smayda and Trainer 2010). This allows them to increase their biomass. The chlorophyll fluorescence concentrations and *L. polyedra* counts continue to rise in between the second and third upwelling events given the suitable conditions (Figures 3.25b and 3.25c; Kahru et al. 2021).

The third upwelling event starts in the beginning of May and shares some similarities to the second upwelling event, such as increased surface temperature and buoyancy (Figures 4.2c and 4.2e). Nitrate increases, and this supports another resurgence of *L. polyedra* as upwelling relaxes (Figures 4.3a and 4.3c).

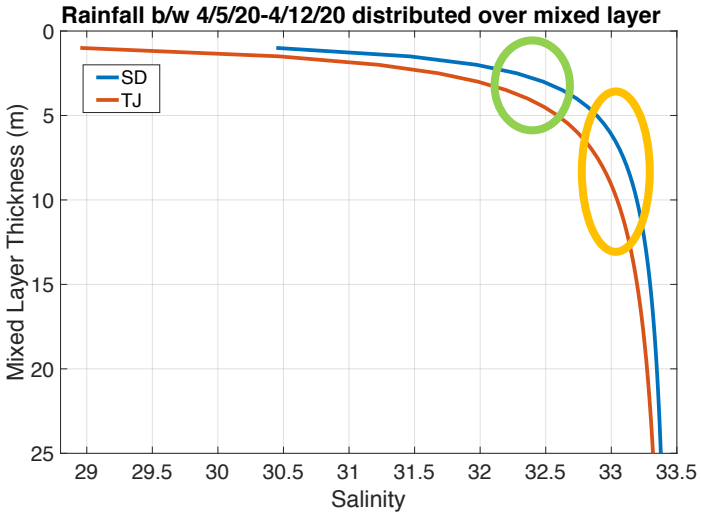

Figure 4.4: Approximated mixed layer thickness based on DM salinity in the upper ocean and measured rainfall in San Diego and Tijuana. The yellow circle highlights the proposed mixed layer during the week of significant rainfall in Figure 4.2f and the green circle highlights these conditions for the time period immediately after the rainfall event.

During the third upwelling event, a nearby profiling device made high-frequency measurements of nitrate, chlorophyll fluorescence, and light (B. Zheng, personal communication, February 19, 2023). These temporally dense measurements sampling the upper ocean observed diel vertical migrations of *L. polyedra. L. polyedra* migrated down to the nutricline at night to take up nitrate and this caused a nitrate loss (B. Zheng, personal communication, February 19,

2023). The loss in nitrate was proportional to the growth in chlorophyll-a concentration supporting the nitrate uptake by *L. polyedra* (B. Zheng, personal communication, February 19, 2023).

During the fourth upwelling event, there is a mild increase in nitrate (Figure 4.3a), a slight uptick in chlorophyll fluorescence (Figure 4.3b), and *L. polyedra* counts remain relatively constant over the upwelling phase of the event but then decrease to very low counts in the relaxation phase of the event (Figure 4.3c). The near surface buoyancy has a net decrease over the upwelling phase (Figure 4.2e). *L. polyedra* counts decrease over the relaxation phase, and by the fifth upwelling event the plankton composition shifted to contain a weaker presence of *L. polyedra* (Figures 4.3b and 4.3c; Kahru et al. 2021).

4.3.2 Physical Factors Initiating and Sustaining the 2020 Red Tide

The red tide timeline of events showed that there were multiple upwelling events that elevated nitrate at a fixed depth (Figure 4.3a). These synoptic upwelling events facilitated the growth of *L. polyedra* by shoaling the nutricline to depths where *L. polyedra* can swim down to uptake nutrients. This section investigates other physical processes that may have supported the red tide in either initiating the event or helping to maintain the event. Two processes that will be examined for their influence on creating coastal conditions favorable for *L. polyedra* are the near surface stratification, i.e., buoyancy frequency, and the cross-shore advection.

4.3.2.1 Stratification

Stratification is a factor that has previously been shown to initiate red tides because the stratified conditions favor dinoflagellates who have a competitive advantage over less motile plankton (Pitcher and Nelson 2006). In the overview of events encompassing the red tide, there were large increases in the near surface buoyancy (Figure 4.2e). This increased surface

stratification is not expected under upwelling when wind-driven mixing typically weakens stratification. To demonstrate how anomalous the stratification was, the near surface stratification and the annual cycle of the near surface stratification are plotted in Figure 4.5a. The annual cycle is computed over 2006 – 2021. This anomalous behavior began at the end of March and continued persistently through April and May. Near surface temperatures are mildly above

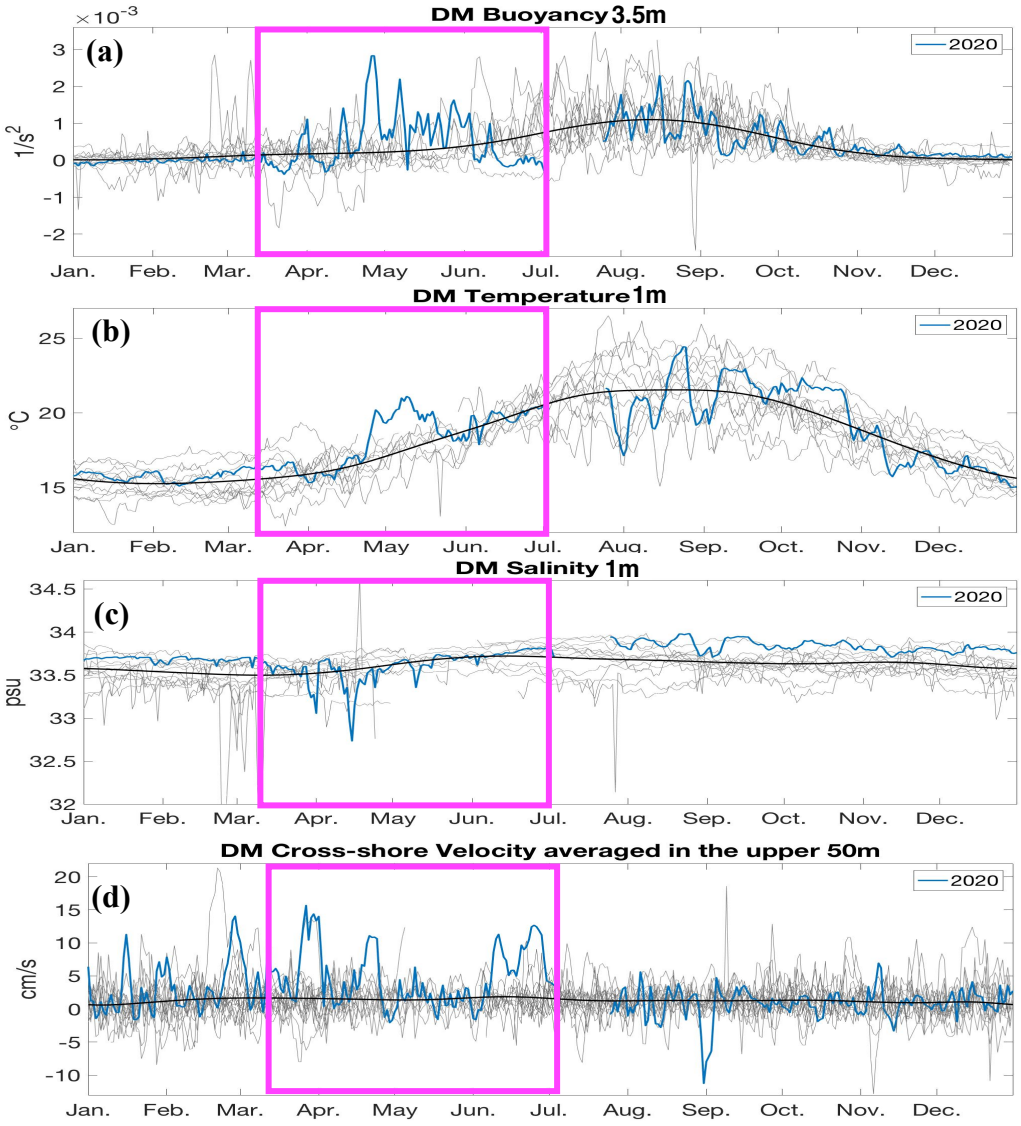

Figure 4.5: DM (a) buoyancy at 3.5 m depth, (b) temperature at 1 m depth, (c) salinity at 1 m depth, and (d) cross-shore velocity averaged in the upper 50 m. Grey lines are all years from 2006 – 2021 except for 2020. Blue line is 2020 and black line is the annual cycle. Magenta boxes encapsulate the 2020 red tide time period.

the climatological average in March (Figure 4.5b), but it is not until the end of March that the stratification abruptly increases due to the decreased salinity (Figures 4.5a and 4.5c).

The stratified conditions were initially due to the cutoff low and atmospheric river, which caused substantial amounts of precipitation and resulted in less saline waters in the upper ocean (Figures 4.2d, 4.2e, 4.2f, and 4.5c). In the week of the atmospheric event, salinity continues to decrease at the surface (Figure 4.2d). The mixed layer thickness is approximated from the in-situ salinity measurements and cumulative rainfall data (Figures 4.2d and 4.2f). Since the salinity decreased down to 32.5 psu, this would imply a mixed layer of about 3 m (green circle in Figure 4.4). The estimated mixed layer is verified by the difference in salinity values at 1 and 6 m depths, with more saline water measured at 6 m depth since it was below the mixed layer (Figure 4.2d).

As salinity returns to climatological values, the surface temperature substantially increases above the climatological curve (Figures 4.5b and 4.5c). The increased temperatures support the additional increase in the near surface buoyancy (Figure 4.5a). It is hypothesized, but not confirmed, that the increased temperatures were due to biological trapping of heat. The increase in *L. polyedra* counts (Figure 4.3c) is suspected to have driven more photosynthesis in the surface layer. The heightened photosynthesis causes more light to be absorbed, resulting in additional heating at the surface and this also causes greater amounts of dissolved oxygen (Seki et al. 1980; Ramp et al. 1991; Wallace and Gobler 2021). This behavior is consistent with the in-situ measurements in Figures 4.2c and 4.3d, and the surface heating would further strengthen the stratification (Figure 4.2e).

Other studies have reported the significance of stratification on HAB dynamics and how it serves as an advantage for dinoflagellates (Ryther 1955; Probyn et al. 2000; Pérez et al. 2010;

Berdalet et al. 2014). In EBUS, relaxation periods can disrupt upwelling phases encouraging restratification through warmer SSTs in coastal regions, e.g., advection of warmer waters or solar radiation (Brink et al. 1981; Send et al. 1987; Graham and Largier 1997). The stronger stratification and shallow mixed layers shift the plankton community structure towards a greater dominance of dinoflagellates (Anderson et al. 2008; Shipe et al. 2008; Fischer et al. 2020).

4.3.2.2 Onshore Advection

Another facilitator of HABs is retentive circulation which can aggregate HAB forming species. Less southward flow was apparent during the relaxation phases of the upwelling events in Figure 4.2b, and this may have helped keep plankton within the SCB. However, the primary attention of this section is on the cross-shore flow in the horizontal circulation. Onshore flows can help aggregate the HAB-forming species close to the coast and this component of the circulation is analyzed.

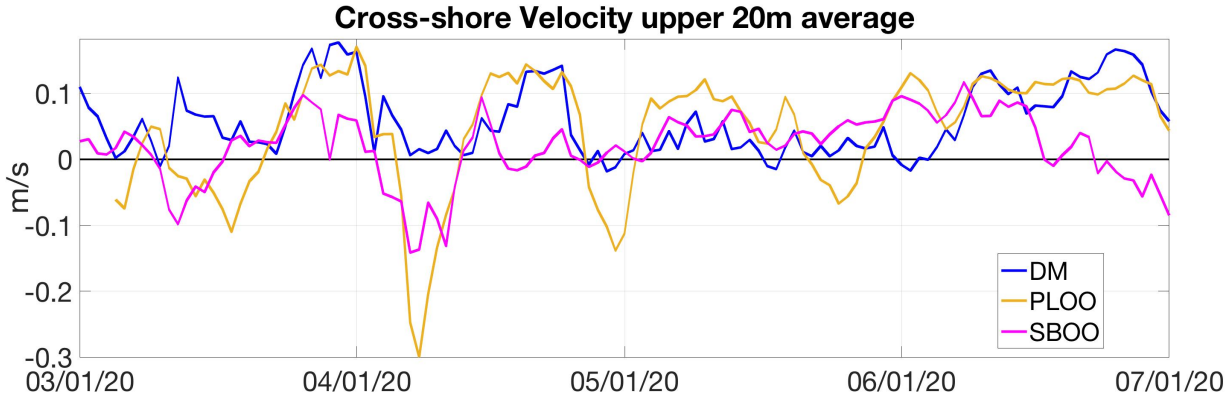

Figure 4.6: Cross-shore velocity averaged in the upper 20 m at DM, PLOO, and SBOO. The cross-shore direction is the east-west orientation and positive values denote onshore flow.

There were large pulses of onshore flow in March and April at DM (Figure 4.5d) and at all three coastal mooring sites (Figure 4.6). While there are some flow reversals at PLOO, the cross-shore flow is relatively persistently onshore over mid-March through June. The suggested

widespread onshore flow over much of the SCB may have helped aggregate *L. polyedra* near the coast.

The onshore flow is attributed to the regional circulation. Typically, the SCE appears in these months (Figure 1.25 from Chapter 1) and the seasonal spin up of the SCE was apparent in the SCE index at this time (Figure 1.23a from Chapter 1). Furthermore, monthly-averaged SSH indicate onshore geostrophic flow stretching between Santa Monica and northern Baja California (Figure 4.7a), which is approximately the geographical range of this particular red tide event

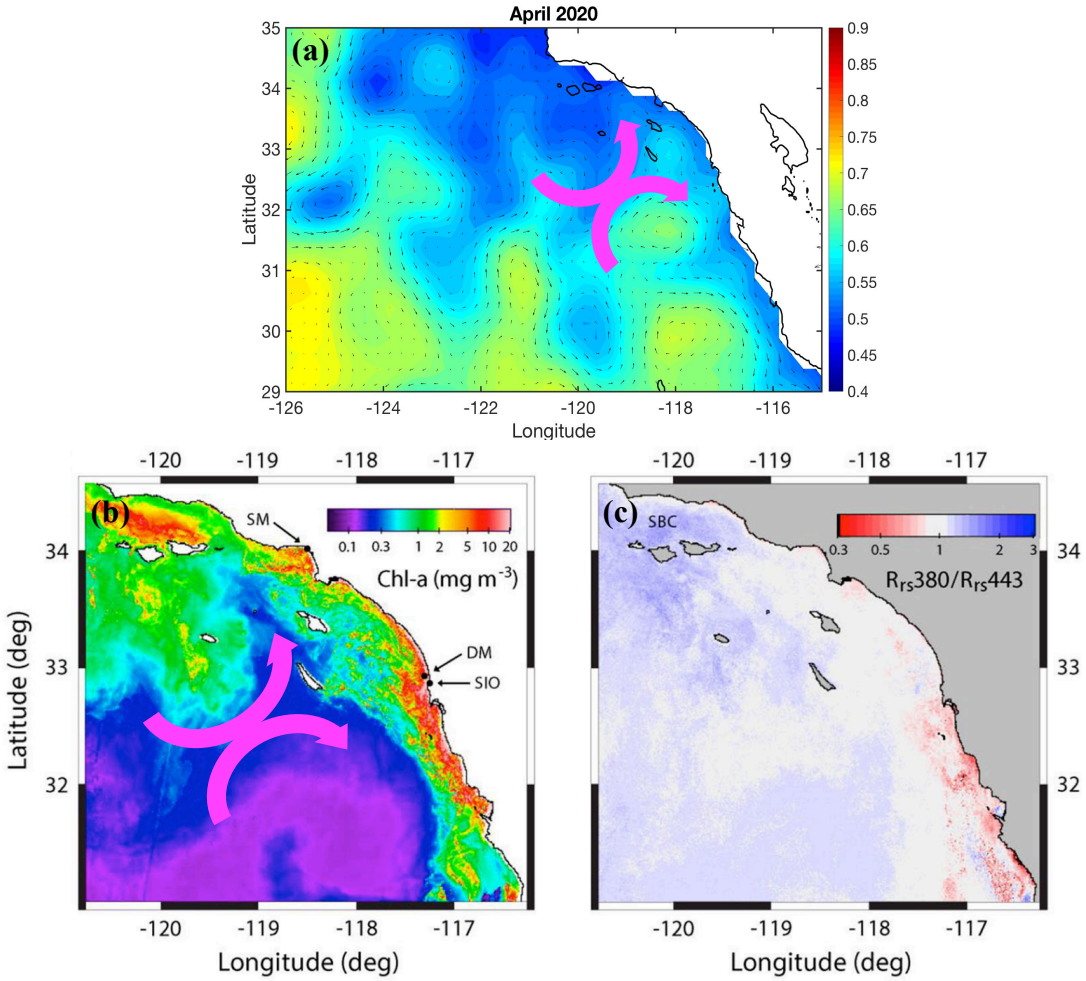

Figure 4.7: (a) CMEMS SSH averaged over April 2020 and the black arrows are the monthly averaged geostrophic currents. (b) Satellite derived chlorophyll-a concentrations and (c) the remote sensing reflectance ratio 380/443 during April – May 2020 modified from Kahru et al. (2021). Magenta arrows emphasize the regional circulation features present during the red tide. In (b), SM refers to Santa Monica.

(Figure 4.7c; Kahru et al. 2021). The cyclonic recirculation of the SCE is schematically shown in Figure 4.7a along with an anticyclonic feature to the southeast of the SCE that reinforces onshore flow towards the coast. Satellite derived chlorophyll-a concentrations capture high concentrations along the coastline (Figure 4.7b), and the presence of the chlorophyll-a concentration pushed up against the coastline is consistent with where onshore flow occurs from both the SCE and the anticyclonic feature (Figure 4.7a).

The onshore circulation related to the SCE and the anticyclonic eddy occurred alongside increased stratification. Retentive circulation has been shown to be an important mechanism for initiating HABs by aggregating HAB causing species (Pitcher and Boyd 1996; Donaghay and Osborn 1997; Smayda 2000; Fischer et al. 2020). Additionally, the retentive circulation along with the local topography, e.g., bays, channels, and lagoons, can trap phytoplankton to form a HAB (Probyn et al. 2010; Pitcher et al. 2010; Fischer et al. 2020), and such topographical features are present in southern California where the red tide occurred.

4.3.3 Red Tide Termination

The decrease in *L. polyedra* counts in May and June indicate the decline of the red tide. This section examines what process likely contributed to the termination of the 2020 red tide and briefly discusses the ecological consequences related to the red tide.

4.3.3.1 Decreased Stratification

The red tide declined at the end of May – early June, which was contemporaneous with a decrease in stratification at the surface (Figures 4.2e, 4.3c, and 4.5a). The decrease in stratification in late May - early June coincides with a decrease in temperature (Figures 4.5a and 4.5b). Wind-driven mixing, as implied by the upwelling favorable winds (Figure 4.2a) and thickening of the mixed layer (Figure 4.8a), mixed the warm surface temperatures downward

causing subsurface temperatures to increase (Figures 4.2c and 4.8b). This is also true at the PLOO mooring (not shown). It is suspected that these processes led to the demise of the red tide.

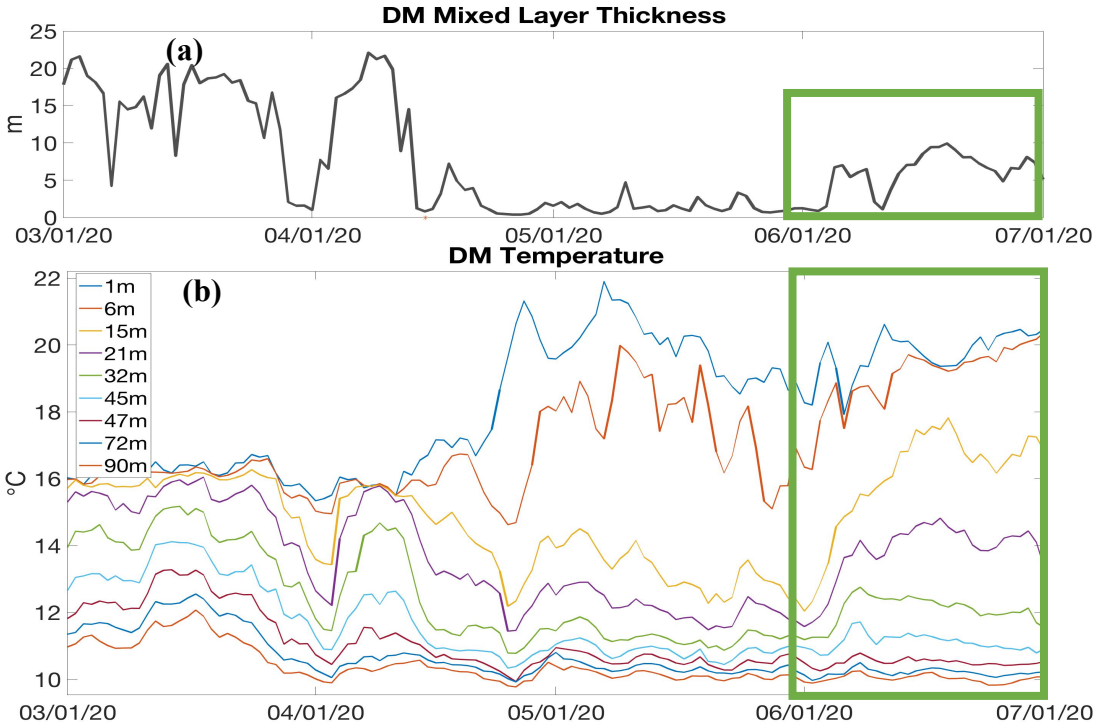

Figure 4.8: (a) Mixed layer thickness approximated at DM based on a density difference of 0.125 kg/m^3 from the density at 1 m depth. (b) DM temperature as measured by the sensors. Green boxes highlight the time period when the mixed layer thickens, and the warmer surface waters are mixed downwards increasing the subsurface temperatures.

To demonstrate the influence of the decreasing temperature on the stratification, the near surface stratification is calculated assuming the salinity does not change and this is compared to the observed stratification (Figure 4.9). The observed stratification fluctuations are similar to the stratification fluctuations that assume salinity is constant. This demonstrates that the variability in the stratification during the red tide and at the end of it is in part due to the temperature field. However, starting in late-May some offset between the two curves is apparent, where the observed stratification is less than the temperature dependent stratification. The lower observed stratification is related to salinity changes, as demonstrated by the stratification time series that

holds temperature constant (Figure 4.9). The gradual decline over May in this stratification time series reflects the slow increase in near surface salinity (Figure 4.2d).

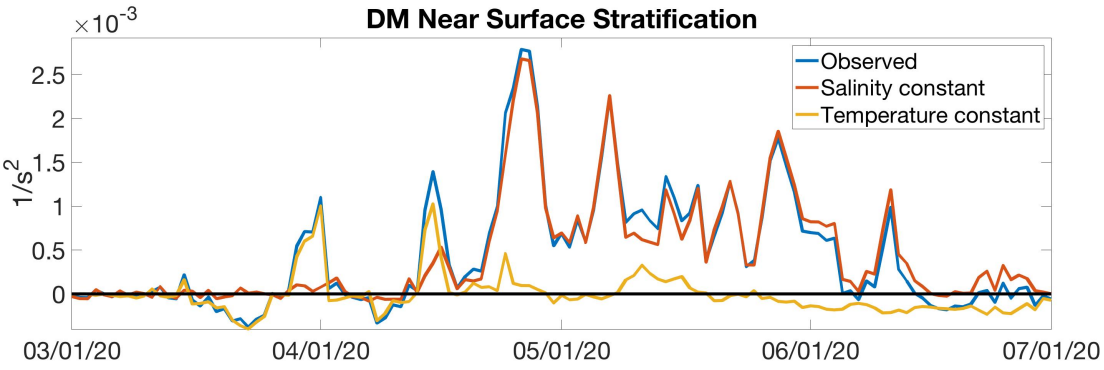

Figure 4.9: Near surface stratification at DM. Stratification based on the observed density (blue curve) is compared against stratification assuming the salinity is unchanged (red curve) and assuming the temperature remains the same (yellow curve).

Figures 4.2c and 4.8b show that the upper ocean temperature decrease in May restores the temperature to climatological values (Figure 4.5b), but the continued decrease in stratification to below climatological values (Figure 4.5a) is caused by a mild increase in the near surface salinities (Figures 4.2d and 4.5c). This behavior is also observed at the PLOO and SBOO moorings starting at the beginning of May (Figure 4.10). Given the distinction in salinity near the surface versus the salinity at the next deepest sensor starting in mid-May, these data suggest that evaporation or advection as potential mechanisms for causing the greater near surface salinity. If evaporation caused the increase in salinity, then the density increase from the salinity change would have contributed to the change in buoyancy in Figure 4.9.

The changes in stratification in May and June likely contributed to the demise of the red tide. The less buoyant conditions favor other planktonic species, like diatoms, and can encourage a shift in the community structure (Smayda 2000; Anderson et al. 2006; Smayda and Trainer 2010). The mortality of *L. polyedra* may have been driven by physical and/or biological processes. Upwelling favorable winds, offshore advection, and shear-inducing turbulence can decrease the biomass of dinoflagellates effectively diminishing the HAB (Pollingher and Zemel

1981; Donaghay and Osborn 1997; Fischer et al. 2020). Biological processes may also lead to the disruption of a HAB, such as zooplankton grazing and algicidal activity (Imai et al. 1995; Park et al. 1998). These different processes driving *L. polyedra* mortality alongside the less favorable physical environment may have discouraged continuation of the red tide through June.

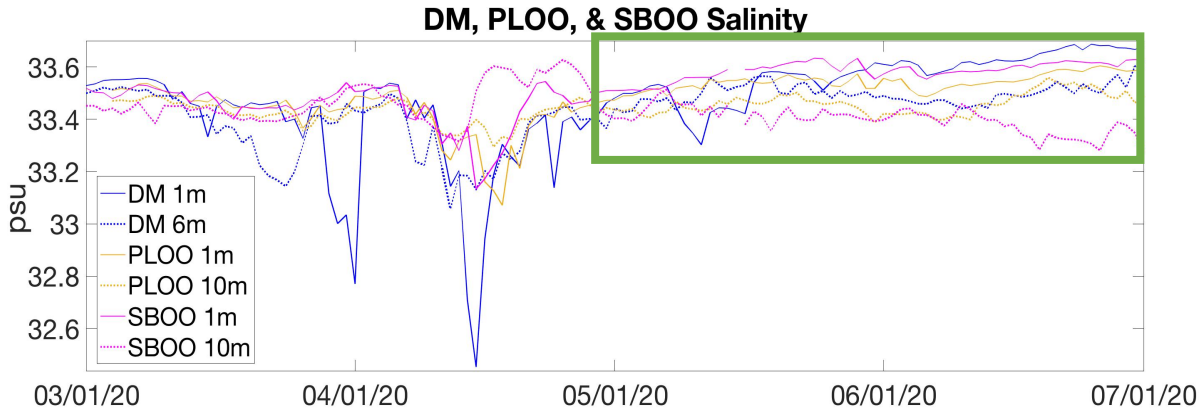

Figure 4.10: Salinity in the upper ocean at DM, PLOO, and SBOO. Green box highlights the time period when the 1 m salinity is saltier than the salinity at the next deepest sensor. Solid lines represent the 1 m sensors and dotted lines denote the second shallowest sensor.

4.3.3.2 Low Oxygen and Ecological Consequences

Oxygen measurements close to the sea floor at the DM mooring recorded dissolved oxygen low enough to classify as hypoxic (Figure 4.3d; Diaz and Rosenberg 2008; Vaquer-Sunyer and Duarte 2008). The decrease in oxygen below 4 mg/L at DM 90 m depth begins in April and persists through early June indicating conditions were hypoxic in the benthic habitat. The water mass results from Chapter 1 indicated higher PEW concentrations and positive PEW anomalies at both 35 and 90 m depth (Figures 1.18 and 1.20). PEW is characterized by lower oxygen (Wyrtki 1967; Lynn and Simpson 1987; Meinvielle and Johnson 2013; Nam et al. 2015). The presence of more PEW at this time could have further negatively impacted the environment by having already established lower background levels of dissolved oxygen.

The decrease in oxygen near the bottom is likely a consequence of the red tide. As the red tide declines, bacteria break down the bloom matter. In this process, bacteria consume oxygen which can create hypoxic or anoxic conditions (Fallon and Brock 1979; Sellner et al. 2003; Al Gheilani et al. 2011; Wallace and Gobler 2021). The consumption of oxygen by bacteria may be exacerbated by strongly stratified conditions, reduced mixing, upwelling of waters that are low in oxygen, and eutrophication (Grantham et al. 2004; Kemp et al. 2009, Levin et al. 2009; Nam et al. 2011; Booth et al. 2012). This is one way *L. polyedra* blooms negatively impact the environment. *L. polyedra* blooms can also produce yessotoxin that may be consumed, and in large quantities can be harmful to marine life (Arévalo et al. 2006; Armstrong and Kudela 2006). The ecological consequences of red tides can impact multiple species such as fish, birds, and marine mammals (Fritz et al. 1992; Anderson et al. 2006; McCabe et al. 2015).

4.4 Conclusion

Coastal upwelling regions are characterized by HABs and a particularly strong red tide event was the focus in this chapter. In-situ high-frequency measurements along the coast of southern California monitored the sequence of events surrounding the 2020 red tide. This event was significant because of its longer lasting duration that caused significant changes in the coastal ocean ecology. Monitoring, understanding, and improving the ability to predict HABs is important because of the consequential impact they have on public health, fisheries and aquaculture, and ecosystem functioning (Anderson et al. 2012; McCabe et al. 2016).

Upwelling events, like those studied in Chapter 3, were a contributor to the 2020 red tide in southern California (Figures 4.2 and 4.3). Other physical factors favorable for conditioning the 2020 red tide were the strong stratification and retentive circulation (Figures 4.2b, 4.2e, 4.5a, 4.5d, and 4.7). An anomalous storm and the biological trapping of heat at the surface initiated

and maintained, respectively, the strong stratification promoting the red tide (Figures 4.2c, 4.2f, and 4.3c). Onshore geostrophic flow from the SCE and an anticyclonic circulation feature southeast of the SCE promoted onshore geostrophic flow aggregating planktonic species close to the coast (Figure 4.7).

Termination of the red tide coincided with decreased stratification (Figures 4.5a and 4.9) that was due to upwelling winds mixing the warmer surface waters downward (Figures 4.2a, 4.8, and 4.9) and by increased salinity near the surface likely from evaporation (Figures 4.9 and 4.10). Ecological consequences of the red tide included hypoxic conditions on the shelf (Figure 4.3d) and mass die off of multiple species, e.g., fish, marine invertebrates, and other benthic organisms. The unpredictability of these events can make them difficult to study, but the maintained moorings monitoring the coastal ocean captured this pronounced HAB exemplifying why it is important to make sustained observations.

Studies have suggested more regular occurrences of HAB events in the last two decades, and such low-frequency variability in the phytoplankton community structure has been linked to large-scale climate indices like the NPGO and PDO (Cloern et al. 2005; Sekula-Wood et al. 2011; Baron et al. 2013; Du et al. 2015; Fischer et al. 2020). These results suggest that the different processes that influence HAB occurrences extend over a range of time and space scales. The multiple physical and physiological processes that contribute to HABs make these events difficult to predict in how they will respond to climate change, but it is suggested that they will increase in frequency and severity (Wells et al. 2015; Pitcher et al. 2017; Fischer et al. 2020). The intricacies of these events with limited long-term data makes future changes difficult to forecast. Given the uncertainty of how HABs will respond to climate change there is general agreement for the need of long-term monitoring that includes physical and biogeochemical

measurements in order to assess how HAB events will change in the future (Kudela et al. 2015; Wells et al. 2015; Pitcher et al. 2017). The southern California observations that continue to make measurements address this scientific consensus and will continue to be important for future work on high-frequency variability in the coastal ocean.

4.5 Acknowledgements

We acknowledge the City of San Diego for sharing the measurements made at the PLOO and SBOO moorings. We would like to thank Heidi Sosik for sharing the IFCB data at the DM mooring. Data from the IFCB is available at https://ifcb-data.whoi.edu/timeline?dataset=SIO_Delmar_mooring. The NOAA NDBC LJPC1 winds used in this study are available at https://www.ndbc.noaa.gov/. The San Diego rainfall data come from the National Weather Service at Lindbergh Field in San Diego and can be downloaded from https://w2.weather.gov/. The Tijuana winds and rainfall data used in this chapter are from the Tijuana River National Estuarine Research Reserve and can be found at http://cdmo.baruch.sc.edu/.

Chapter 4, in part is currently being prepared for submission for publication of the material. Lowcher, Caroline; Send, Uwe; Lankhorst, Matthias. The dissertation author was the primary researcher and author of this material.

References

Aguirre, C., Garreaud, R., Belmar, L., Farías, L., Ramajo, L., and F. Barrera, 2021. High-Frequency Variability of the Surface Ocean Properties Off Central Chile During the Upwelling Season, *Front. Mar. Sci*., **8**, doi:10.3389/fmars.2021.702051.

Al Gheilani, Matsuoka, K., AlKindi, A., Amer, S., and C. Waring, 2011. Fish Kill Incidents and Harmful Algal Blooms in Omani Waters, *J. Agric. Mar. Sci*., **16**, 23-33.

Alexander, M., Bladé, I., Newman, M., Lanzante, J., Lau, N., and J. Scott, 2002. The Atmospheric Bridge: The Influence of ENSO Teleconnections on Air-Sea Interaction over the Global Oceans, *J. Climate*, **15**, 2205-2231, doi:10.1175/1520-0442(2002)015<2205:TABTIO>2.0.CO;2.

Alin et al., 2012. Robust empirical relationships for estimating the carbonate system in the southern California Current System and application to CalCOFI hydrographic cruise data (2005-2011), *J. Geophy. Res.*, **117**, doi:10.1029/2011JC007511.

Allen, W., 1946. "Red Water" in La Jolla bay in 1946, *Trans. Am. Micros. Soc*., **65**, 149-153.

Amaya, D., Jacox, M., Dias, J., Alexander, M., Karnauskas, K., Scott, J., and M. Gehne, 2022. Subseasonal-to-Seasonal Forecast Skill in the California Current System and Its Connection to Coastal Kelvin Waves, *J. Geophy. Res*. *Oceans*, **127**, doi:10.1029/2021JC017892.

Amaya, D., Miller, A. Xie, S., and Y. Kosaka, 2020. Physical drivers of the summer 2019 North Pacific marine heatwave, *Nature Comm.*, **11**, doi:10.1038/s41467-020-15820-w.

Anderson, C., Brzezinski, M., Washburn, L., and R. Kudela, 2006. Circulation and environmental conditions during a toxigenic *Pseudo-nitzschia australis* bloom in the Santa Barbara Channel, California, *Mar. Ecol. Prog. Ser*., **327**, 119-133, doi:10.3354/meps327119.

Anderson, D., Cembella, A., and G. Hallegraeff, 2012. Progress in understanding harmful algal blooms: paradigm shifts and new technologies for research, monitoring, and management, *Ann. Rev. Mar. Sci*., **4**, 143-176, doi:10.1146/annurev-marine-120308-081121.

Anderson, D., Burkholder, J., Cochlan, W., Glibert, P., Gobler, C., Heil, C., Kudela, R., Parsons, M., Rensel, J., Townsend, D., Trainer, V., and G. Vargo, 2008. Harmful algal blooms and eutrophication: Examining linkages from selected coastal regions of the United States, *Harmful Algae*, **8**, 39-53, doi:10.1016/j.hal.2008.08.017.

Antoine, D. and A. Morel, 1996. Oceanic primary production, 1. Adaption of a spectral light-photosynthesis model in view of application to satellite chlorophyll observations, *Global Biogeochemical Cycles*, **10**, 43-55, doi:10.1029/95GB02831.

Aravena, G., Broitman, B., and N. Stenseth, 2014. Twelve Years of Change in Coastal Upwelling along the Central-Northern Coast of Chile: Spatially Heterogeneous Responses to Climatic Variability, *PLoS One 9:e90276*, doi:10.1371/journal.pone.0090276.

Arévalo et al., 2006. First reported case of yessotoxins in mussels in the Galician rias during a bloom of *Lingulodinium polyedrum* stein (dodge), *Proceedings of the 5th International Conference on Molluscan Shellfish Safety*, 184-189.

Armstrong, M. and R. Kudela, 2006. Evaluation of California isolates of *Lingulodinium polyedrum* for the production of yessotoxin, *Afr. J. mar. Sci*, **28**, 399-401, doi:10.2989/18142320609504186.

Atkinson, L., Brink, K., Davis, R., Jones, B., Paluskiewicz, T., and D. Stuart, 1986. Mesoscale hydrographic variability in the vicinity of Points Conception and Arguello during April-May 1983: The OPUS 1983 experiment, *J. Geophy. Res*., **91**, 12899-12918, doi:10.1029/JC091iC11p12899.

Auad, G., Roemmich, D., and J. Gilson, 2011. The California Current System in relation to the Northeast Pacific Ocean circulation, *Prog. Oceanog.*, **91**, 576-592, doi:10.1016/j.pocean.2011.09.004.

Austin, J. and J. Barth, 2002. Drifter Behavior on the Oregon-Washington Shelf during Downwelling-Favorable Winds, *J. Phys. Oceanog.*, **32**, 3132-3144, doi:10.1175/1520-0485(2002)032<3132:DBOTOW>2.0.CO;2.

Bakun, A., 1973. Coastal upwelling indices, West Coast of North America, 1946-71, US Department of Commerce, National Oceanic and Atmospheric Administration, National Marine Fisheries Service.

Bakun, A., 1990. Global Climate Change and Intensification of Coastal Ocean Upwelling, *Science*, **247**, 198-201, doi:10.1126/science.247.4939.198.

Bakun, A. and C. Nelson, 1977. Climatology of upwelling related processes off Baja California, State of California, Marine Research Committee California Cooperative Fisheries Investigations, Reports, XIX, 107-127.

Bakun, A., Black, B., Bograd, S., García-Reyes, M., Miller, A., Rykaczewski, and W. Sydeman, 2015. Anticipated Effects of Climate Change on Coastal Upwelling Ecosystems, *Curr. Clim. Change Rep*., **1**, 85-93, doi:10.1007/s40641-015-0008-4.

Balaguru, K., Van Roekel, L., Leung, L., and M. Veneziani, 2021. Subtropical Eastern North Pacific SST Bias in Earth System Models, *J. Geophy. Res*. *Oceans*, **126**, doi:10.1029/2021JC017359.

Barkhordarian, A., Nielsen, D., and J. Baehr, 2022. Recent marine heatwaves in the North Pacific warming pool can be attributed to rising atmospheric levels of greenhouse gases, *Commun. Earth Environ*., **3**, 131, doi:10.1038/s43247-022-00461-2.

Baron, J., Hall, E., Nolan, B., Finlay, J., Bernhardt, E., Harrison, J., Chan, F., and E. Boyer, 2013. The interactive effects of excess reactive nitrogen and climate change on aquatic ecosystems and water resources of the United States, *Biogeochemistry*, **114**, 71-92, doi:10.1007/s10533-012-9788-y.

Barth, J., Pierce, S., and R. Castelao, 2005. Time-dependent, wind-driven flow over a shallow midshelf submarine bank, *J. Geophy. Res*., **110**, doi:10.1029/2004JC002761.

Barton, E., Field, D., and C. Roy, 2013. Canary current upwelling: More or less?, *Prog. Oceanog.*, **116**, 167-178, doi:10.1016/j.pocean.2013.07.007.

Behrenfeld, M., Marañón, E., Siegel, D., and S. Hooker, 2002. Photoacclimation and nutrient-based model of light-saturated photosynthesis for quantifying oceanic primary production, *Mar. Ecol. Prog. Ser.*, **228**, 103-117, doi:10.3354/meps228103.

Berdalet et al., 2014. Understanding harmful algae in stratified systems: Review of progress and future directions, *Deep Sea Res., Part II*, **101**, 4-21, doi:10.1016/j.dsr2.2013.09.042.

Bograd, S., Buil, M., Di Lorenzo, E., Castro, C., Schroeder, I., Goericke, R., Anderson, C., Benitez-Nelson, C., and F. Whitney, 2015. Changes in source waters to the Southern California Bight, *Deep Sea Res., Part II*, **112**, 42-52, doi:10.1016/j.dsr2.2014.04.009.

Bograd, S., Chereskin, T., and D. Roemmich, 2001. Transport of mass, heat, salt, and nutrients in the southern California Current System: Annual cycle and interannual variability, *J. Geophy. Res*. *Oceans*, **106**, 9255-9275, doi:10.1029/1999JC000165.

Bograd, S. and R. Lynn, 2001. Physical-biological coupling in the California Current during the 1997-99 El Niño-La Niña cycle, *Geophys. Res. Lett.*, **28**, 275-278, doi:10.1029/2000GL012047.

Bograd, S. and R. Lynn, 2003. Long-term variability in the Southern California Current System, *Deep Sea Res., Part II,* **50**, 2355-2370, doi:10.1016/S0967-0645(03)00131-0.

Bograd, S., Schroeder, I., and M. Jacox, 2019. A water mass history of the Southern California current system, *Geophys. Res. Lett.*, **46**, doi:10.1029/2019GL082685.

Bograd, S., Schroeder, I., Sarkar, N., Qiu, X., Sydeman, W., and F. Schwing, 2009. Phenology of coastal upwelling in the California Current, *Geophys. Res. Lett.*, **36**, doi:10.1029/2008GL035933.

Bond, N., Cronin, M., Freeland, H., and N. Mantua, 2015. Causes and impacts of the 2014 warm anomaly in the NE Pacific, *Geophys. Res. Lett.*, **42**, 3414-3420, doi:10.1002/2015GL063306.

Bonino, G., Di Lorenzo, E., Masina, S., and D. Iovino, 2019. Interannual to decadal variability within and across the major Eastern Boundary Upwelling Systems, *Sci. Rep.*, **9**, doi:10.1038/s41598-019-56514-8.

Boon, J., Heitsenrether, R., and W. Hensley, 2012. Multi-sensor evaluation of microwave water level measurement error, *Oceans 2012*, 1-8, doi:10.1109/OCEANS.2012.6405079.

Booth et al., 2012. Natural intrusions of hypoxic, low pH water into nearshore marine environments on the California coast, *Cont. Shelf Res*., **45**, 108-115, dpo:10.1016/j.csr.2012.06.009.

Botsford, L., Lawrence, C., Dever, E., Hastings, A., and J. Largier, 2006. Effects of variable winds on biological productivity on continental shelves in coastal upwelling systems, *Deep Sea Res., Part II*, **53**, 3116-3140, doi:10.1016/j.dsr2.2006.07.011.

Boyer, T., Antonov, J., Baranova, O., Coleman, C., Garcia, H., Grodsky, A., Johnson, D., Locarini, R., Mishonov, A., O'Brien, T., Paver, C., Reagan, J., Seidov, D., Smolyar, I., and M. Zweng, 2013. World ocean database 2013, NOAA atlas NESDIS; 72, doi:doi.org/10.7289/V5NZ85MT.

Bray, N., Keyes, A., and W. Morawitz, 1999. The California Current system in the Southern California Bight and the Santa Barbara Channel, *J. Geophy. Res*., **104**, 7695-7714, doi:10.1029/1998JC900038.

Bresnahan, P., Martz, T., Takeshita, Y., Johnson, K., and M. LaShomb, 2014. Beset practices for autonomous measurement of seawater pH with the Honeywell Duraget, *Methods Oceanogr*., **9**, 44-60, doi:10.1016/j.mio.2014.08.003.

Brink, K., Jones, B., Van Leer, J., Mooers, C., Stuart, D., Stevenson, M., Dugdale, R., and G. Heburn, 1981. Physical and Biological Structure and Variability in an Upwelling Center off Peru near 15ºS During March, 1977, *Coastal Upwelling*, **1**, doi:10.1029/CO001p0473.

Brzezinski, M. and L. Washburn, 2011. Phytoplankton primary productivity in the Santa Barbara Channel: Effects of wind-driven upwelling and mesoscale eddies, *J. Geophy. Res*. *Oceans*, **116**, doi:10.1029/2011JC007397.

Caldwell, P., Merrifield, M., and P. Thompson, 2015. Sea level measured by tide gauges from global oceans — the Joint Archive for Sea Level holdings (NCEI Accession 0019568), Version 5.5, *NOAA National Centers for Environmental Information*, Dataset, doi:10.7289/V5V40S7W.

Caron, D., Garneau, M., Seubert, E., Howard, N., Darjany, L., Schnetzer, A., Cetinic, Filteau, G., Lauri, P., Jones, B., and S. Trussell, 2010. Harmful algae and their potential impacts on desalination operations off southern California, *Water Res*., **44**, 385-416, doi:10.1016/j.watres.2009.06.051.

Castelao, R., Mavor, T., Barth, J., and L. Breaker, 2006. Sea surface temperature fronts in the California Current System from geostationary satellite observations, *J. Geophy. Res*. *Oceans*, **111**, doi:10.1029/2006JC003541.

Castro, C., Chavez, F., and C. Collins, 2001. Role of the California Undercurrent in the export of denitrified waters from the eastern tropical North Pacific, *Glob. Biogeo. Cyc*., **15**, 819-830, doi:10.1029/2000GB001324.

Cavole, L., Demko, A., Diner, R., Giddings, A., Koester, I., Pagniello, C., Paulsen, M., Ramirez-Valdez, A., Schwenck, S., Yen, N., Zill, M., and P. Franks, 2016. Biological impacts of the 2013-2015 warm-water anomaly in the Northeast Pacific: Winners, losers, and the future, *Oceanography*, **29**, 273-285, doi:10.5670/oceanog.2016.32.

Chan, F., Barth, J., Blanchette, C., Byrne, R., Chavez, F., Cheriton, O., Feely, R., Friederich, G., Gaylord, B., Gouhier, T., Hacker, S., Hill, T., Hoffman, G., McManus, M., Menge, B., Nielsen, K., Russell, A., Sanford, E., Sevadjian, J., and L. Washburn, 2017. Persistent spatial structuring of coastal ocean acidification in the California Current System, *Scientific Reports*, **7**, doi:10.1038/s41598-017-02777-y.

Chan, F., Barth, J., Lubchenco, J., Kirinich, A., Weeks, H., Peterson, W., and B. Menge, 2008. Emergence of anoxia in the California Current large marine ecosystem, *Science*, **319**, doi:10.1126/science.1149016.

Chao, Y., Farrara, J., Bjorkstedt, E., Chai, F., Chavez, F., Rudnick, D., Enright, W., Fisher, J., Peterson, W., Welch, G., Davis, C., Dugdale, R., Wilkerson, F., Zhang, H., Zhang, Y., and E. Ateljevich, 2017. The origins of the anomalous warming in the California coastal ocean and San Francisco Bay during 2014-2016, *J. Geophy. Res*. *Oceans*, **122**, 7537-7557, doi:10.1002/2017/JC013120.

Chavez, F. and J. Toggweiler, 1995. Physical estimates of global new production: The upwelling contribution, in *Upwelling in the Ocean: Modern Processes and Ancient Records*, edited by C. P. Summerhayes et al., 313-320, John Wiles, New York.

Chavez, F., Pennington, J., Castro, C., Ryan, J., Michisaki, R., Schlining, B., Walz, P., Buck, K., McFadyen, A., and C. Collins, 2002. Biological and chemical consequences of the 1997-1998 El Niño in central California waters, *Prog. Oceanog*., **54**, 205-232, doi:10.1016/S0079-6611(02)00050-2.

Chelton, D., 1981. Interannual variability of the California Current – physical factors, *CalCOFI Report*, **22.**

Chelton, D., 1982. Large-scale response of the California Current to forcing by the wind stress curl, *CalCOFI Report*, **23.**

Chelton, D., 1984. Seasonal variability of alongshore geostrophic velocity off central California, *J. Geophy. Res*., **89**, 3473-3486, doi:10.1029/JC089iC03p03473.

Chelton, D., Bernal, P., and J. McGowan, 1982. Large-scale interannual physical and biological interaction in the California Current, *J. Mar. Res.*, **40**, 1095-1125.

Chen, S., Wu, R., Chen, W., Yu, B., and X. Cao, 2016. Genesis of westerly wind bursts over the equatorial western Pacific during the onset of the strong 2015-2016 El Niño, *Atmos. Science Lett.*, **17**, 384-391, doi:10.1002/asl.669.

Chereskin, T., 1995. Direct evidence for an Ekman balance in the California Current, *J. Geophy. Res*. *Oceans*, **100**, 18261-18269, doi:10.1029/95JC02182.

Chereskin, T. and P. Niiler, 1994. Circulation in the Ensenada Front – September 1988, *Deep Sea Res.,* **41**, 1251-1287, doi:10.1016/0967-0637(94)90043-4.

Chhak, K. and E. Di Lorenzo, 2007. Decadal variations in the California Current upwelling cells, *Geophys. Res. Lett.*, **34**, doi:10.1029/2007GL030203.

Christensen, N., De La Paz, R., and G. Gutierrez, 1983. A study of the sub-inertial waves off the west coast of Mexico, *Deep Sea Res.*, **30**, 835-850, doi:10.1016/0198-0149(83)90003-1.

Choboter, P. F., Duke, D., Horton, J. P., and P. Sinz, 2011. Exact solutions of wind-driven coastal upwelling and downwelling over sloping topography, *J. Phys. Oceanog*., **41**, 1277-1296, doi:10.1175/2011JPO4527.1.

Cloern, J., Schraga, T., Lopez, C., Knowles, N., Labiosa, R., and R. Dugdale, 2005. Climate anomalies generate an exceptional dinoflagellate bloom in San Francisco Bay, *Geophys. Res. Lett.*, **32**, doi:10.1029/2005GL023321.

Colas, F., Capet, X., McWilliams, J. C., and A. Shchepetkin, 2008. 1997-1998 El Niño off Peru: A numerical study, *Prog. Oceanog*., **79**, 138-155, doi:10.1016/j.pocean.2008.10.015.

Collins, C., Pennington, J., Castro, C., Rago, T., F. Chavez, 2003. The California Current system off Monterey, California: physical and biological coupling, *Deep Sea Res., Part II*, **50**, 2389-2904, doi:10.1016/S0967-0645(03)00134-6.

Connolly, T., Hickey, B., Shulman, I,. and R. Thomson, 2014. Coastal trapped waves, alongshore pressure gradients, and the California Undercurrent, *J. Phys. Oceanog*., **44**, 319-342, doi:10.1175/JPO-D-13-095.1.

Cudaback, C., Washburn, L., and E. Dever, 2005. Subtidal inner-shelf circulation near Point Conception, California, *J. Geophy. Res*., **110**, doi:10.1029/2004JC002608.

Cury, P. and C. Roy, 1989. Optimal environmental window and pelagic fish recruitment success in upwelling areas, *Can. J. Fish. Aquat. Sci*., **46**, 670-680, doi:10.1139/f89-086.

Davis, A. and E. Di Lorenzo, 2015. Interannual forcing mechanisms of California Current transports I: Meridional Currents, *Deep Sea Res., Part II*, **112**, 18-30, doi:10.1016/j.dsr2.2014.02.005.

Davis, R., 2010. On the coastal-upwelling overturning cell, *J. Mar. Res.*, **68**, 369-285, doi:10.1357/002224010794657173.

Davis, R., Ohman, M., Rudnick, D., Sherman, J., and B. Hodges, 2008. Gilder surveillance of physics and biology in the southern California Current System, *Limnol. Oceannogr.*, **53**, 2151-2168, doi:10.4319/lo.2008.53.5_part_2.2151.

Dever, E., Dorman, C., and J. Largier, 2006. Surface boundary-layer variability off Northern California, USA, during upwelling, *Deep Sea Res., Part II*, **54**, 2887-2905, doi:10/1016/j.dsr2.2006.09.001.

Di Lorenzo, E., 2003. Seasonal dynamics of the surface circulation in the Southern California Current System, *Deep Sea Res., Part II*, **50**, 2371-2388, doi:10.1016/S0967-0645(03)00125-5.

Di Lorenzo, E., Miller, A., Schneider, N., and J. McWilliams, 2005. The Warming of the California Current System: Dynamics and Ecosystem Implications, *J. Phys. Oceanog.*, **35**, 336-362, doi:10.1175/JPO-2690.1.

Di Lorenzo, E. and N. Mantua, 2016. Multi-year persistence of the 2014/15 North Pacific marine heatwave, *Nature Climate Change*, **6**, 1042-1048, doi:10.1038/NCLIMATE3082.

Diaz, R. and R. Rosenberg, 2008. Spreading Dead Zones and Consequences for Marine Ecosystems, *Science*, **321**, 926-929.

Donaghay, P. and T. Osborn, 1997. Toward a theory of biological-physical control of harmful algal bloom dynamics and impacts, *Limnol. Oceannogr*, **42**, 1283-1296, doi:10.4319/lo.1997.42.5_part_2.1283.

Dorman, C. and C. Winant, 2000. The structure and variability of the marine atmosphere around the Santa Barbara Channel, *Mon Weather Rev*, **128**, 261-282, doi:10.1175/1520-0493(2000)128<0261:TSAVOT>2.0.CO;2.

Du, X., Peterson, W., and L. O'Higgins, 2015. Interannual variations in phytoplankton community structure in the northern California Current during the upwelling seasons of 2001-2010, *Mar. Ecol. Prog. Ser.*, **519**, 75-87, doi:10.3354/meps11097.

Dugdale, R. and F. Wilkerson, 1989. New production in the upwelling center at Point Conception, California: Temporal and spatial patterns, *Deep Sea Res.,* **36**, 985-1007, doi:10.1016/0198-0149(89)90074-5.

Dugdale, R., Wilkerson, F., and A. Morel, 1990. Realization of new production in coastal upwelling areas: A Means to compare relative performance, *Limnol. Oceannogr*, **35**, 822-829, doi:10.4319/lo.1990.35.4.0822.

Dugdale, R., Wilkerson, F., Hogue, V., and A. Marchi, 2006. Nutrient controls on new production in the Bodega Bay, California, coastal upwelling plume, *Deep Sea Res., Part II*, **53**, 3049-3062, doi:10.1016/j.dsr2.2006.07.009.

Durazo, R. and T., Baumgartner, 2002. Evolution of oceanographic conditions off Baja California: 1997-1999, *Prog. Oceanog.*, **54**, 7-31, doi:10.1016/S0079-6611(02)00041-1.

Edson, J., Jampana, V., Weller, R., Bigorre, S., Plueddemann, A., Fairall, C., Miller, S., Mahrt, L., Vickers, D., and H. Hersbach, 2013. On the Exchange of Momentum over the Open Ocean, *J. Phys. Oceanog.*, **43**, 1589-1610, doi:10.1175/JPO-D-12-0173.1.

Elorriaga-Verplancken, F., Sierra-Rodríguez, G., Rosales-Nanduca, H., Acevedo-Whitehouse, K., and J. Sandoval-Sierra, 2016. Impact of the 2015 El Niño-Southern Oscillation on the Abundance and Foraging Habits of Guadalupe Fur Seals and California Sea Lions from the San Benito Archipelago, Mexico, *PLoS ONE*, **11**, doi:10.1371/journal.pone.0155034.

Enfield, D. and J. Allen, 1980. On the structure and dynamics of monthly mean sea level anomalies along the Pacific coast of North and South America, *J. Phys. Oceanog*., **10,** 557-578, doi:10.1175/1520-0485(1980)010<0557:OTSADO>2.0.CO;2.

Enfield, D. and J. Allen, 1983. The Generation and Propagation of Sea Level Variability Along the Pacific Coast of Mexico, *J. Phys. Oceanog.*, **13**, 1012-1033, doi:10.1175/1520-0485(1983)013<1012:TGAPOS>2.0.CO;2.

ERG (Eastern Research Group, Inc). 2016. The national significance of California's ocean Economy, NOAA, https://coast.noaa.gov/data/digitalcoast/pdf/california-ocean-economy.pdf.

Fabry, V., Seibel, B., Feely, R., and J. Orr, 2008. Impacts of ocean acidification on marine fauna and ecosystem processes, *ICES J. Mar. Sciences*, **65**, 414-432, doi:10.1093/icesjmc/fsn048.

Fairall, C., Bradley, E., Rogers, D., Edson, J., and G. Young, 1996. Bulk parameterization of air-sea fluxes for Tropical Ocean-Global Atmosphere Coupled-Ocean Atmosphere Response Experiment, *J. Geophy. Res.*, **101**, 3747-3764, doi:10.1029/95JC03205.

Fallon, R. and T. Brock, 1979. Decomposition of blue-green algal (cyanobacterial) blooms in Lake Mendota, Wisconsin, *Appl. Environ. Microbiol*., **37**, 820-830, doi:10.1128/aem.37.5.820-830.1979.

Farneti, R., Stiz, A., and J. Ssebandeke, 2022. Improvements and persistent biases in the southeast tropical Atlantic in CMIP models, *npj Clim. Atmos. Sci*., **5**, doi:10.1038/s41612-022-00264-4.

Farrell, T., Bracher, D., and J. Roughgarden, 1991. Cross-shelf transport causes recruitment to intertidal populations in central California, *Limnol. Oceannogr*., **36**, 279-288, doi:10.4319/lo.1991.36.2.0279.

Feely, R., Sabine, C., Hernandez-Ayon, J., Ianson, D., and B. Hales, 2008. Evidence for upwelling of corrosive "acidified" water onto the continental shelf, *Science*, **320**, 1490-1492, doi:10.1126/science.1155676.

Fewings, M., Washburn, L., Dorman, C., Gotschalk, C., and K. Lombardo, 2016. Synoptic forcing of wind relaxations at Pt. Conception, California, *J. Geophy. Res*. *Oceans*, **121**, 5711-5730, doi:10.1002/2016JC011699.

Fewings, M., Washburn, L., and J. Ohlmann, 2015. Coastal water circulation patterns around the Northern Channel Isalnds and Point Conception, California, *Prog. Oceanog*, **138**, 283-304, doi:10.1016/j.pocean.2015.10.001.

Fischer, A., Hayashi, K., McGaraghan, A., and R. Kudela, 2020. Return of the "age of dinoflagellates" in Monterey Bay: Drivers of dinoflagellate dominance examined using automated imaging flow cytometry and long-term time series analysis, *Limnol. Oceannogr*, **65**, 2125-2141, doi:10.1002/lno.11443.

Flores-Vidal et al., 2014. Evidence of inertially generated coastal-trapped waves in the eastern tropic Pacific, *J. Geophy. Res. Oceans*, **119**, 3121-3133, doi:10.1002/2013JC009118.

Frischknecht, M, Münnich, M., and N. Gruber, 2015. Remote versus local influence of ENSO on the California Current System, *J. Geophy. Res*. *Oceans*, **120**, 1353-1374, doi:10.1002/2014JC010531.

Frischknecht, M, Münnich, M., and N. Gruber, 2017. Local atmospheric forcing driving an unexpected California Current System response during the 2015-2016 El Niño, *Geophys. Res. Lett.*, **44**, 304-311, doi:10.1002/2016GL071316.

Fritz, L., Quilliam, M., Wright, J., Beale, A., and T. Work,1992. An Outbreak of Domoic Acid Poisoning Attributed to the Pennate Diatom *Pseudonitzschia australis*, *J. Phycol*., **28**, 439-442, doi:10.1111/j.0022-3646.1992.00439.x.

Fumo, J., Carter, M., Flick, R., Rasmussen, L., Rudnick, D., and S. Iacobellis 2020. Contextualizing Marine Heatwaves in the Southern California Bight under Anthropogenic Climate Change, *J. Geophy. Res. Oceans*, **125**, e2019JC015674, doi:10.1029/2019JC015673.

García-Reyes, M., Largier, J., and W. Sydeman, 2014. Synoptic-scale upwelling indices and predictions of phyto- and zooplankton populations, *Prog. Oceanog*., **120**, 177-188, doi:10.1016/j.pocean.2013.08.004.

García-Reyes, M., Sydeman, W., Schoeman, D., Rykaczewski, R., Black, B., Smit, A., and S. Bograd, 2015. Under Pressure: Climate Change, Upwelling, and Eastern Boundary Upwelling Ecosystems, *Front. Mar. Sci*., **2**, doi:10.3389/fmars.2015.00109.

Gay, P. and T. Chereskin, 2009. Mean structure and seasonal variability of the poleward undercurrent off southern California, *J. Geophy. Res*., **114**, doi:10.1029/2008JC004886.

Gentemann, C., Fewings, M., and M. García-Reyes, 2017. Satellite sea surface temperatures along the West Coast of the United States during the 2014-2016 northeast Pacific marine heat wave, *Geophys. Res. Lett.*, **44**, 312-319, doi:10.1002/2016GL071039.

Godínez, V., Beier, E., Lavín, M., and J. Kurczyn, 2010. Circulation at the entrance of the Gulf of California from satellite altimeter and hydrographic observations, *J. Geophy. Res.*, **115**, doi:10.1029/2009JC005705.

Gómez-Valdivia, F., Parés-Sierra, A., and A. Flores-Morales, 2015. The Mexican Coastal Current: A subsurface seasonal bridge that connects the tropical and subtropical Northeastern Pacific, *Contin. Shelf Res*., **110**, 100-107, doi:10.1016/j.csr.2015.10.010.

Gómez-Valdivia, F., Parés-Sierra, A., and A. Flores-Morales, 2017. Semiannual variability of the California Undercurrent along the Southern California Current System: A tropical generated phenomenon, *J. Geophy. Res*. *Oceans*, **122**, 1574-1589, doi:10.1002/2016JC012350.

Graham W. and J. Largier, 1997. Upwelling shadows as nearshore retention sites: the example of northern Monterey Bay, *Cont. Shelf Res*., **17**, 509-532, doi:10.1016/S0278-4343(96)00045-3.

Grantham, B., Chan, F., Nielsen, K., Fox, D., Barth, J., Huyer, A., Lubchenco, J., and B. Menge, 2004. Upwelling-driven nearshore hypoxia signals ecosystem and oceanographic changes in the northeast Pacific, *Nature*, **429**, 749-754, doi:10.1038/nature02605.

Guinehut, S., Dhomps, A., Larnicol, G., and P. Le Traon, 2012. High resolution 3D temperature and salinity fields derived from in situ and satellite observations, *Ocean Sci*., **8**, 845-857, doi:105194/os-8-845-2012.

Haines, B., Bertiger, W., Desai, S., Kuang, D., Munson, T., Young, L., and P. Willis, 2003. Initial orbit determination results for Jason-1: Towards a 1-cm orbit. *J. Navigation*, **50**, 171-180, doi:10.1002/j.2161-4296/2003.tb00327.x.

Halliwell, G. and J. Allen, 1987. The large-scale coastal wind field along the West Coast of North America, 1981-1982, *J. Geophy. Res*. *Oceans*, **92**, 1861-1884, doi:10.1029/JC0092iC02p01861.

Halpern, D., 1976. Structure of a coastal upwelling event observed off Oregon during July 1973, *Deep Sea Res.*, **23**, 495-508, doi:10.1016/0011-7471(76)90861-5.

Harms, S. and C. Winant, 1998. Characteristic patterns of the circulation in the Santa Barbara

Channel, *J. Geophy. Res*., **103**, 3041-4065, doi:10.1029/97JC02393.

Hautala, S. and D. Roemmich, 1998. Subtropical mode water in the Northeast Pacific Basin, *J. Geophy. Res*. *Oceans*, **103**, 13055-13066, doi:10.1029/98JC01015.

He, J. and A. Mahadevan, 2021. How the Source Depth of Coastal Upwelling Relates to Stratification and Wind, *J. Geophy. Res*. *Oceans,* **126**, doi:10.1029/2021J017621.

Hermann, A., Curchitser, E., Haidvogel, D., and E. Dobbins, 2009. A comparison of remote vs. local influence of El Niño on the coastal circulation of the northeast Pacific, *Deep Sea Res., Part II*, **56**, 2427-2443, doi:10.1016/j.dsr2.2009.02.005.

Hersbach, H., 2011. Sea Surface Roughness and Drag Coefficient as Functions of Neutral Wind Speed, *J. Phys. Oceanog.*, **41**, 247-251, doi: 10.1175/2010JPO4567.1.

Hickey, B., 1979. The California Current System – hypotheses and facts, *Prog. Oceanog*., **8**, 191-279, doi:10.1016/0079-6611(79)90002-8.

Hickey, B., Dobbins, E., and S. Allen, 2003. Local and remote forcing of currents and temperature in the central Southern California Bight, *J. Geophy. Res*., **108**, doi:10.1029/2000JC000313.

Hickey, B. and N. Pola, 1983. The seasonal alongshore pressure gradient on the west coast of the United States, *J. Geophy. Res*., **88**, 7623-7633, doi:10.1029/JC088iC12p07623.

Higgins, B., Pearson, D., and R. Mehta, 2017. El Niño episodes coincide with California moray *Gymnothorax mordax* settlement around Santa Catalina Island, California, *J. Fish Bio*., **90**(4), doi:10.111/jfb.13253.

Hill, E., Hickey, B., Shillington, F., Strub, T., Barton, E., and K. Brink, 1998. Eastern Boundary Current Systems of the World, *The Sea*, **12**, 21-62, K.H. Brink and A.R. Robinson, eds, Wiley and Sons, Inc., New York, NY.

Hu, S. and A. Fedorov, 2016. Exceptionally strong easterly wind burst stalling El Niño of 2014, *PNAS*, **113**, 2005-2010, doi:10.1073/pnas.151418211.

Hughes, C., Elipot, S., Maqueda M., and J. Loder, 2013. Test of a Method for Monitoring the Geostrophic Meridional Overturning Circulation Using Only Boundary Measurements, *J. Atmos. Ocean. Technol.*, **30**, 789-809, doi:01.1175/JTECH-D-12-00149.1.

Hsu, S., Meindl, E., and D. Gilhousen, 1994. Determining the Power-Law Wind-Profile Exponent under Near-Neural Stability Conditions at Sea, *J. Appl. Meteorol*., **33**, 757-765, doi:10.1175/1520-0450(1994)033<0757:DTPLWP>2.0.CO;2.

Huyer, A., 1983. Coastal upwelling in the California Current System, *Prog. Oceanog*., **12**, 259-284, doi:10.1016/0079-6611(83)90010-1.

Huyer, A. and R. Smith, 1985. The signature of El Niño off Oregon, 1982-1983. *J. Geophy. Res.*, **90**, 7133-7142, doi:10.1029/JC090iC04p07133.

Iles, A., Gouhier, T., Menge, B., Stewart, J., Haupt, A., and M. Lynch, 2012. Climate-driven trends and ecological implications of event-scale upwelling in the California Current System, *Global Change Biology*, **18**, 783-796, doi:10.1111/j.1365-2486.2011.02567.x.

Imai, I., Ishida, Y., Sakaguchi, K., and Y. Hata, 1995. Algicidal Marine Bacteria Isolated from Northern Hiroshima Bay, Japan, *Fisheries science*, **61**, 628-636, doi:10.2331/fishsci.61.628.

Jacox, M. and C. Edwards, 2011. Effects of stratification shelf slope on nutrient supply in coastal upwelling regions, *J. Geophy. Res.*, **116**, doi:10.1029/2010JC006547.

Jacox, M. and C. Edwards, 2012. Upwelling source depth in the presence of nearshore wind stress curl, *J. Geophy. Res.*, **117**, doi:10.1029/2011JC007856.

Jacox, M., Edwards, C., Hazen, E., and S. Bograd, 2018. Coastal upwelling revisited: Ekman, Bakun, and improved upwelling indices for the US West Coast, *J. Geophy. Res. Oceans*, **123**, doi:10.1029/2018JC014187.

Jacox, M., Fiechter, J., Moore, A., and C. Edwards, 2015. ENSO and the California Current coastal upwelling response, *J. Geophy. Res. Oceans*, **120**, 1691-1702, doi:10.1002/2014JC010650.

Jacox, M., Hazen, E., Zaba, K., Rudnick, D., Edwards C., Moore, A., and S. Bograd, 2016. Impacts of the 2015-2016 El Niño on the California Current System: Early assessment and comparison to past events, *Geophys. Res. Lett.*, **43**, doi:10.1002/2016GL069716.

Jacox, M., Moore, A., Edwards, C., and J. Flechter, 2014. Spatially resolved upwelling in the California Current System and its connections to climate variability, *Geophys. Res. Lett.*, **41**, 3189-3196, doi:10.1002/2014GL059589.

Kahru, M., Anderson, C., Barton, A., Carter, M., Catlett, D., Send, U., Sosik, H., Weiss, E., and B. Mitchell, 2021. Satellite detection of dinoflagellate blooms off California by UV reflectance ratios, *Elem. Sci. Anth.*, **9**, doi:10.1525/elementa.2020.00157.

Kahru, M., Di Lorenzo, E., Manzano-Sarabia, M., and B. Mitchell, 2012. Spatial and temporal statistics of sea surface temperature and chlorophyll fronts in the California Current, *J. Plankton Res.*, **34**, 749-760, doi:10.1093/plankt/fbs010.

Kahru, M., Kudela, R., Manzano-Sarabia, M., and B. Mitchell, 2009. Trends in primary production in the California Current detected with satellite data, *J. Geophy. Res.*, **114**, doi:10.1029/2008JC004979.

Kamykowski, D., 1974. Possible interactions between phytoplankton and semidiurnal internal tides, *J. Mar. Res*., **32**, 67-89.

Kamykowski, D., 1981. Laboratory experiments on the diurnal vertical migration of marine dinoflagellates through temperature gradients, *Mar. Biol.,* **62**, 57-64, doi:10.1007/BF00396951.

Kamykowski, D. and S. Zentara, 1986. Predicting plant nutrient concentrations from temperature and sigma-*t* in the upper kilometer of the world ocean, *Deep Sea Res.,* **33**, 89-105, doi:10.1016/0198-0149(86)90109-3.

Kanzow, T., Send, U., Zenk, W., Chave, A., and M. Rhein, 2006. Monitoring the integrated deep meridional flow in the tropical North Atlantic: Long-term performance of a geostrophic array, *Deep Sea Res., Part I*, **53**, 528-546, doi:10.1016/j.dsr.2005.12.007.

Kemp, W., Testa, J., Conley, D., Gilbert, D., and J. Hagy, 2009. Temporal responses of coastal hypoxia to nutrient loading and physical controls, *Biogeosciences*, **6**, 2985-3008, doi:10.5194/bg-6-2985-2009.

Kessler, W., 2006. The circulation of the eastern tropical Pacific: A review, *Prog. Oceanog.*, **69**, 181-217, doi:10.1016/j.pocean.2006.03.009.

Kim, H. and A. Miller, 2007. Did the Thermocline Deepen in the California Current after the 1976/77 Climate Regime Shift?, *J. Phys. Oceanog.*, **37**, 1733-1739, doi:10.1175/JPO3058.1.

Kosro, M., 2002. A poleward jet and an equatorward undercurrent off Oregon and northern California, during the 1997-98 El Niño, *Prog. Oceanog*., **54**, 343-360, doi:10.1016/S0079-6611(02)00057-5.

Kudela, R. and R. Dugdale, 1996. Estimation of new production from remotely-sensed data in a coastal upwelling regime, *Adv. Space Res*., **18**, 91-97, doi:10.1016/0273-1177(95)00952-3.

Kudela, R., Bickel, A., Carter, M., Howard, M., and L. Rosenfeld, 2015. Chapter 3 – The Monitoring of Harmful Algal Blooms through Ocean Observing: The Development of the California Harmful Algal Bloom Monitoring and Alert Program, Coastal Ocean Observing Systems, Academic Press, 2015, 58-75, doi:10.1016/B978-0-12-802022-7.00005-5.

Lagarias, J., Reeds, M., Wright, M., and P. Wright, 1998. Convergence Properties of the Nelder-Mead Simplex Method in Low Dimensions, *SIAM Journal of Optimization*, **9**, 112-147, doi:10.1137/S1052623496303470.

Landry, M., Ohman, M., Goericke, R., Stukel, M., Barbeau, K., Bundy, R., and M. Kahru, 2012. Pelagic community responses to a deep-water front in the California Current Ecosystem: overview of the A-Front study, *J. Plankton Res*., **34**, 739-748, doi:10.1093/plankt/fbs025.

Large, W. and G. Danabasoglu, 2006. Attribution and Impacts of Upper-Ocean Biases in CCSM3, *J. Climate*, **19**, 2325-2346.

Large, W. and S. Pond, 1981. Open Ocean Momentum Flux Measurements in Moderate to Strong Winds, *J. Phys. Oceanog.*, **11**, 324-336, doi:10.1175/1520-0485(1981)011<0324:OOMFMI>2.0.CO;2.

Lasker, 1975. Field criteria for survival of anchovy larvae: The relation between inshore chlorophyll maximum layers and successful first feeding, *Fish Bull.*, **73**, 453-462.

Leising, A., Schroeder, I., Bograd, S., Abell, J., Durazo, R., Gaxiola-Castro, G., Bjorkstedt, E., Field, J., Sakuma, K., Robertson, R., Goericke, R., Peterson, W., Brodeur, R., Barceló, C., Auth, T., Daly, E., Suryan, R., Gladics, A., Porquez, J., McClatchie, S., Weber, E., Watson, W., Santora, J., Sydeman, W., Melin, S., Chavez, F., Golightly, R., Schneider, S., Fisher, J., Morgan, C., Bradley, R., and P. Warybok, 2015. State of the California Current 2014-15: Impacts of the Warm-Water "Blob", *CalCOFI Rep.*, **56**.

Lellouche, J., Greiner, E., Bourdallé-Badie, R., Garric, G., Angélique, M., Drévillon, M., Bricaud, C., Hamon, M., Le Galloudec, O., Regnier C., Candela, T., Testut, C., Gasparin, F., Ruggiero, G., Benkiran, M., Drillet, Y., and P. Le Traon, 2021. The Copernicus Global 1/12 Oceanic and Sea Ice GLORYS12 Reanalysis, *Front. Earth Sci.*, **9**, doi:10.3389/feart.2021.698876.

Lentz, S., 1994. The Surface Boundary Layer in Coastal Upwelling Regions, *J. Phys. Oceanog.*, **22**, 1517-1539, doi:10.1175/1520-0485(1992)022<1517:TSBLIC>2.0.CO;2.

Lentz, S. and C. Winant, 1986. Subinertial currents on the southern California shelf, *J. Phys. Oceanog.*, **16**, 1737-1750, doi:10.1175/1520-0485(1986)016<1737:SCOTSC>2.0.CO;2.

Lentz, S. and D. Chapman, 2004. The importance of nonlinear cross-shelf momentum flux during wind-driven coastal upwelling, *J. Phys. Oceanog.*, **34**, 2444-2457, doi:10.1175/JPO2644.1.

Levin, L., Ekau, W., Gooday, A., Jorissen, F., Middelburg, J., Naqvi, S., Neira, C., Rabalais, N., and J. Zhang, 2009. Effects of natural and human-induced hypoxia on coastal benthos, *Biogeosciences*, **6**, 2063-2098, doi:10.5194/bg-6-2063-2009.

Levine, A. and M. McPhaden, 2016. How the July 2013 easterly wind burst gave the 2015-2016 El Niño a head start, *Geophys. Res. Lett.*, **43**, 6503-6510, doi:10.1002/2016GL069204.

Levitus, S., 1982. Climatological Atlas of the World Ocean, NOAA Professional Paper No. 13, U.S. Gov. Printing Office, Wash., D.C., 173 pp.

Lewis, M. and J. Smith, 1983. A small volume, short-incubation-time method for measurement of photosynthesis as a function of incident irradiance, *Mar. Ecol. Prog. Ser.*, **13**, 99-102, doi:

Lilly, L., Send, U., Lankhorst, M., Martz, T., Feely, R., Sutton, A., M. Ohman, 2019. Biogeochemical Anomalies at Two Southern California Current System Moorings During the

2014-2016 Warm Anomaly-El Niño Sequence, *J. Geophy. Res. Oceans*, **124**, 6886-6903, doi:10.1029/2019JC015255.

Locarnini, R., Mishonov, A., Antonov, J., Boyer, T., Garcia, H., Baranova, O., Zweng, M., Paver, C., Reagan, J., Johnson, D., Hamilton, M., and D. Seidov, 2013. *World Ocean Atlas 2013*, *Volume 1: Temperature*. S. Levitus, Ed., A Mishonov Technical Ed.; NOAA Atlas NESDIS 73, 40 pp, doi:10.7289/V5F769GT.

Low, N., Micheli, F., Aguilar, J., Arce, D., Boch, C., Bonilla, J., Bracamontes, M., De Leo, G., Diaz, E., Enríquez, E., Hernandez, A., Martinez, R., Mendoza, R., Miranda, C., Monismith, S., Ramade, M., Rogers-Bennett, L., Romero, A., Salinas, C., Smith, A., Torre, J., Villavicencio, G., and C. Woodson. 2021. Variable coastal hypoxia exposure and drivers across the southern California Current, *Sci. Rep*., **11**, doi:10.1038/s41598-021-89928-4.

Lucas, L., Koseff, J., Cloern, J., Minosmith, S., and J. Thompson, 1999. Processes governing phytoplankton blooms in estuaries. I: The local production-loss balance, *Mar Ecol. Prog. Ser*., **187**, 1-15.

Ludescher, J., Gozolchiani, A., Bogachev, M., Bunde, A., Havlin, S., and H. Schellnhuber, 2014. Very early warning of next El Niño, *PNAS,* **111**, 2064-2066, doi:10.1073/pnas.1323058111.

Lynn, R., Bograd, S., Chereskin, T., and A. Huyer, 2003. Seasonal renewal of the California Current: The spring transition off California, *J. Geophy. Res.*, **108**, doi:10.1029/2003JC001787.

Lynn, R., Bliss, K., and L. Eber, 1982. Vertical and horizontal distributions of seasonal mean temperature, salinity, sigma-*t*, stability, dynamic height, oxygen, and oxygen saturation in the California Current, 1950-1978, *CalCOFI Atlas 30*, 513 pp., State of Calif. Mar. Res. Comm., La Jolla.

Lynn, R. and J. Simpson, 1987. The California Current System: The seasonal variability and physical characteristics, *J. Geophy. Res*., **92**, 12947-12966, doi:10.1029/JC092iC12p12947.

Lynn, R. and J. Simpson, 1990. The flow of the undercurrent over the continental borderland off Southern California, *J. Geophy. Res*., **95**, 12995-13008, doi:10.1029/JC095iC08p12995.

Lynn, R. and S. Bograd, 2002. Dynamic evolution of the 1997-1999 El Niño-La Niña cycle in the southern California Current System, *Prog. Oceanog*., **54**, 59-75, doi:10.1016/S0079-6611(02)00043-5.

Mantua, N., Hare, S., Zhang, Y., Wallace, J., and R. Francis, 1997. A Pacific Interdecadal Climate Oscillation with Impacts on Salmon Production, *Bull. Ameri. Met. Soc.*, **78**, 1069-1080, doi:10.1175/1520-0477(1997)078<1069:APICOW>2.0.CO;2.

Marchesiello, P., McWilliams, J., and A. Shchepetkin, 2003. Equilibrium Structure and Dynamics of the California Current System, *J. Phys. Oceanog*., **33**, 753-783, doi:10.1175/1520-0485(2003)33<753:ESADOT>2.0.CO;2.

Marchesiello, P. and P. Estrade, 2010. Upwelling limitation by onshore geostrophic flow, *J. Mar. Res.*, **68**, 37-62, doi:10.1357/002224010793079004.

Mass, C. and N. Bond, 1996. Coastally trapped wind reversals along the United States West Coast during the warm season. Part II: Synoptic evolution, *Mon. Weather Rev*., **124**, 446-461, doi:10.1175/1520-0493(1996)124<0446:CTWRAT>2.0.CO;2.

McCabe, R., Hickey, B., Kudela, R., Lefebvre, K., Adams, N., Bill, B., Gulland, F., Thomson, R., Cochlan, W., and V. Trainer, 2016. An unprecedented coastwide toxic algal bloom linked to anomalous ocean conditions, *Geophys. Res. Lett.*, **43**, 10366-10376, doi:10.1002/2016GL070023.

McCabe, R., Hickey, B., Dever, E., and P. MacCready, 2015. Seasonal cross-shelf flow structure, upwelling relaxation, and the alongshelf pressure gradient in the Northern California Current System, *J. Phys. Oceanog*., **45**, 209-227, doi:10.1175/JPO-D-14-0025.1.

McClatchie, S., Field, J., Thompson, A., Gerrodette, T., Lowry, M., Fiedler, P., Watson, W., Nieto, K., and R. Vetter, 2016. Food limitation of sea lion pups and the decline of forage off central and southern California, *R. Soc. Open sci*., **3**, doi:10.1098/rsos.150628.

McCreary, J., Kundu, P., and S. Chao, 1987. On the dynamics of the California Current system, *J. Mar. Res.*, **45**, 1-32.

McCreary, J. and S. Chao, 1985. Three-dimensional shelf circulation along an eastern ocean boundary, *J. Mar. Res.*, **43**, 13-36.

McDermott, A., 2015. Red crab tide: Tuna crabs washing up on local beaches, *Monterey Herald*, October 7, 2015, http://www.montereyherald.com/ article/NF/20151007/NEWS/151009807.

McGowan, J., Bograd, S., Lynn, R., and A. Miller, 2003. The biological response to the 1977 regime shift in the California Current, *Deep Sea Res., Part II*, **50**, 2567-2582, doi:10.1016/S0967-0645(03)00135-8.

McGowan, J., Vayan, D., and L. Dorman, 1998. Climate-Ocean Variability and Ecosystem Response in the Northeast Pacific, *Science*, **281**, 210-217, doi:10.1126/science.281.5374.210.

McLain, D. and D. Thomas, 1983. Year-to-year fluctuations of the California Countercurrent and effects on marine organisms, *CalCOFI Rep*., **24**, 165-181.

McPhaden, M., Freitag, H., Hayes, S., and B. Taft, 1988. The Response of the Equatorial Pacific Ocean to a Westerly Wind Burst in May 1986, *J. Geophy. Res.*, **93**, 10589-10603, doi:10.1029/JC093iC09p10589.

Mears, C., Lee, T., Ricciardulli, L., Wang, X., and F. Wentz, 2022. Improving the Accuracy of the Cross-Calibrated Multi-Platform (CCMP) Ocean Vector Winds, *Remote Sens.*, **14**, doi:10.3390/rs14174230.

Meinvielle, M. and G. Johnson, 2013. Decadal water-property trends in the California Undercurrent, with implications for ocean acidification, *J. Geophy. Res. Oceans*, **118**, 6687-6703, doi:10.1002/2013JC009299.

Melton, C., Washburn, L., and C. Gotschalk, 2009. Wind relaxations and poleward flow events in a coastal upwelling system on the central California coast, *J. Geophy. Res.*, **114**, doi:10.1029/2009JC005397.

Menge, B., Daley, D., Wheeler, P., Dahlhoff, E., Sanford, E., and T. Strub, 1997. Benthic-pelagic links and rocky intertidal communities: Bottom-up effects on top-down control?, *PNAS*, **94**, 14530-14535, doi:10.1073/pnas.94.26.14530.

Menke, W, 2012. Solution of the Linear, Gaussian Inverse Problem, Viewpoint 1: The Length Method, *Geophysical Data Analysis*, San Diego, Academic Press, doi:10.1016/B978-0-12-490920-5.X5001-7.

Menkes, 2014. C., Lengaigne, M., Vialard, J., Puy, M., Marchesiello, P., Cravatte, S., and G. Cambon 2014. About the role of Westerly Wind Events in the possible development of an El Niño in 2014, *Geophys. Res. Lett.*, **41**, 6476–6483, doi:10.1002/2014GL061186.

Merrifield, M. and C. Winant, 1989. Shelf circulation in the Gulf of California: A description of the variability, *J. Geophy. Res. Oceans*, **94**, 18133-18160, doi:10.1029/JC094iC12p18133.

Mesinger, F., DiMego, G., Kalnay, E., Mitchell, K., Shafran, P., Ebisuzaki, W., Jovic, D., Woollen, J., Rogers, E., Berbery, E., Ek, M., Fan, Y., Grumbine, R., Higgins, W., Li, H., Lin, Y., Manikin, G., Parrish, D., and W. Shi, 2006. North American Regional Reanalysis, *Bull. Ameri. Met. Soc.*, **87**, 343-360, doi:10.1175/BAMS-87-3-343.

Meyers, S., Melson, A., Mitchum G., and J. O'Brien, 1998. Detection of the fast Kelvin wave teleconnection due to El Niño-Southern Oscillation, *J. Geophy. Res.*, **103**, 27655-27663, doi:10.1029/98JC02402.

Moloney, C., Gield, J., and M. Lucas, 1991. The size-based dynamics of plankton food webs. II. Simulations of three contrasting southern Benguela food webs, *J. Plankton Res.*, **13**, 1039-1092, doi:10.1093/plankt/13.5.1039.

Moore, A., Edwards, C., Fiechter, J., Drake, P., Neveu, E., Arango, H., Gürol, S., and A. Weaver, 2013. A 4D-Var Analysis System for the California Current: A Prototype for an Operational Regional Ocean Data Assimilation System, In L. Xu & S. Park (Eds.), *Data assimilation for atmospheric, oceanic, and hydrological applications*, **2**, 345-366, Berlin: Springer, doi:10.1007/978-3-642-35088-714.

Moorthi, S., Countway, P., Stauffer, B., and D. Caron, 2006. Use of Quantitative Real-Time PCR to Investigate the Dynamics of the Red Tide Dinoflagellate *Lingulodinium polyedrum*, *Microb. Ecol.*, **52**, 136-150, doi:10.1007/s00248-006-9030-3.

Mulet, S., Rio, M., Etienne, H., Dibarboure, G., and N. Picot, 2021. The new CNES-CLS18 global mean dynamic topography, *Ocean Sci.*, **17**, 789-808, doi:10.5194/os-17-789-2021.

Mulet, S., Rio, M., Mignot, A., Guinehut, S., and R. Morrow, 2012. A new estimate of the global 3D geostrophic ocean circulation based on satellite data and in-situ measurements, *Deep Sea Res., Part II*, **77-80**, 70-81, doi:10.1016/j.dsr2.2012.04.012.

Münchow, A., 2000. Wind Stress Curl Forcing of the Coastal Ocean near Point Conception, California, *J. Phys. Oceanog.*, **30**, 1265-1280, doi:10.1175/1520-0485(2000)030<1265:WSCFOT>2.0.CO;2.

Nam, S., Kim, H., and U. Send, 2011. Amplification of hypoxic and acidic events by La Niña conditions on the continental shelf off California, *Geophys. Res. Lett.*, **38**, doi:10.1029/2011GL049549.

Nam, S., Takeshita, Y., Frieder, C., Martz, T., and J. Ballard, 2015. Seasonal advection of Pacific Equatorial Water alters oxygen and pH in the Southern California Bight, *J. Geophy. Res. Oceans*, **120**, 5387-5399, doi:10.1002/2015JC010859.

Nelson, C., 1977. Wind stress and wind stress curl over the California Current, US Department of Commerce National Oceanic and Atmospheric Administration, NOAA Technical Report NMFS SSRF-714, 87 pp.

Neveu, E., Moore, A., Edwards, C., Fiechter, J., Drake, P., Crawford, W., Jacox, M., and E. Nuss, 2014. A historical analysis of the California Current circulation using ROMS 4D-Var: System configuration and diagnostics, *Ocean Modelling*, **99**, 133-151, doi:10.1016/j.ocemod.2015.11.012.

Nishimoto, M. and L. Washburn, 2002. Patterns of coastal eddy circulation and abundance of pelagic juvenile fish in the Santa Barbara Channel, California, USA, *Mar. Ecology Prog. Series*, **241**, 183-199, doi:10.3354/meps241183.

Norton, J., McLain, D., Brainhard, R., and D. Husby, 1985. The 1982-83 El Niño event off Baja and Alta California and its ocean climate context. In: *Niño North, Niño Effects in the Eastern Subarctic Pacific Ocean* (Edited by W. S. Wooster and D. L. Fluharty). Washington Sea Grant Program, University of Washington, Seattle, pp.44-72.

Oakley, N., Orla-Barile, M., Hatchett, B., Burgess, P., and M. Ralph, 2020. Characteristics and Impacts of the April 4-11 2020 Cutoff Low Storm in California, *Center for Western Weather and Water Extremes*, June 3, 2020, https://cw3e.ucsd.edu/characteristics-and-impacts-of-the-april-4-11-2020-cutoff-low-storm-in-california/.

Oey, L., 1996. Flow around a coastal bend: A model of the Santa Barbara Channel eddy, *J. Geophy. Res. Oceans*, **101**, 16667-16682, doi:10.1029/96JC01232.

Oey, L., 1999. A forcing mechanism for the poleward flow off the southern California coast, *J. Geophy. Res.*, **104**, 13529-13539, doi:10.1029/1999JC900066.

Ohman, M., Mantua, N., Keister, J., Garcia-Reyes, M., and S. McClatchie, 2017. ENSO impacts on ecosystem indicators in the California Current System, *CLIVAR & OCB Newsletter*, **15**, 8-15.

Olson, R. and H. Sosik, 2007. A submersible imaging-in-flow instrument to analyze nan-and microplankton: Imaging FlowCytobot, *Limnol. Oceannogr.: Methods*, **5**, 195-203, doi:10.4319/lom.2007.5.195.

Omand, M., Leichter, J., Franks, P., Guza, R., Lucas, A., and F. Feddersen, 2011. Physical and biological processes underlying the sudden surface appearance of a red tide in the nearshore, *Limnol. Oceannogr*, **56**, 787-801, doi:10.4319/lo.2011.56.3.0787.

Palacios, D., Bograd, S., Mendelssohn, R., and F. Schwing, 2004. Long-term and seasonal trends in stratification in the California Current, 1950-1993, *J. Geophy. Res. Oceans*, **109**, doi:10.1029/2004JC002330.

Palacios, D., Hazen, E., Schroeder, I., and S. Bograd, 2013. Modeling the temperature-nitrate relationship in the coastal upwelling domain of the California Current, *J. Geophy. Res. Oceans*, **118**, 3223-3239, doi:10.1002/jgrc.202016.

Park, J., Heisenrether, R., and W. Sweet, 2014. Water Level and Wave Height Estimates at NOAA Tide Stations from Acoustic and Microwave Sensors, *NOAA Tech. Rep. NOS CO-OPS 075*, 41 p.

Park, Y., Park, J., Chung, S., Song, B., Lim, W., Kim, C., and W. Lee, 1998. Isolation of Marine Bacteria Killing Red Tide Microalgae 1. Isolation and Algicidal Properties of Micrococcus sp. LG-1 Possessing Killing Activity for Harmful Dinoflagellate, *Cochlodinium polykrikoides*, *J. Korean Fish. Soc.*, **31**, 767-773.

Parke, M. and S. Gill, 1995. On the sea state dependence of sea level measurements at Platform Harvest, *Marine Geodesy*, **18**, 105-116, doi:10.1080/15210609509379746.

Pauly, D. and V. Christensen, 1995. Primary production required to sustain global fisheries, *Nature*, **374**, 255-257, doi:10.1038/374255a0.

Pérez, F., Padín, X., Pazos, Y., Gilcoto, M., Cabanas, M., Pardo, P., Doval, M., and L. Farina-Busto, 2010. Plankton response to weakening of the Iberian coastal upwelling, *Glob. Chan. Biol.*, **16**, 1258-1267, doi:10.1111/j.1365-2486.2009.02125.x.

Peterson, W., Fisher, J., Strub, T., Du, X., Risien, C., Peterson, J., and C. Shaw, 2017. The

pelagic ecosystem in the Northern California Current off Oregon during the 2014-2016 warm anomalies within the context of the past 20 years, *J. Geophy. Res. Oceans*, **122**, 7267-7290, doi:10.1002/2017JC012952.

Pickett, M. and J. Paduan, 2003. Ekman transport and pumping in the California Current based on the US Navy's high-resolution atmospheric model (COAMPS), *J. Geophy. Res*., **108**, doi:10.1029/2003JC001902.

Pitcher, G. and A. Boyd, 1996. Cross-shelf and alongshore dinoflagellate distributions and the mechanisms of red tide formation within the southern Benguela upwelling system, *Harmful and Toxic Algal Blooms*, Intergovernmental Oceanographic Commission of UNESCO, 243-246.

Pitcher, G., Figueiras, F., Hickey, B., and M. Moita, 2010. The physical oceanography of upwelling systems and the development of harmful algal blooms, *Prog. Oceanog.*, **85**, 5-32, doi:10.1016/j.pocean.2010.02.002.

Pitcher, G. and G. Nelson, 2006. Characteristics of the surface boundary layer important to the development of red tide on the southern Namaqua shelf of the Benguela upwelling system, *Limnol. Oceannogr.*, **51**, 2660-2674, doi:10.4319/lo.2006.51.6.2660.

Pitcher, G., Jiménez, A., Kudela, R., and B. Reguera, 2017. Harmful Algal Blooms in Eastern Boundary Upwelling Systems: A GEOHAB CORE RESEARCH PROJECT, *Oceano*., **30**, 22-35.

Pollingher, U. and E. Zemel, 1981. In situ and experimental evidence of the influence of turbulence on cell division processes of *Peridinium cinctum* forma *westii* (Lemm.) Lefèvre, *Br. Phycol. J.*, **16**, 281-287, doi:10.1080/00071718100650301.

Pringle, J. and E. Dever, 2009. Dynamics of wind-driven upwelling and relaxation between Monterey Bay and Point Arena: Local-, regional-, and gyre-scale controls, *J. Geophy. Res*., **114**, doi:10.1029/2008JC005016.

Pringle, J. and K. Riser, 2003. Remotely forced nearshore upwelling in Southern California, *J. Geophy. Res*., **108**, doi:10.1029/2002JC001447.

Probyn, T., Pitcher, G., Monteiro, P., Boyd, A., and G. Nelson, 2010. Physical processes contributing to harmful algal blooms in Saldanha Bay, South Africa, *S. Afr. J. mar. Sci*, **22**, 285-297, doi:10.2989/02577610078412507.

Ramp, S., Garwood, R., Davis, C., and R. Snow, 1991. Surface heating and patchiness in the coastal ocean off central California during a wind relaxation event, *J. Geophy. Res. Oceans,* **96**, 14947-14957, doi:10.1029/91JC01140.

Ramp, S., McClean, J., Collins, C., Semtner, A., and K. Hays, 1997. Observations and modeling of the 1991-1992 El Niño signal off central California, *J. Geophy. Res*., **102**, 5553-5582, doi:10.1029/96JC03050.

Rasmusson, E. and J. Wallace, 1983. Meteorological aspects of the El Niño/Southern Oscillation, *Science*, **222**, 1195-1202, doi:10.1126/science.222.4629.1195.

Reid, J. and A. Mantyla, 1976. The Effect of the Geostrophic Flow Upon Coastal Sea Elevations in the Northern North Pacific Ocean, *J. Geophy. Res.*, 81, 3100-3110, doi:10.1029/JC081i018p03100.

Reid, J., Roden, G., and J. Wyllie, 1958. Studies of the California Current System, *Calif. Coop. Oceanic Fish. Invest. Rep.*, 1 July 1956-1 January 1958:27-57.

Remote Sensing Systems, 2017. MWIR optimum interpolated SST data set, Ver. 5.0 PO.DAAC, CA, USA, doi:10.5067/GHMWI-4FR05.

Ren, A. and D. Rudnick, 2021. Temperature and salinity extremes from 2014-2019 in the California Current System and its source waters, *Commun. Earth Environ.*, **62**, doi:10.1038/s43247-021-00131-9.

Renault, L., Deutsch, C., McWilliams, J. C., Frenzel, H., Liang, J.-H., and F. Colas, 2016. Partial decoupling of primary productivity from upwelling in the California Current system, *Nature Geoscience*, **9**, doi:10.1038/NGEO2722.

Reyes-Hernández, C., Ahumada-Sempoal, M., and R. Durazo, 2016. The Costa Rica Coastal Current, eddies and wind forcing in the Gulf of Tehuantepec, Southern Mexican Pacific, *Contin. Shelf Res.*, **114**, 1-15, doi:10.1016/j.csr.2015.12.012.

Robinson, C., 2016. Evolution of the 2014-2015 sea surface temperature warming in the central west coast of Baja California, Mexico, recorded by remote sensing, *Geophys. Res. Lett.*, **43**, 7066-7071, doi:10.1002/2016GL069356.

Roden, G., 1971. Aspects of the transition zone in the Northeastern Pacific, *J. Geophy. Res.*, **76**, 3462-3475, doi:10.1029/JC076i015p03462.

Roemmich, D., 1989. Mean transport of mass, heat, salt and nutrients in southern California coastal waters: implications for primary production and nutrient cycling, *Deep Sea Res.,* **36**, 1359-1378, doi:10.1016/0198-0149(89)90088-5.

Roemmich, D. and J. McGowan, 1995. Climatic Warming and the Decline of Zooplankton in the California Current, *Science*, **267**, 1324-1326, doi:10.1126/science.267.5202.1324.

Rosales Quintana, G., Marsh, R., and L. Salas, 2021. Interannual variability in contributions of the Equatorial Undercurrent (EUC) to Peruvian upwelling source water, *Ocean Sci*., **17**, 1385-1402, doi:10.5194/os-17-1385-2021.

Roughan, M., Garfield, N., Largier, J., Dever, E., Dorman, C., Peterson, D., and J. Dorman, 2006. Transport and retention in an upwelling region: The role of across-shelf structure, *Deep Sea Res., Part II*, **53**, 2931-2955, doi:10.1016/j.dsr2.2006.07.015.

Roughgarden, J., Gaines, S., and H. Possingham, 1988. Recruitment dynamics in complex life cycles, *Science*, **241**, 1460-1466, doi:10.1126/science.11538249.

Rudnick, D., Zaba, K., Todd, R., and R. Davis, 2017. A climatology of the California Current System from a network of underwater gliders, *Prog. Oceanog.*, **154**, 64-106, doi:10.1016/j.pocean.2017.03.002.

Rykaczewski, R. and D. Checkley, 2008. Influence of ocean winds on the pelagic ecosystem in upwelling regions, *PNAS*, **105**, 1965-1970, doi:10.1073/pnas.0711777105.

Rykaczewski, R., Dunne, J., Sydeman, W., García-Reyes, M., Black, B., and S. Bograd, 2015. Poleward displacement of coastal upwelling-favorable winds in the ocean's eastern boundary currents through the 21st century, *Geophys. Res. Lett.*, **42**, 6424-6431, doi;10.1002/2015GL064694.

Ryther, J., 1955. Ecology of autotrophic marine dinoflagellates with reference to red water conditions, In The Luminescence of biological systems, *Amer. Ass. Advance Sci.*, 387-413.

Ryther, J., 1969. Photosynthesis and fish production in the sea, *Science*, **166**, 72-76, doi:10.1126/science.166.3901.72.

Schwing, F., Bond, N., Bograd, S., Mitchell, T., Alexander, M., and N. Mantua, 2006. Delayed coastal upwelling along the US West Coast in 2005: A historical perspective, *Geophys. Res. Lett.*, **33**, doi:10.1029/2006GL026911.

Schwing, F., O'Farrell, M., Steger, M., and D. Checkley, 1996. Coastal upwelling indices, West Coast of North America, 1946-95, *Rep. NOAA-TM-NMFS-SWFSC-231*, U.S. Dep. Of Commer.

Seabra, R., Varela, R., Santos, A., Gómez-Gasteira, M., Meneghesso, C., Wethey, D., and F. Lima, 2019. Reduced Nearshore Warming Associated With Eastern Boundary Upwelling systems, *Front. Mar. Sci.*, **6**, doi:10.3389/fmars.2019.00104.

Seki, H., Takahashi, M., Hara, Y., and S. Ichimura, 1980. Dynamics of dissolved oxygen during algal bloom in Lake Kasumigaura, Japan, *Water Res.*, **14**, 179-183, doi:10.1016/0043-1354(80)90235-3.

Sekula-Wood, E., Benitez-Nelson, C., Morton, S., Anderson, C., Burrell, C., and R. Thunell, 2011. *Pseudo-nitzschia* and domoic acid fluxes in Santa Barbara Basin (CA) from 1993 to 2008, *Harmful Algae*, **10**, 567-575, doi:10.1016/j.hal.2011.04.009.

Sellner, K., Doucette, G., and G. Kirkpatrick, 2003. Harmful algal blooms: causes, impacts, and detection, *J. Ind. Microbiol. Biotechnol.*, **30**, 383-406, doi:10.1007/s10295-003-0074-9.

Send, U., Beardsley, R., and C. Winant, 1987. Relaxation from upwelling in the Coastal Ocean Dynamics Experiment, *J. Geophy. Res.*, **92**, 1683-1698, doi:10.1029/JC092iC02p01683.

Seubert, E., Gellene, A., Howard, M., Connell, P., Ragan, M., Jones, B., Runyan, J., and D. Caron, 2013. Seasonal and annual dynamics of harmful algae and algal toxins revealed through weekly monitoring at two coastal ocean sites off southern California, USA. *Environ. Sci. Pollut. Res*., **20**, 6878-6895, doi:10.1007/s11356-012-1420-0.

Shipe, R., Leinweber, A., and N. Gruber, 2008. Abiotic controls of potentially harmful algal blooms in Santa Monica Bay, California, *Cont. Shelf Res*., **28**, 2584-2593, doi:10.1016/j.csr.2008.08.003.

Sievanen, L., Phillips, J., Colgan, C., Griggs, G., Hart, J., Hartge, E., Hill, T., Kudela, R., Mantua, N., Nielsen, K., and L. Whiteman, 2018. *California's Coast and Ocean Summary Report*. California's Fourth Climate Change Assessment. Publication number: SUMCCC4A-2018-011.

Simpson, J., 1983. Large-scale thermal anomalies in the California Current during the 1982-83 El Niño, *Geophys. Res. Lett.*, **10**, 937-940, doi:10.1029/GL010i010p00937.

Simpson, J., 1984. El Niño-induced onshore transport in the California Current during 1982-1983, *Geophys. Res. Lett.*, **11**, 233-236, doi:10.1029/GL011i003p00233.

Skamarock, W., Rotunno, R., and J. Klemp, 2002. Catalina eddies and coastally trapped disturbances, *J. Atm. Sci*., **59**, 2270-2278, doi:10.1175/1520-0469(2002)059<2270:CEACTD>2.0.CO;2.

Smayda, T., 1997. Harmful algal blooms: Their ecophysiology and general relevance to phytoplankton blooms in the sea, *Limnol. Oceannogr,* **42**, 1137-1153.

Smayda, T., 2000. Ecological features of harmful algal blooms in coastal upwelling ecosystems, *S. Afr. J. mar. Sci*., **22**, 219-253.

Smayda, T. and V. Trainer, 2010. Dinoflagellate blooms in upwelling systems: Seeding, variability, and contrasts with diatom bloom behavior, *Prog. Oceanog*, **85**, 92-107, doi:10.1016/j.pocean.2010.02.006.

Smith, W., 1968. Upwelling, *Oceanography and Marine Biology Annual Rev*., **6**, 11-46.

Smith, W., 1981. A comparison of the structure and variability of the flow field in three coastal upwelling regions: Oregon, Northwest Africa, and Peru, in *Coastal Upwelling*, 107-118, edited by F. A. Richards, AGU, Washington, D. C.

Smith, W. and D. Sandwell, 1997. Global seafloor topography from satellite altimetry and ship depth soundings, *Science*, **277**, 1957-1962, doi:10.1126/science.277.5334.1956.

Song, H., Miller, A., Cornuelle, B., and E. Di Lorenzo, 2011. Changes in upwelling and its water sources in the California Current System driven by different wind forcing, *Dyn. Atmos. Oceans*, **52**, 170-191, doi:10.1016/j.dynatmoce.2011.03.001.

Spillane, M., Enfield, D., and J. Allen, 1987. Intraseasonal Oscillations in Sea Level along the West Coast of the Americas, *J. Phys. Oceanog.*, **17**, 313-325, doi:10.1175/1520-0485(1987)017<0313:IOISLA>2.0.CO;2.

Strub, P. and C. James, 2002a. Altimeter-derived surface circulation in the large-scale NE Pacific Gyres. Part 1: seasonal variability., *Prog. Oceanog*., **53**, 163-183, doi:10.1016/S0079-6611(02)00029-0.

Strub, P. and C. James, 2002b. Altimeter-derived surface circulation in the large-scale NE Pacific Gyres. Part 2: 1997-1998 El Niño anomalies, *Prog. Oceanog*., **53**, 185-214 doi:10.1016/S0079-6611(02)00030-7.

Strub, P. and C. James, 2002c. The 1997-1998 oceanic El Niño signal along the southeast and northeast Pacific boundaries – an altimetric view, *Prog. Oceanog*., **54**, 439-458, doi:10.1016/S0079-6611(02)00063-0.

Sturges, W., 1974. Sea level slope along continental boundaries, *J. Geophy. Res*., **79**, 825-830, doi:10.1029/JC079i006p00825.

Su, J., Xiang, B., Wang, B., and T. Li, 2014. Abrupt termination of the 2012 Pacific warming and its implication on ENSO prediction, *Geophys. Res. Lett.*, **41**, 9058-9064, doi:10.1002/2014GL062380.

Sutton, A., Sabine, C., Maenner-Jones, S., Lawrence-Slavas, N., Meinig, C., Feely, R., Mathis, J., Musielewicz, S., Bott, R., McLain, P., Fought, H., and A. Kozyr, 2014. A high-frequency atmospheric and seawater pCO_2 data set from 14 open-ocean sites using a moored autonomous system, *Earth Syst. Sci. Data*, **6**, 353-366, doi:10.5194/essd-6-353-2014.

Sverdrup, H., 1953. On conditions for the vernal blooming of phytoplankton, *J. Cons. Perm. Int. Explor. Mer*., **18**, 287-295.

Swain, D., Singh, D., Horton, D., Mankin, J., Ballard, T., and N. Diffenbaugh, 2017. Remote Linkages to Anomalous Winter Atmospheric Ridging Over the Northeastern Pacific, *J. Geophy. Res. Atmos.*, **122**, 12194-12209, doi:10.1002/2017JD026575.

Thomas, A., Brickley, P., and R. Weatherbee, 2009. Interannual variability in chlorophyll concentrations in the Humboldt and California Current Systems, *Prog. Oceanog*., **83**, 386-392, doi:10.1016/j.pocean.2009.07.020.

Thomson, R. and M. Krassovski, 2010. Poleward reach of the California Undercurrent extension, *J. Geophy. Res*. *Oceans,* **115**, doi:10.1029/2010JC006280.

Tibby, R., 1941. The Water Masses off the West Coast of North America, *J. Mar. Res*., **4**, 112-121.

Todd, R., Rudnick, D., Davis, R., and M. Ohman, 2011. Underwater gliders reveal rapid arrival of El Niño effects off California's coast, *Geophys. Res. Lett.*, **38**, doi:10.1029/2010GL046376.

Todd, R., Rudnick, D., and R. Davis, 2009. Monitoring the greater San Pedro Bay region using autonomous underwater gliders during fall of 2006, *J. Geophy. Res*., **114**, doi:10.1029/2008JC005086.

Tollefson, J., 2014. El Niño tests forecasters, *Nature*, **508**, 20-21.

Toniazzo T. and S. Woolnough, 2014. Development of warm SST errors in the southern tropical Atlantic in CMIP5 decadal hindcasts, *Clim. Dyn*., **43**, 2889-2913, doi:10.1007/s00382-013-1691-2.

Trenberth, K., Large, W., and J. Olson, 1990. The mean annual cycle in global ocean wind stress, *J. Phys. Oceanog.*, **20**, 1742-1760, doi:10.1175/1520-0485(1990)020<1742:TMACIG>2.0.CO;2.

Urton, J., 2014. Squid harvest has been bountiful in Monterey Bay, *Monterey Herald*, December 6, 2014, http://www.montereyherald.com/article/ NF/20141206/SPORTS/141209843.

Valle-Rodríguez, J. and A. Trasviña-Castro, 2017. Poleward currents from coastal altimetry: The west coast of Southern Baja California, Mexico, *Adv. Space Res*, **59**, 2313-2324, doi:10.1016/j.asr.2017.01.050.

Vaquer-Sunyer R. and C. Duarte, 2008. Thresholds of hypoxia for marine biodiversity, *Proc. Natl. Acad. Sci. U.S.A*., **105**, 15452-15457, doi:10.1073/pnas.0803833105.

Vazquez, H. and J. Gomez-Valdes, 2018. Wind relaxation and poleward flow events in the upwelling region off Baja California, Mexico, *Ciencias Marinas*, **44**, 59-70, doi:10.7773/cm.v44i2.2745.

Wallace, R. and C. Gobler, 2021. The role of algal blooms in community respiration in controlling the temporal and spatial dynamics of hypoxia and acidification in eutrophic estuaries, *Mar. Poll. Bull.*, **172**, doi:10.1016/j.marpolbul.2021.1129008.

Wang, D., Gouhier, T., Menge, B., and A. Ganguly, 2015. Intensification and spatial homogenization of coastal upwelling under climate change, *Nature*, **518**, doi:10.1038/nature14235.

Wang, S., Hipps, L., Gilles, R., and J. Yoon, 2014. Probable causes of the abnormal ridge accompanying the 2013-2014 California drought: ENSO precursor and anthropogenic warming footprint, *Geophys. Res. Lett.*, **41**, 3220-3226, doi:10.1002/2014GL059748.

Wang, Y., Walter, R., White, C., Farr, H., and B. Ruttenberg, 2019. Assessment of surface wind datasets for estimating offshore energy along the Central California Coast, *Renewable Energy*, **133**, 343-353, doi:10.1016/j.renene.2018.10.008.

Washburn, L., Fewings, M., Melton, C., and C. Gotschalk, 2011. The propagating response of coastal circulation due to wind relaxations along the central California coast, *J. Geophy. Res. Oceans,* **116**, doi:10.1029/2011JC007502.

Watts, R. and H. Kontoyiannis, 1990. Deep-Ocean Bottom Pressure Measurement: Drift Removal and Performance, *J. Atmos. Ocean. Technol.*, **7**, 296-306, doi:10.1175/1520-0426(1990)007<0296:DOBPMD>2.0.CO;2.

Weber, E., Auth, T., Baumann-Pickering, S., Baumgartner, T., Bjorkstedt, E., Bograd, S., Burke, B., Cadena-Ramírez, J., Daly, E., de la Cruz, M., Dewar, H., Field, J., Fisher, J., Giddings, A., Goericke, R., Gomez-Ocampo, E., Gomez-Valdes, J., Hazen, E., Hildebrand, J., Horton, C., Jacobson, K., Jacox, M., Jahncke, J., Kahru, M., Kudela, R., Lavaniegos, B., Leising, A., Melin, S., Miranda-Bojorquez, L., Morgan, C., Nickels, C., Orben, R., Porquez, J., Portner, E., Robertson, R., Rudnick, D., Sakuma, K., Santora, J., Schroeder, I., Snogdrass, O., Sydeman, W., Thompson, A., Thompson, S., Trickey, J., Villegas-Mendoza, J., Warzybok, P., Watson, W., and S. Zeman, 2021. State of the California Current 2019-2020: Back to the Future With Marine Heatwaves?, *Front. in Mar. Sci.*, **8**:709454, doi:10.3389/fmars.2021.709454.

Wei, X., Li, K., Kilpatrick, T., Wang, M., and S. Xie, 2021. Large-Scale Conditions for the Record-Setting Southern California Marine Heatwave of August 2018, *Geophys. Res. Lett.*, **48**, e2020GL091803, doi:10.1029/2020GL091803.

Welch, C. 2015. Mass death of seabirds in western US is 'Unprecedented', *National Geographic*, January 24 2015, http://news.nationalgeographic.com/news/2015/01/150123-seabirds-mass-die-off-auklet-california-animals-environment.

Wells, M., Trainer, V., Smayda, T., Karlson, B., Trick, C., Kudela, R., Ishikawa, A., Bernard, S., Wulff, A., Anderson, D., and W. Cochlan, 2015. Harmful algal blooms and climate change: Learning from the past and present to forecast the future, *Harmful Algae*, **49**, 68-93, doi:10.1016/j.hal.2015.07.009.

Werner, F. and B. Hickey, 1983. The role of a longshore pressure gradient in Pacific Northwest coastal dynamics, *J. Phys. Oceanog.*, **13**, 395-410, doi:10.1175/1520-0485(1983)013<0395:TROALP>2.0.CO;2.

Whitney, F., 2015. Anomalous winter winds decrease 2014 transition zone productivity in the NE Pacific, *Geophys. Res. Lett.*, **42**, 428-432, doi:10.1002/2014GL062634.

Wilkerson, F., Lassiter, A., Dugdale, R., Marchi, A., and V. Hogue, 2006. The phytoplankton bloom response to wind events and upwelled nutrients during the CoOP WEST study, *Deep Sea Res., Part II*, **53**, 3023-2048, doi:10.1016/j.dsr2.2006.07.007.

Winant, C., Beardsley, R., and R. Davis, 1987. Moored Wind, Temperature, and Current Observations Made During Coastal Ocean Dynamics Experiments 1 and 2 Over the Northern California Continental Shelf and Upper Slope, *J. Geophy. Res.*, **92**, 1569-1604, doi:10.1029/JC092iC02p01569.

Winant, C. and C. Dorman, 1997. Seasonal patterns of surface wind stress and heat flux over the Southern California Bight, *J. Geophy. Res.*, **102**, 5641-5653, doi:10.1029/96JC02801.

Winant, C., Dever, E., and M. Hendershott, 2003. Characteristic patterns of shelf circulation at the boundary between central and southern California, *J. Geophy. Res.*, **108**, doi:10.1029/2001JC001302.

Woodson, C. and S. Litvin, 2015. Ocean fronts drive marine fishery production and biogeochemical cycling, *PNAS*, **112**, 1710-1715, doi:10.1073/pnas.1417143112.

Woodworth, P. and D. Smith, 2003. A One Year Comparison of Radar and Bubbler Tide Gauges at Liverpool, *Int. Hydrograph. Rev*., **4**, 42-49.

Wyrtki, 1967. Circulation and water masses in the eastern equatorial Pacific Ocean, *Int. J. Oceanol.Limnol.*, **1**, 117-147.

Xiu, P., Chai, F., Curchitser, E., and F. Castruccio, 2018. Future changes in coastal upwelling ecosystems with global warming: The case of the California Current System, *Sci. Rep*., **8**, doi:10.1038/s41598-018-21247-7.

Zaba, K. and D. Rudnick, 2016. The 2014-2015 warming anomaly in the Southern California Current System observed by underwater gliders, *Geophys. Res. Lett.*, **43**, 1241-1248, doi:10.1002/2015GL067550.

Zaba, K., Rudnick, D., Cornuelle, B., Gopalakrishnan, G., and M. Mazloff, 2018. Annual and Interannual Variability in the California Current System: Comparison of an Ocean State Estimate with a Network of Underwater Gliders, *J. Phys. Oceanog.*, **48**, 2965-2988, doi:10.1175/JPO-D-18-0037.1.

Zaba, K., Rudnick, D., Cornuelle, B., Gopalakrishnan, G., and M. Mazloff, 2020. Volume and Heat Budgets in the Coastal California Current System: Means, Annual Cycles, and Interannual Anomalies of 2014-16, *J. Phys. Oceanog.*, **50**, 1435-1453, doi:10.1175/JPO-D-19-0271.1.

Zamudio, L., Hurlburt, H., Metzger, E., and C. Tilburg, 2007. Tropical wave-induced oceanic eddies at Cabo Corrientes and the María Islands, Mexico, *J. Geophy. Res.*, **112**, doi:10.1029/2006JC004018.

Zamudio, L., Hurlburt, H., Metzger, J., and O. Smedstad, 2002. On the evolution of coastally trapped waves generated by Hurricane Juliette along the Mexican West Coast, *Geophys. Res. Lett.*, **29**, 56-1-56-4, doi:10.1029/2002GL014769.

Zamudio, L., Leonardi, A., Meyers, S., and J. O'Brien, 2001. ENSO and eddies on the southwest coast of Mexico, *Geophys. Res. Lett.*, **28**, 13-16, doi:10.1029/2000GL011814.

Zamudio, L., Metzger, E., and P. Hogan, 2008. A note on coastally trapped waves generated by the wind at the Northern Bight of Panamá, *Atmósfera*, **21**, 241-248.

Zweng, M., Reagan, J., Antonov, J., Locarini, R., Mishonov, A., Boyer, T., Garcia, H., Baranova, O., Johnson, D., and D. Seidov, 2013. *World Ocean Atlas, Volume 2: Salinity*, S. Levitus, Ed., A. Mishonov Technical Ed.; NOAA Atlas NESDIS 74, 39 pp, doi:10.7829/V5251G4D.